DTIC FILE COPY

②

AD-A187 694

AFWAL-TR-87-1084

DIODE PUMPED FIBER LASER

A. CORDOVA-PLAZA, M.J.F. DIGONNET, K.A. FESLER, C.J. GAETA, S. PING and H.J. SHAW
Edward L. Ginzton Laboratory
Stanford University
Stanford, California 94305-4085

DTIC
ELECTE
NOV 3 0 1987
S
D
D

August 1987

Final Report for Period September 1984 - December 1986

3

REPORT DOCUMENTATION PAGE

Form Approved
OMB No 0704-0188

1a REPORT SECURITY CLASSIFICATION UNCLASSIFIED			1b. RESTRICTIVE MARKINGS			

2a SECURITY CLASSIFICATION AUTHORITY		3 DISTRIBUTION / AVAILABILITY OF REPORT
2b. DECLASSIFICATION / DOWNGRADING SCHEDULE		Approved for Public Release; Distribution is Unlimited

4. PERFORMING ORGANIZATION REPORT NUMBER(S)	5. MONITORING ORGANIZATION REPORT NUMBER(S) AFWAL-TR-87-1084

6a. NAME OF PERFORMING ORGANIZATION Edward L. Ginzton Laboratory Stanford University	6b. OFFICE SYMBOL (If applicable)	7a. NAME OF MONITORING ORGANIZATION Air Force Wright Aeronautical Laboratories Avionics Laboratory (AFWAL/AADO-1)
6c. ADDRESS (City, State, and ZIP Code) Stanford, CA 94305-4085		7b. ADDRESS (City, State, and ZIP Code) Wright-Patterson AFB OH 45433-6543

8a. NAME OF FUNDING / SPONSORING ORGANIZATION	8b. OFFICE SYMBOL (If applicable)	9. PROCUREMENT INSTRUMENT IDENTIFICATION NUMBER F33615-82-C-1749

8c. ADDRESS (City, State, and ZIP Code)	10. SOURCE OF FUNDING NUMBERS			
	PROGRAM ELEMENT NO. 62204F	PROJECT NO. 2001	TASK NO 01	WORK UNIT ACCESSION NO. 99

11 TITLE (Include Security Classification)

DIODE PUMPED FIBER LASER

12 PERSONAL AUTHOR(S)
A. Cordova-Plaza, M. J. F. Digonnet, K. A. Fesler, C. J. Gaeta, S. Ping, and H. J. Shaw

13a. TYPE OF REPORT Final	13b. TIME COVERED FROM 9-84 TO 12-86	14. DATE OF REPORT (Year, Month, Day) August 1987	15. PAGE COUNT 225

16. SUPPLEMENTARY NOTATION

17. COSATI CODES			18. SUBJECT TERMS (Continue on reverse if necessary and identify by block number)
FIELD	GROUP	SUB-GROUP	Nd:YAG Single Crystal Fibers Superfluorescence
20	05		Nd:YAG Fiber Lasers Nd:MgO:LiNbO$_3$ Crystal
20	06		Q-switched Lasers CW-Room-Temperature Laser (over)

19. ABSTRACT (Continue on reverse if necessary and identify by block number)

Q-switching in Nd:YAG fibers was investigated as a particularly interesting technique to generate narrow pulses in miniature solid state lasers. Laboratory models of both mechanically and passively Q-switched Nd:YAG fiber lasers were developed and characterized. The devices were made of a short length of end polished fiber placed between two miniature laser mirrors and optically end-pumped with a dye laser.

Mechanical Q-switching, achieved by modulating the orientation of one of the mirrors, led to the generation of pulse trains with 50 mW peak power and 70 nsec wide individual pulses. The pulse train structure was explained by the slow nature of the switching mechanism, and quantitatively predicted by a novel slow Q-switching theoretical model.

Passive Q-switching was realized in practice by placing a thin film of saturable absorber in the fiber laser cavity, thereby preserving the miniature character of the device. A record pulse width of 6 nsec and peak power of 2 watts were observed in state-of-the-art, Nd:YAG

20 DISTRIBUTION / AVAILABILITY OF ABSTRACT ☒ UNCLASSIFIED/UNLIMITED ☐ SAME AS RPT ☐ DTIC USERS	21. ABSTRACT SECURITY CLASSIFICATION UNCLASSIFIED	
22a NAME OF RESPONSIBLE INDIVIDUAL K. SCHEPLER	22b TELEPHONE (Include Area Code) (513) 255-3084	22c OFFICE SYMBOL AFWAL/AADO-1

DD Form 1473, JUN 86   Previous editions are obsolete.   SECURITY CLASSIFICATION OF THIS PAGE

18. Subject Terms (Cont'd)

Diode Pumped Laser
Photorefractive Damage
Electro-optically Q-switched Laser
Photoconductive Screening Field

19. Abstract (Cont'd)

waveguiding fibers, which is the first report of nanosecond pulse generation in single crystal fibers.

CW and Q-switched laser operation were achieved in $Nd:MgO:LiNbO_3$. True-CW, room temperature laser oscillation was demonstrated for both the high (π) and the low-gain polarizations with thresholds as low as 2 and 3.9 mW respectively. Up to 22 mW output with only 70 mW input and a record slope efficiency of 45% were attained. It was shown that photorefractive damage is almost non-existent in these lasers when pumped in the near infrared, a significant improvement over past non-MgO doped, $Nd:LiNbO_3$ lasers. A laser characterization of $Nd:MgO:LiNbO_3$ showed that it is as good a laser material as Nd:YAG. Two types of laser diodes were characterized. One of them was used to demonstrate laser diode-pumped oscillation in $Nd:MgO:LiNbO_3$.

The integration of an electro-optic cell and a laser medium was achieved in the "Active Internally Q-switched Laser," which emitted 30 nsec pulse widths, 5 W peak power pulses and had 10 mW threshold and less than 300 V switching voltage. A strong screening field (1.5 kV/cm or higher) of photoconductive origin was generated in time intervals of 25-50 nsec. This field was eliminated by applying the voltage as pulses of alternative polarity. The elasto-optically induced loss was shown to have negligible influence when pumping more than three times above threshold.

The laser mode overlap theory was extended to cover the case of resonators not entirely filled by the active medium and the case of time-dependent cavity loss. Comparisons of numerical simulations with the experimental results indicate that further refinement of the theory to include spatially non-uniform gain saturation is necessary.

$Nd:MgO:LiNbO_3$ single crystal fibers were grown and processed for the first time. Difficulties associated with growth, annealing, surface granularity, spurious colorations, mounting and end-face polishing were satisfactorily solved. The first successful fabrication of electrodes on a single crystal fiber was achieved. Lasing threshold was not reached in these fibers. It was theoretically shown that fiber-cladding should reduce the scattering loss by orders of magnitude, thus allowing for efficient fiber lasers.

Superfluorescence emission in Nd:YAG fibers was studied in optically end-pumped fibers of various diameters down to the minimum diameter available in the state-of-art. Emitted fluorescence signals of up to 5 mW were observed, at an emission energy efficiency of a few percent. The signal was typically distributed over a larger number of fiber modes, so that its coupling to a single mode silica fiber was on the order of 0.1%. This study clearly points to the need for near single mode active fibers, such as diffusion-clad $Nd:LiNbO_3$ fibers, to reach superfluorescence threshold.

A miniature, monolithic optical isolator operating at 1.3 µm suitable for use with fiber lasers, and optical fiber systems in general, was designed and constructed. The spectral purity of a fiber laser developed earlier under this contract was measured experimentally with and without the isolator under conditions where optical feedback was present. Spurious sidebands in the output of the fiber laser caused by optical feedback were observed to drop by approximately 50 dB when using the optical isolator.

TABLE OF CONTENTS

A-1

- iii -

Table of Contents (continued)

Table of Contents (continued)

Table of Contents (continued)

Table of Contents (continued)

LIST OF ILLUSTRATIONS

Figure

LIST OF TABLES

I. INTRODUCTION

This is the final report for Contract F33615-82-C-1749, covering the period September 17, 1984 to December 31, 1986. It is concerned with both continuous wave and pulsed lasers in miniature form which can be pumped with laser diodes, which operate at room temperature without cooling, and are capable of coupling efficiently to standard single mode optical glass fibers. In many cases these lasers are entirely in fiber optic form.

The report first describes research on pulsed (Q-switched) lasers in fiber optic form using fibers of single crystal yttrium aluminum garnet (YAG) doped with neodymium. It next covers work on both continuous wave and Q-switched lasers, using both miniature bulk crystals and single crystal fibers of lithium niobate ($LiNbO_3$). The lithium niobate samples are doped with magnesium oxide to reduce photofractive damage, and also doped with neodymium for laser action. Studies of internal optical modulation in lithium niobate for purposes of internal Q-switching of lasers using this material are described. This work uses the electro-optic properties of lithium niobate in both bulk and fiber samples.

We report efficient CW and pulsed laser action in miniature bulk samples of lithium niobate, as was the case for both bulk and fiber samples of yttrium aluminum garnet. However, the state-of-the art of lithium niobate fibers is such that we were not able to achieve laser action in lithium niobate fibers. The latter fibers are much more difficult to grow and process in the forms needed for laser work. Although the technology of lithium niobate fiber fabrication is advancing rapidly, much of it under other auspices in this laboratory, the status reached by the end of this contract did not allow laser action in these fibers. It is expected that the necessary status will be realized in the near future. This will then allow the techniques for both CW and pulsed operation, described in Section III of this report, to be applied directly to lithium niobate fibers having low lasing thresholds.

The report next describes attempts to observe superfluorescent emission from single crystal fibers of neodymium doped YAG. Here the state-of-the-art of YAG fibers comes into play; although it advanced substantially toward the end of the contract, fibers of sufficiently small core size together with adequate diameter control did not become available in time. The measurements made with the fibers available show the fiber requirements, and the techniques developed will allow these superfluorescent sources to be realized as soon as these requirements are met.

The last section describes a new and efficient miniature monolithic yttrium aluminum garnet Faraday isolator for stabilizing lasers used to power fiber optic circuits.

II. FIBER LASERS USING Nd:YAG

A. Introduction

In previous segments of this contract Nd:YAG fibers have been studied exten-
sively as continuous wave guided oscillators operated in the near-infrared spectral
range. Over a period of several years theoretical and experimental investigations
have led to the development of laboratory models of CW fiber lasers exhibiting
output power and efficiency characteristics well beyond initial expectations. At the
outset of the contract covered by this report lasers were routinely operated at either
1.06 μm or 1.32 μm with several tens of milliwatts of output power and excitation-
to-signal energy conversion efficiencies in the 30 to 80% range. A variety of pump
sources have been successfully implemented to excite these fibers, including single
stripe laser diodes, demonstrating the potential of Nd:YAG fiber lasers as miniature,
self-contained coherent sources.

For obvious reasons it was decided that a natural extension of this work would
be the demonstration of Q-switched fiber lasers. This issue was addressed in the
previous part of this contract in the form of a detailed feasibility study. This study
provided a theoretical prediction of Q-switched pulse characteristics, as well as the
identification of two basic Q-switching schemes compatible with the compactness
of a fiber laser cavity.

A typical fiber laser cavity was made of a short Nd:YAG fiber with polished
and antireflection coated ends, placed between two flat laser mirrors. Each mirror
was mounted on a gimbal mount for cavity alignment purposes. The fiber was
excited with the beam of a pump source (usually a tunable dye laser) focused into
the fiber through the back mirror. The first, and simplest, Q-switching method to
implement in a fiber laser was mechanical modulation of the optical alignment of one
of the cavity mirrors, in a manner analogous to the rotating prism method. In this

3

scheme one of the mirrors was mounted on a vibrating assembly, which provided a periodic modulation of the mirror angular deflection in a direction perpendicular to the cavity optical axis.

The second Q-switching method was a passive scheme which involved the introduction of a thin film saturable absorber in the cavity. As is well known from standard Q-switching theory,the intensity dependent optical transmission of saturable absorbers is such that they can lead to the generation of very short Q-switched and mode locked laser pulses.

This and the following section of this report present the results of experimental investigations of these two Q-switching methods, applied to Nd:YAG fibers at 1.064 μm. A short summary of the status of single crystal fiber growth and preparation available during this contract is first presented below as background material for the reader.

B. General Status of Crystal Fiber Development

1. Crystal Fiber Growth

The single crystal fibers used in this work, as well as in other work reported in this report, were grown by the laser heated pedestal growth technique. The principle of this technique is outlined in Figure 2.1. A fiber is grown from a melt, produced from a source material heated by a CW CO_2 laser. The source material (crystal or amorphous) is a small ($\sim$ 1-3 cm) cylindrical rod, onto which the CO_2 laser beam is focused to form a melt zone held onto the source material by surface tension. An oriented crystal seed is dipped into the melt, then slightly pulled to form a molten zone of suitable shape. The seed (fiber) is then drawn at constant speed from the melt, while the source rod is moved upward to feed material into the melt. During growth the equilibrium shape of the melt exhibits the characteristic shape shown in Figure 2.1. The ratio of the source to fiber translation rates determines the ratio of

4
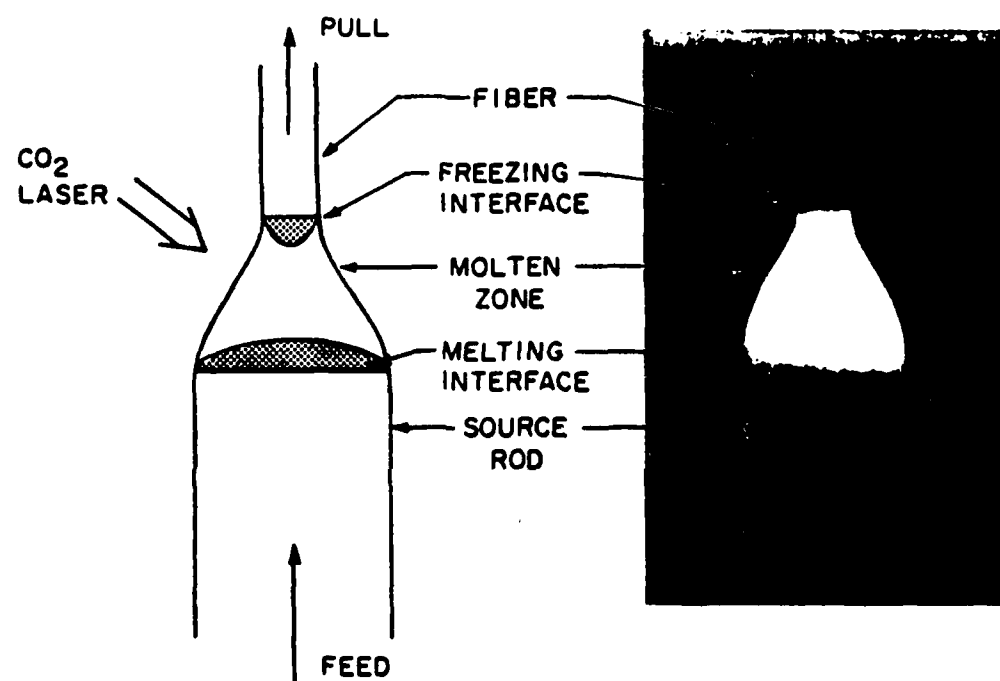
Figure 2.1--Schematic Diagram and Corresponding
Microphotography of Fiber Growth.

their diameters through mass conservation. For stable growth, the fiber pulling rate is usually chosen to be on the order of one millimeter per minute, with a diameter reduction of three to one.

During the course of this contract two crystal fiber growth stations developed at Stanford University under partial Air Force Force support were available. The first one has been extensively described in previous interim reports. The second station was developed at a later time under Professor R. L. Byer's supervision. This second generation station incorporated the basic features of the first station, together with a number of significant modifications which contributed to improvements in crystal fiber quality. This second station, with few exceptions, was therefore used for the generation of the fibers reported herein.

It is known[1] that waveguide loss may arise from optical scattering produced by fiber diameter variations. In order to achieve a constant diameter fiber, a stable fiber growth condition must be achieved, in particular excellent mechanical stability, constant source and fiber translation rates, stable laser power and symmetric heat distribution in the melt zone. The second generation station was designed to better meet these requirements, with a view towards producing fibers with greater diameter stability. The heat source is a 15 watt polarized waveguide CO_2 laser exhibiting power fluctuations of less than 1%. An electro-optic modulator (EOM) controls the input power over a dynamic range greater than 100:1. An optical system focuses the laser beam onto the fiber with a 360° symmetry (to ensure a symmetric heat distribution) using a set of reflective axially symmetric components. The focal spot size can be as small as 30 microns to make the growth of small diameter fibers possible. The fibers are translated parallel to themselves using a motor-drive belt and drive system. The diameter measurement system implements a non-contact

[1] M. J. F. Digonnet, C. Gaeta, D. O'Meara, and H. J. Shaw, "Clad Nd:YAG Fibers for Laser Applications," IEEE Journal of Lightwave Technology, 5, 5, 642-646 (May 1987).

interferometric principle to measure the fiber diameter just above the melt zone, and provides a measurement resolution of 1 part in 10^3. The diameter control system sends the diameter information to an electronic system, which provides an error signal to adjust the motor translator speed.

To grow Nd:YAG fibers the original material is a Nd:YAG rod (with 1% Nd) which is cut from a bulk cyrstal, then ground on a centerless grinder to a 400 μ diameter rod. Rod diameters are rather uniform, with variations less than 3.0% along a one inch length. In order to avoid contact between rod surfaces and the driving belt, the rods are usually mounted in a glass capillary (41 mm length, 500 μm inner diameter tube) to make them translate more smoothly through the belt drive system.

Good quality seed fibers must be chosen to initiate the growth, whose orientation is <111>. Because of details of the operation of the diameter measurer, setting the angular orientation of the seed in the right position is essential and often takes several attempts.

Fiber diameter stability is a function of the diameter reduction between the source rod and the fiber, the molten zone size and the material being grown. Large diameter reductions yield oscillatory fiber diameter variations which ultimately terminate the growth. However, small diameter reductions increase the number of growths to attain a small diameter fiber. A suitable compromise for the reduction ratio is 3:1. For Nd:YAG the growing speed is chosen to be 0.5 to 1.5 mm/min. Other factors that influence the diameter stability are the incident laser power and the heat distribution stability of the molten zone. For this purpose the laser water cooling temperature and room temperature were kept constant to 0.1 °C and 0.5 °C, respectively. Once the fiber growth is initiated, the voltage applied to the E.O. modulator is adjusted to maintain the laser power at the same level.

7

2. Fiber Cladding

Diameter variations perturb the waveguide and can lead to mode conversion in the fiber and coupling to radiation modes.[2] Both mechanisms contribute to a higher loss in the fiber. Decreasing the index difference between the single crystal fiber and the surrounding material can reduce this effect. Placing a cladding material around the fiber with an index close to but less than that of the core will accomplish this objective. The other purpose of a cladding is to decrease the number of guided modes that the fiber can support for a given core radius.

The problems of providing single crystal fibers with a suitable cladding have been addressed for some time under support from Litton Systems, Inc. Efforts have been focused mostly on Nd:YAG and LiNbO$_3$ because of their practical importance. For Nd:YAG both sputtering and extrusion methods have been examined for the deposition of high index glasses. As described in detail elsewhere, the latter was very successful leading to mechanically strong cladding layers and a ten fold loss reduction. An alternative method is diffusion, by which chemical ions are diffused in the crystal fiber outer layer so as to reduce the core radius and produce a lower index outer region. In LiNbO$_3$, the proton exchange and MgO doping by diffusion are promising techniques to achieve step or graded index cladding, and are now under study under other contracts. Diffusion techniques have not yet been applied to Nd:YAG.

Some of the Nd:YAG fibers reported in the following were clad with high index glass under a contract with Litton Systems, Inc., and made available for use in the present program. The glass was deposited onto the fibers using an extrusion process, which provided 50-250 μm thick cladding layers. The glass material used was LA SF30, yielding a step index profile with a step of approximately $\Delta n = 0.045$.

[2] D. Marcuse, "Theory of Dielectric Optical Waveguides," Academic Press, 1974.

3. Fiber Polishing

Prior to optical characterization all fibers had their ends polished by standard mechanical means. In the course of this contract the method used to mount the fiber during the polishing operations was slightly altered to improve end quality. To improve fiber stability the fibers are bonded individually (as opposed to arrays, as done in earlier days) into a close fitting glass capillary. To minimize the amount of (soft) adhesive surrounding the fiber, and thereby facilitate the polishing operations, the tube inner diameter was chosen to be only one or two mils (25 to 50 μm) larger than the fiber diameter. For sub-80 μm diameter fibers, the fiber insertion into the capillary tube was generally difficult. One of the capillary openings was thus slightly widened with a controlled chemical etch in hydrofluoric acid. The capillary tube was held above a plastic rack into which enough HF was poured to reach the bottom of the capillary. For 3 mil and 2 mil capillaries an etching time of one and two hours, respectively, was adequate to obtain suitable openings. This method greatly improved the process reliability by preventing the fiber from accidentally breaking during insertion.

A UV-curing adhesive was used to bond the fiber in the capillary tube. These adhesives are harder than traditional adhesives such as wax, which is helpful in the polishing process. Capillary action was generally not strong enough to pull the adhesive into the tube. The fiber had to be inserted in and out of the tube several times to feed the adhesive inside the tube. The epoxy was hardened by a 20 minute exposure to UV light, at which point polishing could be initiated. Standard grinding and polishing techniques were used for this purpose which provided smooth fiber end faces with typically better than $\lambda/4$ flatness and regular fiber edges.

C. Mechanically Q-switched Fiber Lasers

1. Theoretical Considerations

As described in the introduction, mechanical Q-switching of a single crystal fiber laser cavity involved the mechanical modulation of the optical alignment of one of the cavity mirrors. For this purpose one of the mirrors was mounted on a vibrating assembly. This assembly provided a temporally sinusoidal modulation of the mirror angular deflection with respect to the cavity optical axis. The vibration axis was therefore perpendicular to this axis. Only twice during each cycle was the mirror truly aligned with the cavity axis; this position corresponded to the minimum cavity loss. The generation of a Q-switched pulse occurred when the mirror was in the vicinity of this low loss position. During the remaining of the cycle the cavity loss was high and the population inversion was allowed to build up for the next pulse.

Assuming that the mirror is properly aligned when the angular deflection of the mirror is zero at time $t = 0$, the motion of the mirror may be described by

$$\phi = \phi_{max} sin(2\pi f t) \qquad (2.1)$$

where ϕ_{max} is the maximum angular deflection and f the vibration frequency.

Under the condition that oscillation starts to occur when the mirror is aligned to within $\delta\phi$ of the condition $\phi = 0$ for perfect alignment (and minimum loss), the switching time δt (from the off to the on state) is approximately given by

$$\delta t = \frac{\delta\phi}{\phi_{max}} \frac{1}{2\pi f} \qquad (2.2)$$

where we made use of Equation (2.1) assuming that ϕ is small.

In order to assure that only a single pulse is generated, the vibration frequency

must be high enough so that the mirror does not remain aligned much longer than some maximum time interval Δt_{on}. This sets a lower limit to f through Equation (2.2):

$$f_{min} = \frac{\delta\phi}{\phi_{max}} \frac{1}{2\pi\Delta t_{on}} \tag{2.3}$$

A second requirement is that there be enough time between the *on* states ($\phi = 0$) for the population inversion to build up to near its steady state value. For quasi-cw pumping to be realized the time between *on* states must be at least equal to the upper laser state lifetime τ_f, so that

$$f_{max} = \frac{1}{2\tau_f} \tag{2.4}$$

There combined requirements restrict the practical vibration frequency range to

$$\frac{\delta\phi}{\phi_{max}} \frac{1}{2\pi\Delta t_{on}} \lesssim f \lesssim \frac{1}{2\tau_f} \tag{2.5}$$

Past experience with mechanically chopped Nd:YAG lasers indicates that a switching time on the order of $\Delta t_{on} = 5\mu sec$ is enough to generate a single Q-switched pulse, while cavity alignment normally needs to be achieved to $\delta\phi = 0.1°$. Also, the commercial vibrating mirror used in our experiments has a maximum angular deflection $\phi_{max} = 2°$. This yields a minimum frequency requirement $f_{min} = 1.6$ kHz. The maximum frequency limit, taking $\tau_f = 236\mu sec$ for Nd:YAG, is $f_{max} = 2.2$ kHz. These approximate figures show that a frequency in the range of 1 to 3 kHz should be adequate.

For a typical mirror of dimension l_m along a direction perpendicular to the rotation axis, positioned at a distance d_m away from the end of the fiber, ϕ_{max} must be bounded according to

11

$$\phi_{max} < sin^{-1}\left(\frac{2d_m}{l_m}\right) \qquad (2.6)$$

so that the mirror will not come in contact with the fiber mounting jig at maximum deflection. In our fiber lasers, the mirror has a transverse dimension of 1 mm and is located at least 20 μm from the fiber end-face. Equation (2.6) indicates that the maximum deflection of the mirror must not exceed 2.3°.

The above considerations led us to select a commercially available resonant vibrating assembly with a 2° maximum deflection angle, and a vibration frequency of 2 kHz. In this unit the vibrating element was a small torsional rod onto which the mirror was bonded. The entire assembly was small, about 5 cubic inches, and very light, and was easily mounted on an asjustable tilt micropositioner for cavity alignment purposes.

2. Experimental Arrangement

In the following the fiber laser cavity was made of two flat mirrors (2 × 2 × 0.5 mm) mounted on gimbal mounts, between which the fiber was positioned with a 4 axis micropositioner (2 rotation and 2 linear axes). The back mirror was a high reflector (R > 99.5%) at the signal wavelength (1.064 μm), while the front mirror, through which energy is extracted from the cavity, had a transmission $T_1 \simeq 0.65\%$.

In mechanical Q-switching experiments the back mirror of the Nd:YAG fiber laser was mounted on the torsion bar of a torsional optical scanner. The other end of the torsion bar was fixed. A moving iron armature located near the fixed end excited the rod so that resonance occurs at some natural frequency. In this scheme the frequency was fixed at around 2 kHz. The scanning assembly was mounted on a tilt stage for mirror alignment purposes.

Unless otherwise specified, an argon ion laser tuned to 0.5145 μm served as a pump source. The pump beam was focused onto the fiber through the back mirror

with a single lens. The output signal from the fiber laser was filtered to eliminate the unabsorbed pump light, then sent onto a silicon detector. For cw measurements a large area calibrated EG&G model 550 power meter was used. For Q-switched pulse characterization it was replaced by a small area reversed bias (- 60 V) Si detector with a 0.5 nsec rise time, followed by a 40 dB amplifier and a storage oscilloscope. In this case the laser output was focused onto the small sensitive area to detect all the emitted photons.

Alignment of the mechanically Q-switched cavity proceeded as follows. First, the fiber laser was aligned under cw pumping conditions, with the optical scanner turned off. For this purpose the argonlaser beam was amplitude modulated with a ~ 25 kHz mechanical chopper to reduce its duty cycle (to 3.4%), thereby eliminating the danger of damaging the epoxy surrounding the fiber during initial alignments. After observing quasi-cw laser oscillation, the oscillation threshold was lowered to acceptable levels for cw pumping operation. The chopper was then turned off and the cavity further optimized under cw pumping conditions. At this time the back HR mirror tilt angle was modulated horizontally using the torsional optical scanner.

3. Test Fibers

The fibers tested in the mechanically Q-switched mode included the four fibers of Array No. 17, numbers 17-1 through 17-4, and Fiber No. 23. The fiber characteristics are listed in Table 2.1. Array No. 17 contains fibers clad in epoxy, while Fiber No. 23 is the first LaSF30 glass clad fiber which was successfully brought to CW oscillation. As mentioned elsewhere in this report, these clad fibers were clad under programs funded by other auspices, which made these fibers available to this contract for its own investigations. Also listed in Table 2.1 are the characteristics of a bulk Nd:YAG sample tested for comparison purposes. In the bulk laser the front mirror was replaced by a 5 cm radius of curvature mirror to make the cavity

13

Table 2.1

Nd:YAG Fibers Tested as Mechanically Q-switched Fiber Lasers

Fiber	Diameter (μm)	Cladding	ℓ (mm)
Array No. 17	170	Epoxy	
No. 23	135	LaSF30 Glass	
Bulk	2000 $\times$ 2000	Air	7.5

optically stable.

4. CW Laser Characterization

Prior to the Q-switching experiments, data were taken for each fiber laser as well as for the bulk laser under cw pumping, non Q-switched conditions. As described elsewhere, the characteristic output curve (output power P_{out} versus absorbed pump power P_{abs}) of these devices grows linearly, with a conversion slope efficiency s, above a threshold pump power P_{th}. The output beam of all cw lasers was found to have a clean, Gaussian intensity profile, indicating that the lasers were oscillating on the fundamental mode (TEM$_{00}$ for the bulk laser, and LP$_{01}$ for the fiber lasers).

Although Nd:YAG fiber lasers have generally very good characteristic curves, with slope efficiencies in the range of 10%-50% and thresholds as low as a few mW, the fibers tested under this part of the program yielded fairly poor results. Their thresholds were somewhat higher (10-40 mW) than optimum, and their slope efficiencies on the order of 1/4 to 2%. As we shall see later this situation had a strong bearing on the Q-switching results. No attempt was made to correct this situation to enable research efforts to move on to the potentially more appealing passive Q-switching scheme (see Section I.B.).

5. Experimental Characterization of Q-switched Lasers

5.1 Fiber Lasers

Mechanically Q-switching fiber lasers were successfully achieved for all the samples listed in Table 2.1. As predicted by theory, the threshold of oscillation under Q-switching conditions was found to be approximately the same as that under CW conditions. As anticipated, the relatively slow loss modulation offered by this type of switching led to the generation of more than one pulse. A certain amount of pulse-to-pulse jitter was also found to be present, as the time of onset of the train and the exact distribution of energy among the pulses were sensitive to the small fluctuations in the pump power and in the scanner speed. This jitter was eliminated from our measurements by storing single sweeps on the oscilloscope.

We show in Figure 2.2 a typical train of output pulses obtained with Fiber 17-1 pumped about 5 times above threshold. The first, left-most pulse in the figure is the main pulse. It is the most stable and carries the most energy. The number and amplitude of the secondary pulses, which varied slightly from shot-to-shot, were pump power dependent. The pulse repetition frequency was about 3.8 kHz (corresponding to T = 265 μsec between pulses). The oscillation frequency of the torsion bar was around 2 kHz but since it passed through the rest position (high laser cavity Q position) twice during each cycle, the loss modulation of the laser cavity occurred at twice this frequency.

The main pulse was further expanded in Figure 2.3. The full width at half maximum power (FWHM) is approximately 73 nsec for this pump power level. Using a standard triangular approximation, the pulse width Δt_p defined in the theory as the full width of the base of the triangle fitted to the pulse, is $\Delta t_p \simeq 140$ nsec.

Let $\overline{P}$ be the average power emitted by the laser. If all the energy of a pulse train was contained in a single pulse, the peak power of that pulse would be
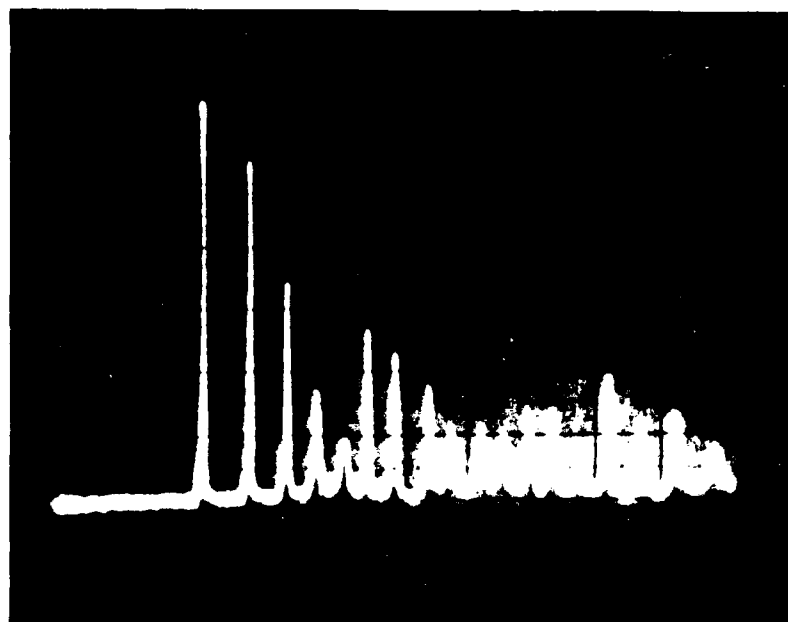
Figure 2.2--Q-switched Pulse Packet from Fiber
No. 17-1 Pumped Five Times Above
Threshold (2 μsec/div).
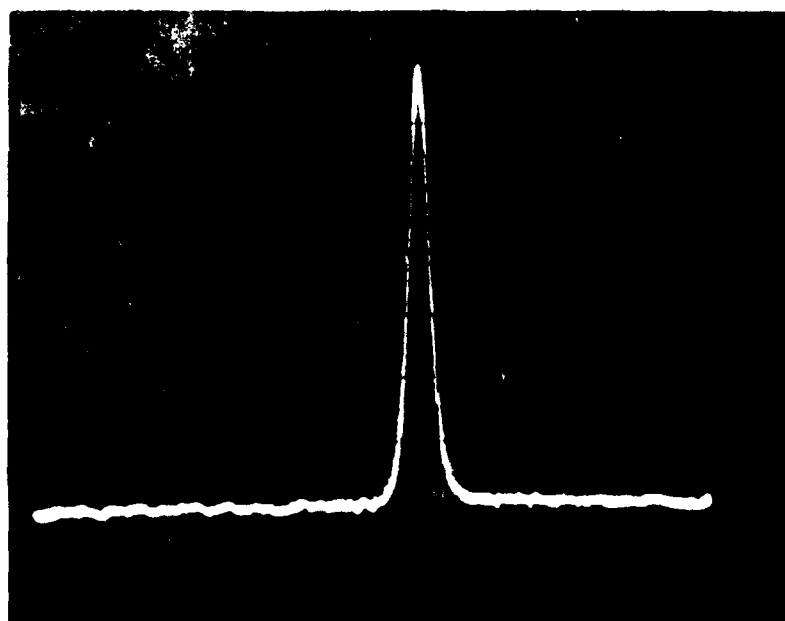
Figure 2.3--Main Pulse in a Q-switched Pulse
Packet from Fiber No. 17-1 (200
nsec/div).

Table 2.2

Q-switched Data for Fiber No. 17-2

P_{abs} (mW)	$\overline{P}$ (μW)	Δt_p (ns)	FWHM (ns)	P_{ep} (mW)	P_{max} (mW)	E (nJ)	No.
6.4	1.7	214	114	4.2	1.1	0.1	15
8.5	74	214	114	183.3	31.6	3.4	18
13.1	118	193	93	324.0	29.6	2.9	28
17.1	176	129	71	723.1	52.5	3.4	36

$$P_{ep} = \frac{2T}{\Delta t_p} \overline{P} \qquad (2.7)$$

where T is the period between pulses. The average power at $\lambda_s = 1.064 \, \mu m$, measured by focusing the laser output into a calibrated Photodyne detector, was $\overline{P} = 88 \, \mu W$. If only one pulse existed in each pulse packet the peak power would have been $P_{ep} = 333 \, mW$. However, the actual peak power in the main pulse was about 58.3 mW. This shows that about 17.5% of the emitted energy resided in the main pulse in this particular situation.

We show in Table 2.2 the energy distribution characteristics of the Q-switched pulse train obtained with fiber 17-2, which yielded the best results of all tested fibers. In this fiber the pump power was increased up to 17 mW, corresponding to 3-5 times above threshold. Assuming a single pulse operation the peak power varied from 4.2 mW to 723 mW as the absorbed pump power was increased from 6.4 mW to about 17 mW. The FWHM pulse width was 71 nsec at the maximum pump power, and the pulse train energy 47 nJ. Actually, a 36 pulse packet was observed at this pump power level. A peak power of 53 mW (3.4 nJ) was measured for the main pulse. Note that only the energy in the main pulse is listed in the table, not the total energy.

Figures 2.4, 2.5, and 2.6 plot the evolution with excitation power of three of the quantities listed in Table 2, namely the average power $\overline{P}$, the pulse width Δt_p,
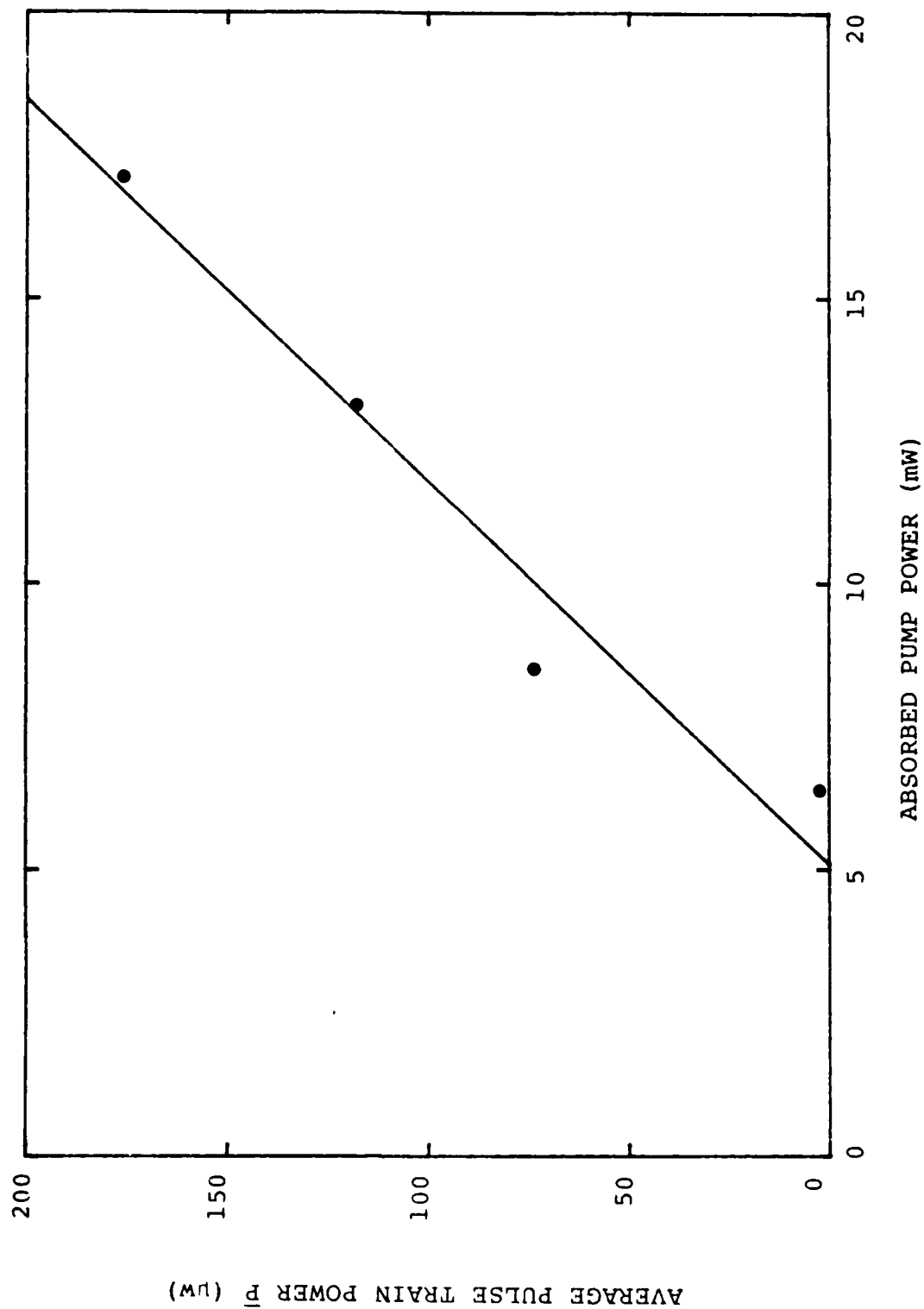
Figure 2.4--Average Pulse Train Power versus Absorbed Pump Power for Fiber No. 17-2 Pumped at 514.5 nm.

PULSE WIDTH vs PUMP POWER

PUMP POWER COUPLED INTO FIBER (mW)

$\lambda_p = 0.5145 \ \mu m$

ABSORBED PUMP POWER (mW)
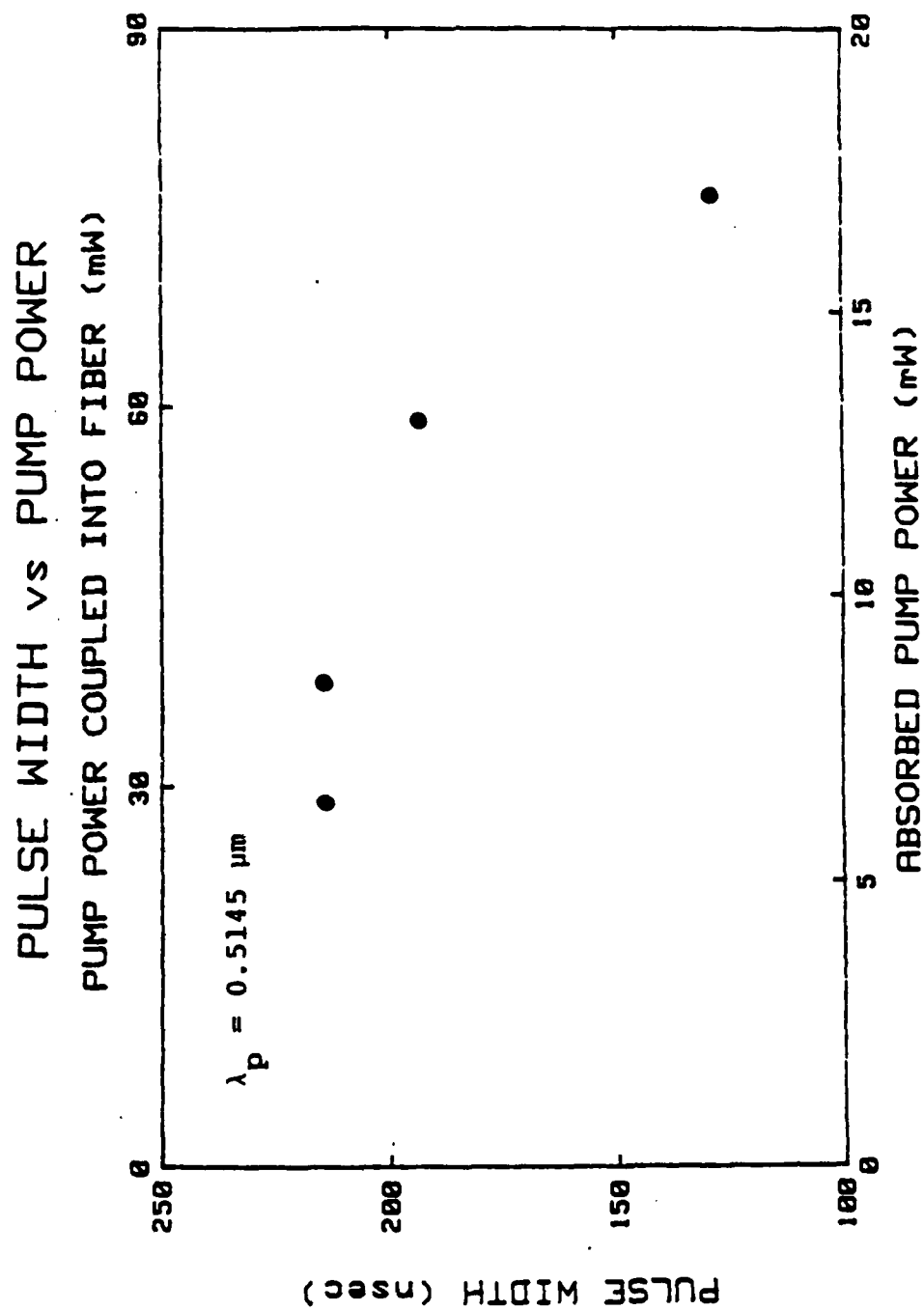
PULSE WIDTH (nsec)

Figure 2.5--Pulse Width Δt_p as a Function of the Pump Power for Fiber No. 17-2.
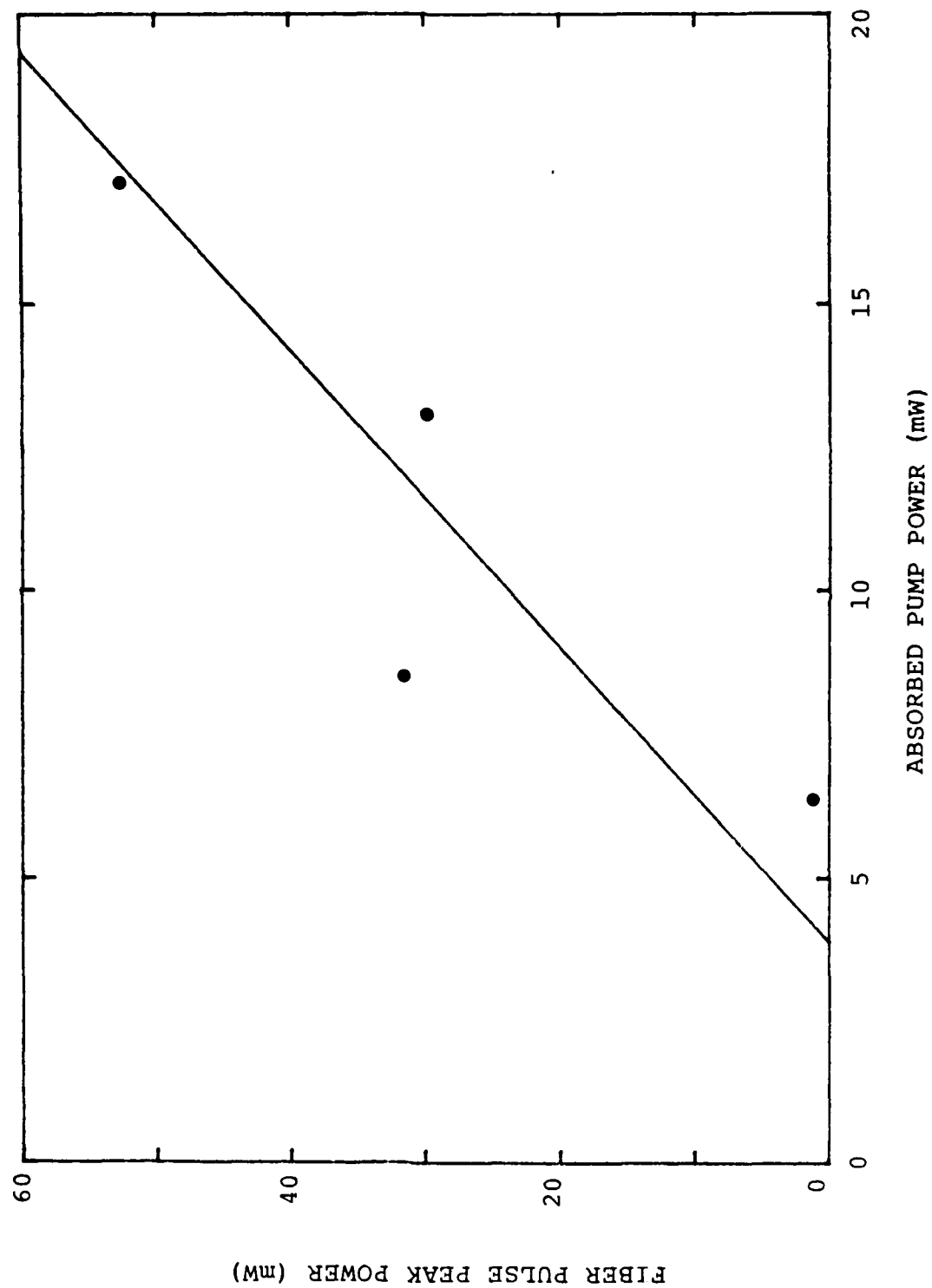
Figure 2.6--Peak Power (in the First Pulse) versus Absorbed
Pump Power in Fiber No. 17-2 Pumped at 514.5 nm.

and the peak power of the main pulse P_{max}. In Figure 2.4, the average power is seen to increase almost linearly with P_{abs}, as expected. The total energy conversion effficiency, defined as

$$s_E = \frac{\overline{P}}{P_{abs} - P_{th}} \tag{2.8}$$

is equal to the slope of this curve, approximately 0.015, or 1.5%. This figure compares favorably with the value of 1.8% measured for the (power) slope efficiency of this fiber oscillating under cw conditions.

The pulse width (Figure 2.5) was found to decrease with increasing pump power, as anticipated, although details of this curve varied from fiber to fiber. In principle, as the pump power is increased the pulse width should decrease, then level off at some minimum value, yielding a curve which is concave. The discrepancy observed for certain fiber lasers, in particular in Fiber No. 17-2, is not well understood, although it is believed that it is related to the low speed of the Q-switching mechanism and the presence of multiple pulses. In the far above threshold limit, the pulse width should be approximated by

$$\Delta t_p = \frac{4n\ell}{c\delta_0} \tag{2.9}$$

where n = 1.82 (material index), $\ell \simeq$ mm (cavity length) $c = 3 \times 10^{10} cm/sec$, and δ_0 is the cavity loss. For typical values of the loss coefficient in the range of 0.1-1.0, Δt_p should be on the order of 0.2-2.0 nsec. The values of the pulse width that we measured are two orders of magnitude higher than predicted for a fast Q-switching mechanism, which was expected since the loss modulation frequency is unusually low in this type of mechanical Q-switch. Clearly, disagreement with our fast switching model was to be expected.

The peak power of the main pulse was found to grow nearly linearly with absorbed pump power (Figure 2.6), as anticipated. However, the absolute value of

Table 2.3

Q-switched Data for Miniature Bulk Laser

P_{abs} (mW)	$\overline{P}$ (μW)	Δt_p (ns)	FWHM (ns)	P_{sp} (W)	P_{max} (W)	E (nJ)	No.
48.0	54	79	43	0.36	0.22	8.7	3
61.7	189	50	29	2.0	0.66	16.5	10
77.3	320	48	28	3.5	0.95	22.9	14
92.0	452	48	28	5.0	1.1	26.4	17

the peak powers generated with this (and other) fiber lasers is much smaller than expected from our model. Again we believe the fact that a slow Q-switch was used is responsible for this situation. This problem will be further addressed in a later section.

5.2 Bulk Laser

Tests of the mechanically Q-switched bulk crystal laser were performed by placing the crystal (see Table 2.1) in the same cavity, after replacing the output coupler by a curved mirror. The radius of curvature of this mirror (R = 5 cm) and the pump mode size ($W_{o,p} \simeq 20 \, \mu$m) were chosen to minimize the laser threshold (within the range of reasonable parameters) following a theoretical model developed under earlier phases of this contract.

Experimental Q-switching results for this miniature bulk laser are shown in Table 2.3. The parameters are the same as in Table 2.2. With this crystal, peak powers were increased to the order of watts. This is due in part to the fact that higher pump power levels (by a factor of about 2) were used for the bulk crystal. Pump power for the fibers was restricted to lower levels to avoid any possible damage to the mounting epoxy or to their softer AR coatings. Pulse energies are in the nano joule range, similar to the fiber lasers. For 92.0 mW of absorbed pump power the energy of a typical pulse packet was close to 120 nJ. If this had all been emitted in

a single pulse, the peak power would have been 5 W. Since there were actually 17 pulses in this case the peak power in the main pulse was 1.1 W corresponding to about 26 μJ. The FWHM for this pulse was 28 nsec.

Both the average power $\overline{P}$ and the main pulse peak power P_{max} exhibit a linear growth with absorbed pump power, as shown in Figure 2.7. From the average power dependence, the energy conversion efficiency is calculated to be 0.009 (0.9%) compared to 0.0111 for the cw mode of operation. Pump power absorbed at threshold for this laser was 39.2 mW in the Q-switched case. The pulse width variation with pump power is found to be highly nonlinear, leveling off at $\Delta t_p = 48$ nsec for large pump powers (FWHM $=$ 28 nsec), as illustrated in Figure 2.8. This curve shows that the pulse width has apparently asymptoted to its minimum value of about 48 nsec (28 nsec FWHM) and cannot be further decreased by increasing the pump power. Note that the curve is directed concave up; it may suggest that in some fibers a mechanism other than slow switching may have been responsible for the different dependence of Δt_p on P_{abs}.

5.3 Analysis

A comparison of the data obtained for the fiber lasers shows that some performed better than others even for fibers of similar diameter, in terms of both peak power and pulse width performance. There was a one to one relationship between the laser peak power and its threshold, showing that the peak power was proportional to the cavity loss of the laser. The same conclusion was generally true for the laser pulse width. The lowest loss fibers (17-2 and 17-4) and the bulk laser exhibited energy conversion efficiencies of the same order of magnitude, while the fiber lasers exhibited $\sim$ 5 to 10 times lower thresholds than the bulk laser. This observation is in agreement with theoretical predictions: bulk and waveguide lasers have similar efficiencies but the waveguide type exhibits a lower threshold due to a
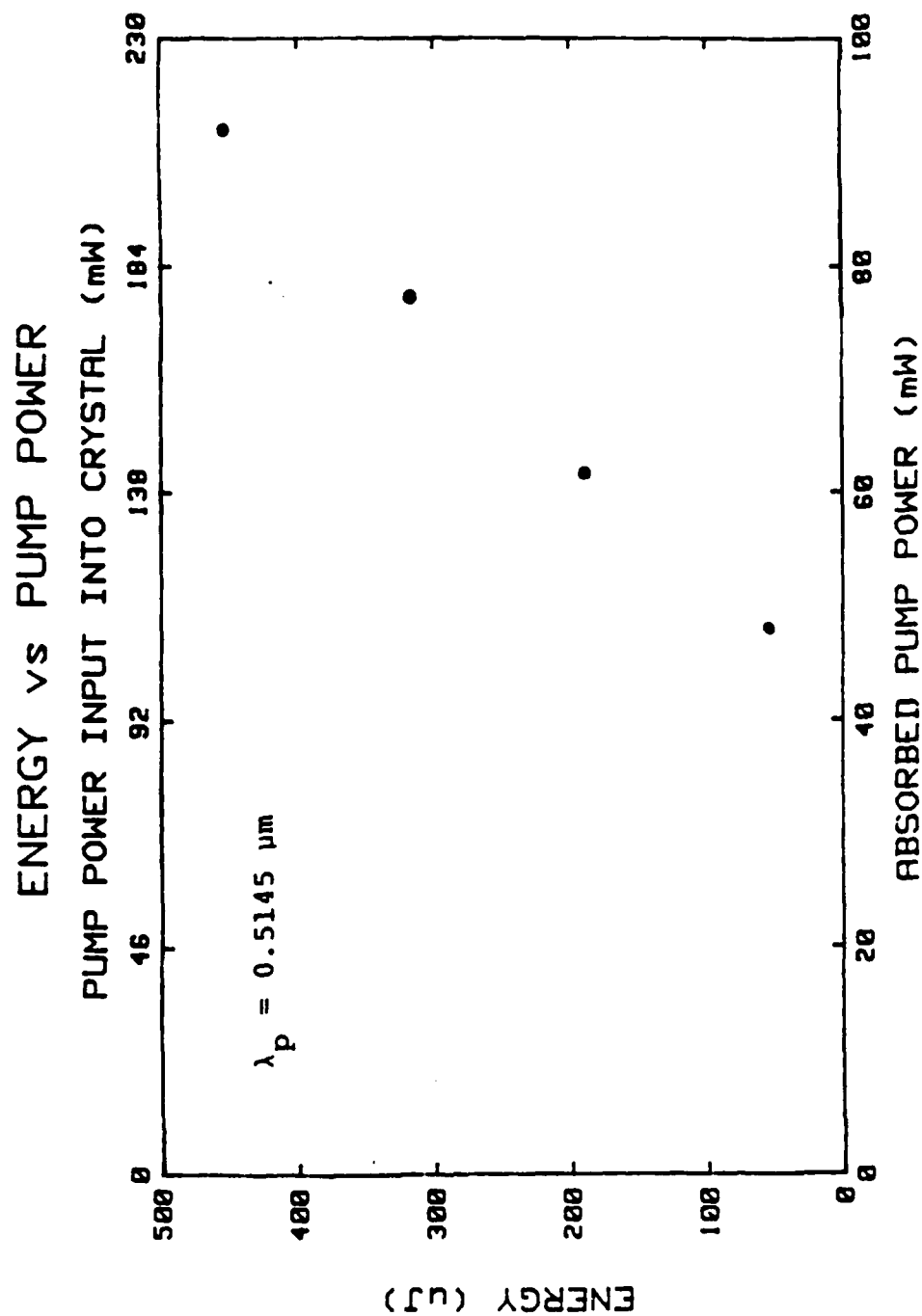
Figure 2.7--A Plot of the Average Output Power versus Pump
Power for the Bulk Laser.
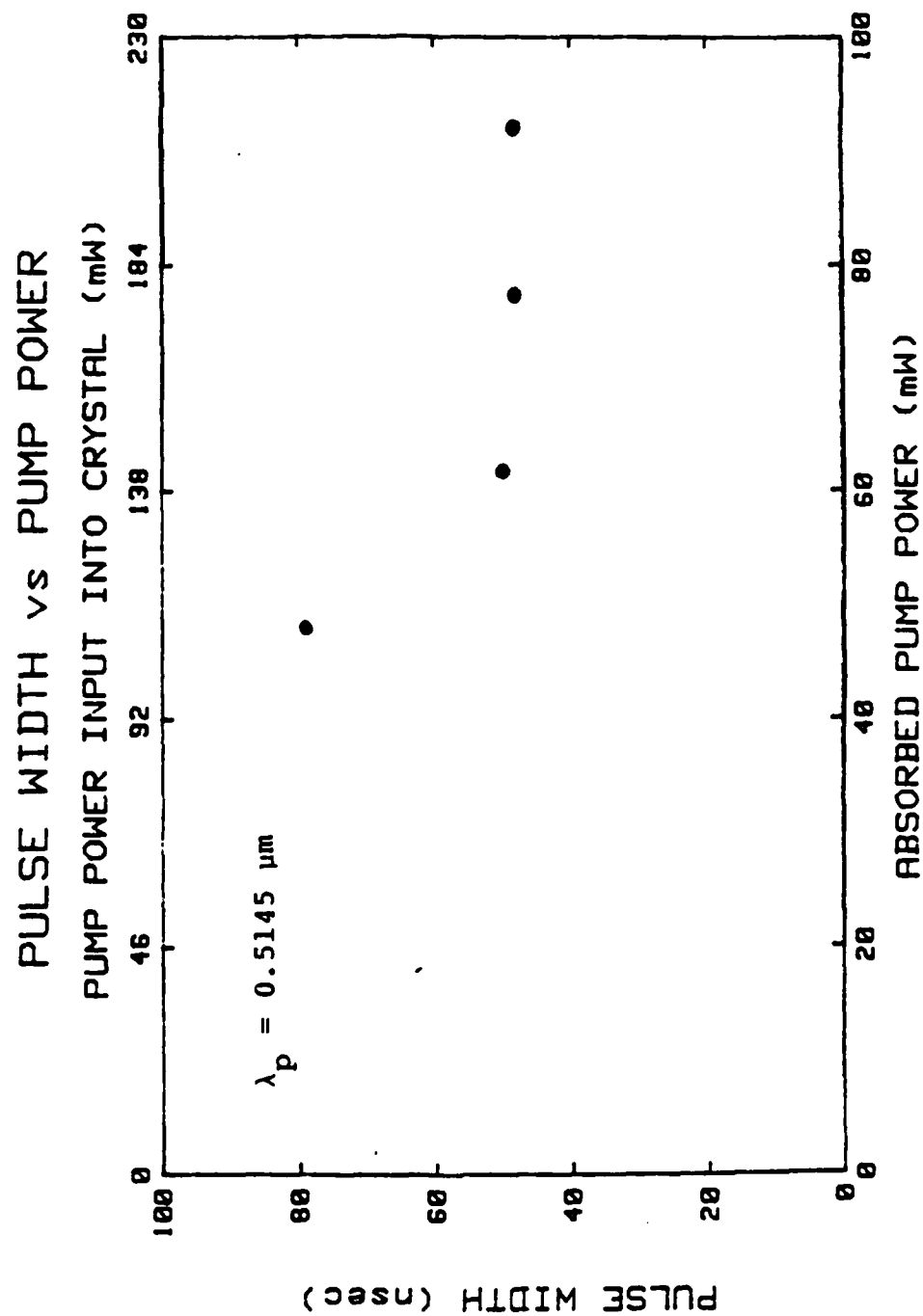
Figure 2.8--Variation of the Pulse Width Δt_p with Pump Power for a Miniature Bulk Laser.

tighter confinement of the pump signal fields over the length of the laser material. This indicates that peak power on the order of watts can be obtained with the present fiber sample. This was not done with the argonion pump laser in order to avoid damaging the fibers prior to testing them at $\lambda_p = 0.808 \, \mu$m.

In general, it can be said that the output pulses of both fiber and bulk Q-switched lasers had the anticipated average power, which was compatible with their internal loss measured by independent means. What differed drastically from what was expected on the basis of traditional, fast Q-switching, was the distribution of this energy along the time scale; we observed multiple pulses with comparatively low peak power and large width. To provide a quantitative as well as qualitative confirmation of this situation, a computer model of slow Q-switching was developed, as detailed in the next section.

5.4 Slow Q-switching Model

As mentioned earlier, the type of mechanical Q-switching that we used is inherently slow, on the order of a few kHz, largely because of a high frequency limit imposed by the large lifetime of Nd:YAG upper laser state. Because the cavity loss does not drop (from its high to low value) fast enough, the initial population inversion (time t = 0, high loss) is not very far above the final population inversion (time $t = t_{f1} \simeq \Delta t_p$) prevailing at the end of the generation of the pulse, since Δt_p is much shorter than the on-off switching time. Therefore (1) the first pulse does not extract much energy from the laser medium, and (2) at the end of the first pulse the conditions are right to support the generation of a 2nd, 3rd, etc. pulse.

To evaluate to what degree this mechanism was responsible for what was observed, we developed computer software to model slow Q-switching and applied it to the miniature bulk laser. A computer program, originally written to model Q-switched fiber lasers in which the switching occurs much faster than the pulse width,

Table 2.4

Measured Versus Theoretical Results for the Bulk Laser (1st Pulse)

P_{abs} (mW)	δ_0	$P_{peak,meas.}$ (mW)	$P_{peak,theory}$ (mW)	$\Delta t_{p,meas.}$ (nsec)	$\Delta t_{p,theory}$ (nsec)
48.0	0.147	220	220	79	104
61.7	0.185	660	666	50	53
77.3	0.23	955	951	48	40
92.0	0.274	1100	1100	48	34

was modified to step through the burst of pulses in a Q-switched pulse packet. This was achieved in two steps. First, the initial inversion for the first pulse was assumed to be that given by the pumping level. The loss factor δ_0 was then adjusted to yield a value of the peak power in the first pulse corresponding to the measured value. Second, the pulse width was computed using this value of the loss factor δ_0 and compared to that obtained experimentally.

As an example, the miniature bulk laser pumped at $P_{abs} = 61.7\ mW$ emitted a train of 10 pulses, with a main, first pulse peak power of 660 mW (see Table 2.3). To match this peak power value the computed loss value was $\delta_0 = 0.185$, from which the computed pulse width came out to be 53 nsec. This is in good agreement with the measured value of 50 nsec, and in order of magnitude agreement with the loss factor inferred from slope efficiency measurements ($\delta_0 = 0.48$). This model was found to predict the pulse width to better than 25% for all the data points taken with the bulk laser, as shown in Table 2.4.

An important point to make is that the loss factor varies with the pumping level (and therefore differs from the threshold value at $P_{abs} = 0$), as expected. As the pump power increases the first pulse occurs sooner, and its duration is shorter, so that it experiences a higher average loss. This is in agreement with the general trend in the computed values of δ_0 (see Table 2.4).

Once the parameters have been obtained for the first pulse, analogous sets of

parameters may be obtained for subsequent pulses in much the same way. The only difference is that the initial inversion level to be used in the calculation is set equal to the final inversion of the previous pulse. The loss factor of the next pulse is then varied until the peak power corresponds to the measured value. A calculation is then made of the pulse width to complete the pulse characterization. This process is iterated to the nth pulse, such that the initial population inversion for the $(n + 1)^{th}$ pulse is below the threshold value.

This approach was used to analyze the sequence of pulses obtained from the miniature bulk laser at four pumping levels. As the pump power was increased the number of pulses increased from 3 to 17 (see Table 2.3). A plot of the variation of the peak power from the first to the last pulse computed for each pumping level is shown in Figure 2.9. The general calculated behavior is in good agreement with what was experimentally observed, namely a 0.5 to 1.0 μsec time interval between pulses, and a generally decreasing, non-monotonic peak power distribution along each pulse train.

An analogous plot of the pulse widths is given in Figure 2.10. Here it is noted that the pulse width for the first pulse decreases with increasing pump power while that of subsequent pulses in a pulse train generally increases but not monotonically. For the highest pumping level the pulse width increases from below 50 nsec to just under 300 nsec for the last pulse, although most of the pulses (except for the last few) have pulse widths under 150 nsec. Again the behavior is in broad agreement with experimental observations.

The behavior of the calculated loss factor is shown in Figure 2.11. At a given pump level the loss decreases monotonically toward a minimum value. As explained earlier, this behavior was expected. When the first pulse is generated, the moving mirror is on its way toward, but not at, minimum deflection (where the cavity loss will be minimum); the loss experienced by each subsequent pulse is therefore smaller

PEAK POWER EVOLUTION FOR BULK LASER

$\lambda_p = 0.5145\ \mu m$

$\lambda_s = 1.064\ \mu m$

$P_{p,abs} =$
92.0 mW
77.3 mW
61.7 mW
48.0 mW

PEAK OUTPUT POWER (mW)

1200
1000
800
600
400
200
0

TIME (usec)

0   2   4   6   8   10
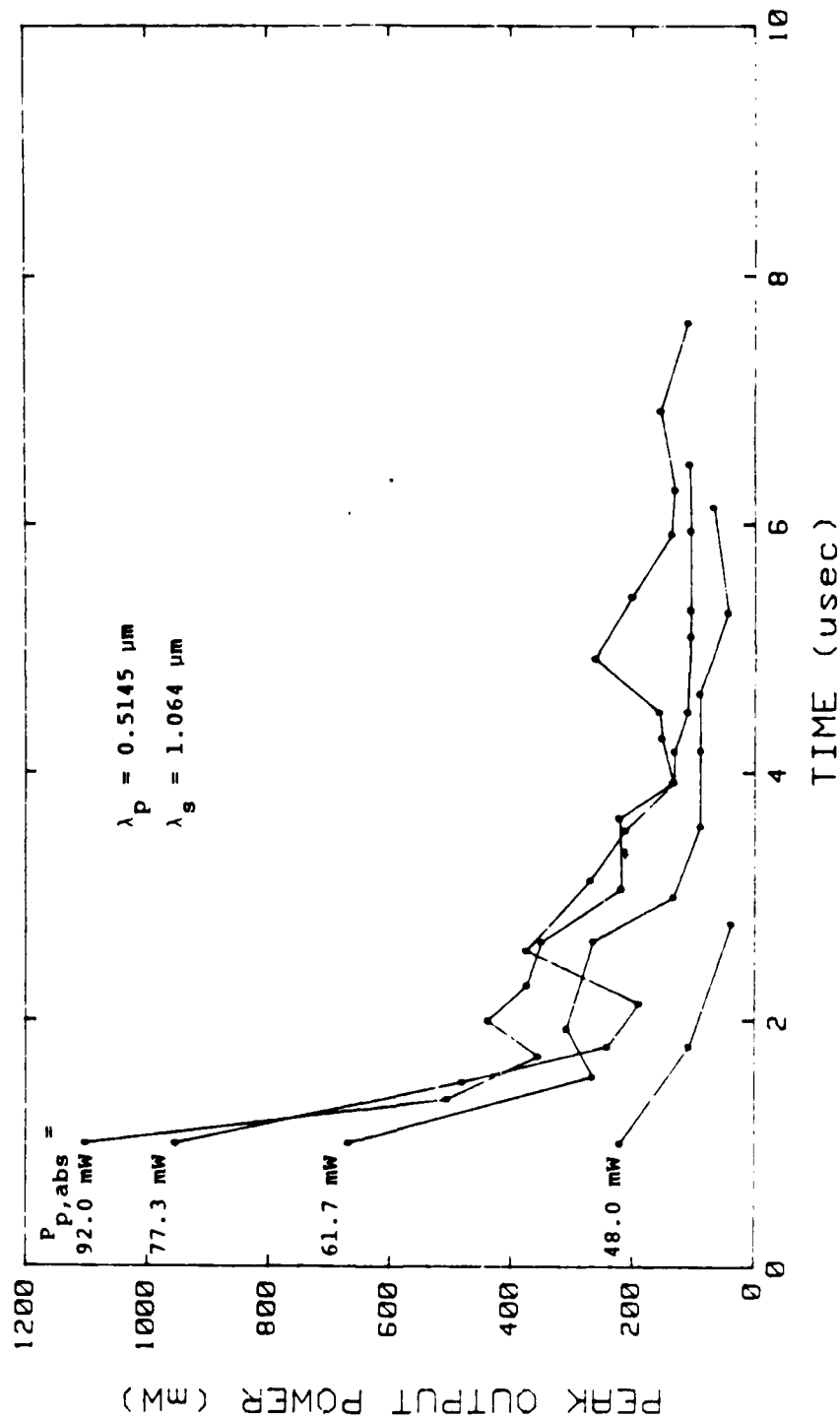
Figure 2.9--Peak Power for Multiple Pulses of a Miniature Bulk Laser for Four Different Pump Power Levels.
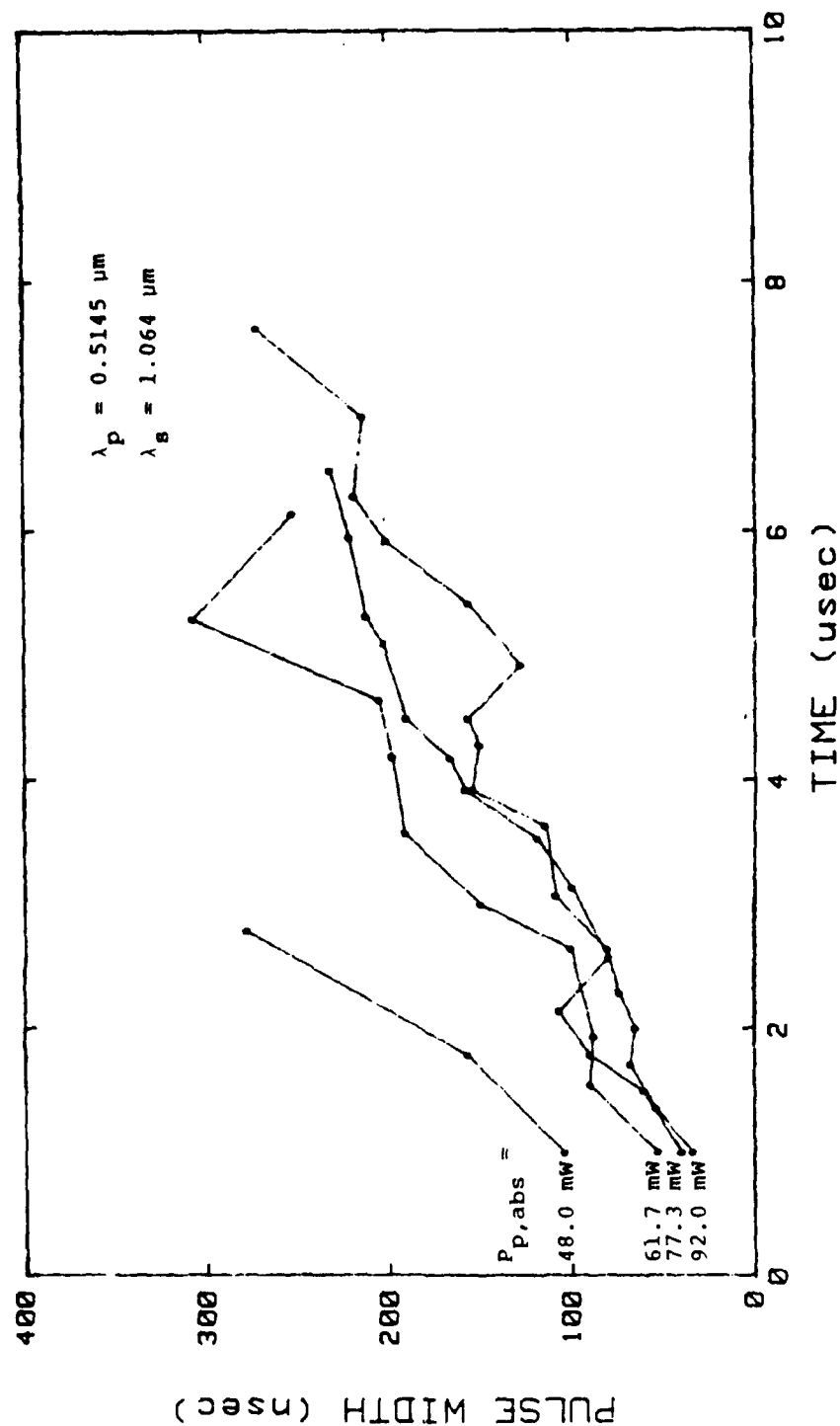
Figure 2.10--Pulse Width Δt_p for Multiple Pulses from a Miniature Bulk Laser.
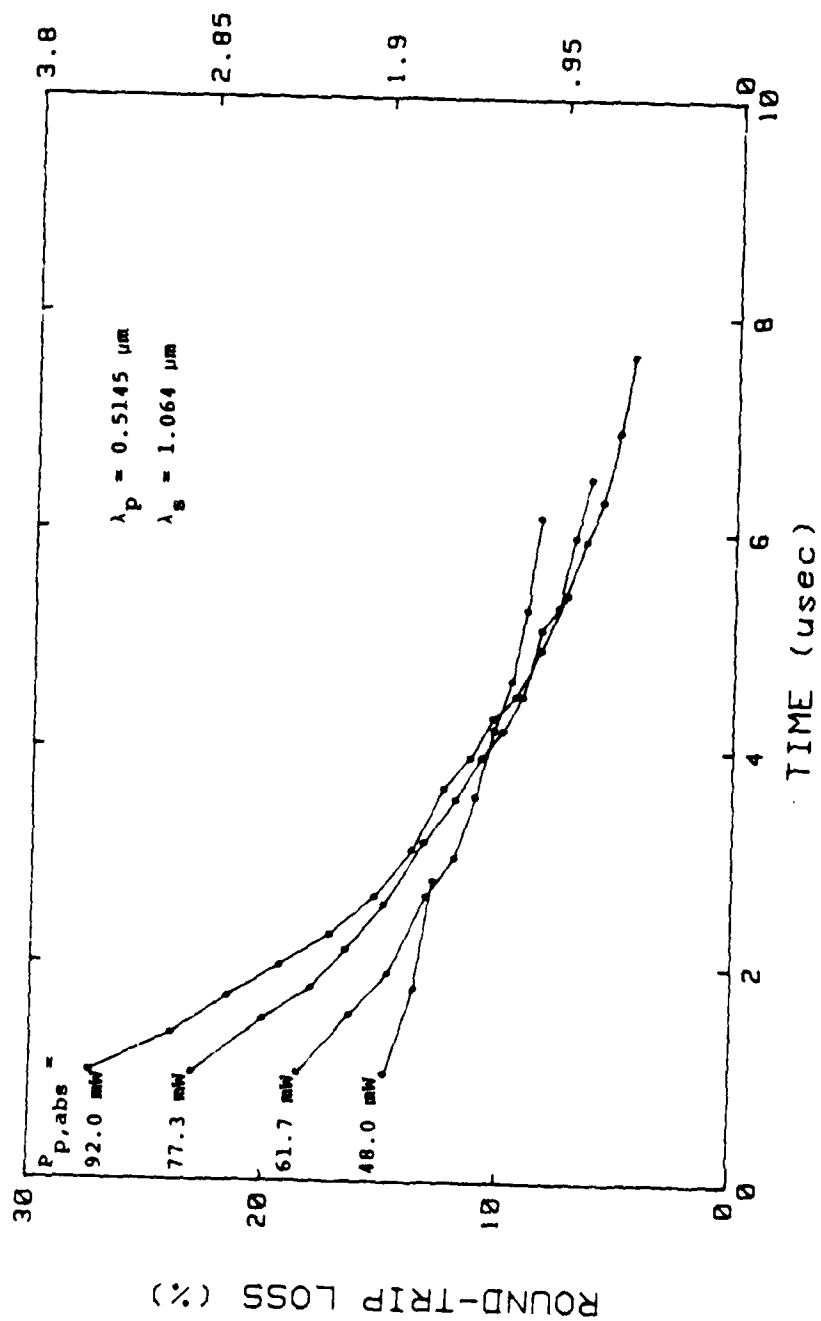
Figure 2.11--Round-trip Loss as a Function of Time for a Mechanically Q-switched Bulk Laser.

than that experienced by the previous pulse.

As mentioned earlier, as the pump power is increased, the first pulse, and all subsequent pulses, are generated sooner, i.e., when the mirror position is further away from zero deflection, and experience higher losses. This is in general agreement with the theoretical model prediction (see Figure 2.11). Furthermore, because the pulse train starts sooner along the mirror deflection, the pulse peak power is expected to be lower than predicted by the theory (which assumes a constant cavity loss as the pump power is increased). The duration of the pulse, on the order of 8 μsec here (see Figure 2.11) is very small compared to the vibration period of the mirror (about 500 μsec), which shows that the pulse train is emitted very near zero mirror deflection. The minimum value is on the order of about 5% for the highest pump power used in contrast to the cw measurement of about 22%. This may be due to the relatively poor alignment tolerance of the tilt stage used to initially orient the mirror scanning mechanism.

6. Conclusion

This study of mechanical Q-switching in Nd:YAG fiber lasers has led successfully to the first generation of Q-switched pulses in a single crystal fiber device. Because of the slow nature of the Q-switching mechanism involved, the observed outputs contained a train of many pulses, as opposed to the single pulse expected with a fast Q-switch. In the best of the tested fibers it was found that 10-20% of the emitted energy was contained in the main (first) pulse. When the excitation level was three times above threshold, the main pulse width was about 70 nsec (FWHM), while its peak power was on the order of 50 mW. The dependence of these various quantities on the pump power level were in general agreement with theory. In particular, the average power of the pulse train agreed well with the value of the fiber laser cavity loss measured independently under CW conditions.

Similar measurements with an unguided bulk Nd:YAG laser yielded similar results, except for higher peak powers (up to 1 watt) and shorter pulse width (30 nsec for the FWHM of the main pulse), primarily because this device was pumped much further above threshold than the fiber lasers.

For both fiber and bulk lasers, it was found that the energy temporal distribution within a pulse train was much different from that predicted by theory for a standard Q-switched device. A slow Q-switch model was therefore developed to confirm our observations. This model was found to predict the observed pulse behavior very well, in particular the multiple pulse generation and the broader individual pulse width, as well as the temporal evaluation of the cavity loss as the mirror is scanned near zero deflection.

The measurements reported in this section were unfortunately made with less than ideal fibers, which exhibited propagation losses somewhat higher than the lowest losses observed at the time this study was made. They showed nonetheless that the fibers were able to support the generation of Q-switched pulses, although it is clear that new generation fibers would probably yield better results.

D. Passively Q-switched Fiber Lasers

1. Theoretical Analysis

As outlined earlier, passive Q-switching of a Nd:YAG fiber laser involves the incorporation of a saturable absorber at the signal frequency in the fiber laser cavity. A simple implementation of this approach compatible with the compactness of the cavity is to use a thin film of saturable absorber held by surface tension between one of the mirrors and fiber ends. When the cavity is cold, the saturable absorber is initially opaque to the signal; the cavity loss is high (the cavity Q is low) and laser emission is impeded.

As the pump is applied to the fiber laser, in an end pumping configuration,
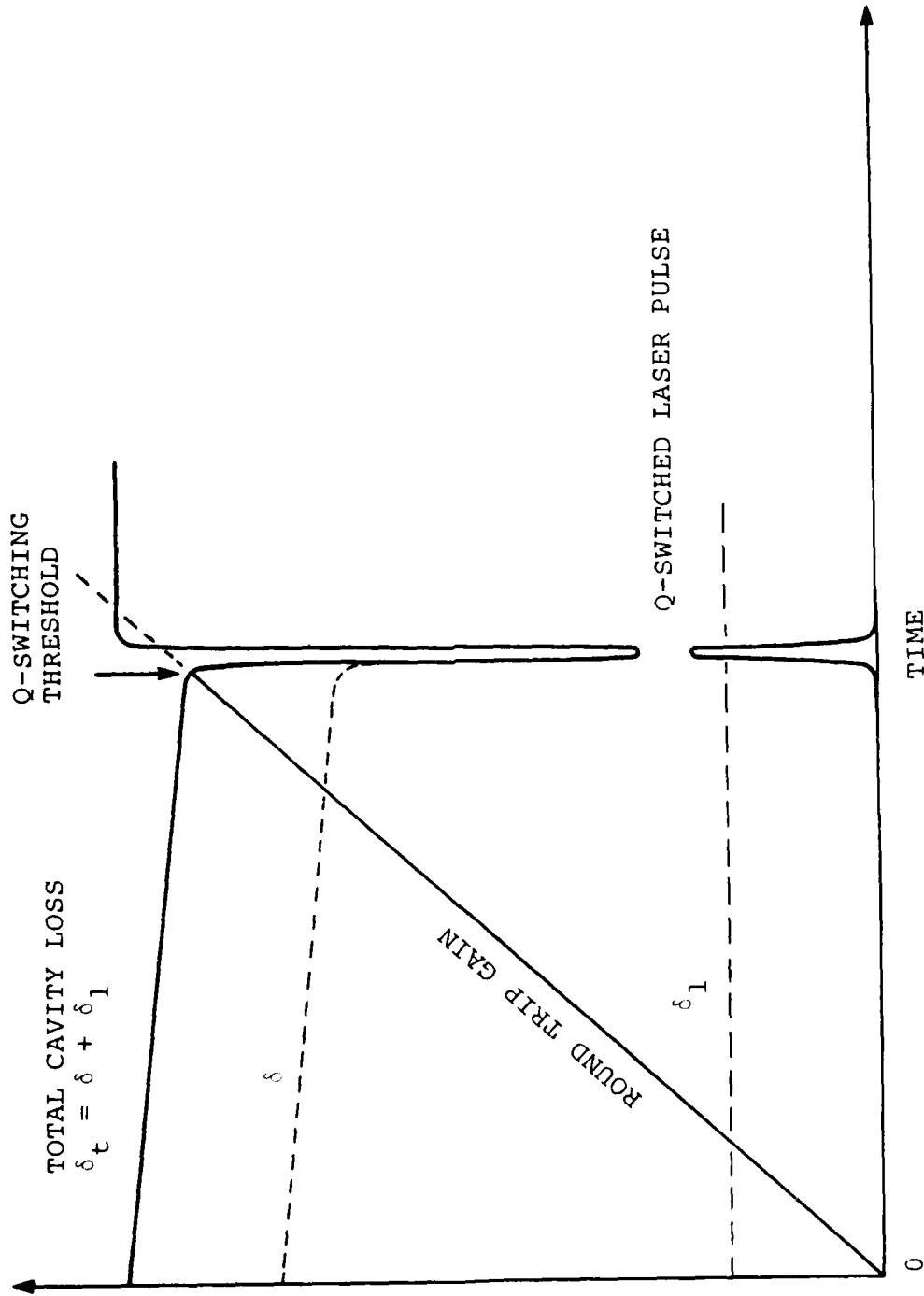
Figure 2.12--Time Evolution of the Round Trip Gain and Cavity Loss
Contributions δ and δ_1 as the Pump Power is Slowly
Increased to Q-switching Threshold.

and the pump power level is linearly and slowly increased, two phenomena occur. First, the gain in the cavity increases, at first and for a wide range of pump power in a linear fashion (see Figure 2.12). Concurrently, an increasing fluorescence signal travels through the fiber. The cavity loss experienced by this signal arises from two terms. The first one is the round trip loss δ_1, due to all cavity loss mechanisms except for the absorption of the dye at the signal wavelength. The second one, δ, is the absorption due to the saturable absorber dye, related to the dye absorption coefficient α and the film thickness t by

$$\delta = 2\alpha t \tag{2.10}$$

As the saturable absorber absorbs the forward traveling fluorescence signal, its absorption coefficient α decreases, and so does the total cavity loss $\delta_t = \delta + \delta$, as indicated in Figure 2.12.

Intuitively, it is clear that the number of signal photons in the cavity does not start increasing significantly until the cavity gain approaches the value of the total loss δ_t. At this point the absorbed pump power has reached the Q-switching threshold value $P_{abs,min}$. as shown in Figure 2.12. From this moment the signal intensity increases inside the cavity, and is helped in its growth by the drop in the thin film loss δ arising from the saturation of the dye absorption line it causes. This is illustrated in Figure 2.12 by a sharp drop in the total cavity loss in the vicinity of $P_{abs,min}$. as a sharp signal pulse is emitted by the laser cavity.

The dye which was selected for our experimental investigations of passive Q-switching in Nd:YAG fiber lasers using the principle outlined above is Eastman No. 14015, also referred to as BDN. It is a multilevel saturable absorber, which may be modeled using a four-state energy level diagram, as shown in Figure 2.13. No fluorescence at infrared wavelengths was reported from this dye which implies that the steady-state population of levels 3 and 4 are nearly zero ($\tau_{32} < \tau_{42} << \tau$). The

36

steady-state populations in levels 1 and 2 are found from the following set of rate equations:

$$N_1 = N_D(1 + \frac{I}{I_s})^{-1} \tag{2.11}$$

$$N_2 = N_D\frac{I}{I_s}(1 + I/I_s)^{-1} \tag{2.12}$$

where N_D is the concentration of BDN molecules in the solvent, I is the forward optical intensity incident on the dye, and $I_s = h\nu_s/\sigma_g\tau$ is the saturation intensity of the absorption line from the ground state. It can be shown from these equations that the total absorption coefficient at frequency ν_s is given by

$$\alpha = \frac{1 + \eta\frac{I}{I_s}}{1 + \frac{I}{I_s}}\alpha_0 \tag{2.13}$$

where $\eta = \sigma_e/\sigma_g$ and $\alpha_0 = N_D\sigma_g$ is the unsaturated absorption coefficient. Here σ_g and σ_e are the absorption cross sections for the $1 \rightarrow 3$ and $2 \rightarrow 4$ transitions, respectively. At $\lambda = 1.064\mu$m, the values for these parameters provided by the manufacturer are $\sigma_g = 1.94 \times 10^{-16}cm^2, \sigma_e = 2.3 \times 10^{-17}cm^2$, and $I_s = 9 \times 10^5 W/cm^2$. The unsaturable absorption loss is $\eta = 12\%$ and the relaxation time $\tau = 1.1\,nsec$.

Superfluorescence studies reported later in this report have shown that the order of magnitude of the fluorescence signal intensity traveling in a Nd:YAG fiber end pumped at even relatively high levels is small compared to the saturation intensity I_s of BDN. As an example, in a 40 μm fiber pumped at 200 mW, the fluorescence intensity is on the order of 1 kW/cm^2 (compared to almost 1 MW/cm^2). For all practical purposes it can therefore be assumed that the total cavity loss δ_t in Figure 2.12 is independent of pump power (up to $P_{abs,min}$).

Just before the Q-switched pulse is emitted, the population inversion n_{in} may
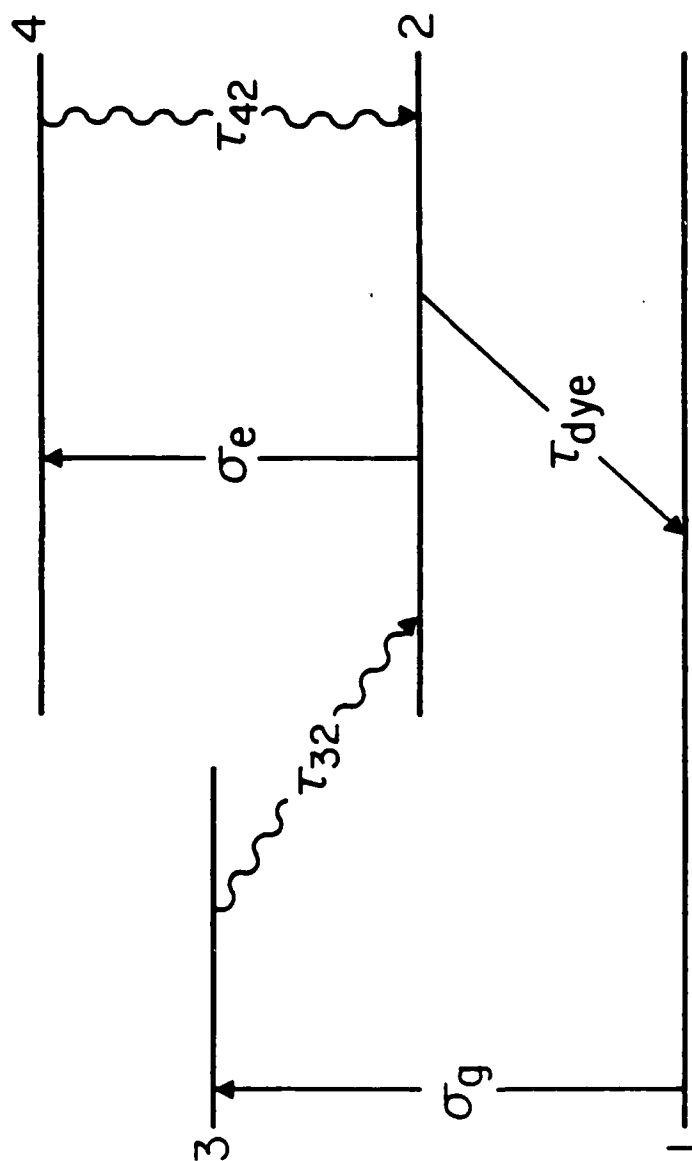
Figure 2.13--Energy Level Diagram for BDN Dye using a Four-Level Model.

be written as

$$2\frac{\sigma n_{in}}{A_{eff}} = \delta_1 + \delta_0 \tag{2.14}$$

where σ is the laser transition emission cross section, n_{in} is the population inversion in the active material, A_{eff} is the fiber effective active area, and $\delta_0 = 2\alpha_0 t$. Because δ does not depend on the pump power level, the population inversion prevailing when the pulse is emitted is uniquely defined by Equation 2.14. The major conclusion of this observation is that the pulse characteristics, such as width and peak power, which depend only on the population inversion at the time of emission, does not depend on the pump power level, but only on the total loss $\delta_t = \delta_0 + \delta$. This point is very important. It stresses a fundamental difference between the present device and traditional Q-switched lasers, in which the cavity loss can be modulated by some externally controlled means *independently* of the pump power level. In this passively Q-switched laser the pulse is emitted when the pump power has reached a given value, function only of the fiber loss. For a given device, the only way to change the pulse characteristic is therefore to change the saturable absorber cold loss δ_0, i.e., its concentration or the film thickness.

When laser oscillation begins the laser intensity increases while the dye absorption coefficient starts to decrease according to Equation (2.13). The laser rate equations show that after some build up time the signal intensity circulating inside the cavity reaches its maximum value (which coincides with the pulse maximum) given by

$$I_{i,max} = \left(\frac{2}{T_1}\right)\left(\frac{P_{i,max}}{A_{eff}}\right) \tag{2.15}$$

Here T_1 is the output coupler transmission, and $P_{i,max}$ is the peak power of the output pulse. The factor of 2 stems from the fact that the intensity which saturates the absorption is the sum of the counterpropagating intensities in the laser cavity.

Equation (2.15) assumes that the laser is operating in a single transverse mode, labelled i, although not necessarily the lowest order mode. The peak power of the pulse, derived in the previous phase of this contract, is

$$P_{i,max} = h\nu_s \frac{cT_1}{2n\ell}\left[n_{t,i}\ell n\frac{n_{t,i}}{n_{in}} - \left(n_{t,i} - n_{in}\right)\right] \qquad (2.16)$$

Here n_{in} is the initial population inversion defined earlier, while $n_{t,i}$ is the value of the population inversion when the intensity of the pulse is maximum, equal to

$$n_{t,i} = \frac{\delta_1 + \delta_b}{2\sigma}A_{eff} \qquad (2.17)$$

The residual dye film loss δ_b at the maximum of the pulse intensity is given by

$$\delta_b = \delta_0\frac{1 + \eta\frac{I_{i,max}}{I_s}}{1 + \frac{I_{i,max}}{I_s}} \qquad (2.18)$$

For large peak intensities such that $I_{i,max} >> I_s/\eta$ the residual loss asymptotes to $2\ \alpha_0 t\eta$. Combining Equations 2.14 and 2.17 we define r as the ratio of population inversion prevailing at the beginning (n_{in}) and at the maximum intensity point $(n_{t,i})$ of the pulse emission:

$$r = \frac{n_{in}}{n_{t,i}} = \frac{\delta_1 + \delta_0}{\delta_1 + \delta_b} \qquad (2.19)$$

This quantity is equivalent to the ratio of initial to threshold population inversion in the standard Q-switching theory, which characterizes how far above threshold (or here above minimum loss) the device is initially pumped. Using this definition of r the pulse peak power (Equation 2.16) may be written as

$$P_{peak} = h\nu_s \frac{cT_1}{2\ell n}\frac{\delta_1 + \delta_b}{2\sigma}A_{eff}(r - 1 - \ell n(r)) \qquad (2.20)$$

To compute this quantity for a given value of the dye concentration (or dye cold loss δ_0) one must solve simultaneously Equations 2.15 and 2.18 through 2.20. This

requires computer evaluation as these equations are generally coupled through the intensity dependence of the dye loss (Equation 2.18). As an example, we considered the case of Fiber No. 24 tested in our experiments, described in the next section. We used a fiber core diameter of 130 μm ($A_{eff} = \pi a^2 / F_{0101} = 1.62 \times 10^{-5} cm^2$, where $F_{0101} = 2.1$ is the pump-to-signal overlap coefficient for a set of LP_{01} modes far from cutoff), a fiber length $\ell = 2.35\,cm$ and index n $= 1.82$, a stimulated emission cross section of $\sigma = 3.2 \times 10^{-19}\,cm^2$ and saturation intensity $I_s = 2.6 \times 10^3\,W/cm^2$ for the 1.064 μm transition of Nd:YAG.

Shown in Figure 2.14 is the theoretical dependence of the pulse peak power on the cold dye loss coefficient δ_1, for various values of the cavity loss δ_i. As expected and as explained earlier, for a fixed value of δ_1 as the dye cold loss is increased the peak power increases, because the allowed pump power increases. These curves assume that the pump power is adjusted for each value of δ_0 to the required minimum value. This value can be deduced from Equation 2.14 as

$$P_{abs,min} = \frac{h\nu_p}{\sigma\tau_f}\frac{\delta_1 + \delta_0}{2}A_{eff} \qquad (2.21)$$

For the parameters of Fiber No. 24 pumped near 810 nm, the value of the operating pump power is simply $P_{abs,min} = 2.68 \times 10^{-2}(\delta_0 + \delta_1)$, expressed in watts.

Similarly, the pulse width is given by (see previously developed pulsed fiber laser theory):

$$\Delta t = \frac{h\nu_s}{P_{peak}}\frac{T_1}{\delta_1 + \delta_b}(n_{in} - n_f) \qquad (2.22)$$

where n_f is the final population inversion, prevailing at the end of the pulse emission. n_f is given by the solution of,

$$n_f = n_{in}e^{(n_f - n_{in})/n_{t,i}} \qquad (2.23a)$$
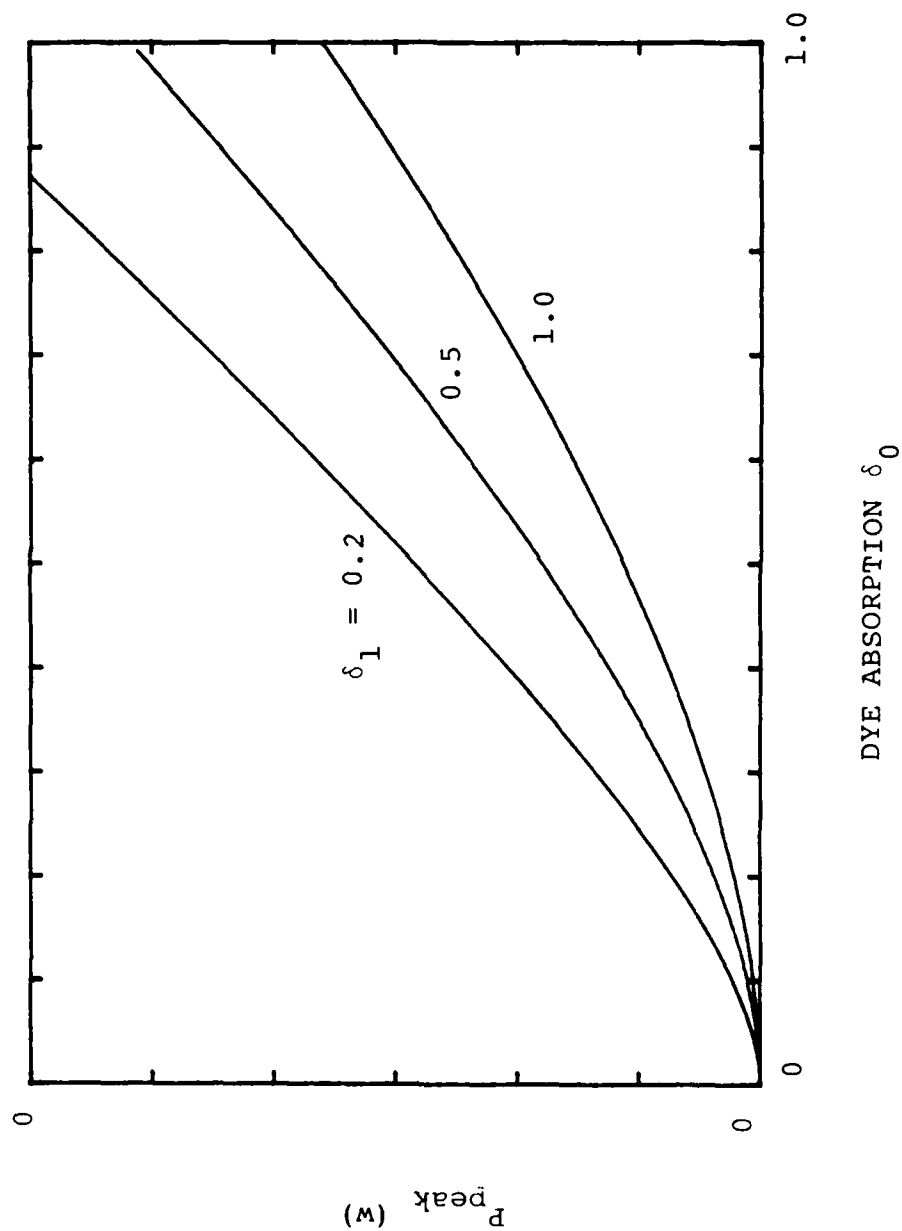
Figure 2.14--Dependence of the Pulse Peak Power on Dye Cold Absorption Loss δ_0 in a Passively Q-switched Laser for Various Values of the Non-dye Loss Coefficient δ_1.

$$= n_{in} e^{(n_f - n_{in})r/n_{in}} \qquad (2.23b)$$

The evolution of the pulse width (FWHM) with dye film loss δ_0, as described by Equation 2.22, is shown in Figure 2.15. For a given value of the cavity loss δ_1 the pulse width decreases monotonically as the film cold loss δ_0 is increased - as expected, since an increase in δ_0 means an increase in the excitation level (which is adjusted to $P_{abs,min}$ for each value of δ_0). For a given value of the film cold loss δ_0 the pulse width decreases as the cavity loss δ_1 is increased - in the limit of very large values of δ_1 the ratio r (or how far above threshold the laser is pumped) becomes vanishingly small.

The conclusion of this analysis is that, as expected, the most intense and narrowest pulses are obtained when the ratio δ_0/δ_1 is the smallest. In this case, and for reasonable cavity parameters, sub-nanosecond pulses with peak powers in the range of several hundred watts can be generated.

So far it has been assumed that the pump power was fixed at the 'threshold' or minimum value $P_{abs,min}$ and was applied in the quasi-CW mode. The population inversion has then reached its quasi steady-state value after the pump has been applied for approximately 4-5 times the lifetime of the upper laser state τ_f, at which point the Q-switched pulse is emitted. Under CW pumping conditions at $P_{abs} = P_{abs,min}$, the frequency of occurence of the pulses is therefore about $(4\text{-}5\,\tau_f)^{-1}$, or about 1 kHz in Nd:YAG ($\tau_f \simeq 230\,\mu sec$). If the pump is lowered ($P_{abs} < P_{abs,min}$), Q-switched pulse emission ceases. If it is increased ($P_{abs} > P_{abs,min}$), the population inversion steady state value will be reached sooner. Assuming that the pulse emission occurs where the population inversion has reached 99% of its steady state value, the pulse emission frequency will be
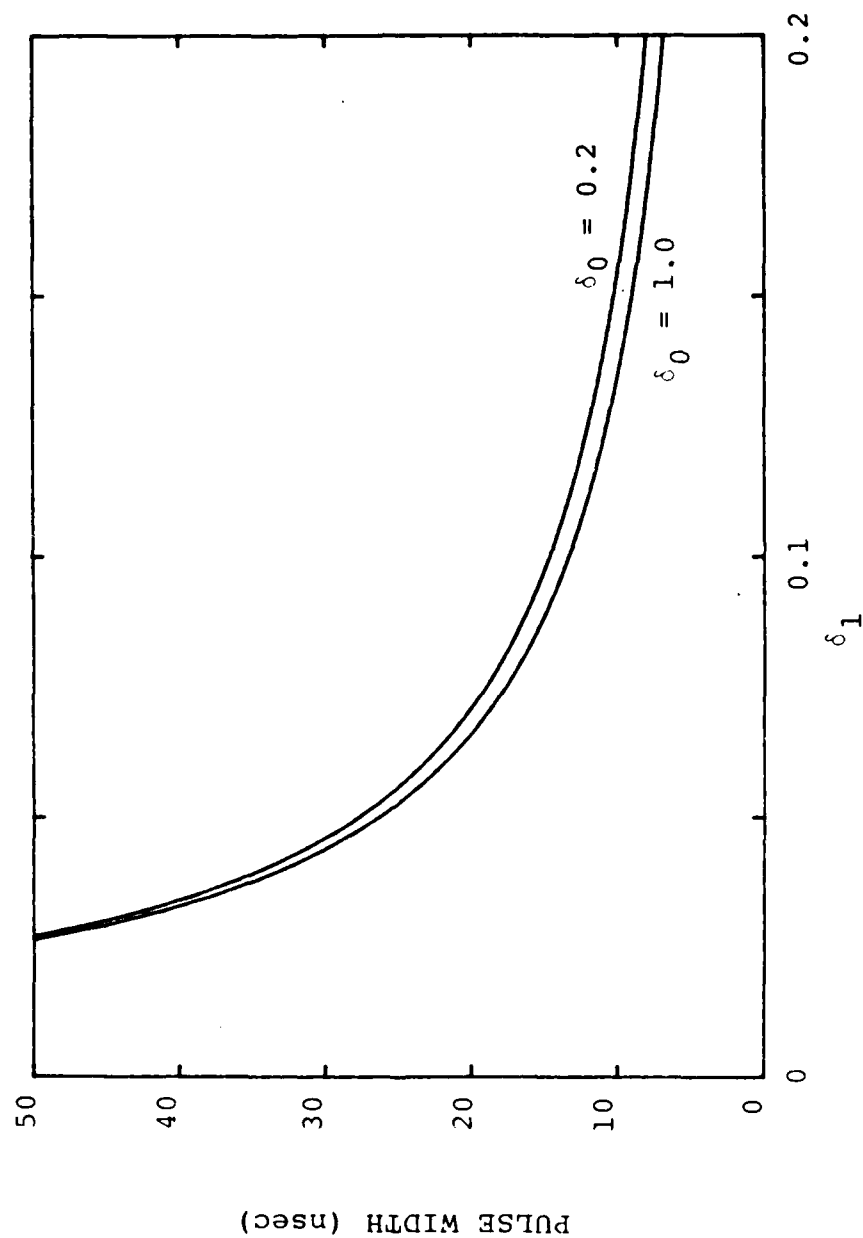
Figure 2.15--Dependence of the Pulse Width on the Cavity Loss δ_1 for Different Cold Dye Film Loss δ_0.

$$f = \frac{1}{\tau_f} \frac{-1}{\ell n[1 - 0.99 \frac{P_{abs,min}}{P_{abs}}]} \qquad (2.24)$$

Therefore, increasing the pump power above the minimum value $P_{abs,min}$ required to obtain pulse emission only increases the emission frequency. If $P_{abs} = 2P_{abs,min}$ the frequency is increased by a factor of 1.5.

2. Experimental Procedure

As described above, passive Q-switching of fiber lasers was obtained by placing a saturable absorber laser dye in the cavity, in the form of a thin film held by surface tension between the output coupling mirror and the fiber end. The film thickness was generally smaller than 500 μm. The dye was Eastman No. 14015, or BDN, a standard, relatively stable saturable absorber used in passively mode locked lasers near 1.06 μm, dissolved in 1, 2-dichloroethane.

A standard end-pumping configuration was used for this investigation, with an argon laser pumped CW dye laser tuned to the strong 808 nm absorption line of Nd:YAG as a pump source. The pump power available from this laser was at most 200 mW, and usually in the range of 80-100 mW, due to difficulties associated with the chemical stablity of the dye molecules under intense illumination, and mechanical stability of the dye laser cavity. In the Q-switched mode the pump power was amplitude modulated at a few kHz rate with a mechanical chopper to provide a reference signal to trigger the oscilloscope. The signal pulses were detected with a fast silicon detector having a response time of about 1-2 nsec.

For these measurements two fibers were used, namely Fiber 17-1 (see Table 2.1) previously involved in mechanically Q-switched investigations, and Fiber No. 24 which is a 23.5 mm long, 130 μm core diameter, glass clad fiber with a core-cladding index difference of 0.015. The fiber aspect ratio is such that both the pump and signal are guided by the fiber core. The fibers were AR-coated at 1.064 μm, usually at both ends, although the presence of a coating on the side receiving the

drop of saturable absorber was not required as the liquid acted as an index matching medium to reduce the Fresnel loss at this interface. On occasions the AR-coating was not present on this side of the fiber.

3. Fiber No. 17-1

Initial passive Q-switching measurements were performed in Fiber 17-1. The CW cavity loss for this fiber (with $T = 4.6\%$) was measured to be $\delta_1 \simeq 0.186$ prior to introducing the saturable absorber. For this fiber the dye concentration was adjusted by trial and error to $N_D \simeq 0.3 \times 10^{+16} cm^{-3}$ until Q-switching was observed. Pulse generation was obtained by placing a drop in the cavity, then adjusting the output coupler orientation until laser oscillation resumed, now in the Q-switched mode.

A photograph of a typical pulse train, obtained under CW pumping conditions is shown in Figure 2.16. Q-switched pulses occurred at a repetition rate of 2.8 kHz. From Equation 2.24 it suggests that the device was pumped 25% above minimum requirement ($P_{abs} = 1.25 \times P_{abs,min}$). A 20% jitter in the time of onset of consecutive pulses was observed, expected from the nature of the Q-switching mechanism.

One of the major difficulties encountered with this fiber was that after about one minute of continuous operation the dye film disappeared from the space between the fiber end and the mirror, either from evaporation or some form of leakage. At this point, the addition of a new drop of dye restored the generation of Q-switched pulses. However, this situation made full characterization of the pulses difficult, and limited data were collected with this sample. The peak power was estimated to be about 110 mW while the pulse width was about 100 ns at the half-power points ($\Delta t_p = 200ns$). These values are somewhat different from what was anticipated, namely peak powers on the order of tens of watts and pulse widths in the range of
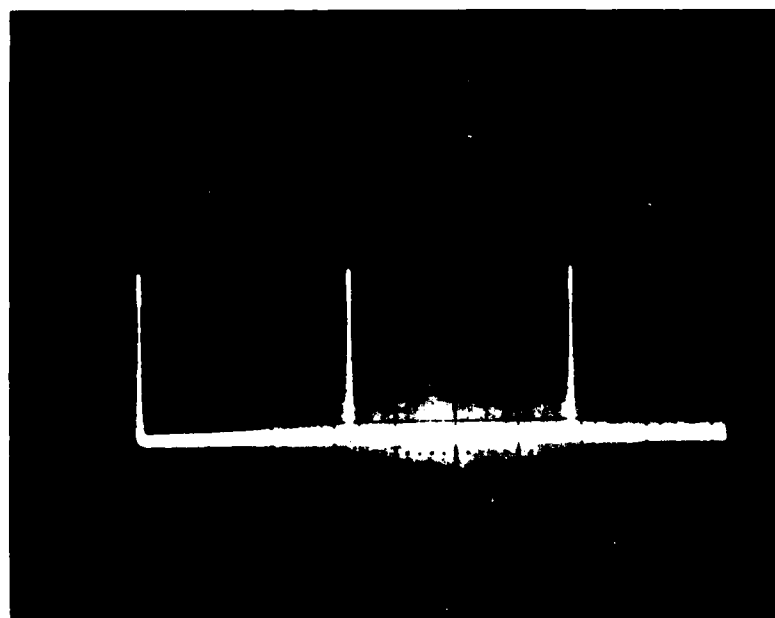
Figure 2.16--Q-switched Pulses from Fiber No. 17-1.

a few to 50 nsec. This discrepancy will be discussed further on.

After a few hours of operation the epoxy used to hold the capillary tubes in the mounting fixture became soft and gradually come out of the fixture. Some chemical reaction was taking place between the epoxy and the dye solvent, which caused the solvent to be gradually soaked up, the epoxy to swell and the individual capillary tubes (in which each fiber is contained) to become loose. The solvent apparently did not affect the bonding agent used to attach the fibers inside the capillaries. Although individual capillary tubes were successfully removed from the fixture at this point, subsequent measurements were performed with Fiber No. 24, as described below.

4. Fiber No. 24

At the time Q-switched oscillation measurements in Fiber No. 24 were initiated, this fiber was the first glass-clad Nd:YAG fiber which had been brought successfully to laser oscillation in a continuous wave mode. The fiber propagation loss (for the fundamental transverse mode LP_{01}) inferred from CW output characterization was one of the lowest achieved at that time, namely on the order of 0.5-0.6 dB/cm. Since the fiber is relatively long ($\ell = 2.35\ cm$), the total round trip loss of a cavity made of this fiber, a high reflector and a 4.6% output coupler was typically $\delta_1 = 0.5$.

When a drop of pure solvent was added to the cavity laser oscillation ceased, and was only restored after readjusting the orientation of the output coupler, as desribed for fiber No. 17-1. After optimizing the output of the CW laser in the presence of the film of solvent, the new round-trip loss was measured to be $\delta_1 = 1.06$. The additional loss contribution of $\Delta\delta_1 = 0.56$ (for a film thickness of about 200 μm) is believed to arise from a combination of (1) frustrated anti-reflection coating operation, (2) decreased output coupler reflection, and (3) solvent optical loss due to inhomogeneity and less than ideal transmisison. The threshold of CW

oscillation was then on the order of $P_{abs} = 45\,mW$, or an incident pump power of 60 mW.

When Q-switching measurements were performed with this fiber, the pump power available from the dye laser did not exceed 80 mW, and was often down to the CW threshold level of the fiber laser. As a result only relatively low dye concentrations could be used to demonstrate passive Q-switching in this fiber. Initial Q-switched laser oscillation was observed with a saturable absorber concentration of $0.26 \times 10^{16}\ cm^{-3}$. It corresponds to an unsaturated absorption coefficient of $\alpha_0 = 0.50\,cm^{-1}$, and an additional (unsaturated) cavity loss of $\delta_0 = 2\alpha_0 t \simeq 0.02 - 0.04$, depending on film thickness. Pulse characterization was conducted while the pump power was set at the maximum power available from the 808 nm dye laser, namely about 80 mW, corresponding to an absorbed pump power of about 60 mW. With the above concentration Q-switched laser operation was obtained routinely. The dye film appeared to remain for several minutes between the fiber end and the laser mirror before leaking out, at which point a new drop was added and Q-switched laser action resumed immediately. The peak power was quite low, on the order of 3 mW, while the pulse width was 240 nsec (FWHM).

The total dye absorption was then increased by increasing the mirror-to-fiber distance, and thus the dye film thickness. An increase in the dye absorption caused the pulse width to decrease to about 80 nsec, and the peak power to increase to 40 mW (see Figure 2.17). This behavior was expected and confims the conclusion of our theoretial analysis which predicts that the pulse peak power should increase, and the pulse width decrease, with increasing cold dye loss, in particular with increasing film thickness.

Other, weaker concentrations were also tested, 0.16 and $0.05 \times 10^{16}\ cm^{-3}$, which provided 0.4 - 1.6 mW peak powers and 400-500 nsec wide pulses. Although the film thickness probably varied somewhat from run to run, these tests definitely

49
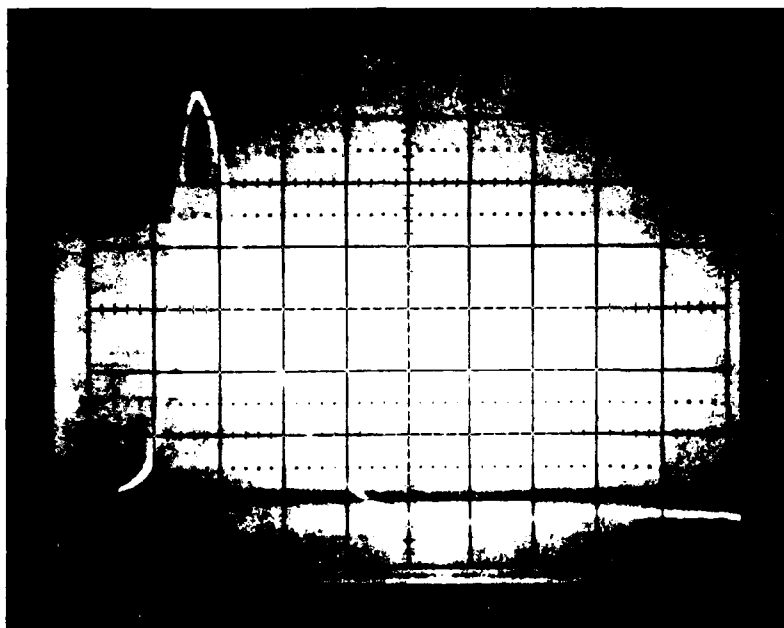
Figure 2.17--Q-switched Pulse from Fiber Laser No. 24 (Horizontal Scale: 50 nsec/div).

indicated that a larger concentration (up to a point) would optimize the pulse characteristic, as anticipated.

Narrower pulses were indeed observed after changing the film concentration back to 0.26×10^{16} cm^{-3}, and carefully aligning the fiber laser cavity. We repeatedly observed the generation of 50-80 nsec pulses, then after further alignment a record pulse width of 6 nsec, as shown in Figure 2.18. The estimated peak power was on the order of 2 watts. These measurements were obtained with an absorbed pump power of about 60-80 mW. To the best of our knowledge this is the narrowest and brightest pulse observed from a single crystal fiber. This measurement, however, was a one-time observation which occurred toward the end of our investigation, so that no further characterizations of this device were performed.

From these measurements one can work out the pump parameter r (Equation 2.20) using either the measured values of Δt or of the peak power. From the value of $\Delta t = 6 nsec$, Equation 2.22 predicts $n_{in-n_f} = 1.49 \times 10^{12}$, which, combined with Equation 2.14 ($n_{in} = 2.76 \; 10^{13}$), provides $n_f = 2.61 \times 10^{13}$. The ratio $(n_{in-n_f})/n_{in}$ is only about 5%, which shows that very little energy was extracted by the pulse. Now from Equation 2.23b one computes $r \simeq 1.03$. Similarly, from the value of $P_{peak} = 2$ watts and Equation 2.20 one computes $r \simeq 1.07$. These two values are in fair agreement, their difference being attributed to a high cavity loss δ_1. Actually, δ_1 was taken to be $\delta_1 = 1.00$ in the above derivation. Had we assumed $\delta_1 = 1.91$, the values of r extracted independently from Δt and P_{peak} would have been identical. This is consistent with the observation that during these tests the CW threshold was actually higher than the lowest measured value, probably due to residual misalignment of the fiber laser cavity.

These results clearly indicate that under the conditions of our experiments, the parameter r was barely larger than unity, in other words that the dye film cold loss δ_0 was much smaller than the cavity cold loss δ_1. The selected dye concentration

6 nsec
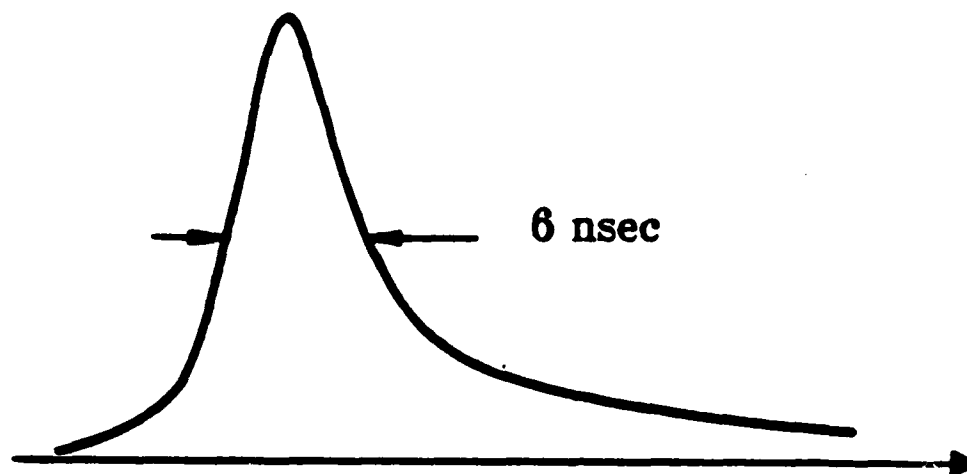
Figure 2.18--Trace of the Shortest Pulse Obtained
from a Guided Passively Q-switched
Fiber Laser (λ_p = 808 nm).

was too low, as the criterion used to select it was not based on the theory presented in this report, which was developed at a later time. As a result the peak power of the pulses generated by this method was not quite as high as originally expected. However, as pointed out earlier, the pulse width depends weakly on the cavity loss δ_1, and fairly short pulses were still observed. For the same reason, experiments were not designed to verify one of the theory's major conclusions, namely that the pulse output characteristics are independent of the pump power level (above some 'threshold' value). A point of particular interest are details in the effect of the pump power on the Q-switched laser operation in the vicinity of $P_{abs,min}$, which the current theory does not address.

5. Conclusion

Passive Q-switching investigations have led to the successful demonstration of the possibility of nanosecond pulse generation in compact Nd:YAG fiber lasers. Studies have shown record pulse widths of approximately 6 nsec and peak powers of 2 watts in guided, 808 nm end-pumped, glass-clad Nd:YAG fibers. This is the first report of nanosecond Q-switching of any type in single crystal fibers.

It has been stressed that the measurements involved in this analysis were difficult, requiring constant efforts to operate a generally unreliable infrared pump source as well as delicate alignment of a high loss optical cavity. Adverse interactions between the various chemical components in the cavity also contributed to increasing the difficulty of the task. A large uncertainty in the results also arose from our lack of knowledge of the exact thickness of the dye film, and from the need to regularly feed drops inside the cavity.

Measurements of the pulse peak power and width, and their dependence on film concentration and thickness, indicate that the dye film contributed to a small fraction of the fiber laser cavity loss. This situation, in part due to a low available

pump power, resulted in a pulse energy and peak power generally lower than expected in an optimum configuration.

Despite these shortcomings, we were able to obtain encouraging results, which points out the potential of Nd:YAG fibers as compact, miniature Q-switched laser sources. The data generated with these fibers made it possible to verify some of the predictions of a novel theoretical analysis of passively Q-switched lasers. From this study it may be useful to suggest a few guidelines for future work in this area. In general it was felt that the fibers involved in this work, in particular Array No. 17, exhibited unusually high CW oscillation thresholds. Since this work was done, much lower loss fibers were fabricated and tested under other auspices, which should clearly be involved in future investigations. They are anticipated to be adequate for much higher dye concentrations than used in this study, with a hope to achieve higher pulse peak powers. A minimal amount of, or a different, epoxy material should also be used as a bonding agent to avoid contamination and interaction with the dye layer. Some means of containing the liquid saturable absorber would also avoid the necessity of continuous addition of dye, as well as provide a basis for dye longevity studies. Alternative, more realizable pump sources, such as a Kr-ion laser or GaAlAs laser diodes, may also be considered for further investigations. We believe that with these improvements nanosecond pulses and peak powers in the tens of watts range should be readily achievable in the generation of new low loss fibers.

III. LASER STUDIES AND MINIATURE LASER DEVICES USING Nd:MgO:LiNbO₃

A. Continuous-Wave Laser Action in Nd:MgO:LiNbO₃

1. Introduction

Laser action in Nd:MgO:LiNbO₃ was achieved at wavelengths around 1.09 μm. This new solid-state laser material exhibits a polarized fluorescence spectrum, characterized by a "low-gain polarization," $\lambda = 1.093$ μm, with the electric field perpendicular to the c-axis, and a π or "high-gain polarization," $\lambda = 1.085$ μm, with electric field parallel to the c-axis.

The first demonstration of true continuous-wave, room-temperature laser oscillation in neodymium lithium niobate was achieved in our laboratories by pumping at 598 nm a c-axis Nd:MgO:LiNbO₃ crystal (low-gain polarization). At this pump wavelength, CW laser operation in a- or b-axis lasers (high-gain polarization) required elevation of the temperature above 50 °C, due to photorefractive damage. However, CW room-temperature laser action for the high-gain polarization could be demonstrated by pumping in the near-infrared at 813 nm.

This section is devoted to the investigation of the main properties of Nd:MgO:LiNbO₃ as a solid state laser material. The section also treats the work on CW and quasi CW Nd:MgO:LiNbO₃ lasers pumped around 600 nm. The next section is concerned with Nd:MgO:LiNbO₃ lasers pumped in the near-infrared, particularly diode-pumped lasers.

We start the section with a brief description of the Nd:MgO:LiNbO₃ samples used in this work, followed by the theoretical considerations leading to the design of the miniature laser resonators. We proceed by presenting the experimental set-up and some of the more representative experimental results. Next, we describe the study of the main laser properties of this material, namely, fluorescence lifetime

and net gain cross section. Finally, a direct comparison with Nd:YAG is made.

2.   Nd:MgO:LiNbO$_3$ Samples

The bulk samples used in this work were cut from three boules grown and provided to us by Crystal Technology. The first two boules were grown from a Li/Nb congruent melt having 5-mol% MgO. They contained 0.15- and 0.2-wt.% Nd$_2$O$_3$ and will be referred to hereafter as the low- and the high-doped boules, respectively. The third boule was grown at a later period. It had a composition of 9 mol% MgO and 0.15 wt. % Nd$_2$O$_3$ and will be referred to as the high-magnesium boule.

Samples cut from the first two boules exhibited striations perpendicular to the c-axis, visible to the naked eye, and having periods on the order of 0.2 to 1 mm. The striations were probably due to refractive index changes caused by composition inhomogeneities. In addition, the high-doped samples contained significant amounts of inclusions. For this reason most of the laser devices were fabricated from low-doped samples.

The initial work on CW and quasi-CW Nd:MgO:LiNbO$_3$ lasers was done with two rectangular b-axis crystals with dimensions 2 $\times$ 2 $\times$ 10 mm and two rectangular c-axis rods with dimensions 2 $\times$ 2 $\times$ 11.5 mm and 1 $\times$ 1 $\times$ 5 mm respectively. All these rods belong to the low Nd doped type. The crystals' end faces were antireflection coated with 1875 Å of SiO$_2$.

Successful laser oscillation was attained in all of these crystals and in others also cut from the low-doped boule. Laser action was also achieved in a high-doped crystal; however, oscillation threshold could not be reached in either of two high-magnesium rods. Scattering of the visible-pump beam was more intense for these high-magnesium crystals. This increased scattering could be due to inhomogeneities such as compositional variations, occurring on a scale of microns that were not easily

Table 3.1

Nd:MgO:LiNbO$_3$ Samples

Sample	Orientation	Dimensions	Composition
C1, C2, C3	c-axis	1 × 1 × 5mm	5% MgO, 0.15% Nd$_2$O$_3$
C4	b-axis	3 × 3 × 10 mm	5% MgO, 0.15% Nd$_2$O$_3$
C5, C6	b-axis	2 × 2 × 10 mm	5% MgO, 0.15% Nd$_2$O$_3$
C7	c-axis	2 × 2 × 11.5 mm	5% MgO, 0.15% Nd$_2$O$_3$
C8, C9, C10	b-axis	(same group as C5, C6)	5% MgO, 0.15% Nd$_2$O$_3$
C11, C12, C13	c-axis	200 μm × 4 × 8 mm	5% MgO, 0.15% Nd$_2$O$_3$
C14	c-axis	2 × 2 × 10 mm	5% MgO 0.2% Nd$_2$O$_3$
C15, C16	c-axis	2 × 2 × 10 mm	9% MgO 0.15% Nd$_2$O$_3$

detected with the naked eye. Probably the large concentration of MgO made the achievement of good optical quality during the growth of this boule difficult.

Table 3.1 describes the Nd:MgO:LiNbO$_3$ samples used in this work.

3. Miniature Laser Resonator Design

The main criterion in the design of the miniature laser resonator is minimization of the threshold pump power. To achieve this goal we must choose the cavity length, mirrors' radii of curvature and focusing lens in such a way as to minimize the effective pump and signal mode volumes inside the crystal.

The mode overlap formalism provides the following expression for the absorbed pump power threshold of a four level laser,

$$P_{th} = \frac{h\nu_p}{\sigma\tau_f}\frac{\delta}{2}\left[\frac{\pi}{2}\left(\overline{W}_p^2 + \overline{W}_s^2\right)\right] \tag{3.1}$$

where $h\nu_p$ is the pump photon energy i, σ, the net gain cross section; τ_f, the lifetime of the upper laser level; δ, the cavity round-trip loss; $\overline{W}_p$ and $\overline{W}_s$, the pump and signal beam radii averaged over the crystal length. The average beam radii are given by,

$$\overline{W}_i^2 = \frac{W_i^2}{\ell} \int_0^\ell \left\{ 1 + \left[\frac{\lambda_i(Z - Z_i)}{\pi W_i^2 n} \right]^2 \right\} dz$$
$$= W_i^2 \left\{ 1 + \epsilon_i \left[\left(1 - \frac{Z_i}{\ell} \right)^3 + \left(\frac{Z_i}{\ell} \right)^3 \right] \right\} \tag{3.2}$$

In this expression, i refers to pump (p) or signal (s); W_i is the beam waist radius, Z_i the location of this waist inside the crystal (assuming $Z = 0$ at the input face of the crystal rod), n the refractive index and ℓ the crystal length. The diffraction term ϵ_i is equal to

$$\epsilon_i = \frac{1}{3} \left(\frac{\lambda_i \ell}{\pi W_i^2 n} \right)^2 \tag{3.3}$$

When the cavity is composed of equal radii mirrors, the beam waist is located at the center of the cavity and Equation (3.2) reduces to,

$$\overline{W}_i^2 = W_i^2 \left(1 + \frac{\epsilon_i}{4} \right) \tag{3.4}$$

The signal (or pump) waist radius $W_{i,opt}$ that minimizes the threshold is obtained from Equations (3.3) and (3.4),

$$W_{i,opt} = \sqrt{\frac{\lambda_i \ell}{\sqrt{12} \pi n}} \tag{3.5}$$

Using Equation (3.5) we calculated the optimum signal and pump waist radii for two representative $Nd:MgO:LiNbO_3$ rods. The results are listed in Table 3.2 together with the corresponding wavelengths and refractive indices.

To attain a signal waist radius close to $W_{s,opt}$ the cavity parameters, i.e., the cavity length L and the mirrors' radii of curvature R_1 and R_2 must be properly chosen. As a function of these parameters, the signal waist radius can be written as:

Table 3.2

Optimum Waist Radii

	Crystal	λ	n	$W_{i,opt}$
Pump		598 nm	(avg) 2.2662	15.6 μm
High Gain	b-axis (1 cm)	1.085 μm	(n_e) 2.1702	21.4 μm
Low Gain	c-axis (1.15 cm)	1.093 μm	(n_0) 2.2326	22.7 μm

$$W_s^4 = \left[\frac{\lambda_s}{\pi}\right]^2 \frac{L_{eff}(2R - L_{eff})}{4} \tag{3.6}$$

where, L_{eff}, the effective cavity length, is equal to

$$L_{eff} = L - \ell(1 - 1/n) \tag{3.7}$$

and we have assumed $R_1 = R_2 = R$.

Figure 3.1 shows a plot of Equation (3.6) versus cavity length with R = 5 cm and $\ell = 1$ cm. Examination of this figure reveals that the optimum signal waist is realized for two cavity lengths, namely $L_1 = 5.44$ mm and $L_2 = 105.31$ mm. Clearly, the first cavity length is not physically realizable due to the finite dimension of the crystal rod. In Figure 3.1 the signal waist radius exhibits a lower bound value of ~ 60 μm corresponding to L $= \ell = 1$ cm. This configuration will be referred to hereafter as the minimum length cavity. The second cavity dimension corresponds to the so-called concentric cavity which lies at the edge of the resonator stability region. An enlarged view of the variation of signal waist radius with cavity length close to the concentric configuration is shown in Figure 3.2. In this plot, the signal waist decreases smoothly with increasing cavity length from 60 μm to about 40 μm and then drops abruptly down to zero as the stability limit is approached. As a compromise between stability and low average signal radius a cavity length of about 10.4 cm was selected. For a longer sample ($\ell = 1.15$ cm) the optimum cavity

SIGNAL WAIST RADIUS VS CAVITY LENGTH
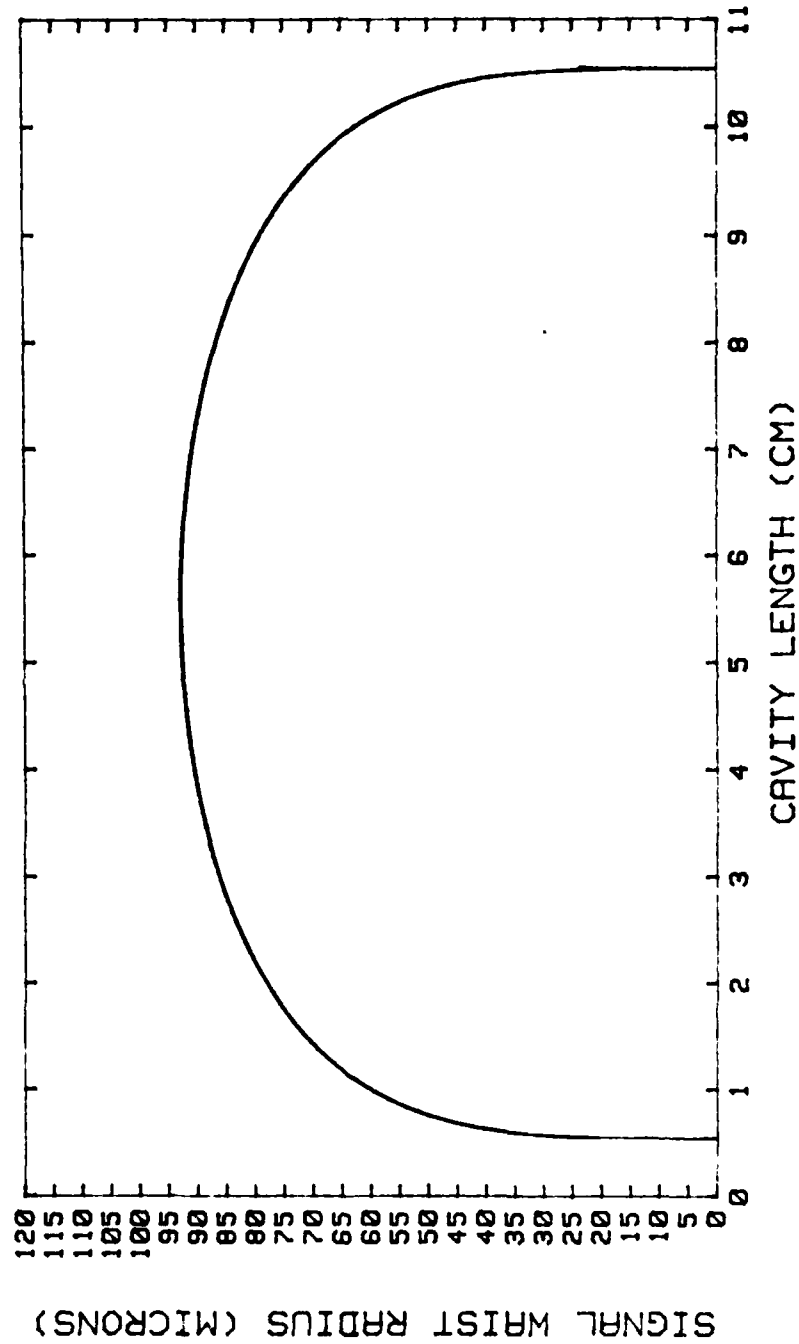
Figure 3.1--Signal Waist Radius as a Function
of the Laser Cavity Length.

SIGNAL WAIST RADIUS
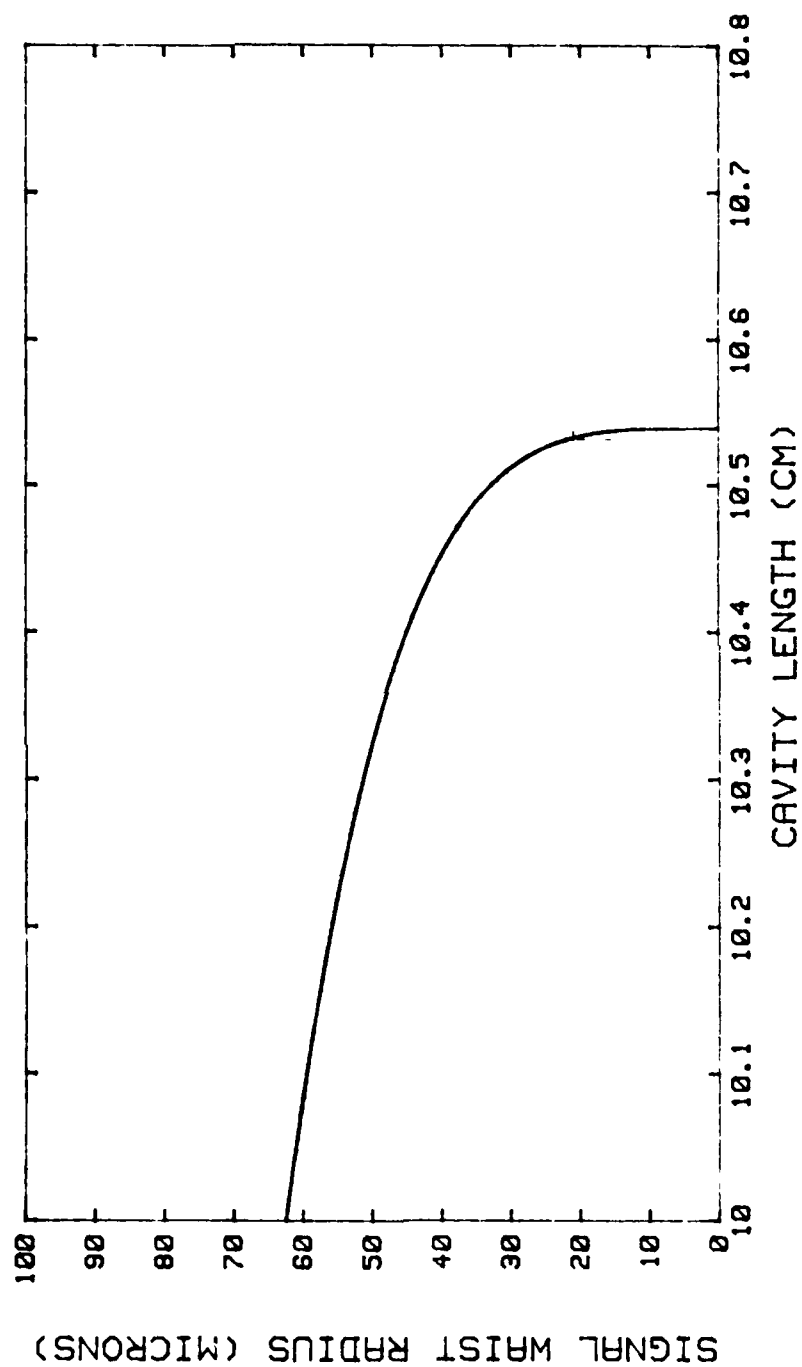
Figure 3.2--Dependence of the Signal Waist Radius on
Resonator Length near the Concentric
Cavity Limit.

length is $\approx$ 10.6 cm.

Concerning the choice of cavity mirrors we were limited by the radii of curvature available, i.e., 5 cm, 10 cm and ∞ (flat mirror). An analysis similar to the previous one revealed that the 5 cm radius mirror was best suited to minimize the threshold.

4. Experimental Set-Up and Results

4.1 CW Laser Set-Up

The experimental arrangement for the CW laser measurements is illustrated in Figure 3.3. It consisted of the pump lasers, a chopper or an acousto-optic cell to control the pump duty cycle, a focusing lens, an optical back-reflections isolator composed of a polarizer and a quarter wave plate, the Nd:MgO:LiNbO$_3$ laser and the detection elements. The pump beam was provided by a Rhodamine 6G dye laser emitting at 598 nm, pumped itself by the 514.5 nm, 2 W radiation of an argon-ion laser. About 300 mW of optical power was provided by the dye laser.

To avoid reduction of output power in the b-axis lasers due to photorefractive damage, a low duty cycle was chosen. The pump beam was modulated at a repetition rate of 25 Hz in intervals of $\sim$ 500 μsec. Since these intervals were more than three times the fluorescence lifetime of the material ($\sim$ 120 μsec) full population inversion was achieved.

4.2 Experimental Results

Both nearly concentric cavities and minimum length cavities were investigated in this work, the former because of their inherent lower threshold and the latter because they provide a way to estimate the net gain cross section of the material.

Figure 3.4 shows plots of the laser output power at $\lambda = 1.085$ μm versus absorbed pump power for b-cut lasers in a short cavity. The first laser consisted of
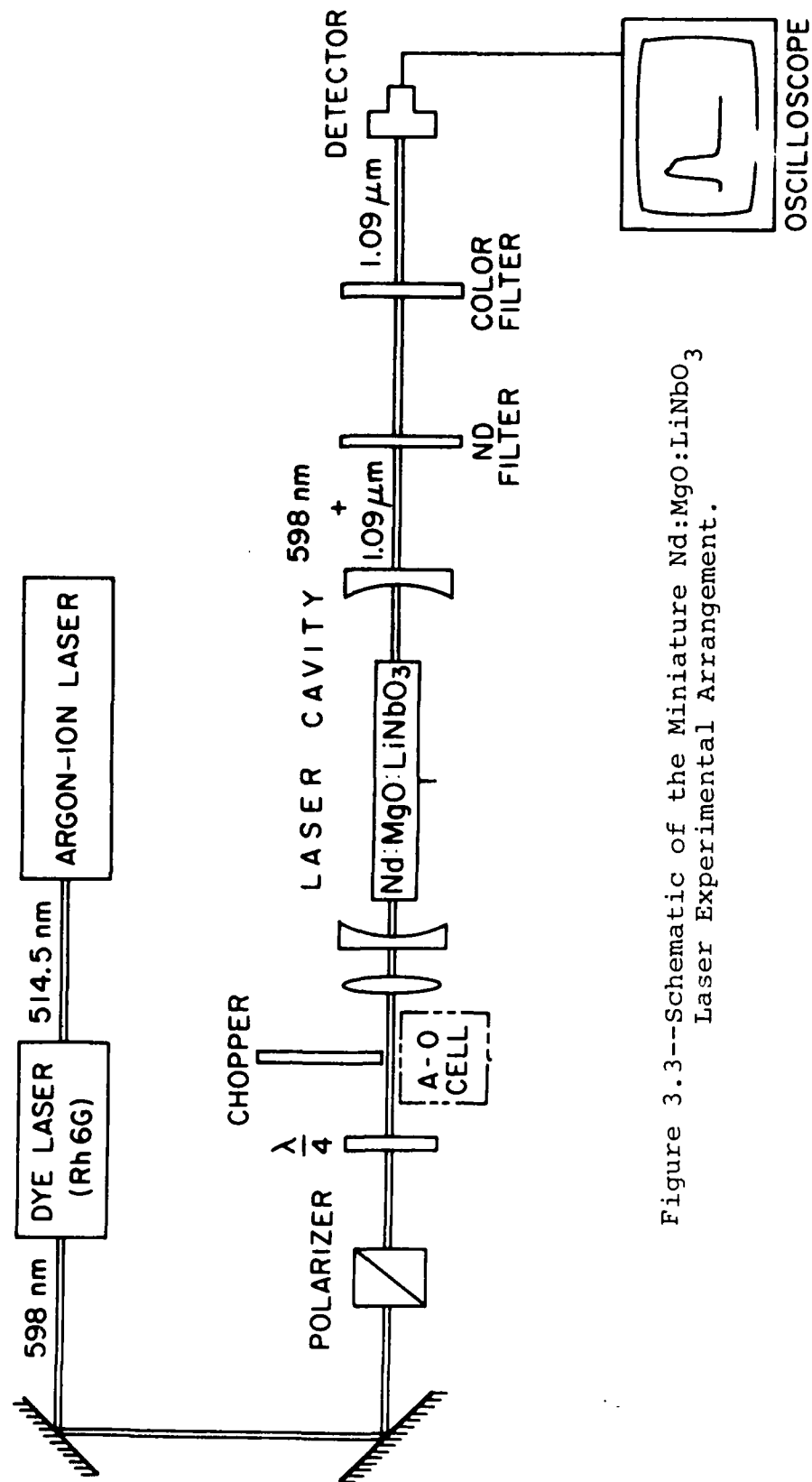
Figure 3.3--Schematic of the Miniature Nd:MgO:LiNbO$_3$ Laser Experimental Arrangement.
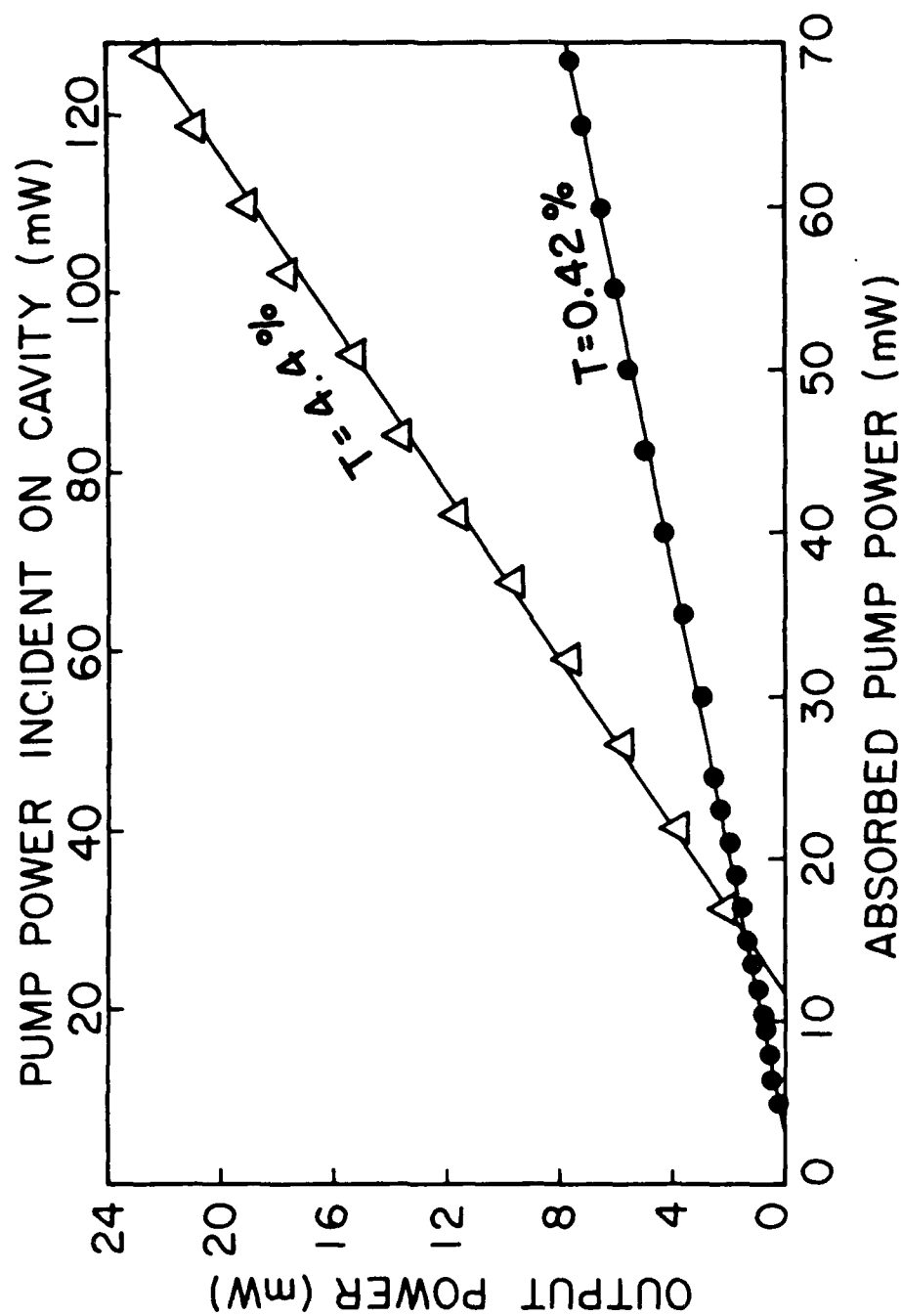
Figure 3.4--Output Power versus Pump Power Curves, π or High Gain Polarization. The Laser Parameters are given in the Text.

two 5 cm radius mirrors, a high reflector and a 0.42% transmissive output coupler separated by a distance of 11.5 mm. The second laser was identical except that the output coupler was 4.4% transmissive with a 10 cm radius of curvature. The oscillation thresholds are relatively low, on the order of 4 to 12 mW. As expected the output grows linearly with the absorbed pump power. A least square fit to a straight line was made to the experimental data (solid lines in Fig. 3.4). The device slope efficiency is defined as the slope of the curve fits, i.e., as the ratio of output energy to input energy above threshold. The slope efficiency of 39% observed with the high transmission output coupler is close to the theoretical limit of 55% given by the ratio of signal to pump photon energy. A maximum quasi-CW output power in excess of 22 mW was observed for an absorbed pump power of 70 mW which corresponds to a maximum available pump power incident on the laser cavity of 128 mW.

Note that the analysis presented previously predicted a pump power threshold much smaller for a nearly concentric cavity than for a minimum length cavity. This was verified experimentally by increasing the mirror separation up to 10.4 cm in the laser having a 0.42% transmissive output coupler. Under these conditions the absorbed pump power required to reach threshold was lower than 1 mW. However, the short term power fluctuations of this laser, about 3 to 6%, were larger than for the short cavity lasers, which were typically 1%. The better stability of the short laser is probably attributable to the less severe influence of pump beam wandering due to the much larger signal mode size.

Figure 3.5 shows the output power characteristic of two low gain, c-cut lasers. The first one was made of the longer crystal in a nearly concentric cavity. This laser was run CW without noticeable output degradation during the time it took to characterize it. To the best of our knowledge this is the first report of CW oscillation in Nd:LiNbO₃. Because of the smaller mode size in this device, its threshold was
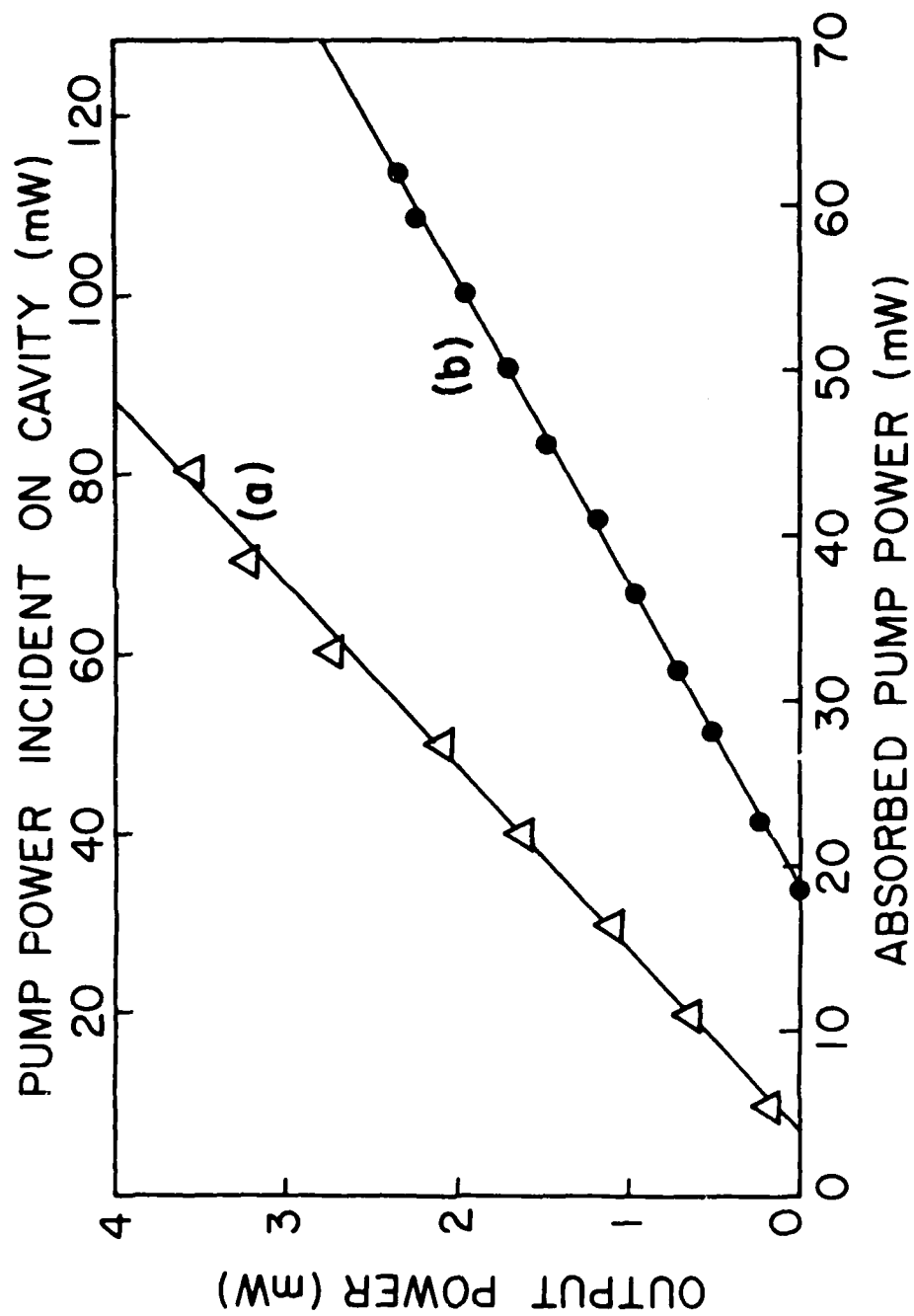
Figure 3.5--Output Power versus Pump Power Curves, Low Gain Polarization. (a) R = 5 cm, L = 106 nm, T = 0.42%. (b) R = 10 cm, L = 6.5 nm, T = 0.30%.

Table 3.3

CW Laser Data

Polarization	Crystal	T	Slope Efficiency	Inferred Crystal Loss	Threshold Power
High Gain	b-axis	4.4%	39%	1.8%	12 mW
High Gain	b-axis	0.42%	11.7%	1.6%	3.6 mW
Low Gain	c-axis	0.42%	9.05%	2.1%	3.9 mW
Low Gain	c-axis	0.3%	5.4%	2.7%	18.8 mW

comparable to that of the previous high gain devices, on the order of 4 mW. The second laser was made of the short crystal placed in a short cavity. The larger mode size is responsible for its higher threshold. The data for the lasers of Figures 3.4 and 3.5 are summarized in Table 3.3.

The cavity round trip loss δ was inferred from the equation

$$s = \frac{T}{\delta}\frac{\lambda_p}{\lambda_s} \tag{3.8}$$

where s is the slope efficiency, δ the round trip cavity loss, T the output coupler transmittance and λ_i the signal (s) or pump (p) wavelength.

A remarkable feature of the results shown in Table 3.3 is that some are comparable to the best results reported for Nd:YAG rods in previous years. As an illustration, Table 3.4 lists the highest slope efficiency and the lowest pump threshold obtained for a b-axis crystal (high gain polarization) and also the corresponding values for Crystal No. 1 of Nd:YAG listed in the final report covering the period April 1982 - May 1983 (Table 5, page 74). A comparison between the laser properties of Nd:MgO:LiNbO$_3$ and Nd:YAG will be presented in Section III A 8.

5. Transverse Mode Structure of the Signal and Pump Beams

In Section III A 4 some of the main properties of the Nd:MgO:LiNbO$_3$ CW

Table 3.4

CW Laser Data for a Nd:MgO:LiNbO$_3$

Sample and a Nd:YAG Crystal Rod

	Nd:MgO:LiNbO$_3$	Nd:YAG
Slope Eficiency with T $\sim$ 5%	39%	43.6%
Quantum Efficiency	70.7%	90.1%
Inferred Round Trip Loss	1.6%	0.75%
Pump Threshold (T $\sim$ 0.5 %)	3.6 mW	5.0 mW

lasers were investigated, namely, output power versus absorbed pump power, slope efficiency, quantum efficiency and inferred crystal loss. A complete characterization of the laser signal must also include a study of the transverse mode structure of the laser beam.

Under optimum alignment conditions all the lasers studied were found to oscillate in the fundamental Gaussian mode (TEM$_{00}$). Preferential excitation of higher order modes could be achieved by slightly misaligning the cavity mirrors.

By using a reticon array of silicon photodiodes, the signal and pump beam transverse mode profiles were analyzed. Figure 3.6 shows the signal transverse mode structure of a minimum-length laser cavity consisting of a 1 cm crystal, a 5 cm radius high reflector and a flat output coupler. The reticon array was located 14 cm behind the output coupler. The individual diode array elements are clearly resolved in the photograph and consequently, the beam diameter can be easily determined by counting array elements. The Gaussian beam radius is defined as the transverse distance coresponding to a $1/e^2$ drop in the intensity. Knowing the diode separation (25 μm), the $1/e^2$ diameter of the signal beam is 61 elements $\times$ 25 μm = 1.52 mm.

Figure 3.7 depicts the transverse profile of the pump beam just before reaching
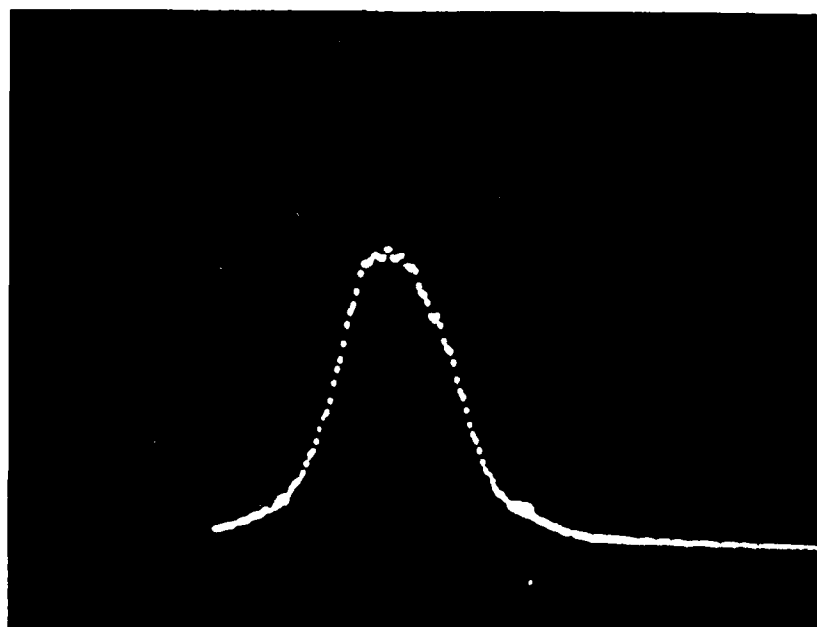
Figure 3.6--Transverse Mode Profile of the Signal
Beam. $1/e^2$ Diameter = 1.52 mm.
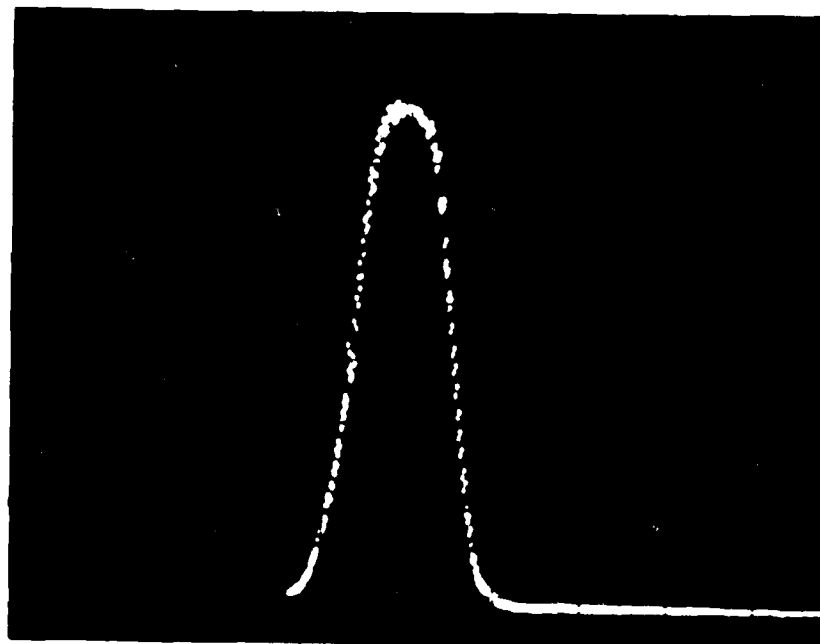
Figure 3.7--Pump Beam Transverse Mode Structure.
Horizontal Scale: 0.1 msec/div.
$1/e^2$ Diameter = 1.96 mm.

- 70 -

the focusing lens. The figure shows that the pump beam profile was also nearly Gaussian with a diameter of 1.96 mm.

The signal and pump beam waist radii (W_s and W_p) inside the laser cavity were determined from the measured beam radii using standard ABCD matrix formalism. Both W_s and W_p were used to estimate the net gain cross section as explained in the next sub-sections.

6. Laser Characterization of Nd:MgO:LiNbO$_3$

The material properties determining the performance of a solid state laser are, basically, the fluorescence lifetime τ_f and the net gain cross section σ. τ_f determines the amount of population inversion N that can be achieved for a given pump rate R_p as $N \simeq R_p \tau_f$ (for a four-level laser in CW or quasi-CW operation). σ determines the gain coefficient g achievable with a given population inversion density n and crystal length ℓ as $g = n\sigma\ell$. This sub-section describes the measurements of τ_f and σ for this new solid state laser material.

6.1 Fluorescence Lifetime

Due to concentration quenching, the fluorescence lifetime τ_f depends on the neodymium doping level. Therefore, a different τ_f was measured for the low- and for the high-doped samples.

To determine τ_f, the crystals were optically excited with a chopped pump dye laser, and the output fluorescence was detected and recorded on an oscilloscope. The measured values of τ_f were 102 μs and 120 μs for the high doped and low doped samples respectively. The measurements were carried out at room temperature. Investigations by another research group at Stanford University indicate no change in τ_f for the high doped sample for temperatures up to 100 °C.

Since only low doped samples were used to make most of the laser devices described in this work, the value $\tau_f = 120$ μs is consistently assumed unless other-

wise specified.

6.2 Net Gain Cross Section

The net gain cross section σ is equal to the estimulated emission cross section σ_e minus the excited state absorption (ESA) cross section σ_{ESA}. As mentioned before, we are interested in the net gain cross section σ because it determines the laser gain (and the laser threshold).

The $^4F_{3/2}$ - $^4I_{11/2}$ transition in Nd:LiNbO$_3$ was investigated by Kaminskii in 1971. He reported the following values for σ: 5×10^{-19} cm^2 for the π or high gain polarization and 2×10^{-19} cm^2 for the low gain polarization.

The net-gain cross section of our Nd:MgO:LiNbO$_3$ crystals was estimated by using three methods. The first method is based on the analysis of the fluorescence spectrum. The second method is based on the quasi-CW and CW laser measurements. This latter method has been extensively used under this contract to characterize Nd:YAG fiber and bulk lasers. It consists of the following: first, the CW or quasi-CW slope efficiency is used to infer the round-trip cavity loss δ; second, the measured pump and signal beam profiles and a matrix formalism are used to determine the waist radii. The average beam radii inside the crystal, $\overline{W}_s$ and $\overline{W}_p$, can then be calculated. Finally by using the measured pump power threshold P$_{th}$ as well as δ, $\overline{W}_s$, $\overline{W}_p$ and τ_f we obtain an estimation for σ from Equation (3.1), Section III.A.3. The major difficulty in this method is to determine the waist radii with high accuracy.

A third approach consists of making another laser with a material of known cross section (such as Nd:YAG), both lasers having the same cavity parameters, i.e., effective cavity length and mirror' radii of curvature. Also, the sample effective lengths must be the same. Under these conditions we can assume that the pump and signal cavity mode volumes are the same in both lasers. Therefore, from knowledge

72

Table 3.5

Mode Sizes and Inferred Cross Section

Crystal	T	Round Trip Loss	Pump Waist Radius	Average	Signal Waist Radius	Average	Inferred Cross Section	Kaminskii Cross Section
b-axis	4.4%	6.2%	19.4 μm	23 μm	74 μm	74.3 μm	6.7×10^{-19} cm^2	
b-axis	0.42%	1.9%	19.4	23	69	69.3	6.1×10^{-19}	5×10^{-19} cm^2
c-axis	0.42%	2.5%	28.9	30.5	36	38.6	3.3×10^{-19}	
c-axis	0.3%	3%	19.4	20.4	69	69.1	1.8×10^{-19}	2×10^{-19} cm^2

of the cavity loss and the lifetimes of both materials and the thresholds, we can relate their cross sections and, thus, infer one of them from the known value of the other. In the following subsection we describe the experimental results leading to the determination of σ.

7. Determination of σ from the Laser Data

The pump and signal waist radii and the average beam radii for the lasers described in Section III.A.4 are listed in Table 3.5 as well as the inferred cross sections for both polarizations. When the waist radii are small, on the order of 30 μm or less, a small error in their determination may introduce a significant error in σ. For this reason the value of σ obtained from the short cavity lasers is more reliable. For these lasers, $W_s \sim 70 \mu$m whereas for the nearly concentric laser, $W_s \sim 36 \mu$m. In addition, for the short cavities, the pump waist radius is much smaller than the signal waist radius and an error in W_p has a less severe influence in the determination of σ_e. (W_p appears in the sum $W_p^2 + W_s^2$ in the expression for σ).

Analysis of the b-axis lasers data yields a value for σ slightly larger than 6×10^{-19} cm^2 (high gain polarization). For the low gain polarization, a discrepancy is observed between the inferred values. However, as explained previously, the value

of 1.8×10^{-19} cm^2 is certainly more reliable.

The cross sections deduced from laser measurements were compared to the cross sections obtained from fluorescence experiments performed by another research group at Stanford on identical samples. The fluorescence experiments yielded 1.8×10^{-19} cm^2 for the high gain polarization and 5.1×10^{-20} cm^2 for the low gain polarization, i.e., about 3 times smaller than the values inferred from laser characteristics. However, the ratio of cross sections for both polarizations is the same in both methods, namely, about 3.5. The fluorescence measurement provides the stimulated emission cross section σ_e, whereas the laser masurement gives the net gain cross section σ. These results indicate that $\sigma_e < \sigma$. However, $\sigma_{ESA} = \sigma_e - \sigma$ cannot be a negative quantity. No satisfactory explanation for this result was found.

8. Direct Comparison with Nd:YAG

As explained previously, the cross section for Nd:MgO:LiNbO$_3$ can be deduced from that of Nd:YAG if similar samples of both materials are investigated in lasers having identical characteristics. Under these circumstances the pump and signal cavity volumes cancel out in the equation of σ (provided they are identical in both lasers.)

Three short cavity lasers were implemented in this study. All of them had 5 cm radius mirrors and 0.12 % output coupling. The first laser had the long c-axis rod and was 1.2 cm long (effective cavity length, $L_{eff} = 0.56$ cm). The second laser contained a b-axis sample ($2 \times 2 \times 10$ mm) in a 1.05 cm long cavity ($L_{eff} = 0.51$ cm). Finally, a Nd:YAG rod ($1 \times 1 \times 7.5$ mm) was placed in the third laser; the cavity length was chosen to match $L_{eff} = 0.51$ cm, i.e., $L = 0.85$ cm. The pump wavelength was the same in all cases, equal to 598 nm.

Table 3.6 lists the results of the quasi-CW laser measurements, namely, slope efficiency and inferred cavity loss. The next to last column lists the

Table 3.6

Direct Comparison between

Nd:MgO:LiNbO$_3$ and Nd:YAG

Laser	Slope Efficiency	Cavity Loss	Pump Threshold	Ratio of Cross Sections	Laser Measured Cross Section
b axis	17.5%	1.3%	7.3 mW	1.42	5.6×10^{-19} cm^2
c axis	11.2%	2%	21	0.76	3.0×10^{-19} cm^2
Nd:YAG	9.8%	2.4%	10	1	3.96×10^{-19} cm^2

ratios $\left(\frac{\delta}{t_f P_{th}}\right)_1 / \left(\frac{\delta}{t_f P_{th}}\right)_2$, where '1' refers to either the b-axis or the c-axis Nd:MgO:LiNbO$_3$ laser and '2' refers to the Nd:YAG laser. This ratio is equal to the ratio of cross sections of both materials according to Equation (1) of Section III.A.3. The Nd:YAG sample had been already investigated in conjunction with the Q-switched fiber laser experiments and was found to have a value of $\sigma = 3.96 \times 10^{-19}$ cm^2. Using this figure and the cross section ratios given in Table 3.6 we inferred the following cross sections for Nd:MgO:LiNbO$_3$: 5.6×10^{-19} cm^2 for the high gain polarization and 3.0×10^{-19} cm^2 for the low gain polarization. These results compare well with the cross sections inferred from the first method. However, they depend on the value assumed for the cross section of Nd:YAG as well as on the assumption of identical pump and signal mode sizes in all three lasers.

B. Diode-pumped Nd:MgO:LiNbO$_3$ Laser

1. Introduction

True CW room-temperature laser operation for the π or high gain polarization in Nd:LiNbO$_3$ was demonstrated in our laboratories by pumping a miniature b-axis Nd:MgO:LiNbO$_3$ laser at a wavelength around 810 nm. This result was followed by the demonstration of diode-pumped laser action for both the high gain and the

75

low gain polarizations. All these lasers operated for extended periods of time (over an hour for the diode-pumped device) without exhibiting any reduction in output power.

In this section we discuss the laser performance of Md:MgO:LiNbO$_3$ when excited by near-infrared radiation. Then we focus our attention on diode-pumping.

Most of the work done under the auspices of the present and previous contracts has utilized either argon-ion lasers or dye lasers as sources of optical excitation. They offer several advantages, including high available power (3W from the Ar-ion at 5145 Å), clean Gaussian mode and tunability in the yellow-orange region of the spectrum (Rhodamine 6G dye). Nevertheless, the ultimate goal in the present program is the utilization of semiconductor laser diodes as pump sources.

A detailed study was carried out on two types of laser-diode pump sources; a high-power, single-stripe device and a phase-locked, multiple-stripe array. One of these devices was used to demonstrate diode-pumped laser oscillation in Nd:MgO:LiNbO$_3$.

2. Infrared-Pumped Nd:MgO:LiNbO$_3$ CW Laser

The pump excitation in this experiment was provided by a CR-599 dye laser operating with the dye styryl 9M. The pump beam was focused into the crystal through the high reflector mirror with a single 10 cm focal length lens. The miniature laser consisted of a b-axis sample (2 × 2 × 10 mm) inside a resonator composed of 5 and 10 cm-radius mirrors. The cavity length was about 1 cm. The pump dye laser was tuned to the largest near-infrared absorption peak of the material, either 809 nm, for pump polarization perpendicular to the c-axis, or 813 nm, for polarization parallel to the c-axis. The laser operated in the π or high-gain polarization.

Figure 3.8 shows the measured output power versus absorbed pump power for
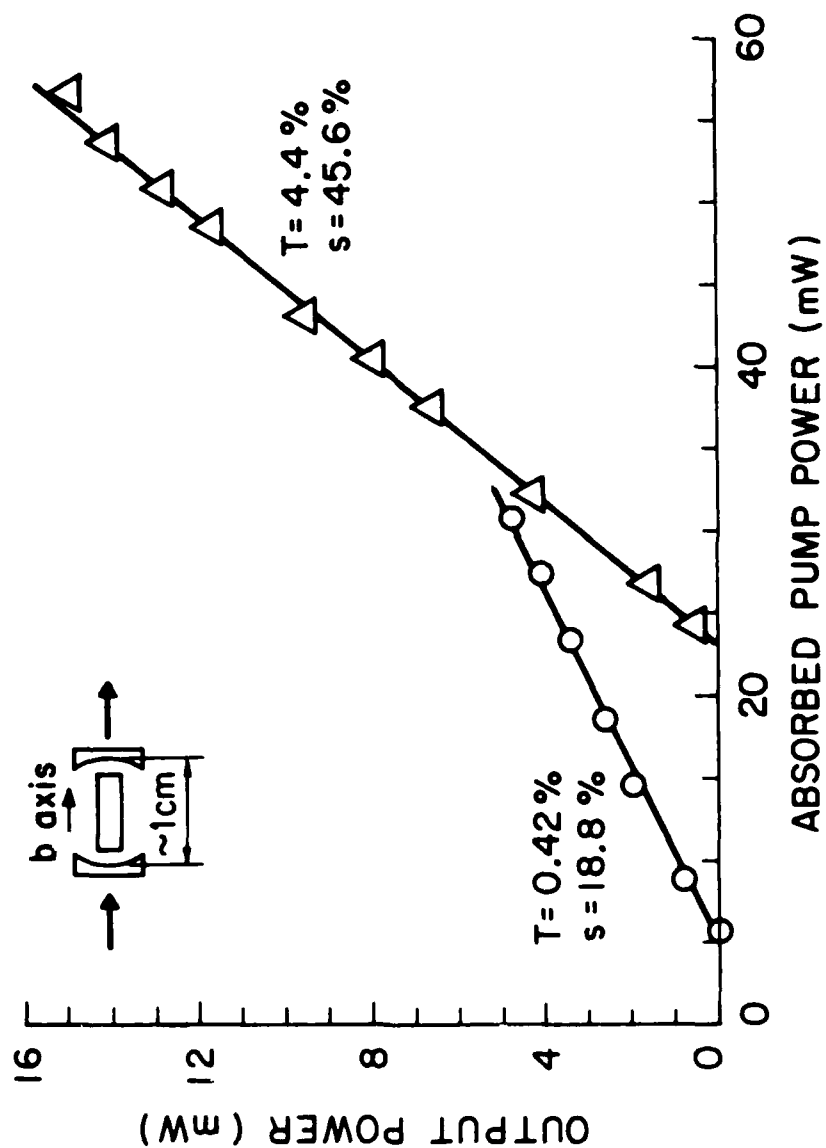
Figure 3.8--CW Laser Output Power versus Absorbed Pump Power. With T = 0.42% a Threshold of only 5 mW was Achieved. With T = 4.4% the Slope Efficiency s was as High as 45.6%.

two different output coupler transmittances T. With $T = 0.42\%$ the absorbed pump power threshold was 5 mW. With $T = 4.4\%$ the threshold was 23 mW and the slope efficiency 45%. This slope efficiency is among the highest slope efficiencies obtained with a neodymium laser.

No reduction in the output power from this laser was observed at room temperature during a time interval of 20 minutes, which is the longest continuous time we monitored this device. During this interval, the laser power stability was only limited by the stability of the infrared dye laser pump. This is a significant improvement over the non-MgO doped Nd:LiNbO$_3$ devices operated in the past. In 1975 Kaminow and Stulz reported the operation of a Nd:LiNbO$_3$ z-polarized laser pumped also in the near-infrared, in this case by a Kr-ion laser ($\lambda = 750\,nm$). At a duty cycle of only 3%, the output from this laser disappeared entirely after several minutes of operation due to the influence of photorefractive damage.

The output beam from the Nd:MgO:LiNbO$_3$ laser could be coupled into a single mode fiber having a core diameter of 5 μm by using a standard 20X microscope objective. Even though the objective was not coated for this wavelength, an overall coupling efficiency of 50% could be achieved. Correcting for the transmission of the objective. The transmission of the objective was and therefore the coupling efficiency was about 0.5 at $\lambda = 50$. This indicates the excellent quality of the laser output phase front. Higher coupling efficiencies are expected by using optimized focusing optics.

3. High Power Laser Diodes for Pumping Nd:MgO:LiNbO

Until recently, laser diodes (LD) with output powers exceeding 20 mW and operating at wavelengths close to 810 nm were not commercially available. The advent of multiple-stripe phase-locked laser-diode-arrays is helping to overcome the power limitation. Also, progress in the fabrication of single-stripe semiconductor

devices has led to the development of single-lobed far-field pattern laser diodes with output powers exceeding 30 mW. Within the realm of this contract two high power LD's were investigated with the purpose of using them to pump miniature Nd:MgO:LiNbO₃ lasers. One is a multiple-quantum-well, multiple-stripe array whose output is coupled directly into a multimode-fiber pigtail, on loan from Litton Systems Inc. The other is a single-stripe LD purchased from Sharp Corporation.

A complete characterization of these pump sources in terms of temperature-wavelength tunability, output power, output polarization and transverse mode-profile and spatial coherence is presented in this section.

3.1 Multiple-Stripe Laser Diode Array

The array, supplied by Spectra Diode Laboratories, is a multi-...consisting of 10 coupled, gain-guided stripes ... The fiber-coupled package provides ... a 0.3 numerical aperture silica fiber. ... lies between 780 and ... MHz ... The diode array we used was not ... We measured the wavelength ... 0.8 nm resolution. The diode ... 25 C. In making this measurement the ... radiator which prevented ... internal heat dissipation. According ... shifted with temperature at a ... 20°C. From the data we see that an operating tem-... 809 nm absorption peak shown in Figure ...infrared absorption spectrum of Nd:MgO:LiNbO₃ ... laser spectrophotometer.

79

Figure 3.9--Absorption Coefficient (α) of Nd:MgO:LiNbO₃ at Near Infrared Wavelengths.

To raise the diode temperature to the desired value we suppressed the finned radiator and thermally isolated the diode case from the optical table. The diode temperature was raised by heat dissipation until a thermal equilibrium with the surrounding air was reached. At 39°C we measured $\lambda = 807$ nm, in agreement with the data given previously.

By using a Glan-Thompson polarizer we determined that the diode array output was either unpolarized or close to circularly polarized. Therefore, the effective absorption coefficient of a b-axis Nd:MgO:LiNbO$_3$ crystal is given by the average of the π and σ values shown in Figure 3.9, i.e., 0.9 cm^{-1} at $\lambda = 809$ nm. Radiation from the multimode fiber was collected and collimated by means of a 20X microscope objective, then refocused into the 1 cm long b-axis sample. The focusing lens had $f = 5.2$ cm. We measured a transmission through the crystal of 49%. This figure does not include the loss due to the lens.

The beam waist after the 5.2 cm focusing lens was imaged by using another 20X microscope objective into a reticon array and is illustrated in Figure 3.10. Most of the beam energy was concentrated in an inner circle of diameter $\sim 150\ \mu$m which is surrounded by a larger annulus of diameter $\sim 300\ \mu$m. In spite of the short focal-length lens used, the waist radius is very large, one order of magnitude larger than the waist radius of a focused Gaussian beam having the same diameter before focusing. This can be attributed to the spatial incoherence of the radiation coming from the highly multimoded fiber pigtail.

An attempt was made to pump a b-axis Nd:MgO:LiNbO$_3$ miniature laser with the radiation from the laser diode array. The details of the experimental set-up and cavity alignment are similar to those discussed in III.B.4. The output power from this LD (30 mW incident, 11 mW absorbed) was not enough to reach oscillation threshold. Since the focused LD beam waist radius is, as we said before, one order of magnitude larger than that of a focused Gaussian beam, the threshold should be
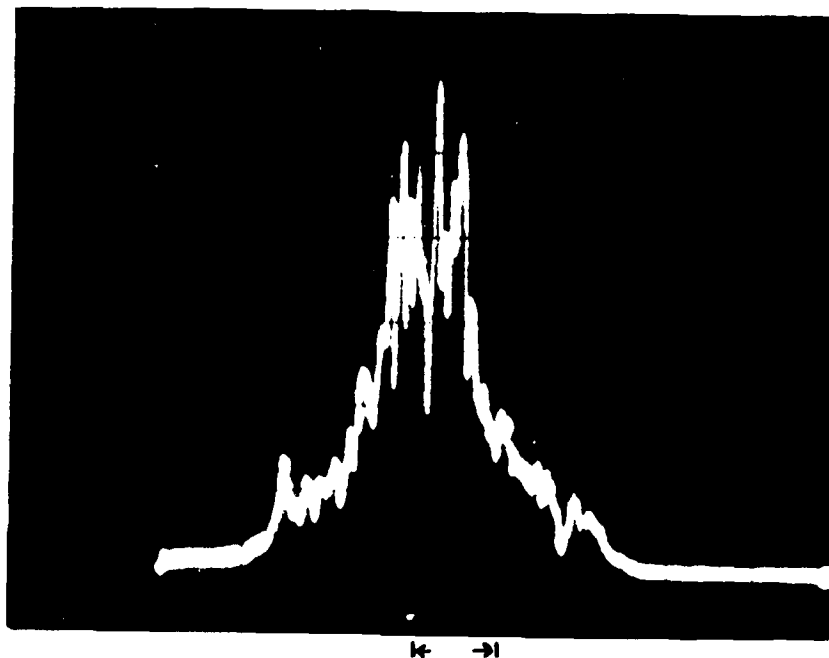
Figure 3.10--Transverse Mode Profile of the L.D. Array
Beam after an f = 5.2 cm Lens and Imaged
with a 20X Objective. Horizontal Scale:
1.3 mm/div.

two orders of magnitude higher.

A multiple-stripe, phase-locked diode array without a fiber pigtail exhibits a two-lobe far field pattern. Each lobe is spatially coherent and, thus, it can be focused to a tens-of-microns spot. Besides focusability, such an array has the same characteristics as the array described in this section. It would be very convenient to acquire one of these arrays for future diode-pumped laser work.

3.2 Single-Stripe Sharp Laser Diode

The diode LTO15MD can provide 30 mW of output at a wavelength of 830 ± 15 nm. Upon our request the vendor selected a diode whose wavelength lies within the lower interval of the specified range. At room temperature this wavelength is 820 nm.

This LD must be cooled in order to attain a strong near-infrared absorption peak of Nd:MgO:LiNbO$_3$ (see Figure 3.9). A solid copper holder fabricated earlier under this contract was used as a heat-sink. A small trapezoidal holder supported the LD, its inner walls being in good thermal contact with the diode case. Each side face of the trapezoid was pressed against a planar thermoelectric-cooler whose hot surface firmly contacted the heat sink. With the aid of the thermoelectric coolers a temperature gradient as high as 30 °C could be achieved between the diode holder and the heat sink (room temperature).

The output from the single-stripe Sharp diode was collected and collimated by a 20X microscope objective. The collimated beam was refocused by using a 10 cm focal length lens into a 1 cm long b-axis Nd:MgO:LiNbO$_3$ crystal. Transmission through the sample was recorded as a function of laser diode temperature, and the results are shown in Figure 3.11. Prior to the measurement the polarization of the diode laser beam was adjusted to be parallel to the crystal c-axis (π-polarized). Comparing Figures 3.9 and 3.11 we conclude that this particular laser diode must
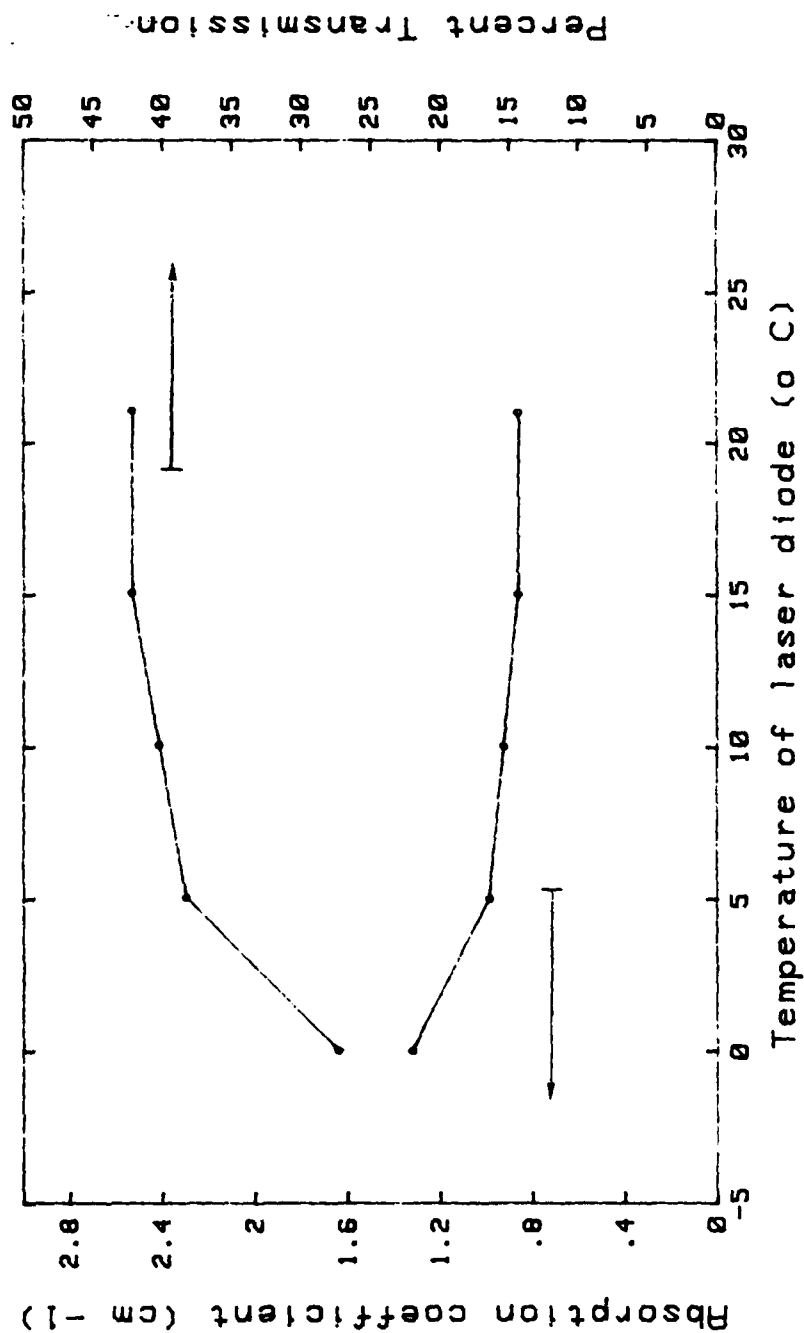
Figure 3.11--Percent Transmission and Absorption Coefficient (α) for a b-axis Nd:MgO: LiNbO$_3$ Sample. The Peak Absorption $\alpha = 1.3$ cm^{-1} at 0°C Corresponds to a Wavelength $\lambda \sim 813$ nm.

- 84 -

be cooled to about 0 °C to emit at the 813 nm peak-absorption-wavelength. The corresponding rate of change with temperature is

$$\Delta\lambda/\Delta T = 7\,nm/25\,°C \sim 2.8\,\text{Å}/°C \tag{3.9}$$

The transverse profile of the LD beam was analyzed by means of a Reticon array of silicon photodiodes. The beam cross section after the 20X microscope objective was elliptical with $1/e^2$-axes of 1.88 and 4.08 mm respectively. The ratio of axes (2.6) is approximately equal to the ratio of divergence perpendicular to divergence parallel to the diode active layer as specified by the manufacturer. This laser diode was damaged during its characterization, and it was replaced by a similar diode provided by another research group at Stanford.

4. Laser Diode-Pumped Nd:MgO:LiNbO$_3$ CW Laser

4.1 Experimental Procedure

The miniature laser consisted of a 3 cm long resonator composed of 10 cm and 2.5 cm radius mirrors and containing a 1 cm long b-axis sample. The laser-diode utilized was a Sharp LT015MD model very similar to that described in Section III.B.3. This diode emitted at a wavelength of 826 nm at room temperature. It needed to be cooled about 10 °C to reach the 823 nm absorption peak of Nd:MgO:LiNbO$_3$ (see Figure 3.9). At this particular wavelength only half of the power incident on the crystal was absorbed.

The near-infrared radiation emitted by the L.D. was collected and collimated by a 20X microscope objective. This collimated light, and the 598 nm beam from the Rhodamine 6G dye laser were combined by a special beam splitter. The splitter transmitted about 80% of the visible light and reflected close to 100% of the near-infrared radiation incident at 45°. Both beams were focused by a 10 cm focal-length

lens into the crystal passing through the front high-reflector mirror.

Cavity alignment proceeded as follows. First, the pump beams were positioned to be collinear by adjusting the micropositioners supporting the collimating microscope objective. Then, the LD beam was blocked and the miniature resonator alignment was performed under Rh 6G laser pumping alone. A chopper was required to avoid photorefractive damage due to the visible pump illumination. When lasing was attained, the L.D. beam was unblocked and cavity alignment was refined. A sharp increase in the Nd:MgO:LiNbO$_3$ laser output power was observed when a good mode overlap between the laser beam and the two pump beams was achieved. The final adjustment consisted of displacing axially the laser cavity trying to overlap the signal waist and the laser diode beam waist. The last step was necessary because due to the differences in wavelength and size between the two pump beams, they were focused at slightly different locations. Finally, by blocking the dye laser beam we verified that the L.D. pump excitation alone was sufficient to sustain laser action.

4.2 Experimental Results

We already reported in Section III.B.1 that photorefractive damage is almost nonexistent in Nd:MgO:LiNbO$_3$ 'a' or 'b' axis lasers pumped at a wavelength of 810 nm or higher. We also verified the significant reduction of photorefractive damage under diode-pumping conditions. The (π-polarized) Nd:MgO:LiNbO$_3$ laser operated in true continuous wave mode during periods of one hour in duration without exhibiting any reduction in output power. In addition, the short-term laser output stability was much better than under infrared-dye laser pumping. This improved performance was due to the better power stability of the laser diode source which could be temperature-stabilized by an electronic feedback loop.

The laser output power at 1.085 μm was measured versus absorbed pump power
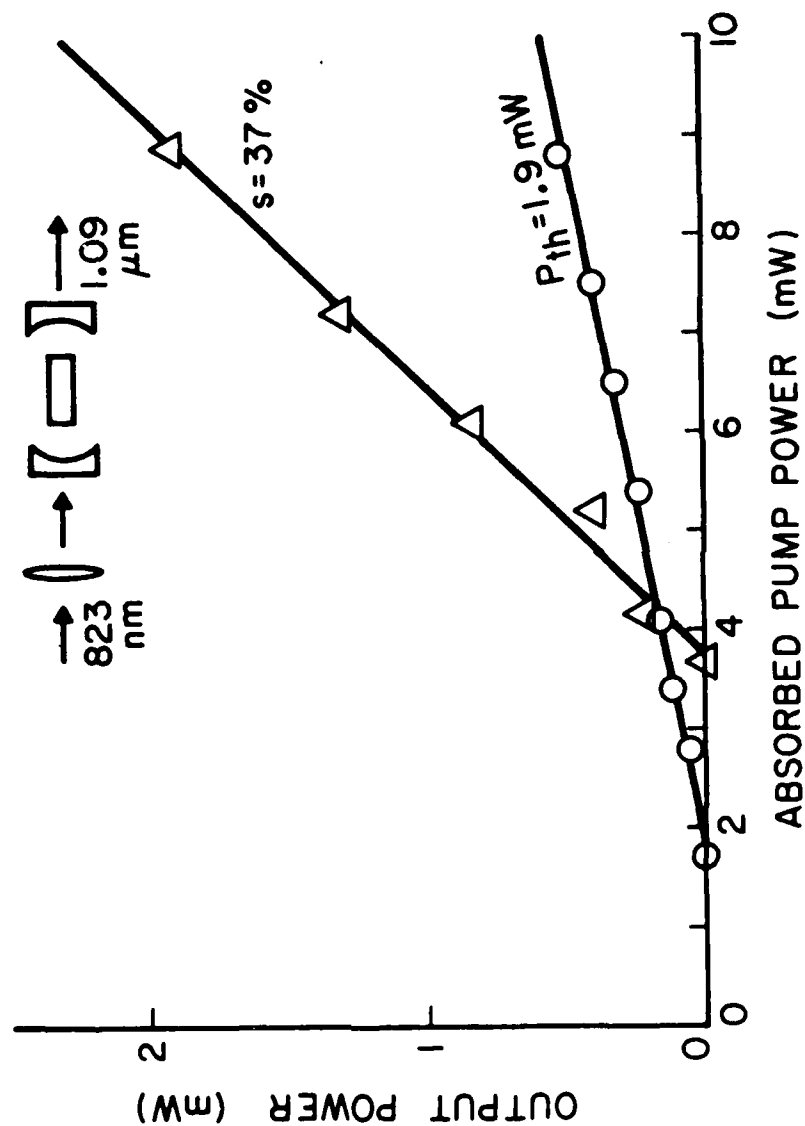
Figure 3.12--Output Power versus Absorbed Pump Power.

at 823 nm. These results are shown in Figure 3.12. The two curves correspond to different output mirror transmittances T. With a 0.8% transmissive output mirror the absorbed pump power threshold was 4 mW and the slope efficiency 37%. By using a nominally high reflector mirror the threshold was less than 2 mW. This latter value is about the same as the lowest threshold reported in the literature for diode-pumped monolithic Nd:YAG laser oscillators. The maximum output power observed was 2 mW corresponding to an absorbed pump power of 9 mW. With the same incident pump power ($\sim$ 20 mW), this output power could be increased by a factor of two if the laser diode wavelength was 809 or 813 nm (because of the much stronger absorption at these wavelengths).

Diode-pumped laser action was also demonstrated in a c-axis Nd:MgO:LiNbO$_3$ crystal (low gain polarization). The absorbed pump power threshold was 8 mW.

4.3 Alignment Method

We have proposed and utilized a laser alignment method that uses two collinear copropagating pump beams, one of them more intense than the other. A special beam splitter combines the two beams. We have been able to demonstrate Nd:MgO:LiNbO$_3$ lasers pumped by a laser diode by using this method. Its main advantage resides on the fact that it allows an easy lateral and axial mode-overlap of the two focused pump beams. The method is particularly useful when the laser diode power is not much higher than the threshold for operation of the end-pumped laser. However, it offers the disadvantage of locating the diode source relatively far away from the cavity. Therefore, the tolerances on the positioning of the collimating objective are very stringent.

An alternative alignment method was utilized in the predecessor to the present contract. In this second method one of the pump beams is focused through the front laser mirror. The other pump beam is focused through the back laser mirror by a

different lens. Because of the use of two different lenses a good mode overlap between the two counterpropagating pump beams is more difficult to attain. Attempts to obtain diode-pumped laser action by using this second method were unsuccessful.

C. The Photorefractive Effect in Nd:MgO:LiNbO$_3$

Recent studies made by Bryan, Gerson and Tomasche[3] indicate that the addition of MgO into LiNbO$_3$ causes a hundredfold increase in the photoconductivity σ_{ph} of this material. The increased σ_{ph} implies a significant reduction in the refractive-index changes caused by the photovoltaic effect. The resulting improvement on Nd:LiNbO$_3$ laser performance is readily apparent from the demonstration of true CW room temperature laser action for the π polarization (see Section III.B).

In this section we discuss the effect that the increased material photoconductivity has on both CW and Q-switched lasers. For the latter, we show that an internal screening field is generated. A detailed study of the screening field as well as a simple way to overcome it are also presented.

1. Effect of Increased Photoconductivity on CW Lasers

In non-MgO doped LiNbO$_3$, σ_{ph} is so low at visible wavelengths that the influence of external electric fields on photocarrier transport is negligible. These carriers are generated by donor impurities (like Fe^{2+}) when illuminated by short wavelength radiation. In non-MgO doped LiNbO$_3$ the dominant photocarrier transport occurs along the c-axis due to the bulk photovoltaic effect.

The photovoltaic current density J_{ph} (along the c-axis) is given by:

$$J_{ph} = k\alpha I_{ph} \qquad (3.10)$$

where k is the photovoltaic constant which depends only on the wavelength and the

[3] Applied Physics Letters **44**, 847 (1984).

nature of the absorbing centers, α the absorption coefficient of these centers and I_{ph} the illuminating intensity.

When the carriers reach the edge of the illuminated area, they are trapped, producing an internal space-charge field E_{sc} directed along c. This field is responsible for the refractive-index variations, via the electro-optic effect, that distort and scatter the light beam. This effect is particularly important when light propagates perpendicular to c, because the charge separation is then on the order of the pump beam radius (a few tens of microns). It is well known that in LiNbO$_3$ the photorefractive space charge disappears when heating the crystal above about 150 °C. However, in the present work we were interested mostly in room-temperature devices.

The field E_{sc} generates a photoconductive current $J_{\sigma p}$ that opposes J_{ph}. $J_{\sigma p}$ is given by:

$$ J_{\sigma p} = \sigma_{ph}(I_{ph})E_{sc} \tag{3.11} $$

σ_{ph} is directly proportional to I_{ph}; this dependence is implicit in Equation (3.11). In this equation we have assumed that the dark conductivity σ_d is much smaller than σ_{ph}. If this is not the case, the total conductivity $\sigma_{ph}(I_{ph}) + \sigma_d$ should replace σ_{ph} in Equation (3.11).

A dynamic steady-state is reached when $J_{\sigma p} = J_{ph}$. From this condition we can deduce the maximum space-charge field or saturation field E_{sat}. E_{sat} is found by equating Equations (3.10) and (3.11).

$$ E_{sat} = \frac{k\alpha I_{ph}}{\sigma_{ph}(I_{ph})} \tag{3.12} $$

In this expression I_{ph} appears in both the numerator and the denominator of the right-hand side. As a result, E_{sat} is independent of the illuminating intensity. This

conclusion is valid if $\sigma_{ph} >> \sigma_d$. In non-MgO doped LiNbO$_3$ $E_{sat} \sim 10^5 \ V/cm$ which accounts for a refractive index change of $\sim 10^{-3}$.

A hundredfold increase of σ_{ph} in LiNbO$_3$ due to the addition of MgO results in a significant reduction of E_{sat}. According to Equation (3.12), $E_{sat} \sim 10^3 \ V/cm$ for MgO:LiNbO$_3$. The corresponding refractive index change is on the order of 10^{-5}. The scattering and distortion of a light beam due to this index variation is very small.

The reduced scattering loss is greatly beneficial for a-or b-axes lasers. It made possible room temperature, true-CW laser operation for the π or high gain polarization as previously stated. We could also achieve room temperature, true-CW oscillation in c-axis crystals (low gain polarization). However, the effect of the increased σ_{ph} on the latter devices is unclear. For this crystal configuration the carrier migration along the c-axis results in an accumulation of charge near the end faces of the crystal. The effect of this charge on light scattering should be small independently of σ_{ph}. Therefore, it is possible that c-axis non MgO-doped Nd:LiNbO$_3$ CW lasers also exhibit small photovoltaic photorefractivity simply because of the crystal configuration.

2. Effect of Increased Photoconductivity on Q-switched Lasers

In a Q-switched c-axis laser, an electric field is applied along the a-axis during the low-Q state (see Sections III.D and III.F). Due to the increased σ_{ph}, a significant amount of photogenerated electrons drift along the direction of the applied field (a-axis). They are trapped outside the illuminated area producing a space-charge field which masks the externally applied field. Since no photovoltaic effect is present along the a-axis, the steady state of carrier transport is reached either after complete ionization of the donor impurities or when the net electric field inside the illuminated area is zero. Clearly, for Q-switched operation the second situation

91

must be avoided. In addition, earlier measurements of photorefractivity in LiNbO$_3$ (Chen, 1969) indicate another type of steady state at low intensities. This occurs when the carrier retrapping rate exceeds the rate at which the carriers drift out of the illuminated area. In the next subsection a detailed investigation of the screening field is presented.

3. The Screening Field

3.1 Measurement

To determine the strength and build-up time of the screening field we measured the response of a c-axis laser to step increments in the applied voltage. A typical time evolution of the laser output is shown in Figure 3.13 for the c-axis laser operated under continuous-wave pumping at 598 nm. At $t = 0$ the laser was operating three times above threshold. At $t = t_1$ a D.C. voltage of 290 volts was applied to the crystal to suppress laser action via increased loss at the Brewster window. For $t > t_1$ the laser output built up as a result of the generation of the internal electric field and the consequent reduction of the net electric field inside the illuminated zone. At $t = t_2$ the applied voltage was turned to zero and, as a consequence, the laser output vanished under the action of the internal field alone. For $t > t_2$ laser oscillation built up again due to the relaxation of the internal field.

The time τ_{sc} required to create a significant internal space-charge field can be inferred from Figure 3.13. The portion of the curve that corresponds to the generation of the screening field (between t_1 and t_2) can be approximated by an exponential of the form $A\left[1 - exp(-\frac{t}{\tau_{sc}})\right]$ with $A = 0.9$ and a characteristic time τ_{sc} of 25 sec. The characteristic time for relaxation of the field is about the same. Figure 3.13 also shows that the built-up laser output attained 90% of the initial output power. This indicates that the applied voltage was almost entirely screened by the internal field. These results clearly indicate that a strong screening field can
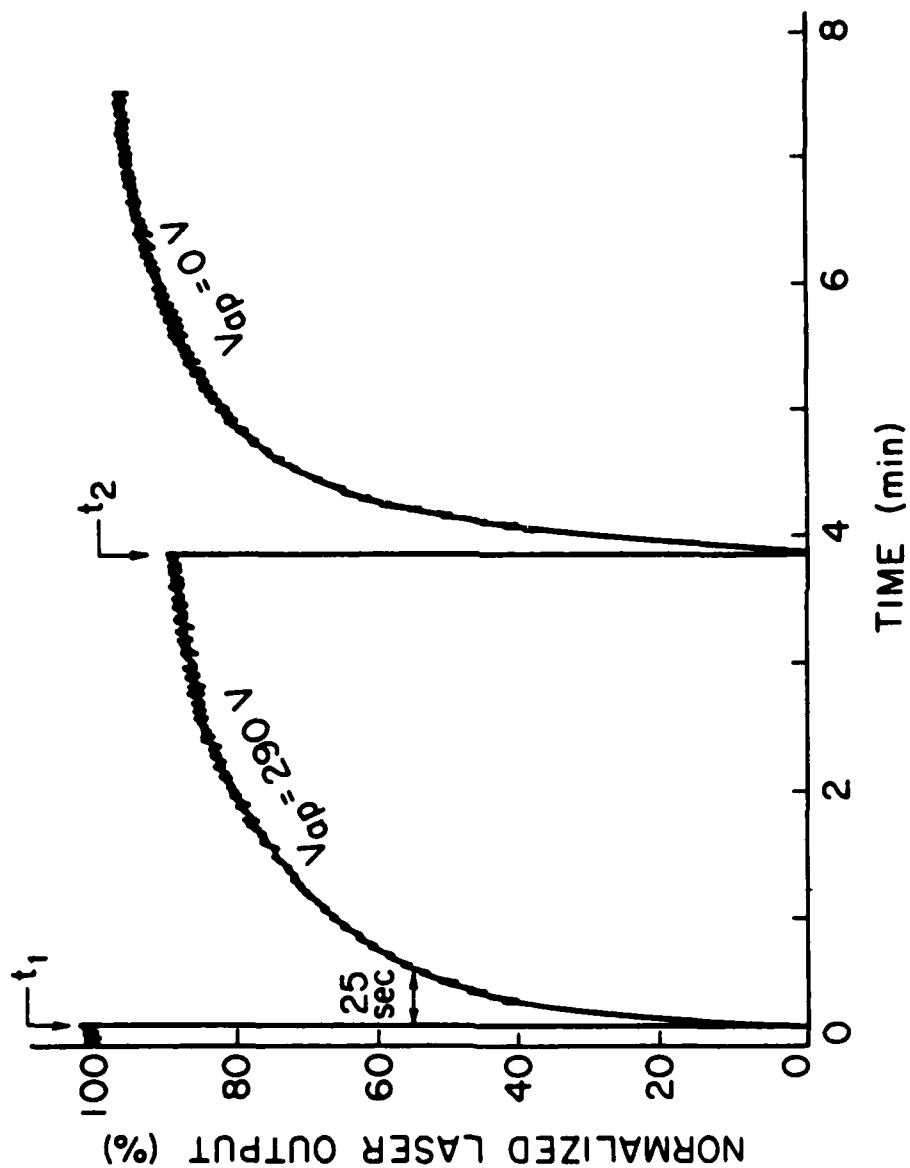
Figure 3.13--Build-up of the Laser Output Power due to the Generation (or Relaxation) of the Internal Screening Field. The Pump Power and Pump Illuminating Intensity, Averaged Over the Crystal Length, are ~ 37 mW and 2 kW/cm² Respectively.

be produced (on the order of $\frac{290V}{2mm} = 1.5$ kV/cm or higher).

The build-up of laser oscillation due to the generation (or relaxation) of the internal space-charge field was measured for different pump powers, applied voltages and lasing portions of the crystal (lasing spots). In most cases, the laser output evolved in time in a way similar to the one illustrated in Figure 3.13. However, some unusual time-evolutions, like the one in Figure 3.14, were also encountered. In Figure 3.14, the laser output, when applying a D.C. voltage, exceeded the initial output P_0 for $t_3 > t > t_2$. Besides, the laser output after removing the voltage did not increase monotonically as in Figure 3.13. Instead, the output increased to a maximum higher than P_0 and then decreased. A possible explanation for this behavior is that, before applying the voltage, the angular alignment of the crystal for that particular lasing spot was not optimized with respect to the axis of the Brewster plate. As a consequence, a slight increase in the birefringence due to a small net electric field E_1 could increase instead of decrease the output. However, for net electric fields E higher than E_1 the output was reduced and eventually suppressed. Thus, Figure 3.14 can be explained as follows. At $t = t_1$, 270 V are applied to the crystal producing a net field E high enough to suppress laser action. For $t > t_1$, E decreased due to the generation of the photorefractive space-charge field and reached a steady-state value close to E_1. The final laser output power was, therefore, higher than P_0. At $t = t_3$ the voltage was removed. The output vanished under action of the space-charge field. For $t > t_3$, E decreased due to the relaxation of the space-charge. The laser output reached a maximum when $E \sim E_1$ and decreased with further reduction of E.

3.2 Interpretation of Data

In the previous sub-section the functional form of the built-up power versus time curve was assumed to be $1 - e^{-t/\tau_{rc}}$ with the purpose of estimating the charac-
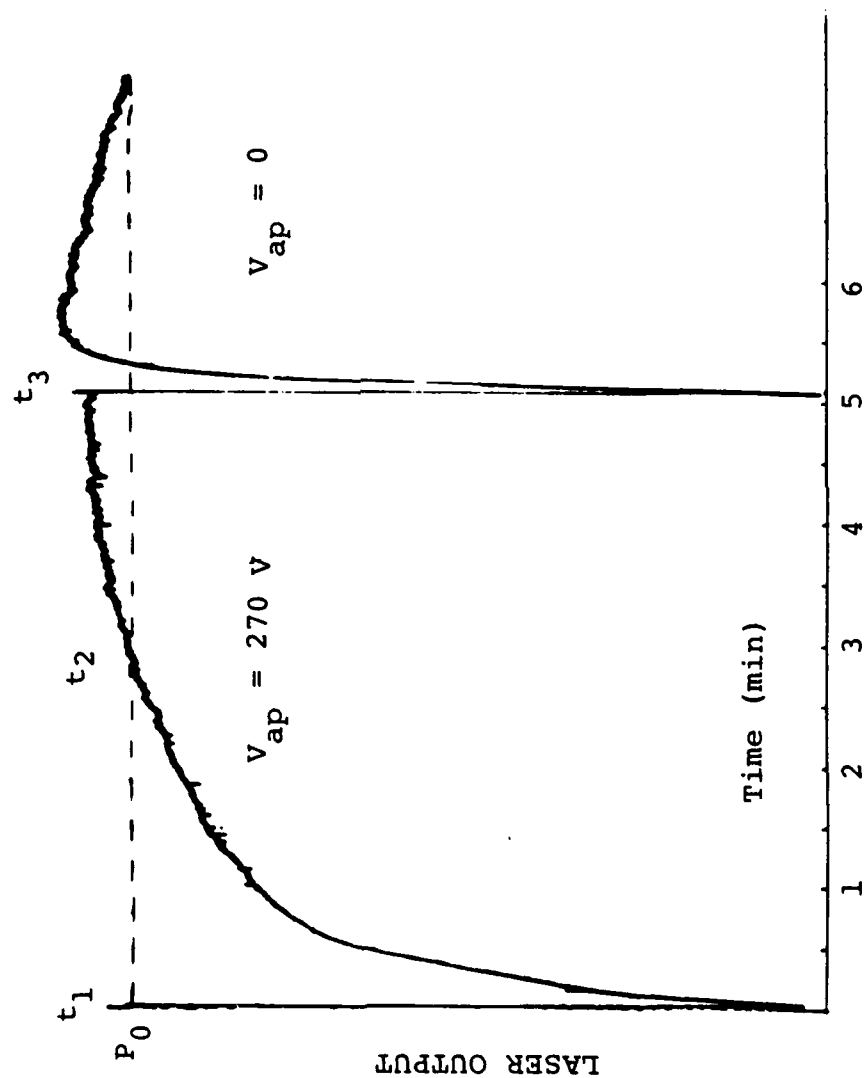
Figure 3.14--Build-up of Laser Oscillation due to the Generation (or Relaxation) of the Screening Field. See Text for an Explanation.

teristic time τ_{sc}. This functional form should be rather associated to the build-up of the space-charge field in which case the cavity loss (in the small loss approximation) decays exponentially and, therefore, the assumed output power versus time dependence is not correct. Nevertheless, the value estimated for τ_{sc} is correct within an order of magnitude. In this section we examine more carefully the time dependences of the output power and the cavity loss, particularly in the region $t_1 < t < t_2$ of Figure 3.13.

The output power P(t) can be expressed in terms of the ratio of signal to pump frequencies ν_s/ν_p, the output coupling T, the cavity loss $\delta_0 + \delta(t)$, (where δ_0 is the zero-voltage loss and $\delta(t)$ the loss due to the net electric field), the absorbed pump power P_{abs} and the threshold power P_{th} in the absence of time-dependent loss, as follows

$$P(t) = \frac{\nu_s}{\nu_p} \frac{T}{\delta_0 + \delta(t)} \left[P_{abs} - P_{th} \left[1 + \frac{\delta(t)}{\delta_0} \right] \right] \tag{3.13}$$

The initial or zero-voltage output power P_0 is found by making $\delta(t) = 0$ in this equation.

$$P_0 = \frac{\nu_s}{\nu_p} \frac{T}{\delta_0} (P_{abs} - P_{th}) \tag{3.14}$$

Normalizing $P(t)$ with respect to P_0 we obtain

$$\frac{P(t)}{P_0} = P_n(t) = \frac{1 - \frac{1}{r-1} \frac{\delta(t)}{\delta_0}}{1 + \frac{\delta(t)}{\delta_0}} \tag{3.15}$$

where $r = P_{abs}/P_{th}$. We see from this equation that if the loss $\delta(t)$ decays exponentially as $\delta_1 e^{-t/\tau_{sc}} + \delta_2$, then the normalized output power versus time dependence is more complicated than $1 - e^{t/\tau_{sc}}$. Conversely, the actual time dependence of $\delta(t)$ can be inferred from the measured output power versus time curve and,

$$\frac{\delta(t)}{\delta_0} = \frac{1 - P_n(t)}{\frac{1}{r-1} + P_n(t)} \qquad (3.16)$$

The time-evolution of the cavity loss $\delta(t)$ corresponding to the screening field generation in Figure 3.13 was determined by applying Equation (3.16) to the corresponding experimental points. An analysis of the data concluded that $\delta(t)$ does not decay as a simple exponential of the form $\delta_1 e^{-t/\tau_{sc}} + \delta_2$ but the decay time increased from an initial $\tau_{sc} \sim 25$ sec to ~ 50 sec. Further investigations are necessary to determine the reasons for this behavior.

3.3 Elimination of the Screening Field

During Q-switched laser operation, to avoid the generation of the screening field, we applied the voltage in the form of pulses of alternating polarity. This procedure effectively eliminates the screening field if the characteristic time τ_{sc} is much longer than the pumping interval τ_p. In this way only a small amount of photocarriers is generated during each pumping interval, and the contributions from consecutive voltage pulses to the average internal field tend to cancel each other. The condition is fulfiled since $\tau_{sc} \sim 25$ or $50 \, sec \gg \tau_p = 700 \, \mu sec$.

To generate the required voltage waveform we built a simple circuit consisting of two common-emitter stages, each containing a single avalanche transistor. Each stage is triggered on alternate pump pulses and provides voltage pulses of adjustable amplitude, between 0 and 350 V.

D. The Electro-optic Effect in Nd:MgO:LiNbO$_3$

Lithium niobate has been widely used both as an amplitude and as a phase electro-optic light modulator. The electro-optic properties of Nd:MgO:LiNbO$_3$ are expected to be very similar to those of LiNbO$_3$. In fact, our measurements indicate that the electro-optic coefficient of interest for Q-switching is the same in both

Table 3.7

Electro-Optic Coefficients (cm/volt)

$r_{33} = 30.8 \times 10^{-10}$	$r_{42} = 28.0 \times 10^{-10}$
$r_{13} = 8.6 \times 10^{-10}$	$r_{22} = 3.4 \times 10^{-10}$ (high frequency)
	$= 6.3 \times 10^{-10}$ (low frequency)

$LiNbO_3$ and $Nd:MgO:LiNbO_3$ (Section III.D.3). We start by reviewing the main features of the linear electro-optic (or Pockels) effect in these materials. Our goal is to identify the most convenient configuration for the optimum design of an intra-cavity amplitude electro-optic modulator.

Lithium niobate is a uniaxial crystal belonging to the 3m point symmetry group. Consequently, the electro-optic tensor for this material contains only four non-vanishing independent coefficients. The values of these coefficients are listed in Table 3.7. Wave propagation in anisotropic crystals is conveniently described by means of the impermeability tensor **b** which relates the three components of the dielectric displacement vector $\vec{D}$ to the three components of the optical vector $\vec{c}$. It can be shown that for a given direction of wave propagation there are two orthogonal polarizations for the $\vec{D}$ vector, called eigenpolarizations, to which we can associate a well defined phase velocity and refractive index. If the light wave is not polarized along one of these priviliged directions, it won't propagate through the crystal as a pure wave, but instead it will split into two orthogonally polarized waves traveling at different velocities. To find the eigenpolarizations and their associated refractive indices the usual approach consists of diagonalizing the **b** tensor and then to use the so-called index ellipsoid, or optical indicatrix to obtain the indices. For an uniaxial crystal the principal values of the **b** tensor are $b_{11} = b_{22} = \frac{1}{n_0^2}$ and $b_{33} = \frac{1}{n_e^2}$ where n_0 and n_e are the ordinary and the extraordinary refractive indices respectively.

Upon application of the external electric field $\vec{E}$, the **b** tensor is modified and the eigenvalue problem must be solved again. Figure 3.15 shows the **b** tensor for

$$\vec{D} = \overset{\leftrightarrow}{b} \cdot \vec{\epsilon}$$

$$\overset{\leftrightarrow}{b} = \begin{bmatrix} \dfrac{1}{n_O^2} - r_{22}E_y + r_{13}E_z & - r_{22}E_x & r_{42}E_x \\[3mm] - r_{22}E_x & \dfrac{1}{n_0^2} + r_{22}E_y + r_{13}E_z & r_{42}E_y \\[3mm] r_{42}E_x & r_{42}E_y & \dfrac{1}{n_e^2} + r_{33}E_z \end{bmatrix}$$

Figure 3.15--Impermeability Tensor for Lithium
Niobate upon Application of an
Electric Field E. ϵ Denotes the
Optical Field.

LiNbO$_3$ modified by the application of an E-field (in the principial axes coordinate system). To reduce the voltage requirement it is preferred to apply the E-field perpendicularly to the direction of propagation (transverse E-field). Under these conditions, three possible configurations can be identified, as discussed below.

1. Configuration for a Transverse Intra-Cavity Amplitude Electro-Optic Modulator

Configuration 1 - Propagation along the c or z axis and E-field applied either along x or y (a or b). When only E_x is applied, the eigenpolarizations are at 45° with respect to the x-y axes. When only E_y is applied the eigenpolarizations remain parallel to the principal axes.

Configuration 2 - Propagation either along x or y and E-field parallel to c. In this case the eigenpolarizations remain parallel to the principal axes, ie., x and z for propagation along y, or y and z for propagation along x.

Configuration 3 - Propagation either along x or y and E-field perpendicular to c. Under these conditions the polarizations are rotated with respect to the principal axes by an angle that is a function of the applied field. However, this angle is exceedingly small even for applied fields over 10^3 V/mm.

Figure 3.16 shows the eigenvalues of the tensor **b** for these three configurations. When passing through the crystal the two eigenpolarizations experience different phase delays ϕ_1 and ϕ_2 given by $\phi_1 = \frac{2\pi}{\lambda} n_i L$ where i = 1 or 2, L is the crystal length, λ the wavelength and n_i is the refractive index associated with the ith eigenpolarization. The difference in phase delays $\phi_1 - \phi_2$ for the three configurations is listed in Figure 3.16. In our computation, the applied E-field equals V/d, where V is the applied voltage and d the separation between the electrodes.

Inspection of Figure 3.16 (particularly column 5) reveals some important similarities and differences between the configurations. First, the change in birefringence induced by an applied voltage V is proportional to the quotient L/d (L/d^2

Configuration	Direction of Propagation	Direction of the Applied E-Field	Eigenvalues of the $\vec{b}$ Tensor	Phase Difference Between Eigenpolarizations
1	c axis	x or y axes	$b_1 = \dfrac{1}{n_0^2} + r_{22}E_i$ $b_2 = \dfrac{1}{n_0^2} - r_{22}E_i$ (1)	$\dfrac{2\pi}{\lambda} n_0^3 r_{22} \dfrac{LV}{d}$
2	x axis or y axis	c axis c axis	$b_1 = \dfrac{1}{n_e^2} + r_{33}E_z$ $b_2 = \dfrac{1}{n_0^2} + r_{13}E_z$	$\dfrac{2\pi}{\lambda} L \left[(n_0 - n_e)\right.$ $\left. - \dfrac{V}{2d}(n_0^3 r_{13} - n_e^3 r_{33})\right]$
3	x axis y axis	y axis x axis	$b = \dfrac{1}{2}\left(\dfrac{1}{n_0^2} + \dfrac{1}{n_e^2}\right)$ $\pm \sqrt{\dfrac{1}{4}\left(\dfrac{1}{n_0^2} - \dfrac{1}{n_e^2}\right)^2 + r_{42}^2 E_i^2}$ (2)	$\dfrac{2\pi L}{\lambda} \left[(n_0 - n_{e\perp})\right.$ $\left. + \dfrac{n_0^2 n_e^2}{2} r_{42}^2 \dfrac{V^2}{d^2}\right]$ (3)

(1) i means x or y

(2) $E_i = E_x$ for propagation along y $E_i = E_y$ for propagation along x

(3) We have assumed that $2\, r_{42}E_i \ll 1/n_0^2 - 1/n_e^2$

Figure 3.16--Possible Configurations for a LiNbO$_3$ Amplitude Electro-Optic Modulator.

for the third configuration). Therefore, a given voltage will be more efficient (i.e., produce a larger change in birefringence) when the separation betwen electrodes is much smaller than the length of the crystal. In the case of a longitudinal amplitude modulator d = L, and for this reason the transverse modulator is preferred. Second, the birefringence induced by an applied voltage in configuration 1 is proportional to $r_{22}n_0^3 = 6.9 \times 10^{-9} \ cm/V$ which is smaller than $\frac{n_e^3 r_{33} - n_0^3 r_{13}}{2} \approx 10^{-8} \ cm/V$ (configuration 2). Also we may expect that the factor $r_{42}^2 (\approx 10^{-22} \frac{m^2}{V^2})$ will significantly reduce the induced birefringence in configuration 3. Consequently, configuration 2 is more efficient that the other two. This point will be discussed further when we address the question of Q-switching.

2. Design of a Nd:MgO:LiNbO₃ Q-switched Laser

2.1 Review of Electro-Optic Q-switch Operation

The two most common arrangements for an electro-optic Q-switch are shown in Figure 3.17. In both arrangements the polarizers are set at 45° with respect to the principal axes of the electro-optic cell. Light reaching the cell splits into two orthogonal and independent components that experience different phase shifts when passing through the cell. The phase delay difference is a function of the applied voltage as indicated in Figure 3.16, column 5.

In the arrangement of the top of Figure 3.17, a quarter wave voltage $V_{1/4}$ must be applied, i.e., a phase delay of $\pi/2$, to keep the laser in the low-Q state. The linearly polarized beam is transformed into circularly polarized by the electro-optic crystal. Later, it becomes linearly polarized again but at 90° to its initial direction and, thus, it is rejected by the polarizer. Turning off the applied voltage restores the cavity high Q.

In the second arrangement, the cavity loss is maximum with zero applied voltage because the polarizers are crossed. Applying a half wave voltage $V_{1/2}$ to
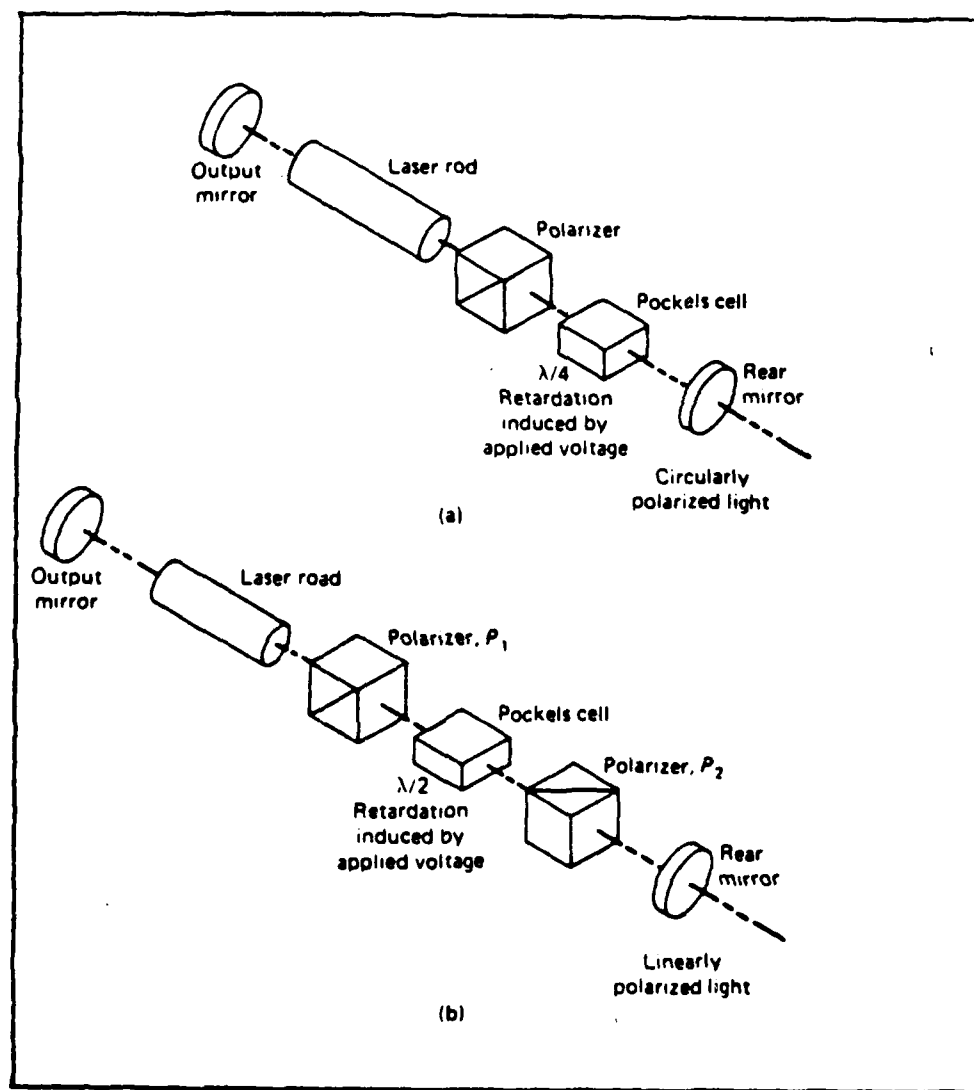
Figure 3.17--Common Arrangements for Q-Switched
Laser Operation. (From Koechner,
Solid State Laser Engineering.)

Table 3.8

Quarter Wave Voltages

Configuration	$V_{1/4}$	$V_{1/4}$ for a Bulk Laser (L/d = 5)	$V_{1/4}$ for a Fiber (Laser L/d = 125)
1	$\frac{\lambda}{4n_0^3 r_{22}}\frac{d}{L}$	812 volts	32 volts
2	$\frac{\lambda}{2(n_e^3 r_{33} - n_0^3 r_{13})}\frac{d}{L}$	488 volts	20 volts
3	$\frac{\sqrt{\lambda}}{\sqrt{2}n_0 n_e r_{42}}\frac{d}{\sqrt{L}}$	110 kilo volts	4.4 kilo volts

the cell causes a 90° rotation of the plane of polarization, thus, turning the cavity from low to high-Q. In this case an electric field E must be applied to transmit the beam. Because of the lower voltage required, the first arrangement of Figure 3.17 is often preferred, and it is the one we will adopt.

2.2 Evaluation of the Three Configurations

The first criterion for evaluation consists of a comparison of the quarter wave voltages. Expressions for $V_{1/4}$ in terms of the refractive indices $n_0 = 2.2$ and $n_e = 2.17$, the crystal dimensions L and d, the wavelength $\lambda = 1.09\,\mu m$, and the relevant electro-optic coefficient are given in Table 3.8.

In configurations 2 and 3 the crystal exhibits a natural birefringence that must be compensated either by an applied voltage or by an external retardation plate. In this case we define $V_{1/4}$ as the voltage required to induce a $\pi/2$ phase delay difference after the natural birefringence has been compensated.

Table 3.8 lists some typical values of $V_{1/4}$ for two devices of interest. The first is a bulk laser with L = 1 cm, d = 2 mm. The second is a crystal fiber laser of diameter 80 μm and length 1 cm.

From Table 3.8 it is clear that configuration 2 is the most interesting since it has the lowest quarter wave voltage. However, this configuration exhibits two major

drawbacks when compared to configuration 1. First of all, as stated previously, it is necessary to compensate for the natural birefringence of the material. A more serious objection has to do with the polarization properties of the laser radiation in a or b axis Nd:MgO:LiNbO$_3$ crystals. Laser action in configuration 2 or 3 is accomplished with the lasing field being linearly polarized either parallel to the crystal c axis (π or high gain) or orthogonal (low gain) to it (see Section III.A). Laser mode competition prevents simultaneous oscillation of both polarizations. Therefore, in configuration 2 the crystal tends to lase with the E-field polarized along one or the other crystallographic axes. An applied voltage cannot change the state of polarization of this field unless it induces also a rotation of the principal axes. This does not occur in configuration 2. The axes do rotate in configuration 3 but the angle of rotation is exceedingly small even for very high applied voltages. We conclude that configuration 1 is the best suited for Q-switched operation. Its main characteristics will be described below.

? Q-switching in a C-axis Crystal (Configuration 1)

In the case of configuration 1 the laser host LiNbO$_3$ does not exhibit any priviliged polarization direction. As a consequence, the fluorescence emitted by the active ion Nd^{3+} is unpolarized. When lasing occurs, the polarization of the E-field is fixed by mechanisms non-intrinsic to the laser medium, e.g. preferential losses, a polarizer, or pump polarization

In this configuration the medium does not exhibit a natural birefringence, only ordinary waves (refractive index n_0) propagate through. Under the influence of an applied voltage an induced birefringence appears. This birefringence is given by

$$\Delta n = n_0^3 r_{22} \frac{V}{d} \tag{3.17}$$

The value of the induced birefringence does not depend on the direction of the

105

applied E-field. However, it can be shown, by diagonalizing the reduced imper-
meability tensor, that the principal axes are rotated under the action of this field
by an amount that depends on the direction of the field as follows.

$$\theta = \beta/2 \tag{3.18}$$

where θ is the angle by which the axes are rotated and β the angle between the
external E-field and the original y axis. The rotation is maximum and equal to 45°
when the field is parallel to the initial x axis ($\beta = 90°$). This case can be fully
exploited to realize a Q-switched laser.

Referring to Figure 3.18(a) assume that an intracavity device forces the c-cut
Nd:MgO:LiNbO₃ crystal to lase with the E-field parallel to the crystallographic x
axis. This device can be a low loss polarizer or a thin transparent plate set at
Brewster's angle. Upon application of an E-field along the x axis the principal
axes are rotated by 45° as stated previously and they occupy the positions x/ and
y/ as shown. If the applied voltage is equal to the quarter wave voltage for the
material, the crystal behaves exactly like a quarter wave Pockels cell as in Figure
17(a). Thus, we can achieve the integration of a laser medium and an electro-optic
cell into the same crystal rod. This device will be named ACTIVE INTERNALLY
Q-SWITCHED LASER. Cutting the end face of the crystal at Brewster's angle as
illustrated in Figure 3.18(b) can eliminate the need for the polarizer.

3. Measurement of the Electro-optic Coefficient

For Q-switched operation, it is the low-frequency r_{22} coefficient that determines
the voltage required to hold off laser action (Section III.D.2). Thus, we set up an
experiment to measure this coefficient in Nd:MgO:LiNbO₃. The crystal utilized
was a thin, c-axis slab, 200 μm wide, 8 mm long. The probe beam was provided
by a CW Nd:YAG laser operating at 1.064 μm. By using this long wavelength we

106
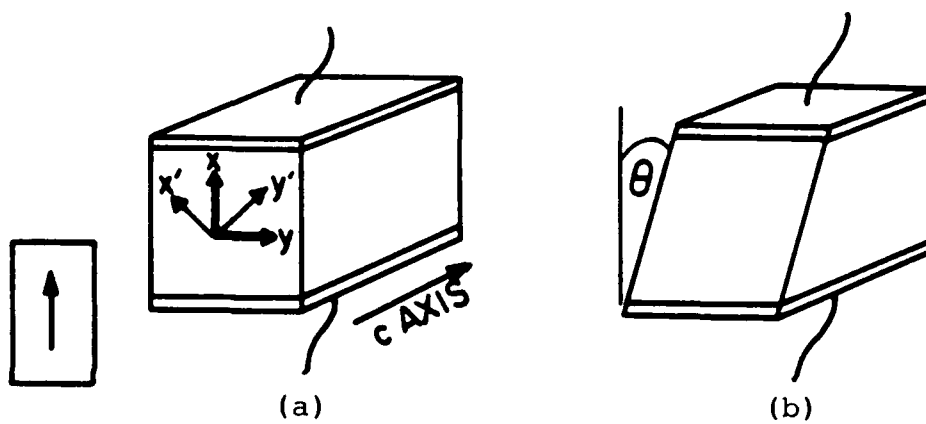
Figure 3.18--Nd:MgO:LiNbO$_3$ Q-switched Laser Configuration.

(a)   With a Polarizer.
(b)   With the End Face cut at
      Brewster's Angle.

assured a negligible absorption of the photoreractive centers and, thus, a negligible screening field (see Section C). The sample was placed between two calcite polarizers having their axes parallel to each other. The transmission through the sample was monitored while aplying a DC electric field parallel to the crystal x-axis. To focus the beam to a diameter compatible with the sample's thickness, a $f = 7.8$ cm positive lens was placed between the first polarizer and the sample.

We found that the transmission through the crystal was minimum for an applied voltage of about 170 volts. In the configuration that we studied this should correspond to the half-wave voltage of the crystal $V_{1/2}$. The coefficient r_{22} is related to $V_{1/2}$ by the following expression:

$$V_{1/2} = \frac{\lambda d}{2n_o^3 r_{22} L} \tag{3.19}$$

where the ordinary index is n_o=2.2, the crystal dimensions are d=0.02 cm and L=0.8 cm, and the wavelength is λ=1.064 μm. If we take as r_{22} the low frequency (or constant stress) electro-optic coefficient of lithium niobate, 6.3×10^{-10} cm/V and replace these values in the equation we obtain

$$V_{1/2} = 198 \ volts \tag{3.20}$$

The calculated value is in good agreement with the measured voltage, indicating that the low frequency r_{22} electro-optic coefficient for Nd:MgO:LiNbO$_3$ is approximately the same as for congruent LiNbO$_3$.

E. The Elasto-optic Effect in Nd:MgO:LiNbO$_3$

Researchers in the past have found that the piezoelectric character of LiNbO$_3$ Q-switches can seriously affect the efficiency of a Q-switched laser by creating a time-dependent loss via the elasto-optic effect. In LiNbO$_3$ Pockels cells the applied voltage induces a mechanical compression of the crystal via the piezoelectric effect

which remains for some interval of time after the voltage has been removed, creating an additional birefringence modulation via the elasto-optic effect. A polarization sensitive element inside the cavity transforms this modulation into an additional time-dependent cavity loss. The acoustic oscillations following the initial relaxation of the compression were considered irrelevant for Q-switching due to their long periods, on the order of several μsec. In our experiments we found that these oscillations had a significant influence on device operation when pumping close to threshold. The reason is twofold. First, to reduce the voltage requirement we made the crystal transverse dimension several times smaller than that of conventional LiNbO$_3$ Q-switches. The periods of the piezoelectric resonances were thereby reduced to the sub-μsec range. Second, when pumping close to threshold the pulse build-up times become comparable to the acoustic periods.

In this section we present a careful investigation on the influence of piezoelectricity and the elasto-optic effect on the behavior of Q-switched Nd:MgO:LiNbO$_3$ lasers. The section starts with an experiment to investigate the transient elasto-optic effects in Nd:MgO:LiNbO$_3$, MgO:LiNbO$_3$ and LiNbO$_3$.

1. Transient Response of LiNbO$_3$ Modulators to an Applied Voltage Step

The experimental setup consisted of a HeNe laser emitting at 1.15 μm, a focusing lens, the crystal under investigation placed between crossed calcite polarizers, a small-area Ge detector and a 5 MHz bandwidth amplifier. The long wavelength radiation was chosen to avoid the generation of a screening field. The beam was focused in order to probe different small areas of the crystal. The samples studied were a 5 $\times$ 5 $\times$ 25 mm LiNbO$_3$ rod, a 2 $\times$ 1.5 $\times$ 10 mm MgO:LiNbO$_3$ crystal and Nd:MgO:LiNbO$_3$ rod (2 $\times$ 2 $\times$ 10 mm). The last two crystals contained the same percentage of MgO (5%). In all cases, light propagated along the c-axis and an electric field was applied along the a-axis. The applied voltage was switched from

several hundred volts to zero in a time interval on the order of tens of nanoseconds. It had the shape shown in the lower traces of Figures 3.19 and 3.20.

The transmission through the LiNbO$_3$ rod was displayed on an oscilloscope and is shown in Figure 3.19 (upper trace). As the figure indicates, just after the voltage switching the crystal undergoes several superimposed acoustic oscillations having periods of 1 μsec and 2 μsec approximately.

We also measured the frequency response of the LiNbO$_3$ amplitude modulator by applying 40 volt peak to peak sinusoidal waveforms. The polarizer axes were set at 45° to each other in order to bias the modulator to the linear part of its characteristic cosinusoidal response. The frequency of the applied signal voltage was scanned from D.C. to 20 MHz. Within that range only three strong fundamental piezoelectric resonances were found, at 366 kHz, 425 kHz and 495 kHz. Strong piezoelectric response was also observed at the third harmonic of the main resonances.

In the first experiment the application of a fast voltage step excited several acoustic resonances. In Figure 3.19, the oscillation periods observed (1 and 2 μsec) correspond fairly well to the periods of the third piezoelectric resonance (2.0 μsec) and the third harmonic of the first resonance (0.91 μsec).

Similar piezoelectric responses to a voltage step were observed with both the MgO:LiNbO$_3$ and the Nd:MgO:LiNbO$_3$ crystals. The oscillation periods scaled with the transverse dimension of the rods. The transmission through the MgO:LiNbO$_3$ rod is shown in Figure 3.20.

2. Measurement of the Elasto-optically Induced Cavity Loss

The elasto-optically induced cavity loss was directly measured in a Nd:MgO:LiNbO$_3$ c-axis laser. We used the non-absorbed part of the Rh6G dye laser pump beam as a probe and recorded the temporal variations of part of the
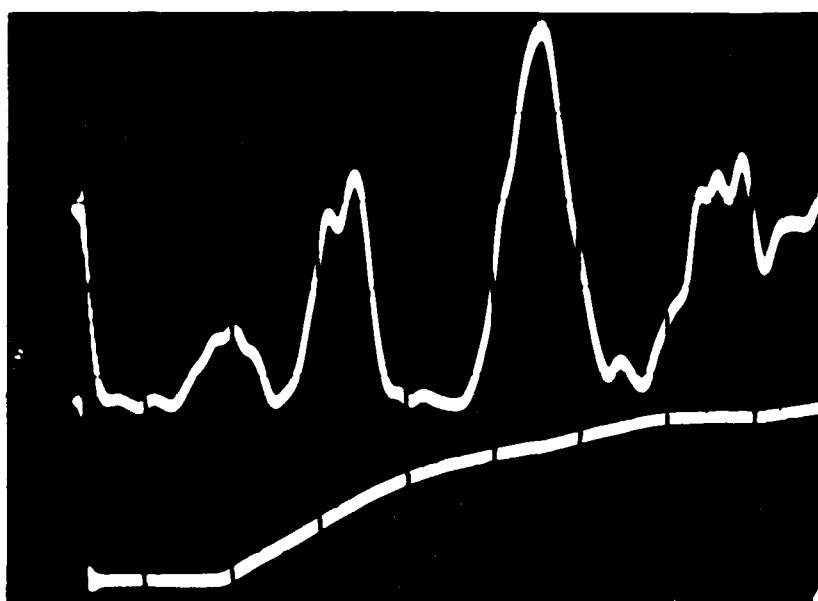
Figure 3.19--Transmission through the LiNbO$_3$
Sample (Upper Trace). Applied
Voltage Step (Lower Trace).
Horizontal Scale: 1 μsec/div.
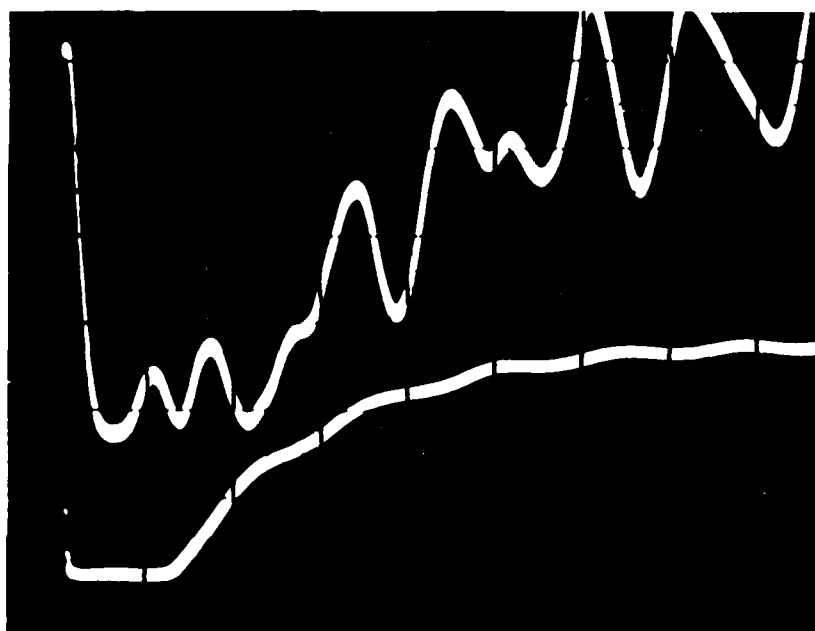
Figure 3.20--Transmission through the MgO:
LiNbO$_3$ Sample (Upper Trace).
Applied Voltage (Lower Trace).
500 nsec/div.

probe reflected by the Brewster plate just after applying a voltage step. An oscilloscope trace of this probe signal is shown in Figure 3.21. For this measurement, a voltage of 300 V was applied to the crystal and then switched to zero at t = 0. The D.C. level remaining after the acoustic oscillations have been attenuated is proportional to the D.C. loss contribution of the plate. The latter quantity was determined from quasi-CW slope efficiency measurements to be about one-third of the total D.C. cavity round-trip loss δ, which provided the absolute calibration of the vertical axis of Figure 3.21. The peak-to-peak elasto-optic loss is as high as 7-2.5 = 4.5 %, that is, 1.5 times δ. The crystal was also probed with the 1.15 μm beam of a HeNe laser. The loss modulation pattern shown in Figure 3.21 was the same at both probe wavelengths, and it scaled linearly with the applied voltage.

3. Effect on the Q-switched Pulses

During Q-switched operation we have observed very large delays between the action of the voltage switch and the emission of the Q-switched pulse. In addition, at low pump levels a particular kind of pulse jitter has been encountered. We could correlate the occurence of these two effects with the elasto-optic loss by recording simultaneously the Q-switched pulses and the probe signal, as shown in Figure 3.22.

The Q-switched pulse in Figure 3.22(a) is emitted 4.5 μsec after the action of the electrical switch. At this pump level (r = 1.2 times above threshold) the pulse build-up time should be only 1.5 μsec. However, the first two peaks of the time-dependent oscillating loss (lower trace of Figure 3.22(a)) retard the emission of the pulse. Assume that the gain level coincides with the line ABCD in Figure 3.22(a). The Q-switched pulse starts building up when the cavity loss $\delta(t)$ reaches point A, i.e., when the gain exceeds the loss. After point B, less than 1.5 μsec later, the loss exceeds the gain. Thus the pulse decays exponentially between B and C. Pulse emission can only occur after point E, i.e., after the first two acoustic cycles,
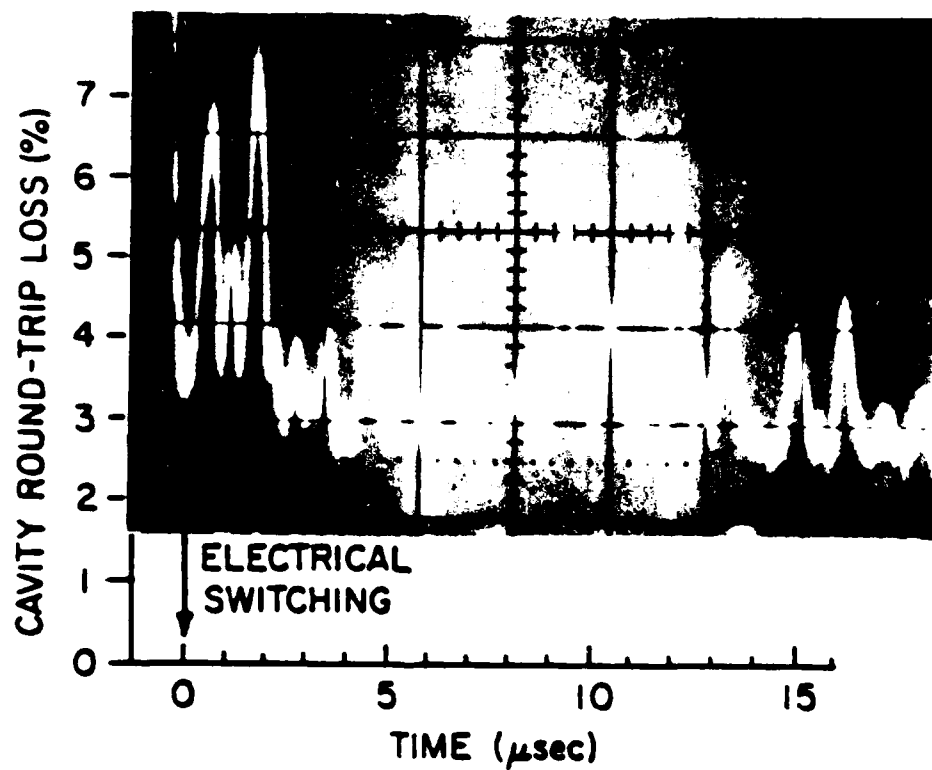
Figure 3.21--Total Cavity Round-Trip Loss after
Switching the Applied Voltage to
Zero.

- 114 -
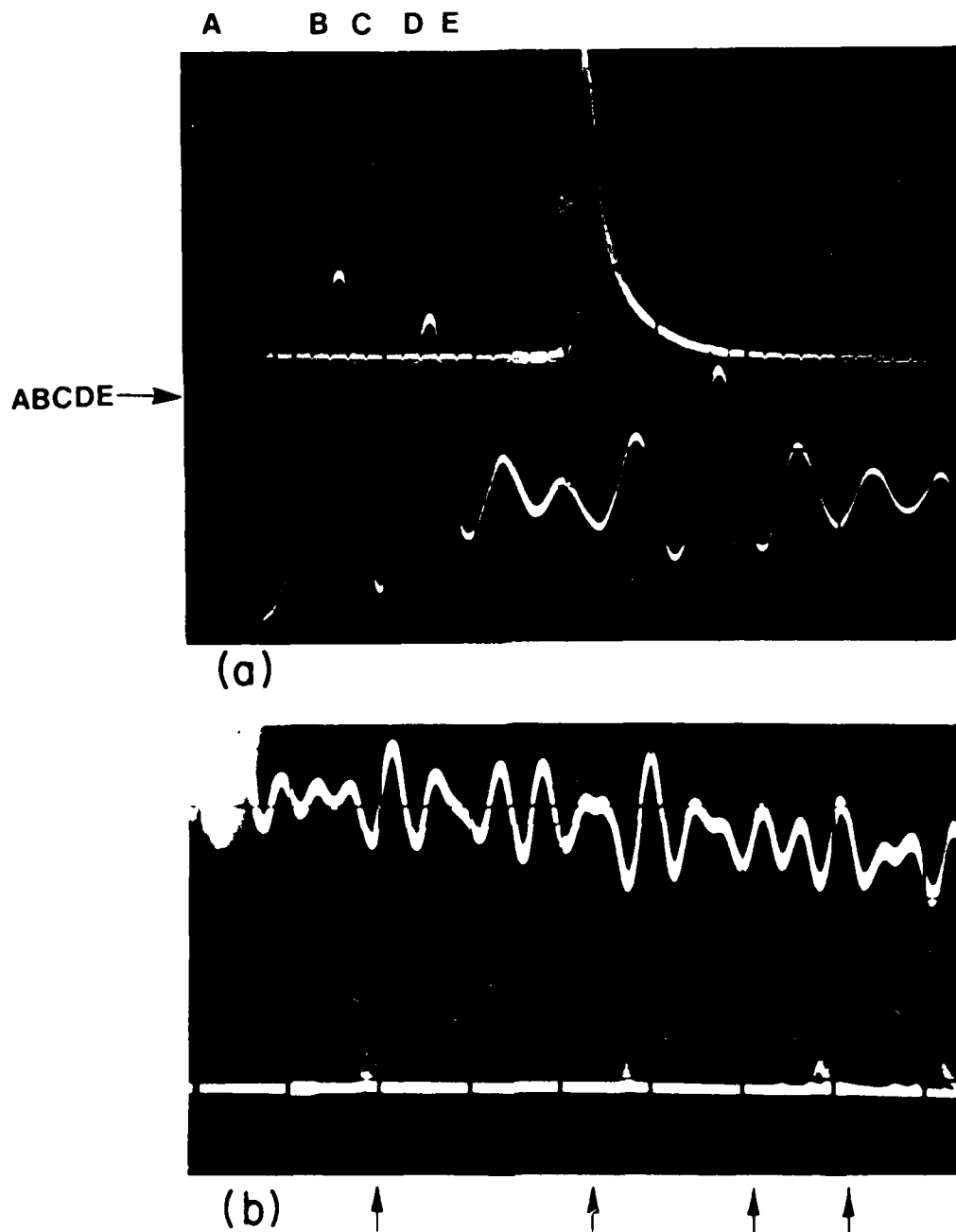
Figure 3.22--Simultaneous Recording of Q-switched Pulses and Probe-Beam Transmittance (through a Crossed Polarizer). (a) 1 μsec/div. (b) Superposition of Consecutive Shots. 2 μsec/div. Arrows point to Positions of Pulses.

when the cavity loss dropped below the gain level for more than 1.5 μsec.

Figure 3.22(b) shows the superposition of several consecutive Q-switched pulses (lower trace). The pulse jitter is readily apparent in this figure. One of the most striking characteristics of this jitter is that pulse emission occurs at very precise moments, separated by fixed intervals of time. Comparing with the time-dependent loss (upper trace in Figure 3.22(b)), it is clear that these fixed separations are just multiples of the acoustic periods. The moment of pulse emission coincides with a minimum of the oscillatory loss (Figure 3.22(b)). In addition, the loss peaks preceding the corresponding minimum are always low-amplitude peaks, in agreement with the explanation given with respect to Figure 3.22(a). The explanation of this jitter is associated with small pump fluctuations inducing small changes in the pulse build-up time. Such fluctuations can make a particular pulse "just miss" a particular minimum of the time-dependent loss.

To avoid the effects of the elasto-optic loss modulation two alternatives were possible.

- To operate the Q-switched laser well above threshold in such a way that the build-up time is shorter than half a period of the highest-frequency piezoelectric resonance.

- To attenuate the acoustic oscillations by bonding to the crystal surfaces blocks of material having the appropriate acoustic impedance and acoustic damping.

The first solution was the simplest and the one selected. In the experiments performed, when pumping more than about three times above threshold, no pulse jitter or unusually long delays were observed.

F. Active Internal Q-switching

One of the most attractive properties of $Nd:MgO:LiNbO_3$ is the ability to

116

generate laser radiation that can be electronically controlled within the crystal itself. We have called the integration of a laser medium and an electrooptic cell in the same crystal rod active internal Q-switching, made possible by Nd:MgO:LiNbO$_3$. The operation principle of this device has already been presented in Section III.D.2. This section is devoted to an experimental and theoretical study of active internal Q-switching.

1. Early Experiments - First Observation of Active Internal Q-switching

The miniature laser cavity with which active internal Q-switching was demonstrated contained a 2 × 2 × 11.5 mm c-cut crystal rod. The laser cavity, designed following the criterion of minimum CW pump threshold, consisted of two 5 cm radius mirrors, one a high reflector and the other a T = 0.42% output coupler. The configuration corresponded to a nearly concentric cavity with mirror separation or cavity length equal to 10.6 cm.

Prior to Q-switched operation the c-cut crystal rod was made to lase under quasi-CW conditions. As explained in Section III.D.2, the lasing E-field, at a wavelength of 1.093 μm, is basically unpolarized unless a polarizing mechanism is implemented. With this purpose a thin quartz plate, set at Brewster's angle, forced the E-lasing field to be linearly polarized along the crystal a axis.

Subsequent Q-switched action proceeded by applying an electric field step to the crystal. As the applied voltage was increased from zero, the quasi-CW laser output was broken into a set of narrower pulses whose number diminished as we increased the voltage. When applying 250 V, a unique Q-switched pulse was observed. The laser was being pumped twice above threshold.

A photograph of the pulse, taken on the screen of a storage oscilloscope is shown in Figure 3.23. The pulse width, full width at half maximum (FWHM), is 500 nsec.
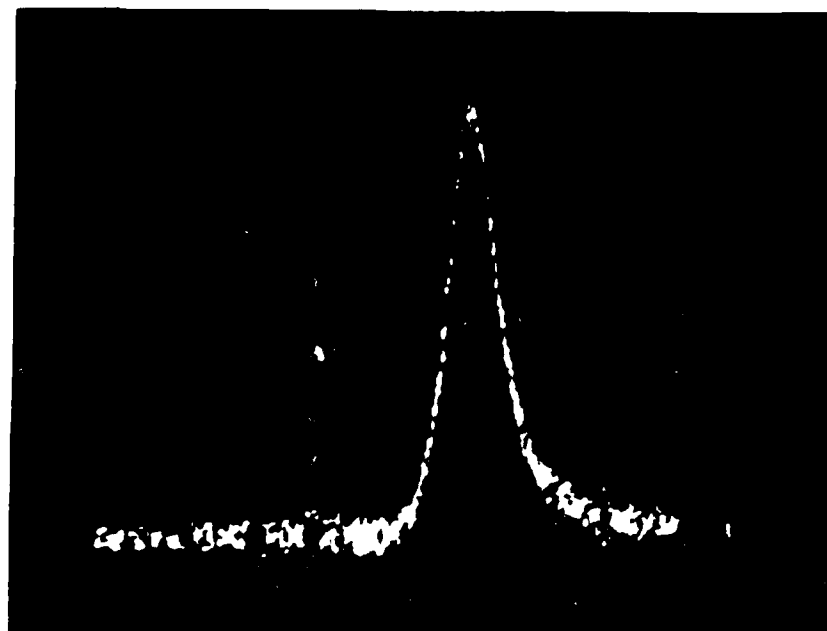
Figure 3.23--Q-switched Pulse from the Miniature
Nd:MgO:LiNbO$_3$ Laser. Horizontal
Scale: 500 nsec/div. FWHM = 500 nsec.

2. Short-Cavity Q-switched Laser

The interest in short cavity laser devices arises quite naturally in the trend towards miniaturization. Besides, a short cavity Q-switched laser emits shortened pulses having higher peak powers. The reduction in the pulse width is a consequence of the decreased cavity round trip transit time.

In Section III.A we presented a detailed analysis of the design of low threshold CW and quasi-CW lasers. In that analysis both cavity mirrors were assumed to have the same radius of curvature and, as a consequence, the signal waist was located at the center of the cavity. In the present case, the presence of the Brewster plate breaks the symmetry, and the crystal must be located necessarily closer to one of the mirrors. This mirror must have a larger radius of curvature if the signal waist is to be located inside or very close to the crystal. The other mirror must have a very small radius to minimize the mode volume inside the crystal.

The smallest radius mirror available was a 2.5 cm high reflector. Once this mirror was selected we needed to choose the cavity length L and the other mirror radius R1. Figure 3.24 shows plots of the average signal radius inside the crystal, $\overline{W}_e$ as a function of L for different values of R1. As the plots show, the value of R1 does not significantly affect the average radius. The optimum cavity length L = 3.1 cm gives a minimum W_e of 45 microns. This value is only slightly larger than the average radius for the nearly concentric cavity ($\sim$ 38 microns).

An additional feature of the design is the use of the Brewster window plate as the output coupling element. In this way, both cavity mirrors can be high reflectors at the signal wavelength, resulting in a reduced cavity loss, and thus, a reduced threshold. A fraction of the circulating power is tapped out of the cavity by reflection. This laser exhibits two outputs corresponding to the two main reflections of the signal beam onto the plate.
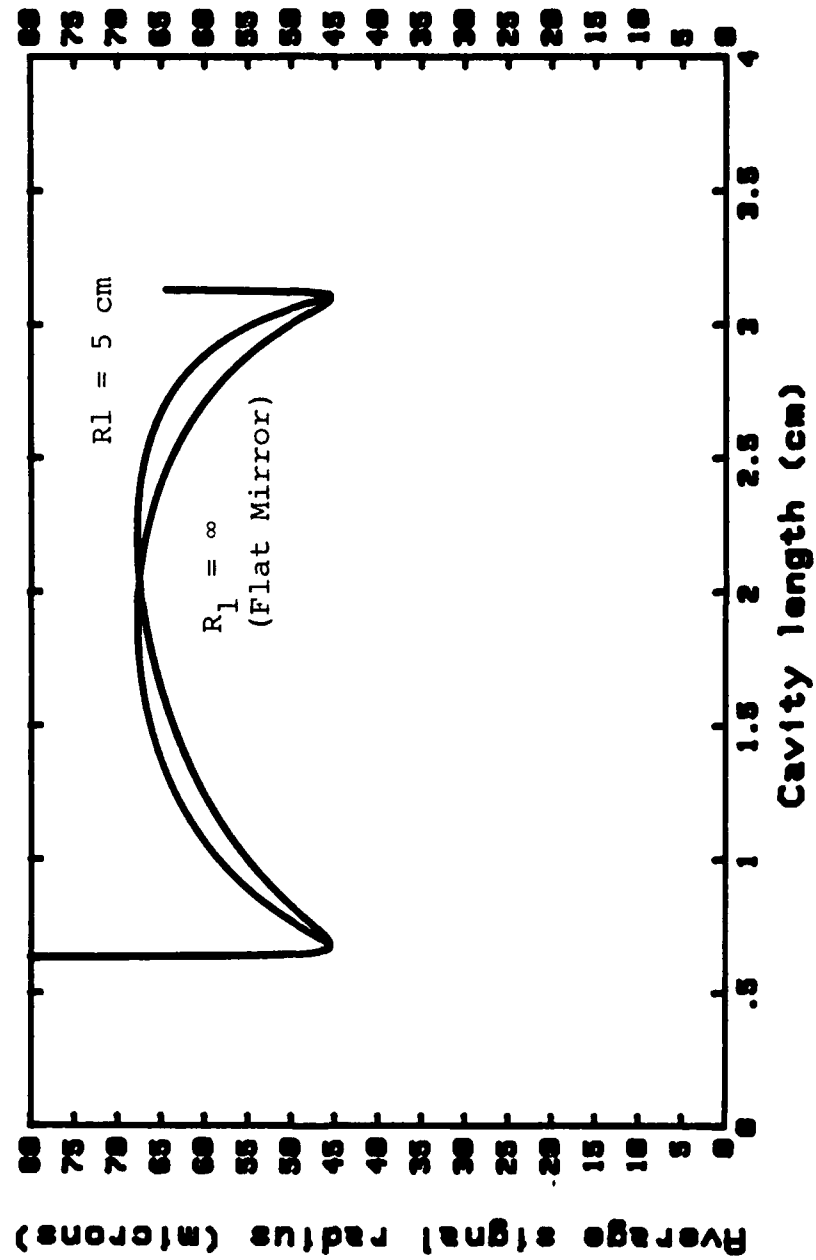
Figure 3.24--Short Cavity Laser. $\overline{W}_s$ versus L for Different Mirror Radii.

3. Active Internal Q-switching Experiments

The experimental set-up for the Q-switching experiments is shown in Figure 3.25. It consisted of the following: a pump dye laser, either Rh6G at 598 nm or Styryl 9M at 809 nm; an acousto-optic cell or a chopper to produce well defined pumping intervals at a repetition rate of $\sim$ 20 Hz; a 10 cm focal length lens; the Nd:MgO:LiNbO$_3$ laser containing a Brewster window; and the detection elements. For Q-switching, a voltage pulse was applied just before the beginning of each pumping interval with amplitude high enough to hold off quasi-CW oscillation. Turning this voltage to zero just before the end of the pumping interval resulted in the generation of a Q-switched pulse.

Throughout this contract several Q-switching experiments were performed with the nearly concentric laser and the short-cavity laser described in the previous subsection. In early experiments, the voltage pulses were applied with the aid of a 20 volt-pulser followed by a high voltage amplifier. Because of the narrow bandwidth of the amplifier (50 KHz), the switching time was very long. To avoid multiple Q-switched pulse generation, we carefully adjusted the relative delay between the voltage and pump pulses. However, this resulted in a deterioration of the Q-switched pulsed peak power.

As a second step, a high voltage pulse generator (HP 214B) emitting 100 volt-pulses with 15 nsec fall times was rented. The fall times were short enough for efficient Q-switching. However, the voltage amplitude was not large enough to prevent quasi-CW oscillation at high pump levels. Figure 3.26 shows the measured pulse widths and peak powers versus absorbed pump powers for the 3 cm long short-cavity laser. The maximum peak power observed was close to 3 W. The theoretical expression for the pulsewidth, included in the inset, has been plotted for comparison. The measured pulse widths are larger than what Q-switched laser theory predicts. This discrepancy was encountered repeatedly in all the Q-switching
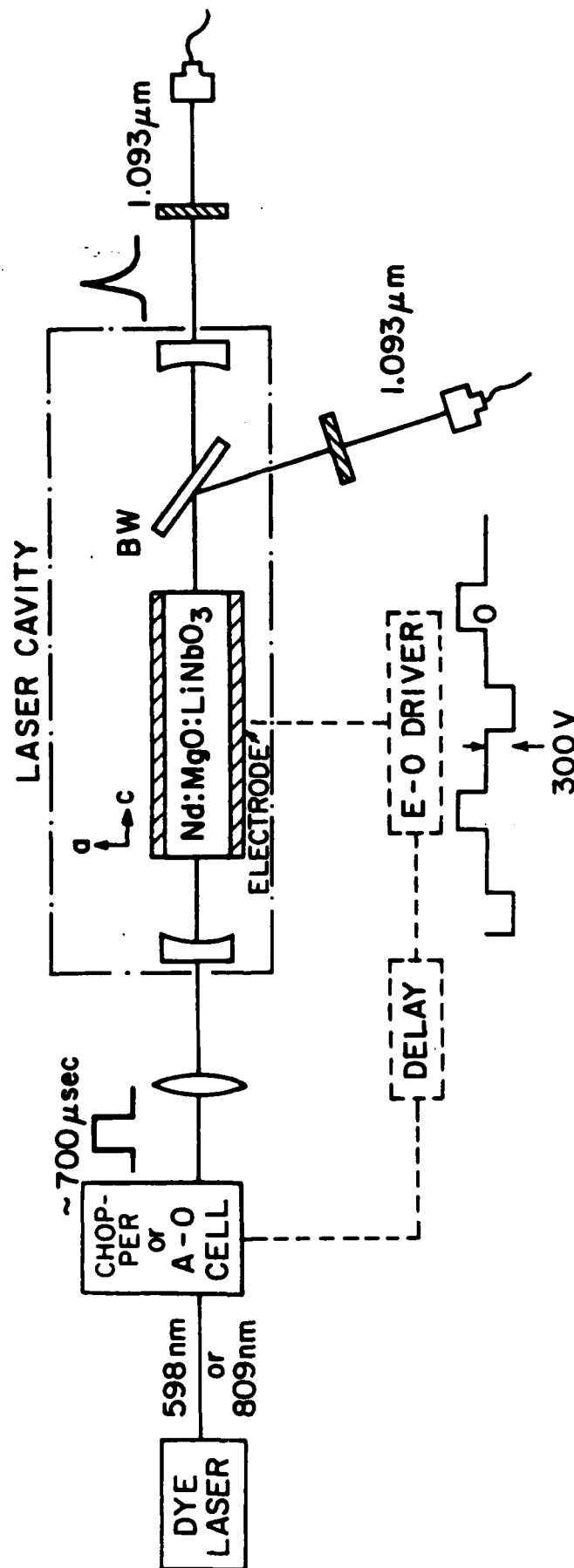
Figure 3.25--Experimental Set-up for Active Internal Q-switching.
BW = Brewster Window. F = Color Filter.
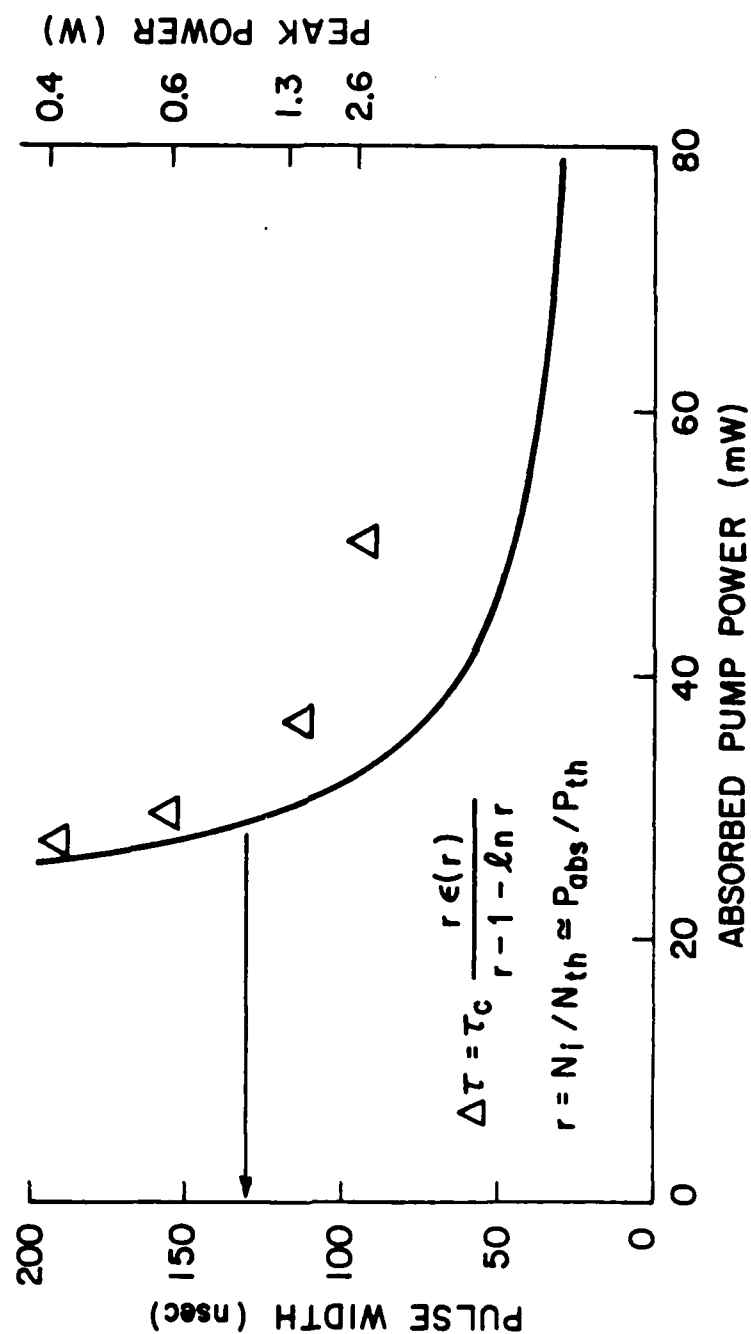
Figure 3.26--Width and Peak Power of the Q-Switched Pulse.

experiments and is discussed in detail in Section III.F.6. Figure 3.27 depicts the Q-switched pulse energy versus pump power. The energy conversion efficiency is high, $S_E = 1.8\%$ in spite of the low output coupling, $T \sim 0.5\%$.

Because of the generation of the screening field, the Q-switched pulses became unstable after a few minutes of operation. As explained in a previous section, this problem was alleviated by using a home made transistor circuit that applied voltage pulses of alternating polarity.

4. Latest Experiments

4.1 Experimental Results

Measurements on the short-cavity Q-switched laser were performed by applying voltage pulses of alternating polarity. This procedure eliminates the screening field due to the material photoconductivity as discussed in a previous section.

Figure 3.28 shows the measured widths and peak powers of the Q-switched pulses versus absorbed pump power at 598 nm. A peak power of 5 W was attained when pumping about five times above threshold. The peak power increases approximately linearly with pump power as shown. The zero intercept of the linear fit indicates that the absorbed pump power threshold was only 10 mW. The pulse widths decrease monotonically with increasing pump power and approach asymptotically a value of $\sim$ 45 nsec, which is about three times larger than the pulse width predicted by the Q-switched rate-equations.

The required voltage in this experiment was only 170 V when pumping three times above threshold and 200 V when pumping four times above threshold.

When one of the high-reflector mirrors was replaced by a 1.4% transmission output coupler, shorter pulse widths were attained, essentially due to the reduced cavity photon lifetime. Figure 3.29 shows the oscilloscope trace of a Q-switched pulse. The minimum pulse width observed (full-width at half maximum) was 30
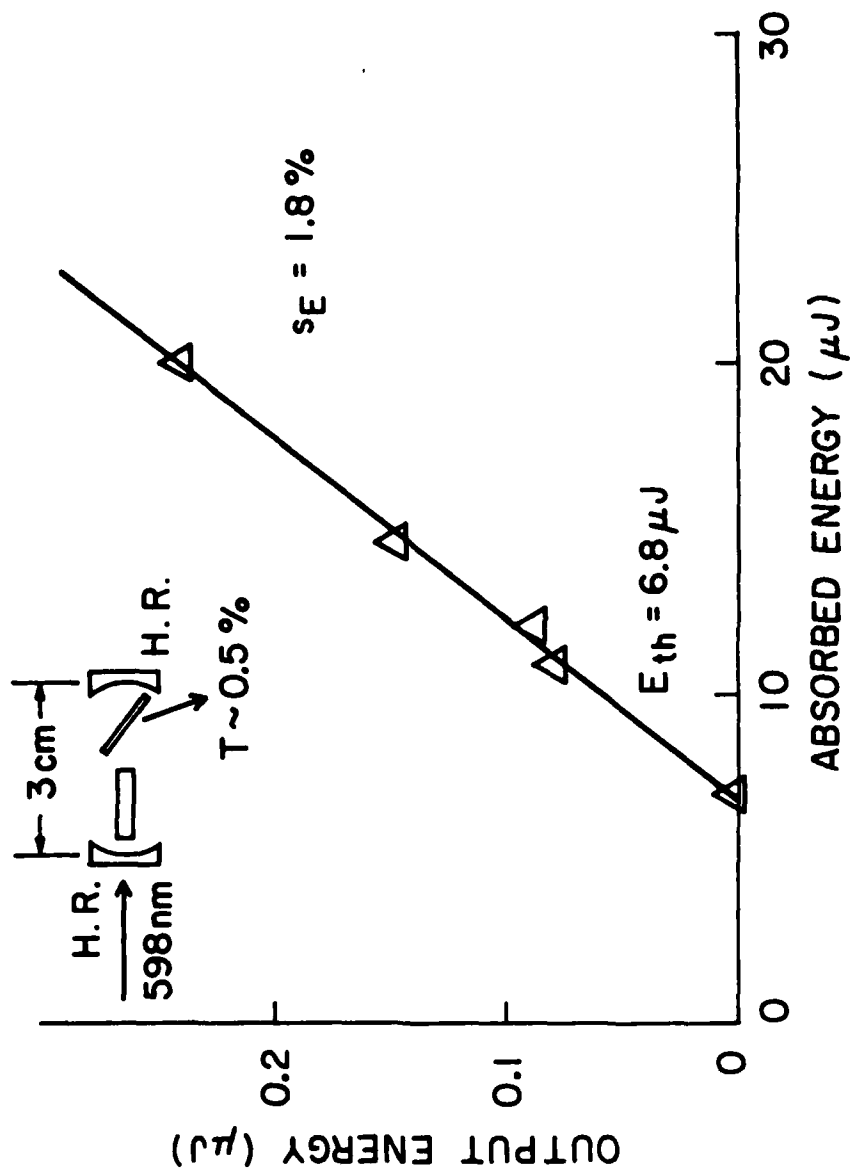
Figure 3.27--Q-switched Pulse Energy versus Pump Energy.
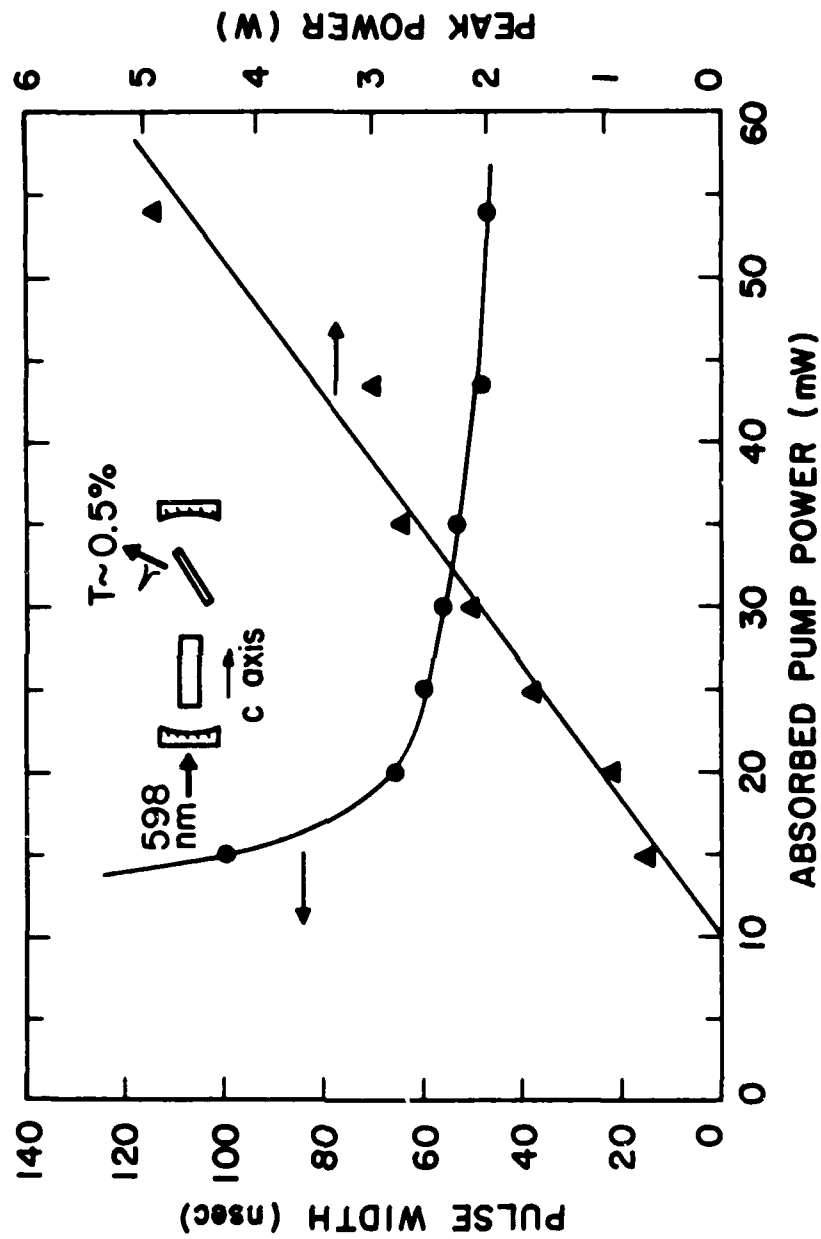
Figure 3.28--Pulse Widths and Peak Powers versus Absorbed Pump Power. Solid Lines are Fits to the Experimental Data.

Q-SWITCHED PULSE
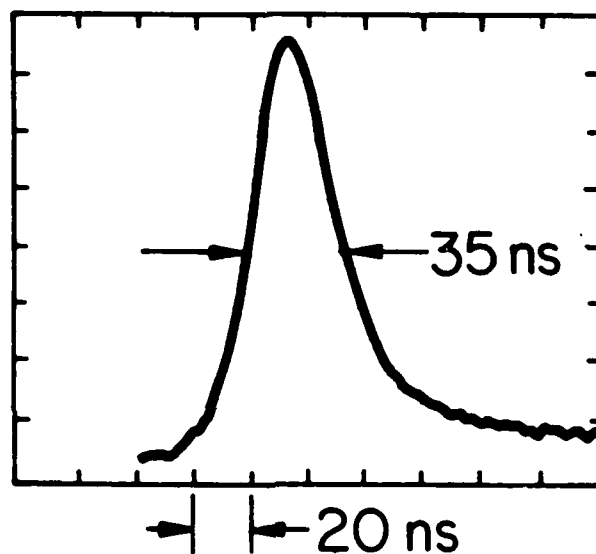
Figure 3.29--Oscilloscope Trace of a
            Q-switched Pulse. Full-
            Width at Half Maximum is
            35 ns.

nsec.

4.2 Discussion

Discrepancies have been observed between the measured Q-switched pulse widths and peak powers and the predictions of Q-switched laser theory. First, the measured peak powers are about one order of magnitude smaller than the predicted ones. Second, the pulse widths are about three times larger than what we expected from knowledge of the cavity photon lifetime. These discrepancies suggest that a theoretical study is required.

First of all, the mode overlap theory used throughout this and previous contracts is valid only when the laser medium fills the optical cavity entirely. This is a very reasonable assumption for the case of mechanically Q-switched Nd:YAG fiber lasers as well as for fiber lasers using a saturable absorber. For both types of Q-switched fiber lasers the cavity mirrors can be placed very close to the fiber end faces (and it is highly advantageous to do so to avoid diffraction of the laser beam between the fiber end and the mirror). However, in the Q-switched Nd:MgO:LiNbO$_3$ laser the presence of a polarizing element makes the resonator longer than the crystal. As we will show in the next sub-section, to take this into account, modifications of the laser rate equations are required.

A second important step in the theory is the inclusion of a time-dependent loss term. Since, as we have shown, the application of an electrical step excites piezoelectric resonances that induce a time-dependent loss.

5.   Laser Mode-Overlap Theory

The laser mode-overlap theory used in the current and previous contracts requires some modifications in order to be applied to the Nd:MgO:LiNbO$_3$ Q-switched laser. In this section we modify the laser equations to account for the

case of an optical resonator which is not entirely filled by the active (laser) medium. Next, we derive the Q-switched laser equations corresponding to single-transverse-mode operation and compare them to the predictions of a simpler analysis that does not account for modal overlaps. Finally, we include two extra terms, the contribution of spontaneous emission to the laser signal and the time-dependent elasto-optically-induced loss.

5.1 Laser Equations

In a four-level laser system such as Nd:MgO:LiNbO$_3$, the time evolution of the population inversion density $n(x,y,z,t)$ and the signal photon density in the ith transverse mode $s_i(x, y, z, t)$ are described by the following differential equations:

$$\frac{dn(x, y, z, t)}{dt} = r(x, y, z, t) - \frac{n(x, y, z, t)}{\tau_f} - c\sigma \frac{l}{l_{op}} n(x, y, z, t)$$
$$\times \sum_{i=1}^{m} s_i(x, y, z, t) \tag{3.21}$$

$$\frac{dS_i(t)}{dt} = c\sigma \frac{l}{l_{op}} \int\int\int_{cavity} n(x, y, z, t) s_i(x, y, z, t) dV - \frac{S_i(t)}{\tau_{ci}} \tag{3.22}$$

Here $S_i(t)$ is the total number of photons in the ith mode, τ_f is the fluorescence lifetime, σ the net gain cross section, c the velocity of light in free space, $r(x, y, z, t)$ the pumping rate per unit volume, l the length of the laser medium, l_{op} the optical length of the resonator and τ_{ci} the photon lifetime for the ith mode. τ_{ci} is related to the round-trip cavity loss for the ith mode δ_i by

$$\tau_{ci} = \frac{2l_{op}}{c\delta_i} \tag{3.23}$$

When the laser medium entirely fills the resonator, the optical cavity length is $l_{op} = n_1 l$, where n_1 is the refractive index of the laser material. In this case, Equations (3.20) and (3.21) reduce to the well known rate-equations used throughout previous

contracts.[4]

5.2 Overlap Integral and Q-switched Laser Equations

Following the derivation in Part C of the cited reference, we introduce the normalized population inversion, signal and pump distributions n_0, s_{0i} and r_0, and define the overlap integral F_i as follows:[5]

$$F_i = \int \int \int_{laser\ medium} n_0(x, y, z) s_{0i}(x, y, z) dV \qquad (3.24)$$

For Q-switched operation it is valid to neglect the pumping and spontaneous emission terms in Equation (3.21) which are significant only for time durations much longer than the characteristic times of the Q-switched pulses. Neglecting the first two terms on the right side of Equation (3.21), integrating over the cavity volume and using Equation (3.24), we get

$$\frac{dN(t)}{dt} = -\frac{c\sigma l}{l_{op}} N(t) \sum_{j=1}^{m} F_j S_j(t) \qquad (3.25)$$

Similarly, Equation (22) gives

$$\frac{dS_i(t)}{dt} = \frac{c\sigma l}{l_{op}} N(t) F_i S_i(t) - \frac{S_i(t)}{\tau_{ci}} \qquad (3.26)$$

In Equations (3.25) and (3.26), $N(t)$ and $S_i(t)$ are the total population inversion and total photon number in the ith mode respectively.

We will only consider here the case of single mode operation. Equations (3.25) and (3.26) reduce to

---

[4] See for example Equations (2) and (3), p. 13, Interim Report, AFWAL-TR-84-1159, "Diode Pumped Fiber Laser," (December 1984).

[5] Outside the laser medium $n_0(x, y, z) = 0$, therefore, the limits of integration can be extended to cover the entire resonator volume.

$$\frac{dN(t)}{dt} = \frac{c\sigma l}{l_{op}} F N(t) S(t) \tag{3.27}$$

$$\frac{dS(t)}{dt} = \frac{c\sigma lF}{l_{op}} N(t)S(t) - \frac{c\delta}{2l_{op}} S(t) \tag{3.28}$$

where the subscript 'i' has been dropped.

For the Nd:MgO:LiNbO$_3$ laser, the total round-trip cavity loss δ during Q-switched operation can be separated into two contributions. The first is the D.C. loss δ_0 which is also present during CW operation. The second is the elasto-optically-induced time-dependent loss $\delta(t)$. Thus,

$$\delta = \delta_0 + \delta(t) \tag{3.29}$$

Starting from Equation (3.22) we can show that the population inversion required to reach threshold during CW operation is

$$N_t = \frac{\delta_0}{2\sigma lF} \tag{3.30}$$

Substituting expressions (3.29) and (3.30) into Equations (3.27) and (3.28) we get:

$$\frac{dN(t)}{dt} = -\frac{1}{\tau_c} \frac{N(t)}{N_t} S(t) \tag{3.31}$$

$$\frac{dS(t)}{dt} = [\frac{N(t)}{N_t} - 1 - \frac{\delta(t)}{\delta_0}]\frac{S(t)}{\tau_c} \tag{3.32}$$

where the D.C. or CW cavity lifetime τ_c is given by

$$\tau_c = \frac{2l_{op}}{c\delta_0} \tag{3.33}$$

Equations (3.31) and (3.32) are the starting point for the computer analysis of the miniature Q-switched laser. We still need to mathematically model the loss $\delta(t)$.

131

5.3 Discussion

It is important to point out that Equations (3.31) and (3.32) (neglecting the time-dependent loss) are essentially the same as the differential equations derived in conventional Q-switched laser theory.[6] In that theory, the population inversion density $n(x, y, z, t)$ and the photon density $s(x, y, z, t)$ are substituted by their spatial-averages over the cavity volume. The equations are then solved as if both 'n' and 's' were uniform over the entire laser medium. By using mode-overlap theory, we have arrived at the same equations. The only information concerning the spatial distributions of 'n' and 's' is contained in the threshold inversion N_t through the overlap integral F.

The way in which the overlap integral is written here (Equation (3.24)) suggests that the normalized distribution n_0 is independent of time. This is unlikely to be true because the population inversion can saturate differently in different regions of the laser medium. This point will be addressed in Section III.F.6.4.

5.4 Spontaneous Emission Term and Initial Photon Number

The angle ϕ and the solid angle θ subtended by the TEM_{00} laser signal mode in the far-field pattern are given by

$$\phi = \frac{2\lambda_s}{\pi n_1 W_s}$$
$$\theta = \frac{\pi \phi^2}{4} \qquad (3.34)$$

where $\lambda_s = 1.093 \mu m$ is the signal wavelength $n_1 = 2.23$ is the refractive index and W_s is the signal waist radius. The total rate of spontaneous emission is equal to $N(t)/\tau_f$. Assuming that this emission is uniformly distributed over a unitary sphere, that is, over a solid angle of 4π, we find that the rate of spontaneous emission into the solid angle of the laser mode is

---

[6] See for example W. Koechner, *Solid State Laser Engineering*, Springer-Verlag (1976).

$$R_{spon} = \frac{\theta}{4\pi} \frac{N(t)}{\tau_f} \qquad (3.35)$$

Setting the time origin at the moment of opening of the Q-switch, we can calculate the number of signal photons present at $t = 0$ as follows. The photons present in the laser mode at this time are created by spontaneous emission only. They have a lifetime τ_c. Thus the initial photon number S_0 is given by

$$S_0 = R_{spon}(t = 0)\tau_c \qquad (3.36)$$

5.5 Time-dependent Cavity Loss

We already stated that during Q-switched operation the total round-trip cavity loss can be separated into a D.C. or CW loss δ_0 and a time-dependent, elasto-optically-induced loss $\delta(t)$.

In Section III.E we discussed in detail the effects of the elastooptic loss on the Q-switched pulses. At low pump levels the emission of the pulse is delayed by the occurence of consecutive oscillatory-loss peaks. Besides, due to pump power fluctuations the moment of emission can alternate ('jitter') between several fixed positions in time. In this latter case the amplitude of the pulse fluctuates. When pumping more than about three times above threshold, the jitter and amplitude fluctuation disappear. At these pump levels the Q-switched pulse is emitted during the first semi-cycle of the oscillatory-loss. Therefore, in our mathematical model we only need to include this first semicycle, since we are mostly interested in high-pump level operation.

Figure 3.30 shows the total cavity round-trip loss measured by the method described in Section F. The voltage applied during the low-Q state was 200 V. The D.C. loss δ_0 corresponds in this figure to the loss level observed after the acoustic oscillations have been attenuated. δ_0 is equal to $\approx 3\%$. From Figure 3.30 we find
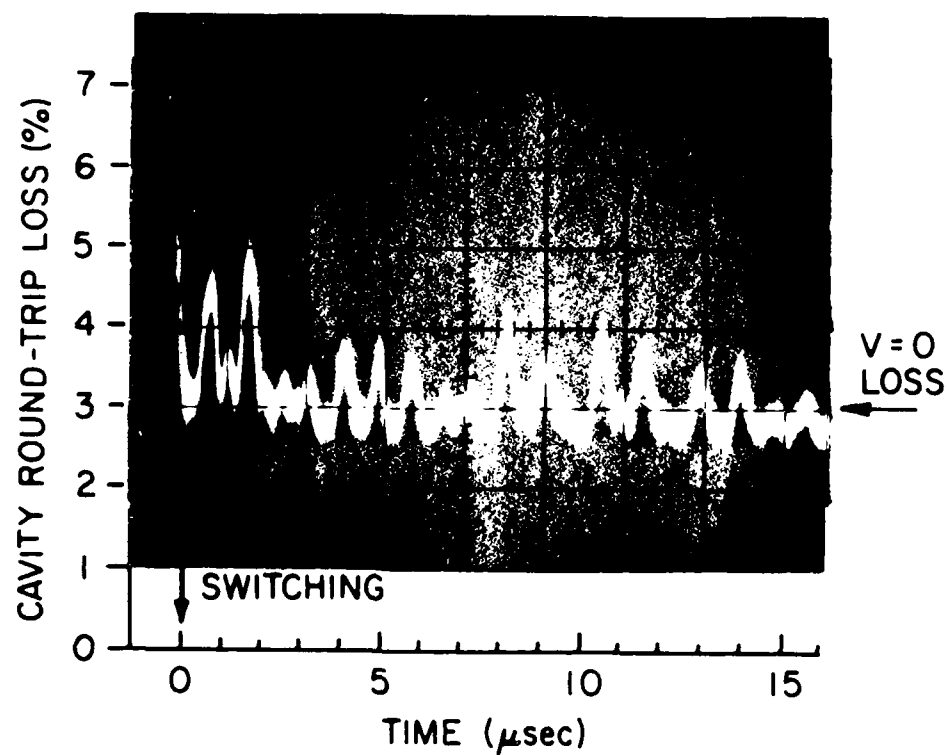
Figure 3.30--Time Evolution of the Cavity
Round-Trip Loss after Switching
the Voltage from 200 V to Zero.

- 134 -

that the first semi-cycle of $\delta(t)$ can be modeled as follows:

$$\delta(t) = 0.01(1 - \sin\frac{2\pi t}{1\mu sec}) \qquad (3.37)$$

5.6 Final Form of the Equations

The Q-switched laser equations for single-mode operation can be written as

$$\frac{dN(t)}{dt} = -\frac{N(t)}{N_t}\frac{S(t)}{\tau_c} \qquad (3.38)$$

$$\frac{dS(t)}{dt} = [\frac{N(t)}{N_t} - 1 - \frac{\delta(t)}{\delta_0}]\frac{S(t)}{\tau_c} + R_{spon} \qquad (3.39)$$

5.7 Numerical Values

For fundamental Gaussian signal and pump modes the overlap integral F is given by

$$F = \frac{1}{\frac{\pi}{2}(\overline{W}_s^2 + \overline{W}_p^2)} = \frac{1}{A_p^* l} \qquad (3.40)$$

with $\overline{W}_s = 45\mu m$ and $\overline{W}_p = 34\mu m$, then $A_p^* = 5 \times 10^{-5}\,cm^2$. The net gain cross section (low-gain polarization) is $\sigma = 1.8 \times 10^{-19}\,cm^2$ and the D.C. loss $\delta_0 = 3\%$. Therefore, the threshold inversion calculated from Equations (3.30) and (3.40) is

$$N_t = 4.2 \times 10^{+12}\,atoms \qquad (3.41)$$

The optical cavity length is $l_{op} = 4.5\,cm$, thus, from Equaton (3.33) we get

$$\tau_c = 10\,nsec \qquad (3.42)$$

The solid angle (Equation 3.34) is $\theta = 3.8 \times 10^{-5}\, sr$, and the fluorescence lifetime $\tau_f = 120\,\mu sec$. Thus, the initial number of photons is (from Equations (3.35) and (3.36))

$$S_0 = 2.5 \times 10^{-10} N(t = 0) \tag{3.43}$$

and, the initial inversion is

$$N(t = 0) = N_0 = \frac{P_{abs}}{P_{th}} N_t \tag{3.44}$$

where P_{abs}/P_{th} is the ratio of absorbed to threshold pump powers.

6. Computer Analysis of the Miniature Q-switched Laser

The Q-switched laser equations derived in the previous section were solved numerically with the aid of a computer. We present here results from this computer analysis. The calculated peak powers, pulse energies and pulse widths are compared to the measured ones. The need for a more refined theory, to account for the experimental results, is discussed. This theory should consider spatial effects in the saturation of the laser gain (i.e., the population inversion).

6.1 Instantaneous Output Power

Prior to addressing the problem of solving the laser equations, we want to find an expression for the instantaneous output power P_i in terms of the photon number S. At a given time t, the total laser signal energy inside the resonator is given by the product of the photon energy $h\nu_s$ and the photon number. The rate at which this energy is lost is $Sh\nu_s/\tau_c$, where τ_c is the cavity lifetime or average lifetime of a photon inside the resonator. The fraction of this energy which is utilized as laser output is determined by the ratio of output coupling T to cavity loss δ. Therefore, the instantaneous output power is given by:

$$P_i(t) = \frac{T}{\delta} \frac{h\nu_s}{\tau_c} S(t) = \frac{cT}{2\, l_{op}} h\nu_s\, S(t) \tag{3.45}$$

Here l_{op} is the optical cavity length and c the velocity of light in vacuum.

In most of the experiments performed, the laser output was obtained from reflection on the Brewster plate. Due to elasto-optic birefringence modulation, this reflection was time-dependent. Therefore, like the total cavity loss, the output coupling can be separated into a D.C. or CW term T_0 and a time-dependent term $T(t)$, where $T(t)$ equals one-half of the elasto-optic loss $\delta(t)$. Thus, we can write

$$T = T_0 + \frac{\delta(t)}{2} \tag{3.46}$$

The CW output coupling was determined from the CW slope efficiency to be $\sim 0.5\%$. The CW cavity round-trip loss was $\delta_0 \sim 3\%$.

6.2 Solution of the Laser Equations

We need to solve a set of two nonlinear, first-order differential equations, (Equations (3.38) and (3.39). For the case of time-independent loss, that is, $\delta(t) = 0$, we can obtain a simple analytical expression relating the photon number $S(t)$ to the population inversion $N(t)$. However, it is not possible to express N and S as functions of time in terms of known mathematical functions. On the other hand, the differential equations can be solved numerically without major difficulty even for the case of time-dependent loss.

A computer program was written that solves the differential equations by using sixth-order Runge-Kutta method. The program calculates the time-evolution of the Q-switched laser photon number, the instantaneous output power or the population inversion (laser gain) for different absorbed pump powers. The pulse energy is evaluated by integrating numerically the instantaneous output power. The values of the parameters used in the computer analysis are given in Section III.F.5.7.

Figures 3.31 and 3.32 show the computer-generated time-evolution of the instantaneous output power for two absorbed pump powers P_{abs} of 35 mW and 50 mW respectively. The time-dependent part of the cavity loss $\delta(t)$ has been included in the figures. For $P_{abs} = 35$ mW the peak of the pulse occurs 120 nsec after the electrical switching, when the total loss is $\delta = 3.3\%$ and the output coupling $T = 0.65\%$. For $P_{abs} = 50$ mW the pulse peak occurs at $t = 75$ nsec, when the cavity loss is 3.55% and the output coupling is 0.77%.

6.3 Comparison with the Experimental Results

The pulse energies, pulse widths and peak powers calculated with the aid of the program are plotted versus absorbed pump power in Figures 3.33, 3.34, and 3.35. For comparison we have included in the figures the experimental results given in Section III.F.4.

Figure 3.33 shows that except for the first two points, the measured pulse widths are larger than the predicted ones. The ratio of experimental to theoretical pulse width increases with increasing pump power from 1.4 to 2.3 for absorbed pump powers between 30 and 55 mW.

The pulse energy versus pump power plots of Figure 3.34 can be approximated by straight lines with zero-vertical-axis intercept at $P_{abs} = 10$ mW. The slope corresponding to the theoretical predictions is $1.7 \times 10^{-5} sec^{-1}$ or $0.0176 \, \mu J/mW$. A best linear fit to the experimental points has a slope of $0.0087 \, \mu J/mW$. Thus, there is a factor of two discrepancy between the experimental and theoretical slope efficiencies.

The largest discrepancy between theory and experiment is encountered in the peak powers as illustrated in Figure 3.35. The measured peak powers are lower than the theoretical ones by factors ranging from 2 to 7.
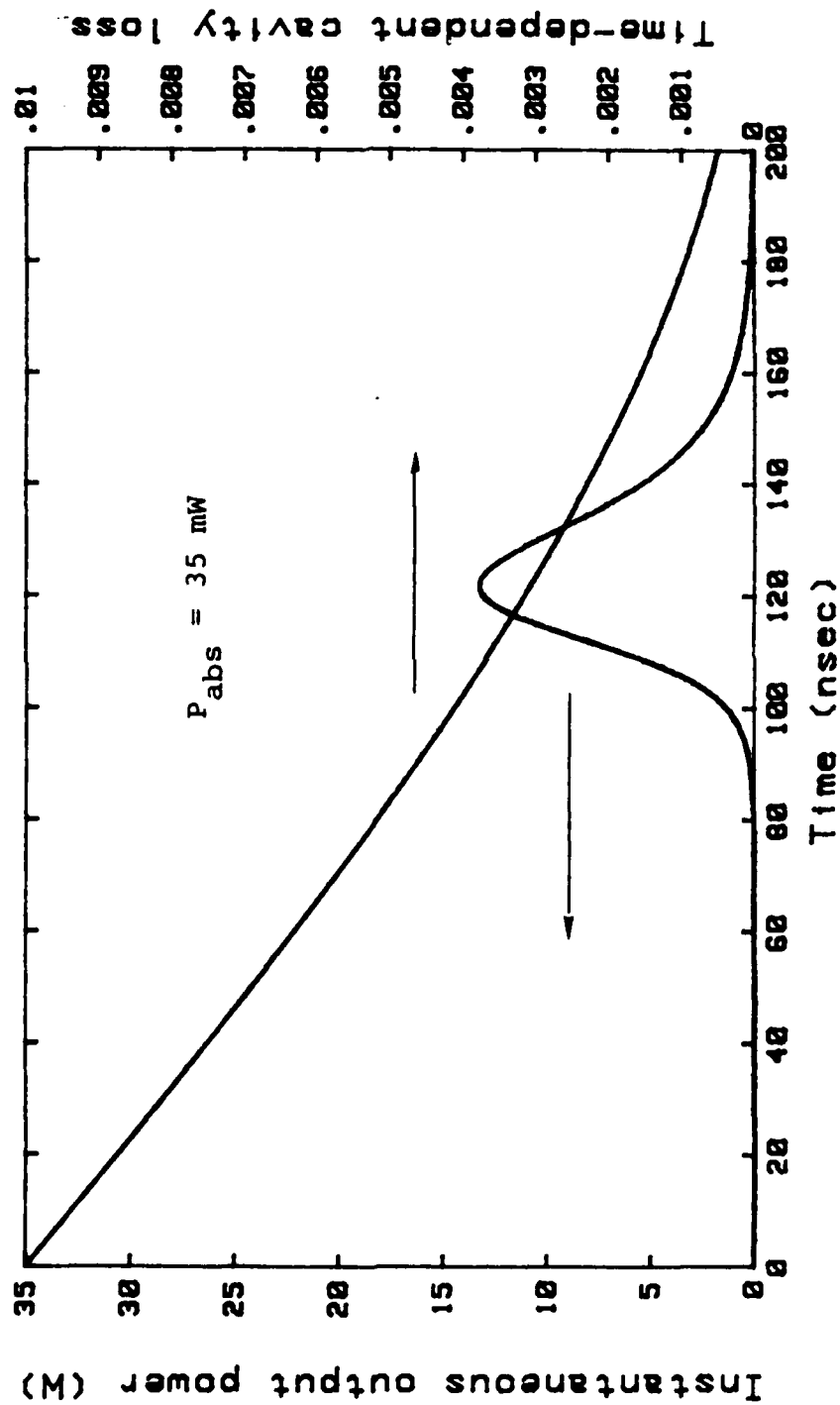
Figure 3.31--Time Evolution of the Instantaneous Output Power Predicted by the Computer Program.

- 139 -
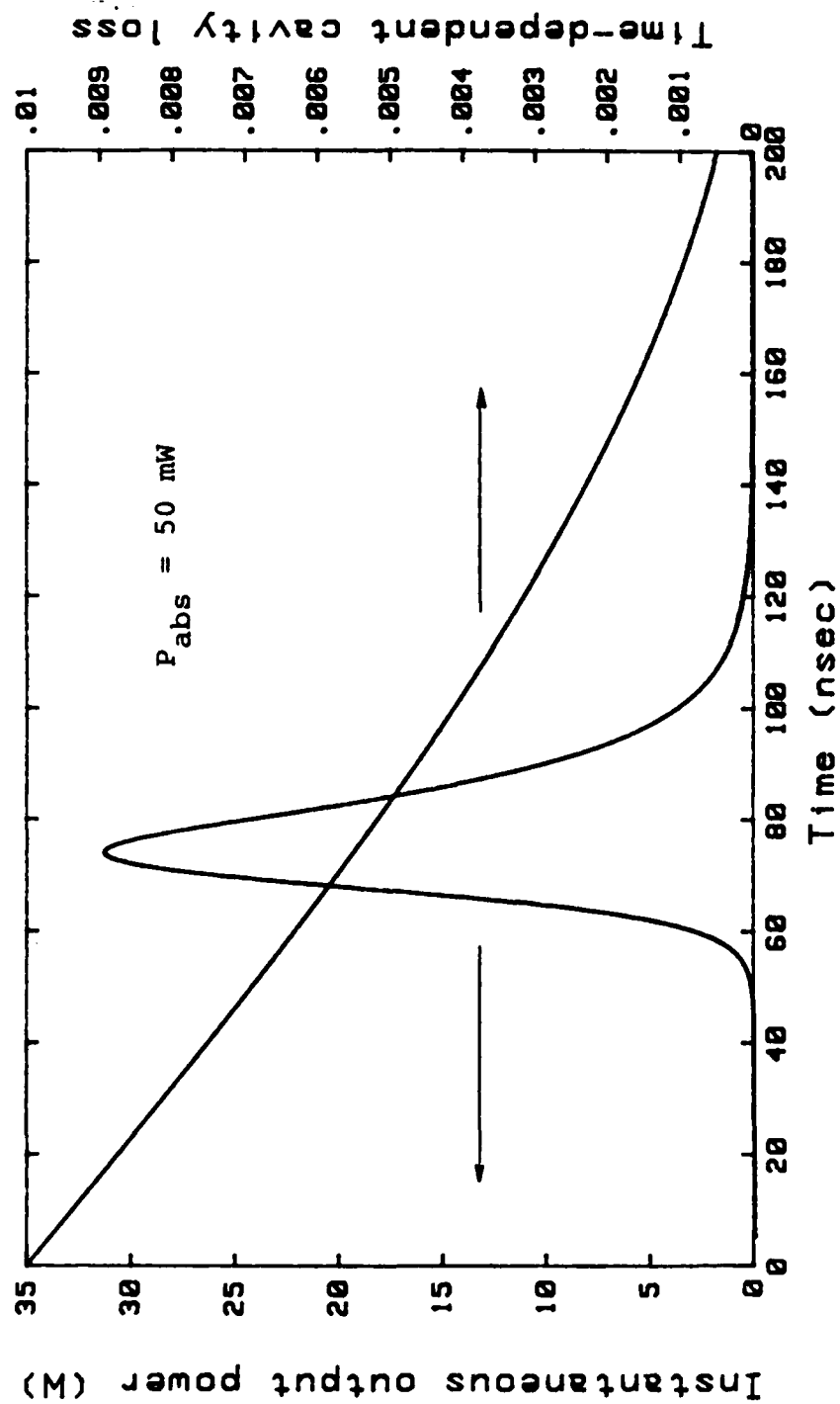
Figure 3.32-- Time Evolution of the Instantaneous Output Power
Predicted by the Computer Program.
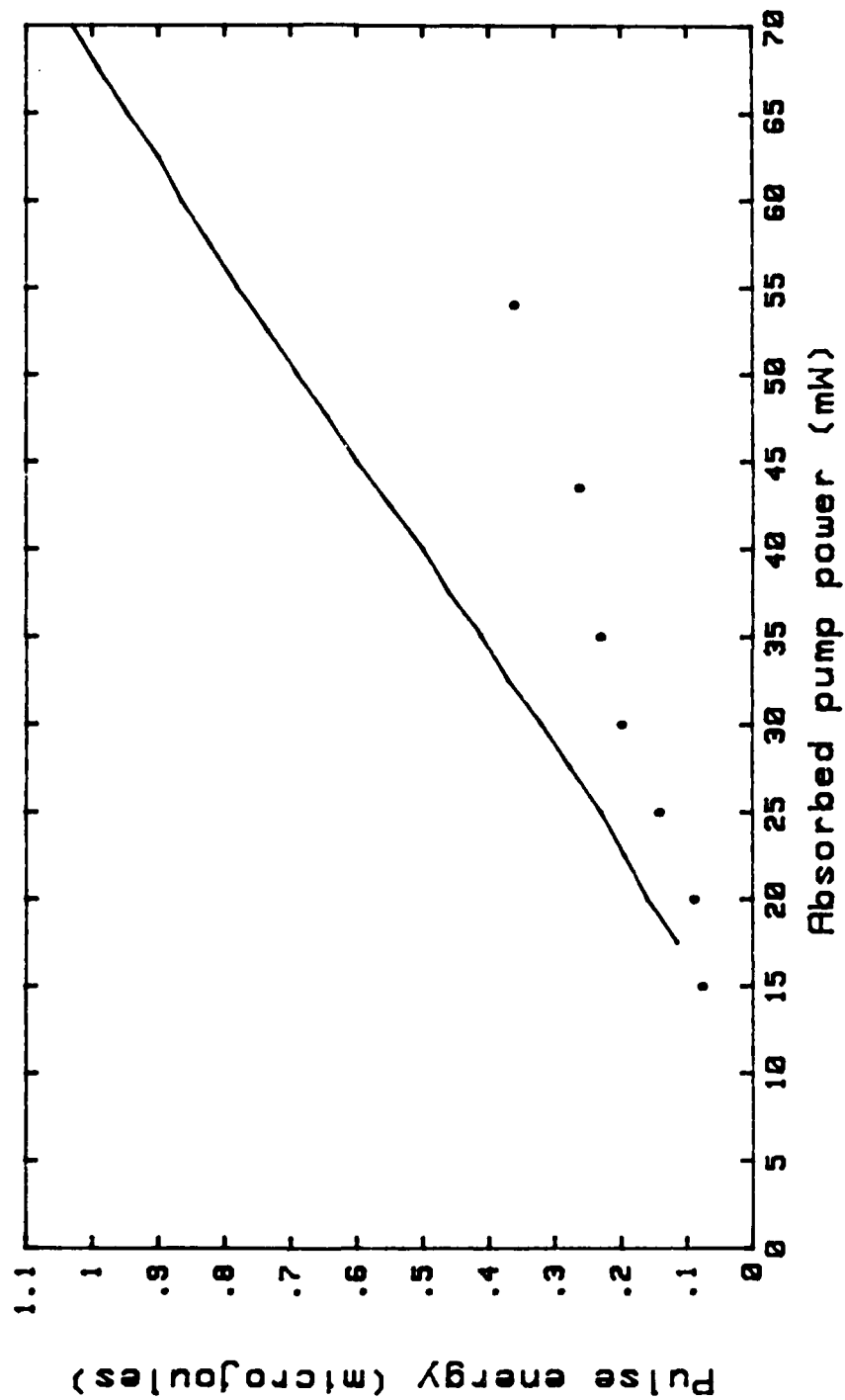
Figure 3.33--Q-switched Pulse Energy versus Absorbed Pump Power. The Solid Line was generated by the Computer Program. The Points are Experimental Results.
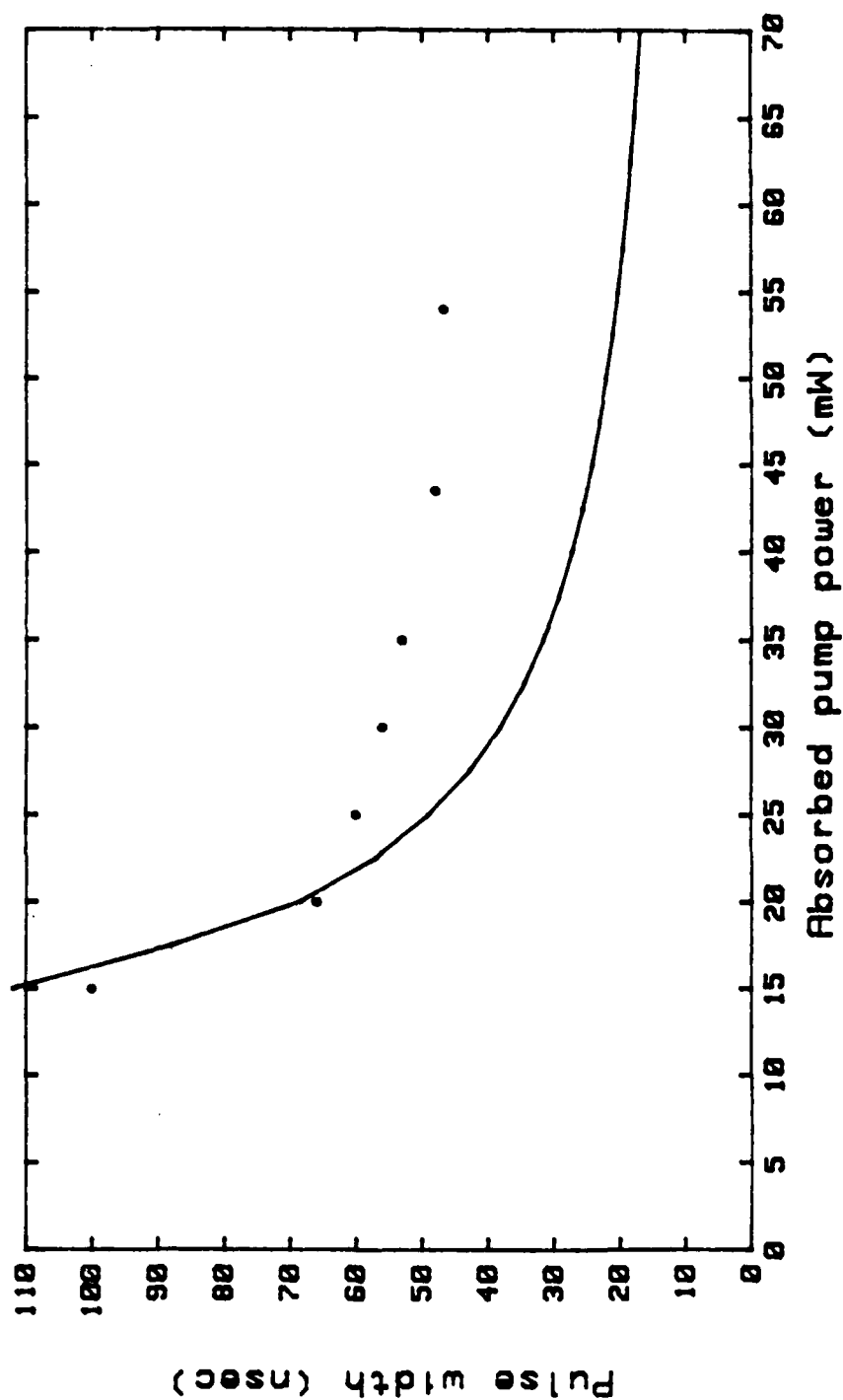
Figure 3.34--Q-switched Pulse Width versus Absorbed Pump Power. The Solid Line was generated by the Program. The Points are measured Values.
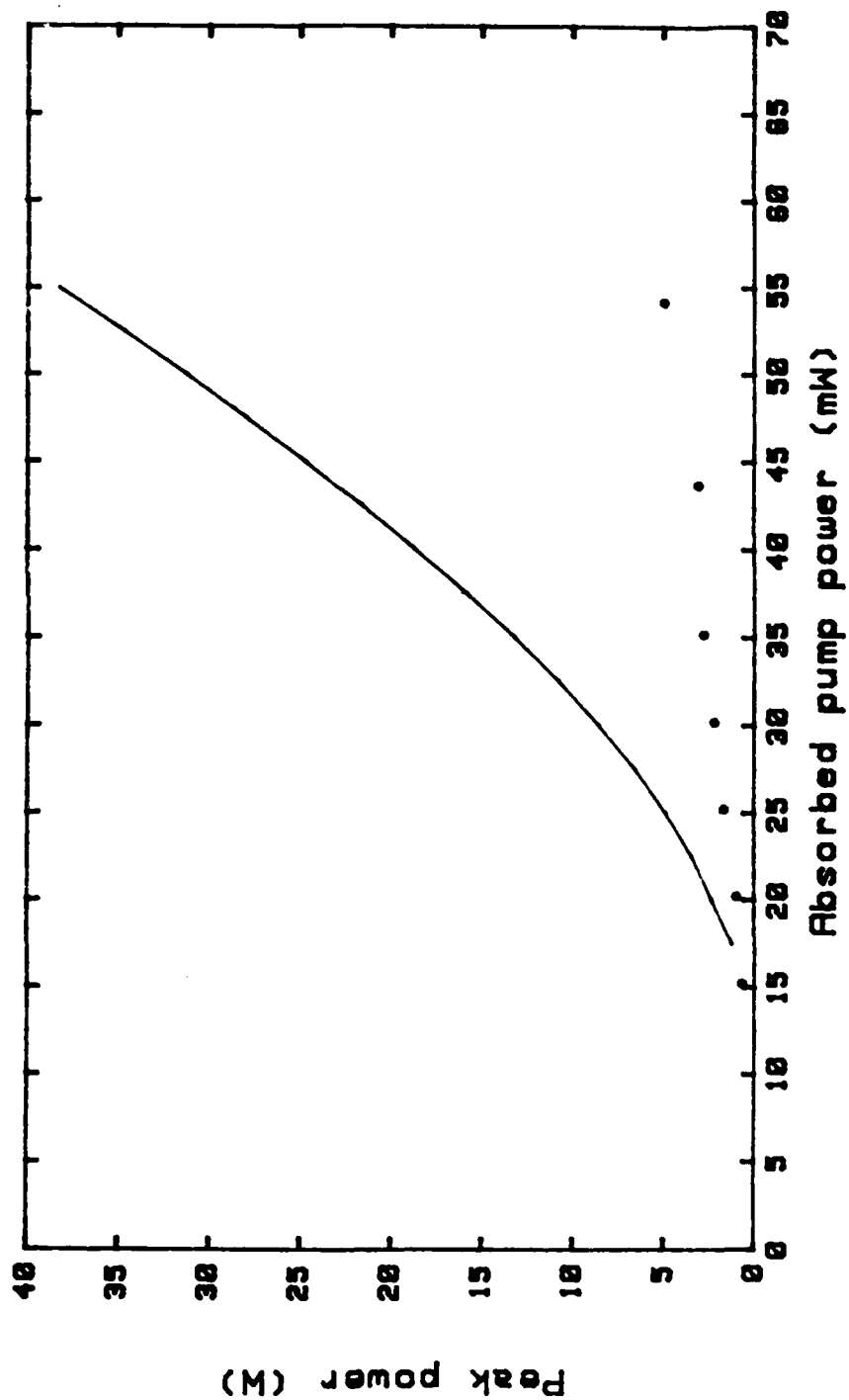
Figure 3.35--Peak Power versus Absorbed Pump Power. The Solid
Line is Theoretical. The Points are Experimental.

6.4 Discussion

The output coupling T utilized in the computer program was inferred in part from CW laser measurements ($T_0 \sim 0.5\%$) and in part from elasto-optic modulation measurements ($T(t) \sim \delta(t)/2$). Due to the large non-uniformity in the birefringence of our Nd:MgO:LiNbO$_3$ samples, the output coupling can vary by factors of two or more from one lasing spot to another. This can account for the factor-of-two discrepancy between the theoretical and experimental pulse energies. To assure that neither the output coupling nor the crystal loss change from one measurement to another, it is necessary to perform the CW-laser, elasto-optic modulation and Q-switching experiments on the same lasing spot. This requirement would be unnecessary with samples exhibiting better uniformity and optical quality.

An erroneous estimation of the output coupling T can explain the discrepancies between theory and experiment for the pulse energy and, in part, for the peak power. This is not true for the Q-switched pulse width which does not depend on T. To account for the larger pulse widths encountered experimentally we would need to assume a smaller cavity loss δ. However, a smaller δ would imply even higher predicted pulse energies than those shown in Figure 3.34.

One possible explanation for the larger pulsewidths and, in part, for the lower peak powers observed experimentally is the presence of several longitudinal modes during Q-switched operation. In this case, the laser output is the superposition of several pulses having different widths, build-up times and peak-heights. The resulting pulse is wider and lower in peak power than the pulse from a single mode laser. Another possible explanation concerns non-uniform saturation of the population inversion along the transverse dimensions of the laser medium. In this case the output is again the superposition of pulses having different characteristics and proceeding from different annular regions of the crystal cross section. Because the initial population inversion is much higher at the crystal axis, the photon density

grows much faster near the axis, saturating the gain first. A more refined theory that accounts for these effects is needed in order to explain quantitatively the experimental results.

G. Nd:MgO:LiNbO$_3$ Single Crystal Fibers

1. Introduction

During the present contract, the first single crystal fibers of neodymium lithium niobate were grown and processed, using the second-generation growth station (Section II.B.1). Difficulties associated with growth, annealing, surface granularity, spurious colorations (brown or yellow), mounting and end-face polishing were satisfactorily solved. A brief description of fiber growth and processing is given in this section.

Initial attempts to achieve laser action in unclad Nd:MgO:LiNbO$_3$ fibers were performed. The threshold for laser oscillation in these unclad fibers could not be attained with the pump powers available. We show theoretically in this section that a cladding should reduce the fiber laser threshold by more than an order of magnitude. LiNbO$_3$ fibers very recently were successfully cladded under auspices of other contracts. The cladding technique of Mg-in diffusion allowed the demonstration of two-mode propagation in a LiNbO$_3$ single-crystal fiber.[7] It is expected that this technique will be applied in the future to Nd:MgO:LiNbO$_3$ fiber lasers.

2. Growth of Nd:MgO:LiNbO$_3$ Single-Crystal Fibers

During the present contract the first Nd:LiNbO$_3$ single-crystal fibers were grown by using the laser-heated miniature pedestal technique. A total of nine fibers having diameters around 170 μm and lengths ranging from 2.5 to 5.0 cm were grown.

---

[7] S. Sudo, A. Cordova-Plaza, R. L. Byer, and H. J. Shaw, "MgO:LiNbO$_3$ Single-Crystal Fiber with Mg-ion In-diffused Cladding," submitted to Optics Letters.

The starting source material consisted of 0.5 mm-wide rods originating from the second-generation Nd:MgO:LiNbO$_3$ boule which contained 0.2 wt% Nd$_2$O$_3$ and 5 mol % MgO in the melt (see Section A.2). Pulling rates were 1 mm/min for the first fibers and 2 mm/min for the latest ones. All the fibers were grown along the c-axis.

It is known that LiNbO$_3$ crystals with oxygen deficiency exhibited a brownish color indicative of an undersirable high absorption at visible wavelengths. To prevent oxygen loss during the Nd:MgO:LiNbO$_3$ fiber growth, a wet oxygen atmosphere was provided. In spite of this precaution, a slight brownish coloration could be observed in the first two fibers when examined under the microscope. Experience with past LiNbO$_3$ fibers indicates that the coloration disappears after annealing in an oxygen-rich atmosphere, yielding a clear, transparent material perfectly suited for fiber-optic devices

The first Nd:MgO:LiNbO$_3$ fibers exhibited transverse ridges at regular spacings, over certain areas of the fiber. These ridges were caused by small jerks of either the upper or the lower translators. During growth, the capillary tubes holding the fiber and/or source rod are pressed between an aluminum V-groove and a rubber belt. The pulling mechanism is provided by motors acting on the belts. In an ideal situation the friction between the capillary and the belt should be infinite whereas the friction between the capillary and the V-groove should be zero. The finite frictions as well as small imperfections in the belts result in occasional jerking. This problem was solved by replacing the aluminum V-grooves with teflon V-grooves (teflon is a material with a very low coefficient of friction). As a consequence, the latest fibers are almost free of transverse ridges.

The work with miniature bulk lasers showed that a length of active material between 1 and 1.5 cm was a good compromise between low crystal loss (1% per cm for the bulk material) and high pump power absorption (1/e^2 absorption depth of

$\sim$ 1 cm at 598 pump wavelength). Thus each of the grown fibers could be cut in two or three pieces, the best pieces being candidates for fiber lasers. After cutting, each fiber needs to be placed inside a diameter-matched capillary-tube and firmly held with the aid of epoxy or wax. This constitutes a preparation for end-face polishing.

Prior to mounting and polishing, two steps are required in the crystal fiber processing. The first step is annealing. Annealing releases the internal mechanical stress induced during growth. High stress results from the temperature gradients, typically on the order of $1000°$ $C/(1/2$ mm) or higher. Therefore, annealing significantly increases the mechanical resistance of the fiber which, otherwise, is brittle and easy to break. In addition, if the process is performed in an oxygen-rich atmosphere those fibers exhibiting a brownish coloration acquire the required transparency.

The second step is fiber cladding. The work with Nd:YAG fiber lasers demonstrated that a great improvement in laser performance is achieved when a cladding material is deposited around the fiber. The reason for the improvement is the big reduction in surface scattering which is the main loss mechanism in fiber lasers. In the case of $LiNbO_3$ fibers different cladding methods have been investigated under the auspices of other contracts. The most promising methods consist of magnesium in-diffusion and proton-exchange in a solution of benzoic acid. In the method of proton-exchange most of the fibers tended to etch in the bath of benzoic acid. On the other hand, the technique of magnesium in-diffusion has given very good results.

3. Fiber Processing

3.1 Alumina Oven

A new alumina oven was prepared for the processing of $LiNbO_3$, $MgO:LiNbO_3$ and $Nd:MgO:LiNbO_3$ single crystal fibers. The oven was purchased recently under

147

an NSF grant provided to the Center for Materials Research at Stanford for crystal fiber research.

Alumina was used instead of quartz because of previous undesired results obtained when annealing MgO:LiNbO$_3$ fibers in a quartz oven. Some samples annealed in a quartz tube acquired a cloudy appearance. This could be caused by an impurity diffusing and/or reacting with lithium niobate. Since quartz is slightly porous at high temperatures, an outside impurity could have diffused through the tube walls. Silicon from the tube itself could be also responsible for the observed behavior.

The alumina oven was used for fiber annealing and lithium and/or oxygen equilibration.

3.2 Fiber Processing System: Description and Characterization

The processing temperature for lithium niobate fibers T_p was chosen to be $1050°C$. Since LiNbO$_3$ loses its ferroelectric single-domain structure at temperatures above the Curie point T_c, it was important to keep a reasonably safe margin between T_p and T_c. We needed to take into account that T_c varies from $\sim$ 1100 °C to $\sim$ 1200 °C depending on lithium and magnesium concentration and that lithium out-diffuses readily at high temperatures.

The temperature gradients at the center of the oven were measured with a probe thermocouple. When the temperature was $\sim$ 1000 °C, we measured an axial gradient of 8 °C/cm and a radial gradient of 1 °C/ 2.5 cm = 0.4 °C/cm. Since we wanted to keep the temperature of a fiber uniform within 1 °C or less, it was clear that the fibers should be positioned radially rather than axially. The alumina-tube inner diameter is 5 cm, large enough to accommodate the fiber lengths of interest (typically 1 to 2 cm).

To avoid oxygen loss during fiber processing, a constant flow of this gas was

provided. The flow rate was 1 ℓ/min. A typical fiber processing sequence was: heating from room temperature to 1050 °C (1 hour), processing at 1050 °C (2 hours) high temperature cooling from 1050 °C to 570 °C (1 hour), free cooling. The duration of the high temperature cooling period was important since a fast cooling could lead to sample cracking whereas a slow cooling could cause a solid-state phase transition. Researchers working with LiNbO$_3$ waveguides typically use a cooling rate of 8°C/min which equals our cooling rate of $\frac{(1050-570)° C}{1 hour}$.

As-grown lithium niobate fibers exhibit a particular kind of surface granularity. Originally this surface defect was associated with impurities present on the surface of the source rods used for fiber growth. An improved cleaning procedure by means of an ultrasonic bath reduced the amount of granules but it did not eliminate them completely.

At present we believe that the granules consist mainly of lithium oxide, Li$_2$0, that evaporates from the molten zone during growth and condenses onto the cooler sections of the growing fiber. The sublimation point of Li$_2$0 is 1200 °C, close to the processing temperature $T_p = 1050 °C$. Therefore, we could get rid of most of the surface granularity by annealing the fibers at 1050 °C.

3.3 Fiber Annealing and Lithium Equilibration

When processing lithium niobate or related compounds, Li ions tend to out-diffuse. Lithium deficiency is not as critical as oxygen difficiency (as long as a phase-transition does not occur). However, material properties such as the Curie temperature strongly depend on the exact lithium concentration. A standard procedure used in the past to avoid lithium out-diffusion during fiber growth or processing was to include water vapor in the oxygen flow (wet oxygen). During the experiments performed in the new alumina oven, two MgO:LiNbO$_3$ fibers acquired a slight yellowish coloration when annealed in wet-oxygen. On the other hand, all the fibers

annealed in dry-O_2 were perfectly transparent. With the purpose of explaining this anomalous behavior, different tests were performed.

From the tests we concluded that the yellowish coloration only appeared during the simultaneous occurence of the following: the sample was doped with MgO, water vapor was present, alumina was present. Therefore, it seemed that a reaction between water vapor, $A\ell_2O_3$ and Mg, probably releasing $A\ell$, was responsible for this behavior. In the past, $LiNbO_3$ bulk samples with $A\ell$ impurities have also exhibited a yellowish coloration.[8]

In view of these results, we decided to perform every fiber processing step in a dry-O_2 instead of a wet-O_2 atmosphere. To prevent excessive Li out-diffusion, a lithium-rich environment was provided. The fiber was placed in platinum foil, suspended above lithium-rich powder (a mixture of Li_3NbO_4 and $LiNbO_3$). During the processing, an equilibrium was established between the sample and the powder via vapor transport. This process is called vapor-phase equilibration (VPE).

4. Nd:MgO:LiNbO$_3$ Fiber Preparation for Fiber Lasers

It has been emphasized in the present and previous contracts that an excellent end-face surface-quality is a requirement for the operation of a crystal fiber laser. Surface defects such as microscopic scratches or small imperfections contribute significantly to the scattering losses and can prevent the attainment of laser oscillation. Previous work on end-face crystal fiber preparation had concentrated on Nd:YAG fibers only. During the present contract a good amount of effort was devoted to investigating procedures that could yield good end-face quality in Nd-doped lithium niobate fibers. As described later, we have achieved excellent end-face quality as required for laser operation.

End-face fiber polishing was done using a commercially available machine fabri-

___

[8] Prof. Byer - private communication.

cated by Buehler. The fiber was rigidly mounted in a fixture and pressed against polishing paper containing either aluminum oxide or silicon carbide. The paper was itself mounted on a rotating metallic disk. Different grit (or grain) size paper was available, namely, 240 and 600 grit, 12, 9, 3, 1 and 0.3 μm grain size. During polishing, water ran almost continuously over the paper to remove the small particles generated by polishing.

Prior to polishing, the fiber was mounted in a rigid structure for easy handling and polishing. As done in the past with Nd:YAG fibers, the Nd:MgO:LiNbO$_3$ fibers were mounted in ID-matched capillary tubes. Wax or U.V. cured epoxy was the bonding material. Three different kinds of wax were utilized, namely, beeswax (yellow color), jewelers wax (red) and high-vacuum wax (black). One of the most important properties of the bonding material is its hardness. If it is too soft or too brittle the fiber is not firmly held during polishing and fiber-edge chipping can result. From the three waxes used, vacuum wax is the most brittle while jewelers wax is the least brittle. In spite of this disadvantage, excellent results could be attained when using vacuum wax because of the precautions taken. The use of vacuum wax or epoxy was necessary since fiber lasers require vacuum deposition of antireflection-coating layers.

The first step in the polishing procedure consisted of rough grinding. Enough glass should be removed from the end face of the capillary tube for the end face of the fiber to be visible. This step was realized with 240 or 600-grit paper. For the subsequent polishing steps, different grain-sizes and times were tried, yielding different end-face qualities. A typical sequence yielding very good results was: 12 μm paper for 10 minutes, 3 μm paper for 30 minutes to an hour and 0.3 μm paper for 10 minutes. The longest step in the sequence determined the final shape of the fiber end face. Variations in the polishing procedure had to be allowed according to the bonding material and the condition of the fiber end face after rough grinding.
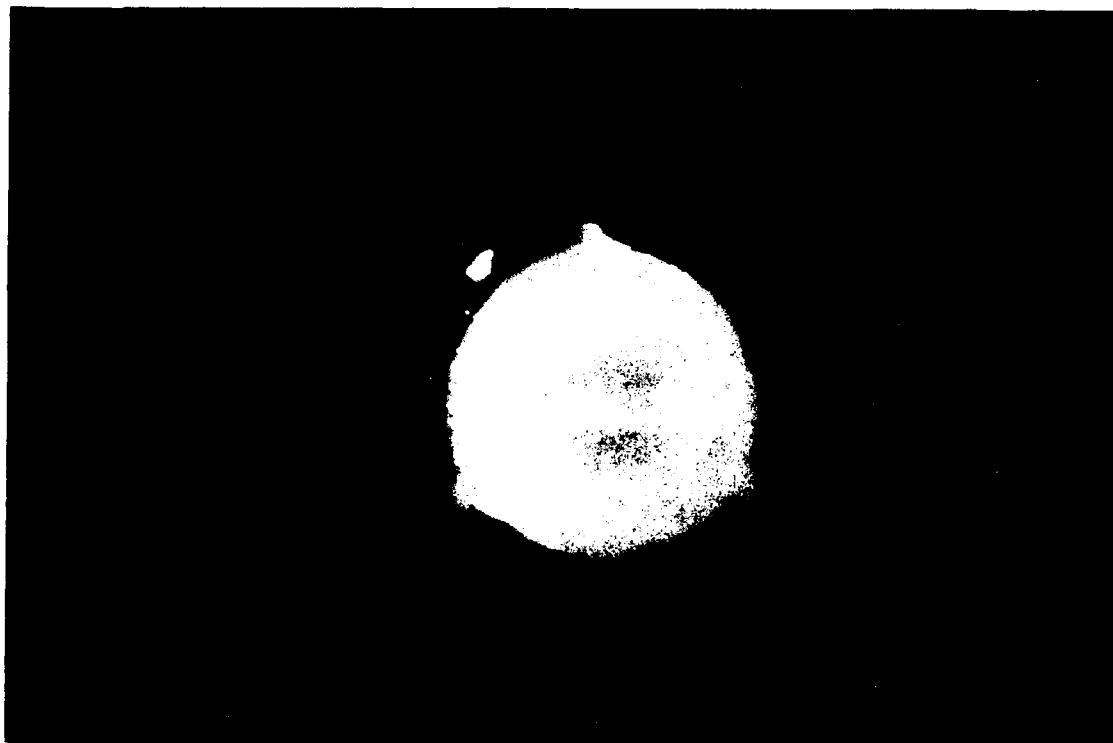
Figure 3.36--Photograph of a C-axis Nd:MgO:LiNbO$_3$ Fiber. Very Good End Face Quality was Achieved. Notice the Three Growth Ridges Indicative of the Trigonal Crystallographic Structure of LiNbO$_3$.

Figure 3.36 shows the photograph of a c-axis Nd:MgO:LiNbO$_3$ fiber end face polished following the above guidelines. The bonding material is vacuum wax. The three ridges indicative of the trigonal symmetry of LiNbO$_3$ are clearly seen in this photograph.

Figure 3.37 shows a photograph of an a-axis MgO:LiNbO$_3$ fiber prepared in a similar way as the c-axis fiber but mounted with jewelers red wax. The cross section of every a-axis fiber is elliptical rather than circular, exhibiting two ridges instead of three. All of these features are clearly seen in Figure 3.37. The minor dimension of the ellipse corresponds to the c-axis whereas the major dimension corresponds to the b-axis.

5. Nd:MgO:LiNbO$_3$ Fiber Lasers

5.1 Experiment

Four Nd:MgO:LiNbO$_3$ c-axis fibers were mounted and polished with the purpose of making CW laser tests pursuant to future Q-switched tests. The fibers had lengths ranging from 0.5 to 1.0 cm and diameters of $\sim$ 170 μm. All fibers were antireflection coated at 1.09 μm with 1875Å of SiO$_2$. The fibers were placed in a laser cavity with mirror gimbal mounts. The resonator consisted of two flat mirrors, a high reflector and a 1.0^c_c transmissive output coupler. The mirrors were placed very close to the fiber ends.

The pump was provided by a Rh6G dye laser operating at 598 nm. The focusing lens had f = 10 cm.

The transmitted pump beam was multimoded in all the four fibers. However, scattering of the pump beam through the fibers was not unusually high. No laser action could be observed in any of the fibers with incident pump powers in excess of 200 mW. We recall that under the same experimental conditions, a 170 μm Nd:YAG fiber laser exhibits typically an incident pump power threshold of a few tens of mW.
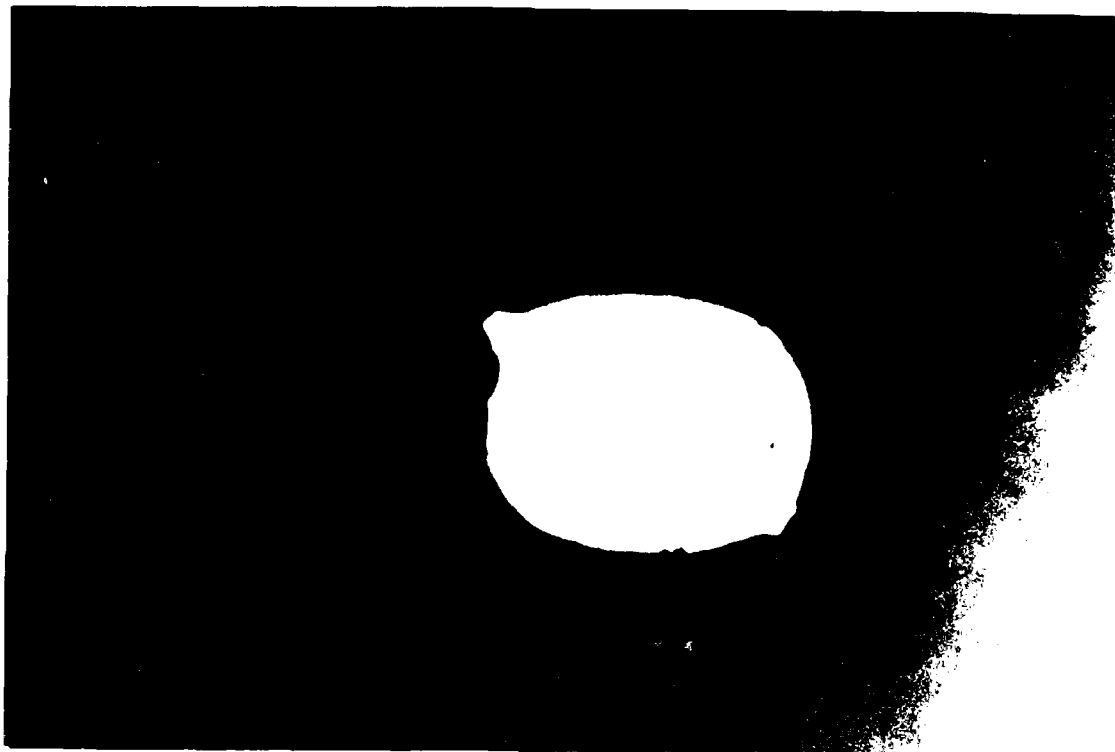
Figure 3.37--Photograph of a A-axis MgO:LiNbO$_3$
Fiber. Notice the Elliptical Shape
and the Two Growth Ridges.

5.2 Interpretation

Nd:MgO:LiNbO$_3$ c-axis samples (low gain polarization) exhibit, as discussed in Section A.8, three times less gain than Nd:YAG. Therefore, the threshold to reach laser oscillation should be at least three times higher. In addition, LiNbO$_3$ has a refractive index of 2.2 versus 1.8 of YAG. As a consequence, the larger refractive index step Δn at the fiber edge makes LiNbO$_3$ more subject to surface scattering loss. Assuming a refractive index of 1.5 for the bonding material (wax or epoxy) we see that $\Delta n = 0.7$ for LiNbO$_3$ whereas $\Delta n = 0.3$ for YAG. A quantitative analysis of surface scattering loss in Nd:MgO:LiNbO$_3$ fibers and its dependence on Δn is presented in the next subsection.

5.3 Surface Scattering Loss

It has been pointed out throughout this contract and previous ones that the main loss mechanism in crystal fiber lasers is surface scattering loss due to surface imperfections such as fiber diameter variations. It is possible to calculate the power, originally in the fiber fundamental mode, that is scattered into higher order modes via surface (or bulk) refractive index-inhomogeneities, by using coupled mode theory.[9]

When applying coupled local-mode theory to crystal fiber lasers, it can be shown that the loss coefficient for the fundamental mode depends strongly on the cladding-core refractive index difference. The loss coefficient is given by [10]

$$\alpha = K\left[h(\Delta)\right]^2 n_{co}\Delta^{3/2} \tag{3.47}$$

---

[9] A. W. Synder and J. D. Love, Optical Waveguide Theory, Chapters 27, 28, 31, 33, Chapman and Hall (1983).

[10] Martin Fejer, Ph.D. Thesis, Chapter 2, Stanford University (1986).

where

$$\Delta = \frac{n_{co}^2 - n_{c\ell}^2}{2n_{co}^2} \quad , \tag{3.48}$$

$$h(\Delta) = \left[(1 + 4\Delta)\left(1 + \left(\frac{n_{co}}{n_{c\ell}}\right)^2\right) + 2\Delta \right]/2 \quad , \tag{3.49}$$

$n_{co}, n_{c\ell}$ = refractive indices of the core and the cladding respectively, and K = proportionality constant. K depends on the fiber diameter, the wavelength of light and the properties of the diameter-variation distribution (assumed random). For the purpose of comparing Nd:YAG and Nd:MgO:LiNbO$_3$ fibers having the same diameter and surface quality, K can be considered a constant.

5.4 Estimation of the Laser Threshold

Let $n_{c\ell} = 1.5$ (epoxy or wax), $n_{co} = n_{LN} = 2.2$ for lithium niobate fibers and $n_{co} = n_Y = 1.8$ for YAG fibers. Thus, Equations (3.47), (3.48), and (3.49) yield

$$\Delta_{LN} = 0.27, h(\Delta_{LN}) = 3.55, \alpha_{LN} = 3.9K \tag{3.50}$$

for Nd:MgO:LiNbO$_3$ and

$$\Delta_Y = 0.153, h(\Delta_Y) = 2.2, \alpha_Y = 0.52K \tag{3.51}$$

for Nd:YAG. Therefore, a Nd:MgO:LiNbO$_3$ fiber exhibits 7.5 times more scattering loss than a Nd:YAG fiber having the same surface quality, due to the larger core-cladding refractive index difference.

The threshold for laser action is proportional to the fiber loss. Also, the gain of c-axis Nd:MgO:LiNbO$_3$ fibers is three times less than the gain of Nd:YAG fibers. Therefore, the threshold for the former must be $3 \times 7.5 = 22.5$ times higher.

Typical absorbed pump power thresholds for Nd:YAG fibers are $\sim$ 10 mW. Therefore, the expected absorbed pump power threshold for a c-axis Nd:MgO:LiNbO$_3$ fiber is 225 mW.

It is clear from Equations (3.47), (3.48), and (3.49) that reducing the core-cladding refractive index difference Δn can significantly reduce the scattering loss. For example, for Δn = 0.01 (instead of the present value of 0.7 for lithium niobate fibers) we calculate

$$\Delta = 4.5 \times 10^{-3}, h(\Delta) = 1.03, \alpha = 7 \times 10^{-4} K \qquad (3.52)$$

Comparing (3.50) and (3.52) we see that a reduction of three orders of magnitude in the scattering loss can be achieved by providing the Nd:MgO:LiNbO$_3$ fiber with a cladding with refractive index close to that of the core.

H. Electrode Fabrication and Electro-optic Effect in MgO:LiNbO$_3$ and Nd:MgO:LiNbO$_3$ Fibers

1. Introduction

MgO:LiNbO$_3$ single-crystal fibers are of great interest because of their potential as in-line fiber optic devices that take advantage of the excellent electro-optic (or acousto-optic) properties of this material. We can mention phase and amplitude modulators among many other possible devices. Nd:MgO:LiNbO$_3$ single crystal fibers offer the potential of highly-efficient Q-switched lasers with a greatly reduced voltage requirement.

The afore-mentioned devices require the efficient application of an electric field across the transverse dimension of the fiber. Because of the large dielectric constant of LiNbO$_3$ the electrodes must be deposited directly on the curved surface of the fiber. We started the study on electro-optic effect in LiNbO$_3$ fibers by considering the problem of electrode deposition.

Direct deposition of electrodes on a crystal fiber is complicated by the small diameter and the curved surface of the fiber. A simple method to deposit gold electrodes consists of the following. The fiber is mounted on a metallic holder and placed inside the evaporation chamber. After this first deposition, the fiber-holder is rotated by 180 degrees about an axis perpendicular to its surface. Now, the portion of fiber directly opposite to the first electrode is exposed to the gold atoms and the second electrode is deposited. During the two evaporations some gold is also deposited between the electrodes. However, it forms a layer much thinner than the ones in the portions directly exposed. This excess metal can be removed by using special gold solvents. This method is particularly attractive because of its simplicity. However, it does not allow a precise control of the transverse dimension of the electrodes.

A second method consists of fabricating a mask containing a slot or V-groove with the desired electrode dimensions. These dimensions are about 1 cm in length and 50-100 μm in width. Very precise control of V-groove dimensions can be achieved in silicon wafers by using preferential etching. Chemical agents such as KOH can etch (100) crystalographic planes 400 times faster than (111) planes. KOH-etching of a silicon wafer with <100> surface orientation results in the formation of V-grooves where the sides of the V are (111) planes. The angle between the V-side and the surface is 54.74°. For our application as a crystal-fiber mask, the silicon wafer must have V-grooves that pass through the wafer. During electrode deposition the smaller base of the trapezoidal V-groove is placed in contact with the fiber surface whereas the larger base of the trapezoid is exposed to the gold atoms. If two masking-wafers are made, the fiber can be clamped between the two wafers. This method offers a very precise control of the electrode dimensions.

We have called the first of these methods EEEM (*evaporation followed by etching of excess metal.*) The second method is referred to as ESM (*evaporation*

using a silicon mask). As we shall see, the EEEM method, in spite of its simplicity, yielded very good results when applying it to lithium niobate single crystal fibers.

This section treats the description and the actual application of the EEEM method. This technique, developed in our laboratories, allowed the first successful fabrication of electrodes on a single crystal fiber. Second, this section deals with the measurement of the electro-optic effect on these fibers.

2. Electrode Fabrication on Single Crystal Fibers

2.1 Fiber Holders

To support the crystal fiber during metal evaporation we initially used a stainless steel holder. One end of the fiber was firmly grasped by a clip attached to the holder whereas the other fiber end was free. Due to the slight curvature of the holder surface the fiber was not in direct contact with the holder except at the position of the clip. The way in which the fiber was mounted allowed the deposition of the electrodes on diametrically opposite portions of the fiber without the need for removing and reinstalling the fiber in the holder. However, this holder did not allow orienting the fiber around its axis.

Preliminary results indicated that before the gold deposition, the fiber should be oriented in the holder to avoid accumulation of gold on undesired regions of the fiber surface. One situation that we wanted to avoid was the formation of three electrodes instead of two which resulted from the symmetric deposition of metal around each one of the three longitudinal ridges of the c-axis fiber. Thus, a new metallic holder was made to support the fiber during gold evaporation. It consisted of two pieces of aluminum, one of which contained V-grooves where one or two fibers could sit. The procedure for mounting and orienting the fiber prior to gold deposition was as follows. The tip of the fiber was inserted into a capillary tube and cemented with alumina bond. The capillary was then placed on one of the holder

V-grooves, with the fiber protruding from the aluminum holder. The capillary was rotated by hand under microscope observation of the fiber surface, until one of the longitudinal ridges was centered on the microscope image. As we shall see below, this orientation procedure yielded, after etching, one electrode centered about the top ridge and the other electrode filling the region between the two bottom ridges. Finally, the capillary tube was firmly secured by screwing the second aluminum piece on top of the first piece.

2.2 Metal Evaporation

Gold deposition was the next step in the fiber electrode fabrication. The fiber and fiber holder were placed inside a vacuum evaporation chamber where an electron beam heated a metallic target. After a first deposition, the holder was rotated 180° without moving the fiber. A second deposition followed. Typically, the thicknesses of the deposited layers were $\sim$ 100 Å of chrome and 2 μm of gold. The chrome layer served to enhance the adhesion of gold.

Due to the finite divergence of the evaporating beam, some metal was also deposited on the portions of fiber located between the electrodes. However, these inter-electrode layers were thinner than the electrodes themselves and could be removed by using chemical etchants, as described below.

2.3 Etching of Excess Metal

The gold etchant consisted of a solution of potassium iodide and iodine in water (100 g KI, 100 g I_2 and 200 ml H_2O). The chromium etchant was composed of cerium sulfate, nitric acid and water (27 g H_4 Ce $(SO_4)_4$, 100 ml HNO_3, 400 ml H_2O).

The EEEM method depends upon a complete removal of the inter-electrode or 'excess' metal while simultaneously avoiding an excessive etching of the electrodes themselves. As we will see below, the metal-removal time is a critical parameter for the accomplishment of this objective. During the initial tests, the gold etchant was

further diluted in water in proportions of 1 to 5. It was found that the removal time was only a few seconds ($\sim$ 5 sec). Thus, stringent tolerances in immersion time resulted.

In a later utilization of the EEEM method the gold etchant was diluted in water by a ratio 1/20 instead of 1/5 as was done before. The etching time for one fiber was 25 seconds in the diluted gold etchant, followed by 20 seconds in the chrome etchant. A second fiber was immersed in the gold etchant more than once to remove a thin metallic strip at the center of one of the inter-electrode zones. For this second fiber the total gold etching time was 40 seconds. After each etching, the fiber was immersed in deionized water to remove the excess etchant. The immersion time in the chrome etchant was not very critical since the chrome underneath the gold electrodes was protected by the gold itself.

2.4 Results

One MgO:LiNbO$_3$ fiber and two Nd:MgO:LiNbO$_3$ fibers were successfully electroded by using the EEEM technique. Some problems were encountered at the beginning with three fibers. As discussed previously, these problems were solved by allowing rotation-orientation of the fiber in its holder before evaporation and by diluting the gold etchant. The following description refers to the results achieved with the two Nd:MgO:LiNbO$_3$ fibers.

The quality of the resulting interelectrode zone can be seen in Figure 3.38. This is a microscope photograph of the fiber surface showing the electrodes on the top and the bottom of the figure. The electrode edge is quite smooth and only a few specks of gold remain in the inter-electrode zone. Both features are illustrated in Figure 3.38. The inter-electrode zones for this fiber have widths of 30 μm and 50μm respectively. For the second fiber the inter-electrode spacings were $\sim$ 35 and $\sim$ 60 μm respectively.
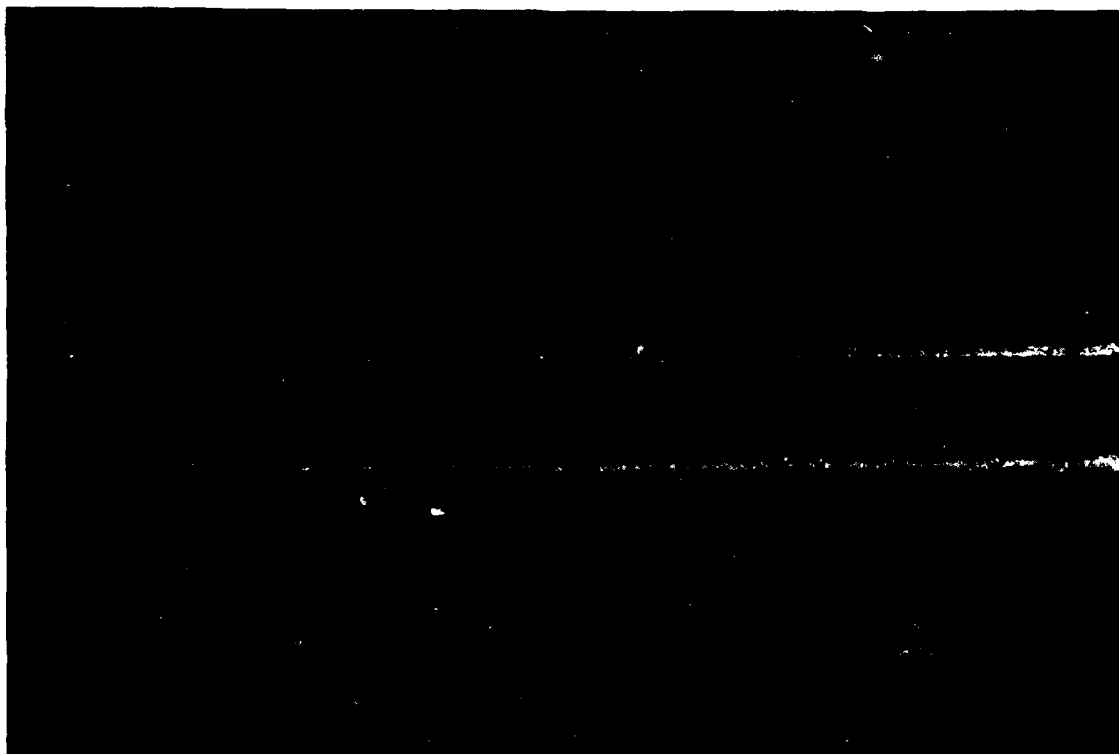
Photograph of a Fiber's Side
win the Gold Electrodes (Top
the Figure). The Electrode
m.

Figure 3.39--Polished End Face of a Nd:MgO:LiNbO$_3$ Fiber Showing the Gold Electrodes.

Figure 3.39 depicts the end face of one of these fibers after polishing. The microscope photograph shows the inner wall of the capillary tube, the red wax used as bonding material and the c-axis fiber with the three characteristic ridges. The gold electrodes are also readily apparent. One electrode is located symmetrically about the left-top ridge in the figure. The other electrode lies betwen the other two ridges, almost filling the space between them. The electrode location is a consequence of the orientation procedure previously described.

2.5 Fiber Mounting and Wire Bonding

The fiber had to be mounted in a fixture that allowed fiber end-face polishing as well as easy access to the electrodes. With these objectives in mind, we prepared capillary tubes with slots on the side surface. Two slots, approximately 1 mm wide, were cut on each capillary tube with the aid of a diamond saw. The slots were diametrically opposite to each other and located at different positions along the tube. They were just deep enough to reach the inner hole of the capillary tube.

The mounting procedure was as follows. The electroded fiber was inserted into the capillary tube and oriented such as to expose each electrode to one of the slots. The bonding material selected was wax, since epoxy would introduce undesired stress due to shrinking while drying. The capillary tube and the fiber were heated on a hot plate up to the melting point of the wax. At that moment, wax was allowed to flow into the tube by capillary action. To prevent the wax from reaching the slots, thus covering the exposed portions of the electrodes, the capillary tube was rapidly cooled by removing it from the hot plate. The following step was end-face fiber polishing.

The final step was wire-bonding. A small diameter wire was introduced into the slot and gently placed on top of the exposed electrode. Electrical contact between the electrode and the wire was made by melting a very small piece of indium-metal

on top of them with the aid of a blow dryer. The cohesion of molten indium prevented it from migrating around the fiber, thus there was not a risk of short-circuiting the electrodes.

3. Study of the Electro-Optic Effect in Nd:MgO:LiNbO$_3$ Fibers

3.1 Experiment

The experimental set-up to measure the electro-optic effect in a Nd:MgO:LiNbO$_3$ fiber consisted of the following elements. A HeNe laser at 632.8 nm, a quarter wave plate followed by a polarizer to rotate the plane of polarization of the linearly polarized beam to any desired position, a focusing lens, the fiber, an analyzer, and a detector. The output power from the HeNe laser was very small ($\approx 100\,\mu$W) to avoid the generation of a screening field.

Different lenses and microscope objectives were used to attempt to launch only the fiber fundamental mode. The best results were obtained with a $f = 6.9$ cm lens. However, the output from the fiber was still multimoded.

The extinction ratio was determined from the ratio of power transmitted between crossed polarizers to power transmitted between axes-aligned polarizers. Special attention was taken to locate the birefringence-axes of a possible stress-induced birefringence to maximize the extinction ratio. However, the largest extinction was 7 dB (a factor of 5). The reason for this low value can be fiber mode-coupling as further discussed below.

A sinusoidal voltage signal at 30 kHz ($\sim$ 25 volts peak to peak) was applied to the fiber. To maximize the device response, we set the polarizers at 45° to each other. The measured device response was too low to be distinguished from the detected noise.

With the aid of a lock-in amplifier we were able to measure a sinusoidal signal at 30 kHz contained in the detected light. Its peak-to-peak amplitude V_{pp} was 20

μV. On the other hand, full modulation corresponded to a signal of $V_{pp} = 11$ mV. Thus, the modulation depth in our experiment was $20\ \mu V/11$ mV $\sim 0.2\%$.

3.2 Interpretation

The half-wave voltage of this device can be determined from

$$V_{1/2} = \frac{\lambda}{2n_0^3 r_{22}}\frac{d}{\ell} \tag{3.53}$$

where $\lambda = 0.6328\mu$m; $n_0 = 2.2$; $r_{22} =$ relevant electro-optic coefficient $= 6 \times 10^{-12}\ m/V$; d $=$ electrode separation $\approx 170\ \mu$m; $\ell =$ fiber length $= 9.25$ mm. Thus, $V_{1/2} = 91\ V$. Therefore, the expected modulation depth was $25/91 = 27\%$, whereas the observed modulation was two orders of magnitude lower.

We believe that the low modulation depth observed is due to the multimode character of the fiber radiation. By using a ray picture we can see that different modes experience different path lengths when passing through the fiber. Thus, the associated phase shift difference between eigenpolarizations is mode-dependent. Since the distribution of phase shift differences is most likely to be random, the net modulation depth of the light beam is greatly diminished.

To have an efficient fiber modulator we should launch a single mode in a multimode LiNbO$_3$ fiber and avoid mode coupling inside the fiber. In Section III.F.5 we presented theoretical calculations indicating that mode coupling is reduced by orders of magnitude when the crystal fiber is cladded. Therefore it is clear that the use of clad fibers would be greatly beneficial for both fiber modulators and fiber lasers.

166

IV. SUPERFLUORESCENT EMISSION IN Nd³⁺:YAG SINGLE CRYSTAL FIBERS

A. Introduction

This section reports investigations of the possibility of generating a superfluorescent signal along the length of a single-crystal Nd:YAG fiber. Although superfluorescence in laser materials has been known for quite some time, its experimental observation in (active) optical waveguides has been very rarely reported, mainly because of the lack of such waveguides until relatively recently. Superfluorescence is generated by subjecting the laser material to a very high excitation, or pump intensity, thereby creating a medium in which the probability of stimulated emission exceeds by far that of spontaneous emission. This situation usually arises only along one spatial direciton, usually the laser medium longest dimension, which coincides with the direction of highest (unsaturated) optical gain. Under such conditions a strong stimulated signal (superfluorescent signal) is generated along this direction, which can extract most of the stored energy from the active medium. This signal has a broadband spectrum, while being intense, which makes it appealing for some single mode fiber sensor applications, in particular fiber gyroscopes.

In the previous phase of this contract we confirmed the potential of Nd:YAG fibers as superfluorescence sources by developing a theoretical model of this type of interaction in optical fibers. The following investigations were aimed at the experimental demonstration of superfluorescence in these fibers. We proposed to induce and identify superfluorescence by launching a pump beam into the Nd:YAG fiber and observing the fluorescence signal at the fiber output. The objective of this work was to characterize the fluorescent emission of Nd:YAG near 1.064 μm and to attempt observing the onset of superfluorescence in small diameter fibers. For this

purpose we were also concerned with the miniature pedestal growth of crystal fibers with sub-50 μm diameters, required to provide a high energy confinement and an enhanced emission.

In Section IV.B the process of fiber fabrication is described including growth, cladding and polishing. In Section IV.C some of the most relevant theoretical aspects of superfluorescence in lasers are presented. Section IV.D describes the experiments in Nd:YAG fibers and rod, followed by Section IV.E which summarizes test results and their analysis.

B. Fiber Device Fabrication

1. Fiber Growth

The Nd:YAG fibers used in this work were grown by the laser heated miniature pedestal growth technique. Some of these fibers were grown earlier in this program for fiber laser studies. They exhibit diameters of 100 - 120 μm and rms diameter variations on the order of 5 to 10 %. The remaining fibers were grown in the period covered by this report specifically for superfluorescence studies. For these the starting material was a Nd:YAG rod (with a 1% Nd:$^{3+}$ doping) cut from a bulk crystal then ground to a 400 μ diameter rod on a centerless grinder. The diameters of the new generation fibers are more uniform than those of earlier fibers, with typically less than 3.0% rms variations along a one inch length. Some of the more recent fibers were grown under diameter control conditions and exhibited improved diameter stability.

As shown in a previous theoretical analysis, the excitation power required to reach the onset of superfluorescence in a fiber made of a laser material can be reduced by reducing the diameter of the fiber. A great deal of effort was therefore spent on the growth of sub-50 μm diameter fibers, which required detailed understanding of issues concerning fiber diameter stability during growth. As

- 168 -

Table 4.1

Summary of the Characteristics of Nd:YAG Fibers

Fiber	Length (mm)	Diameter (μm)	Variation (%)
Y-104	10	135	0.75
Y-106	13	135	0.48
Y-108	7	135	0.65
Y-112	5	45	not recorded
Y-116	8	45	not recorded

described earlier, the use of the second generation growth station for this purpose greatly facilitated this task. A total of 32 Nd:YAG fibers were available for this study. Seven Nd:YAG fibers were grown under diameter control conditions. The diameter characteristics of some of these fibers are described in Table 4.1.. The implementation of the diameter controller reduced their diameter fluctuations to less than 0.75% along a greater than 10 millimeter length. Figure 4.1 shows the diameter variations of fiber Y-106 as a function of position along the fiber length, as measured during growth. To reduce surface scattering loss, some of these fibers were clad with LaSF30 glass, as described earlier. It should be noted that some of the clad fibers used in superfluorescence measurements were originally prepared for cladding studies under other auspices.

2. Fiber Polishing

For the purpose of fiber end face preparation individual fibers were inserted into a close-fitting glass capillary tube with adhesive and mechanically polished, as described earlier. For the purpose of superfluorescent investigations, the degree of perpendicularity between the fiber ends and the fiber axis is not a critical parameter, and polishing operations were considerably simplified. The fiber ends were ground and polished with a small commercial fiber end polisher (Buehler Fiberment Optical
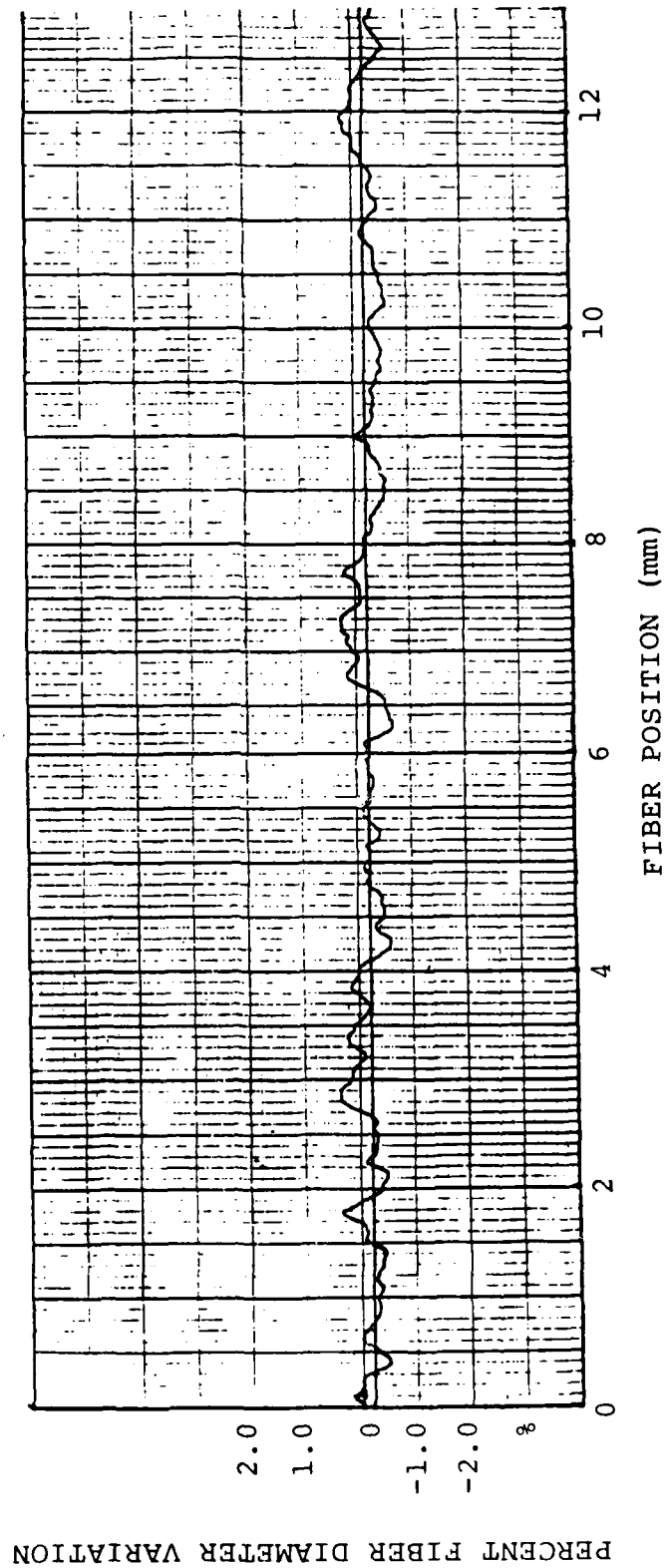
Figure 4.1--Y-106 Fiber Diameter Variations as a Function of Length.

FIBER POSITION (mm)

PERCENT FIBER DIAMETER VARIATION

Fiber Polisher), which drastically reduced processing time compared to the standard polishing procedure. With this unit, grinding with a 400 grit paper for 15-30 seconds, followed by polishing on 3μ and 0.3μ grit for two minutes each, gave satisfactory end faces. During these operations the capillary tube was polished directly against the lap, without the need for additional support as its outside diameter ($\sim$ 4-6 mm) was large enough to withstand lateral stress. The fiber end was inspected under an optical microscope after each step to detect any serious chipping of the fiber edges, in which case the process was started from the beginning, after adding more epoxy if necessary.

C. Physical Principle of Superfluorescence in Nd:YAG Fibers

As background information on the physical principle of fluorescence and superfluorescence in a laser system, we show in Figure 4.2 the energy level diagram of Nd:YAG, a four-level laser system. When neodymium-ions are excited by an energy source (the pump), ground state electrons ($^4I_{9/2}$) undergo a transition to the pump band, and then quickly relax via phonon interaction to the upper laser level ($^4F_{3/2}$). As they relax to the $^4I_{11/2}$, $^4I_{9/2}$ and $^4I_{13/2}$ levels, spontaneous emission occurs near the fluorescence wavelengths of 1064 nm, 946 nm and 1319 nm, respectively.

Superfluorescence emission, also often referred to as amplified spontaneous emission, is different from both spontaneous fluorescence emission and resonant laser emission. It is produced by an assembly of atoms (or ions and molecules) which are coupled together via their common radiation field and decay cooperatively. For this coupling to occur, the applied excitation (or pump) field must be very high. In terms of stimulated emission, under a high excitation field the density of photons generated by spontaneous emission is sufficiently large to induce a high probability of stimulated emission, which then becomes the dominant emission mechanism.
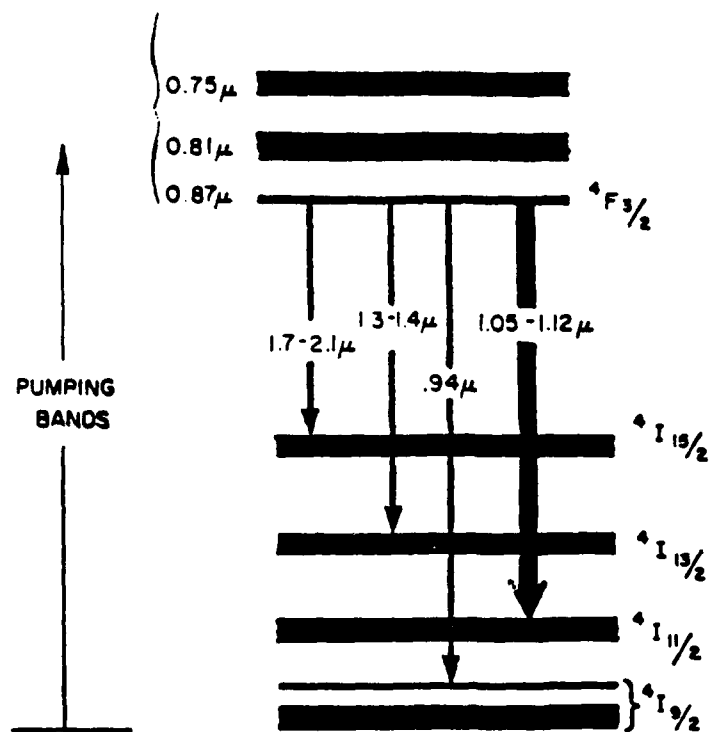
Figure 4.2--A Simplified Energy Level
Diagram of Nd:YAG.

In a standard, resonant laser cavity this situation is reached by increasing the signal photon density by placing the optical gain medium in an optical resonator, thereby relaxing the pump field (or threshold) requirement. A superfluorescent laser operates without an optical resonator. The threshold requirement is therefore considerably higher, and the emitted signal bandwidth larger, than that of a conventional laser. The implementation of an optical fiber as the gain medium, however, is expected to contribute to a drastic reduction of the threshold pump power (but no reduction of the bandwidth) as a result of the high energy confinement achievable in a fiber over sizeable distances.

A theoretical analysis of superfluorescence in active fiber devices for fiber system applications was recently developed under this contract. This analysis presented a model for the optical gain and the level of ASE in optically end pumped active fibers. An accurate description of the situation occuring in a crystal fiber was obtained by taking into account the mode structure of the interacting pump and signal fields, and the degree of spatial overlap between them. This model predicts a linear growth of the signal at low pump intensity, followed by a sharp, nonlinear increase at higher pump (threshold), above which the growth is again quasi-linear, as illustrated in Figure 4.3. Simple closed-form expressions for the threshold, energy conversion efficiency (ratio of signal output power to pump power absorbed by the fiber) and bandwidth of both single mode and multimode superfluorescent fiber lasers were derived. In Nd:YAG devices end pumped near 810 nm, thresholds of a few mW and conversion efficiencies possibly as high as 38% per output face were predicted in low loss, near single mode fibers. The threshold was found to be minimum in fibers with a V number of 1.7, while the slope efficiency was maximum when $V > 4$. An interesting finding was that this type of device is only slightly affected by even moderately high fiber propagation losses.

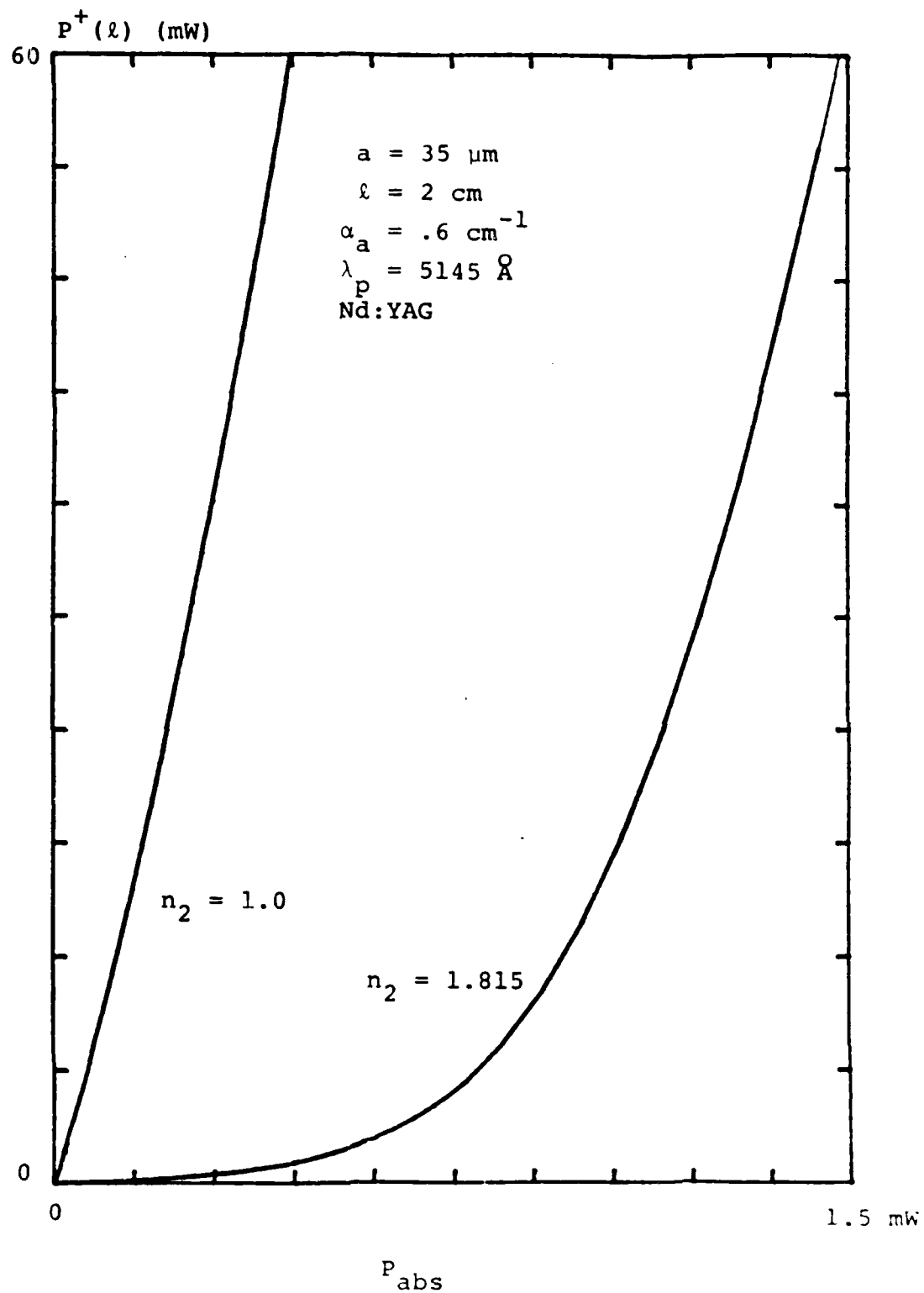For a Nd:YAG fiber end-pumped near 580 nm (as produced in our experimental

Figure 4.3--Computer Results of Output Power
versus Absorbed Pump Power.

investigations by a an ar-ion laser pumped Rh6G dye laser) with a core diameter of 40 μm, a step index difference of 0.005, and a negligible loss, the threshold is as low as 200 mW. This value drops as the square of the fiber core dimension, so that in 20 μm diameter fibers it is reduced to only about 50 mW. Although high relative to resonant laser thresholds, such values can easily be achieved with conventional CW dye lasers.

In the limit of large pumping rates, i.e. several times above threshold, it was shown that the output power of a superfluorescent fiber laser may be approximated by:

$$P_{out} = \frac{1}{2} \frac{h\nu_s}{h\nu_p} P_{abs} \eta \qquad (11)$$

where $h\nu_s$ and $h\nu_p$ are the signal and pump photon energy respectively, P_{abs} is the pump power absorbed by the fiber, and η is a dimensionless parameter nearly equal to unity in the case of a uniform ...

Figure 4.4--Schematic of Experimental Arrangement.

measured at the laser output port with a first calibrated EG&G power meter. The laser beam was focused with a single spherical lens into the crystal fiber sample, held in place with an xyz positioner. To reduce potential thermal damage to the fiber and surrounding epoxy, and to check the dynamic behavior of the fluorescence signal, the pump laser beam was amplitude modulated with a mechanical chopper into approximately 1 msec long square pulses at a 1%-2% duty cycle. A 20X microscope objective was positioned at the output end of the fiber to collect the fluorescence emission. Two color filters were placed after the objective to separate the fluorescence emission from the residual pump signal unabsorbed by the fiber. The transmission of the combined filters was measured with a spectrophotometer to be $T = 73\%$ for wavelengths between 850 nm and 1100 nm. The filtered signal was detected with an EG&G power meter.

2. Experimental Procedure

The fluorescence signal, viewed on an oscilloscope, exhibited the typical temporal behavior of fluorescence emission from a laser medium pumped by a square pulse. This behavior is illustrated with a theoretical curve in Figure 4.5. The time constant of the exponentially decaying experimental curves was about $\tau_f = 230 - 250 \, \mu sec$, in good agreement with the well-known fluorescence lifetime of Nd:YAG.

Quasi-CW pumping is achieved when the top portion of the fluorescence signal trace reaches its asymptotic value before the end of the pump pulse. In practice the pump pulse duration t_p was chosen to be a few times τ_f, which explains the selection of $t_p \simeq 1 \, msec$ in our measurements.

To maximize the interaction between the pump and the fluorescence signal in the fiber, care had to be taken to launch low order pump fiber modes, ideally only the fundamental mode LP_{01}. In practice, this required careful selection of the focal length of the focusing lens, and a fine adjustment of the fiber angular alignment
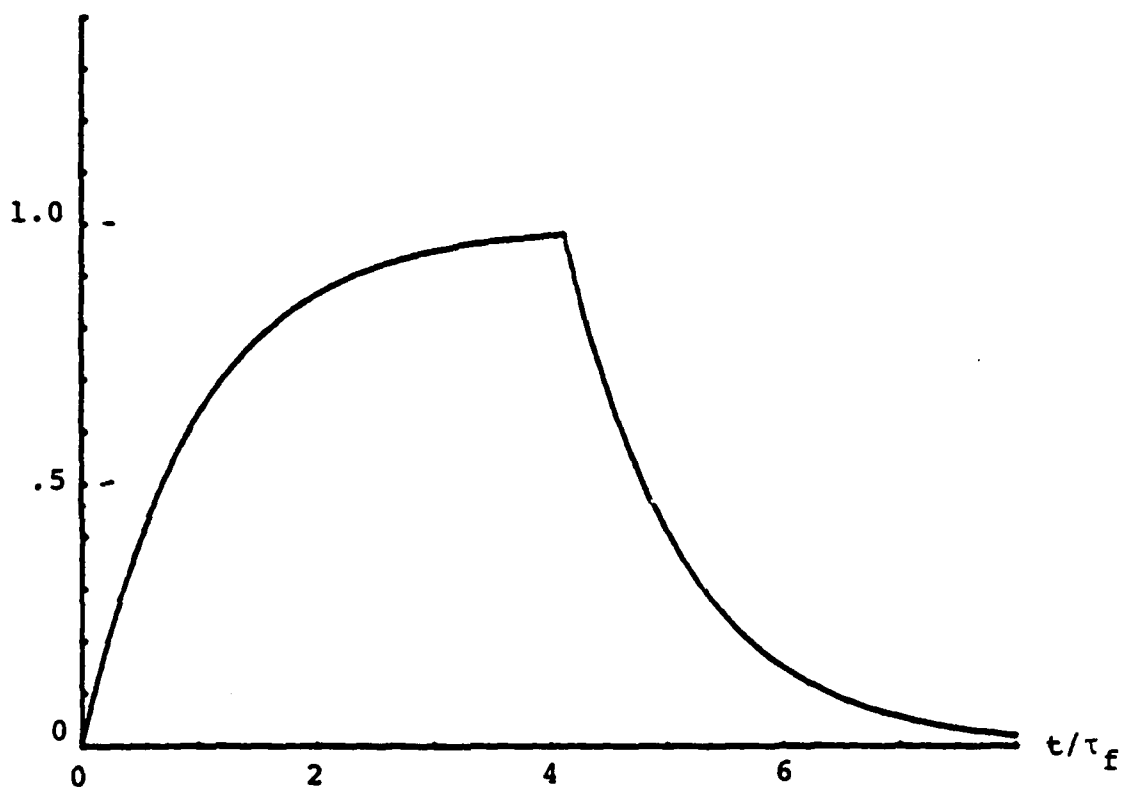
Figure 4.5--Theoretical Fluorescence Output
versus Time Pumped with a Square
Pulse of Duration 950 μsec (τ_f =
μsec).

- 178 -

FIBER

TWO DIMENSION
TILT STAGE

X-Y-Z POSITIONER
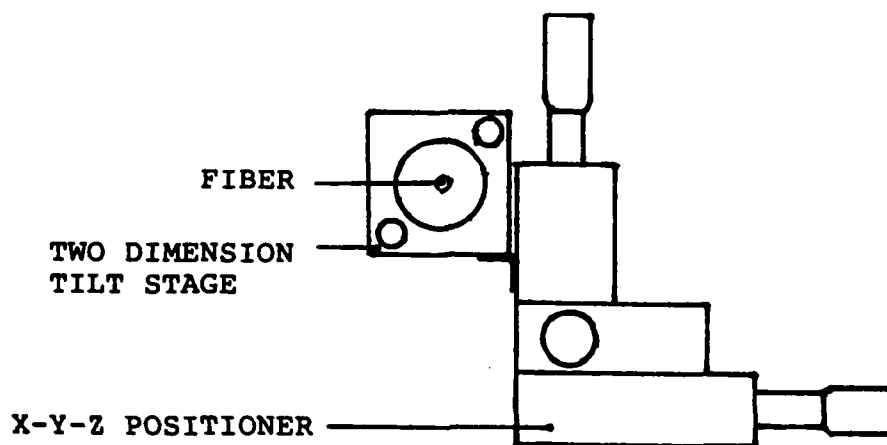
Figure 4.6--Schematic of Holding Fiber.

with respect to the incident pump beam, using the arrangement of Figure 4.6. The fibers that were tested possessed sufficiently good waveguiding properties to make possible the launching of most of the pump power into the LP_{01} mode after these conditions were satisfied. These steps were found to be essential to optimize the amount of fluorescence power emitted at the fiber output.

During our investigations the primary quantity of interest was the dependence of the fluorescence power emitted by the fiber (via ASE) on the absorbed pump power. As mentioned earlier, theory predicts a linear growth at low pump intensity levels, a nonlinear growth around superfluorescence threshold and a quasi-linear growth as the pump power is increased well above threshold (see Figure 4.3). The measurement of this dependence was therefore the main focus of this study as a means of identifying the onset of superfluorescence. Prior to performing these measurements, a number of calibrations were needed, which are described in the next section.

3. Calibrations

3.1 Spectrum

The signal emitted by the fiber end contains all the fluorescence lines of Nd:YAG, which are centered near 0.91 μm, 1.064 μm, 1.32 μm and 1.85 μm. The power meter, having a silicon detector head, only responds to the first two lines (which are also both passed by the color filters). The signal read from the oscilloscope therefore included two lines, which needed to be separated in order to select only the 1.064 μm line of interest.

To this end the near infrared fluorescence spectrum of Nd:YAG was recorded. From it the relative contribution of each line to the detected signal was evaluated. The measurement arrangement is shown in Figure 4.7. The output of a Nd:YAG fiber excited near 600 nm was analyzed by a monochrometer equipped with a
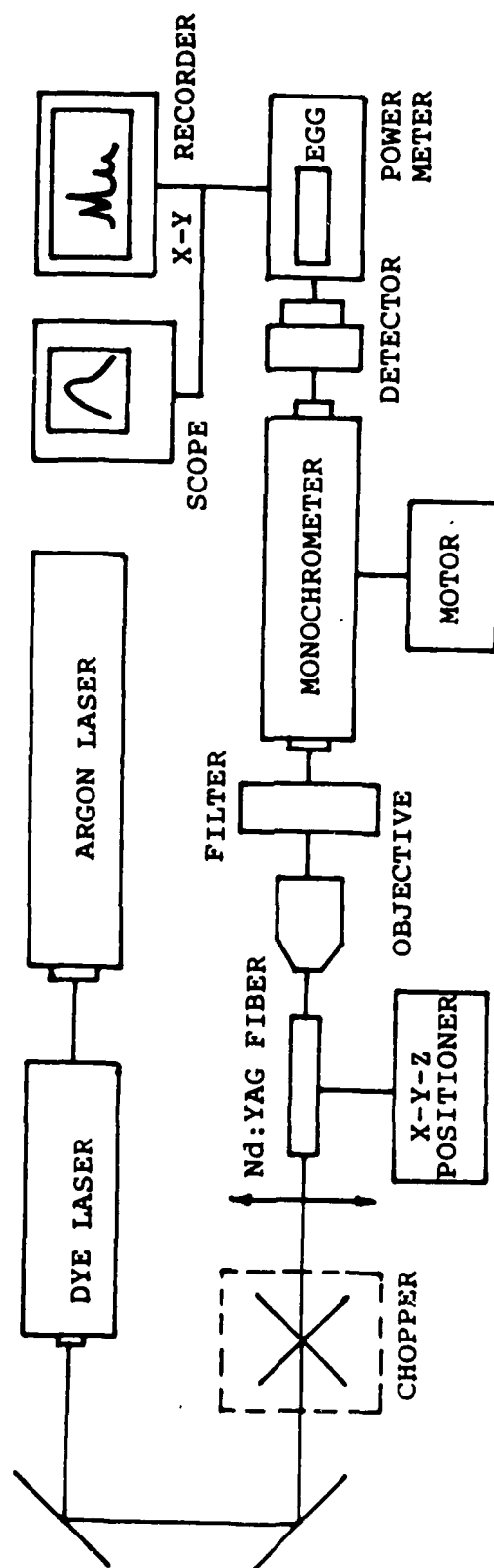
Figure 4.7--Schematic of Measurement Arrangement of Fluorescence Spectrum.

motorized wavelength scanner. The fluorescence emission was measured between 860 nm and 1090 nm with a resolution of 2 nm, using the same calibrated EG&G detector that was used to measure the total fluorescence power emitted by a fiber. The spectrum is shown in Figure 4.8.

Let $P_{1.06}$ and $P_{0.91}$ be the actual power carried by the fluorescence emission in the 1.06 μm and 0.91 μm line, respectively. When measuring the total output power of a fiber, the EG&G detector at the 1.06 μm calibration setting provides a signal

$$P_f = P_{1.06} + \frac{S_{0.91}}{S_{1.06}} P_{0.91} \qquad (4.2)$$

where $S_{1.06}$ and $S_{0.91}$ are the relative sensitivities of the detector at 1.06 μm and 0.91 μm, respectively. When recording the fluorescence spectrum (Figure 4.8), the (same) detector provides a signal $V(\lambda) = S_\lambda P_\lambda$ over a range of wavelengths λ. Assuming S_λ is constant over each line of interest (while $S_{1.06} \neq S_{0.91}$), the power carried by each line is proportional to the area subtended by the spectrum of the corresponding line, namely $A_{1.06}$ and $A_{0.91}$. From Figure 4.8 we measured

$$\frac{S_{1.06} P_{1.06}}{S_{0.91} P_{0.91}} = \frac{A_{1.06}}{A_{0.91}} = 0.42 \qquad (4.3)$$

For our system, $S_{0.91}/S_{1.06} \simeq 3.45$, so that from the measured value P_f (Equation 4.2) we deduced $P_{1.06}$ and $P_{0.91}$ simply from

$$P_{1.06} = 1.45 P_{0.91} = 0.296 P_f \qquad (4.4)$$

$$P_t = P_{1.06} + P_{0.91} = 0.5 P_f \qquad (4.5)$$

where P_t is the total fluorescence power carried by the 1.06 μm and 0.91 μm lines. The slope efficiency $s_{1.06}$ for the 1.06 μm line is therefore related to the total slope

(a)

(b)

860 nm   890 nm   920 nm   950 nm

(c)

1048 nm   1058 nm   1068 nm   1078 nm
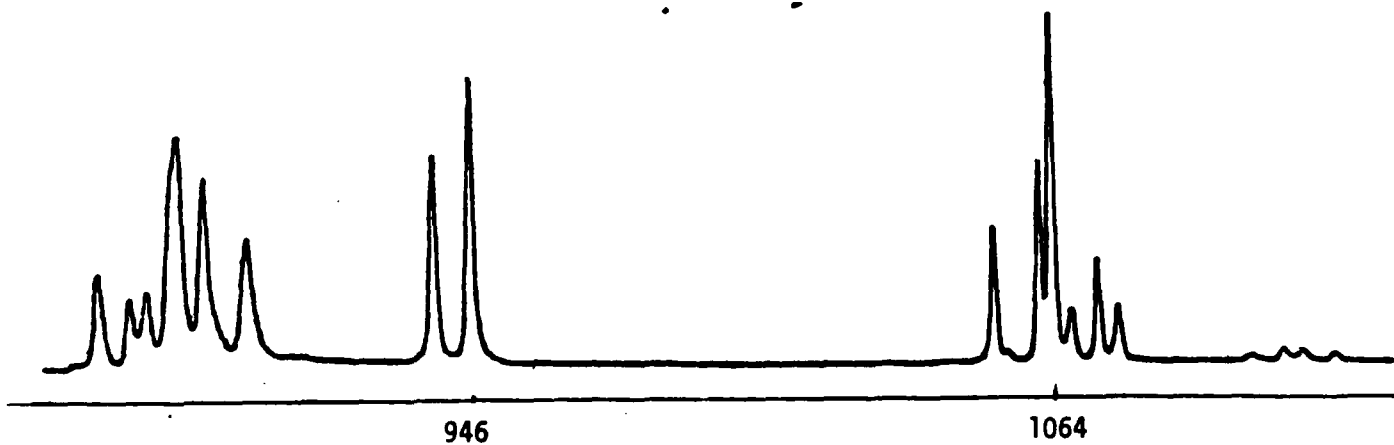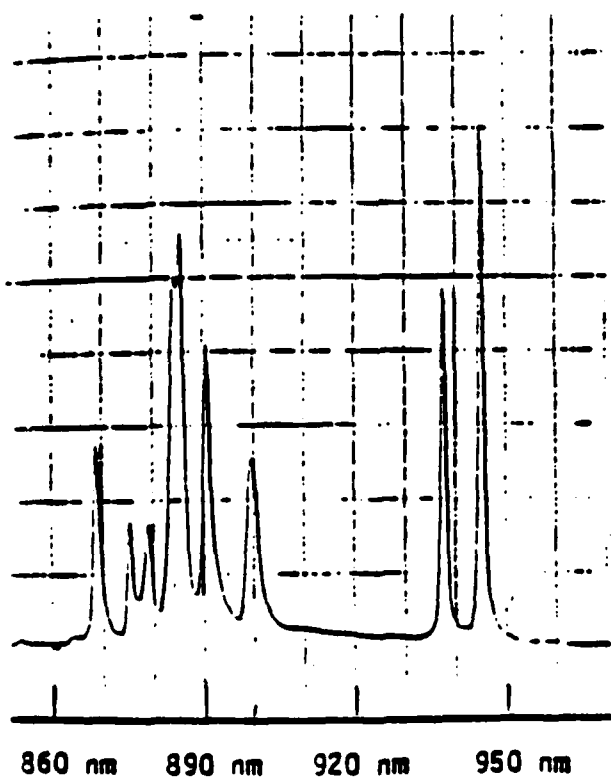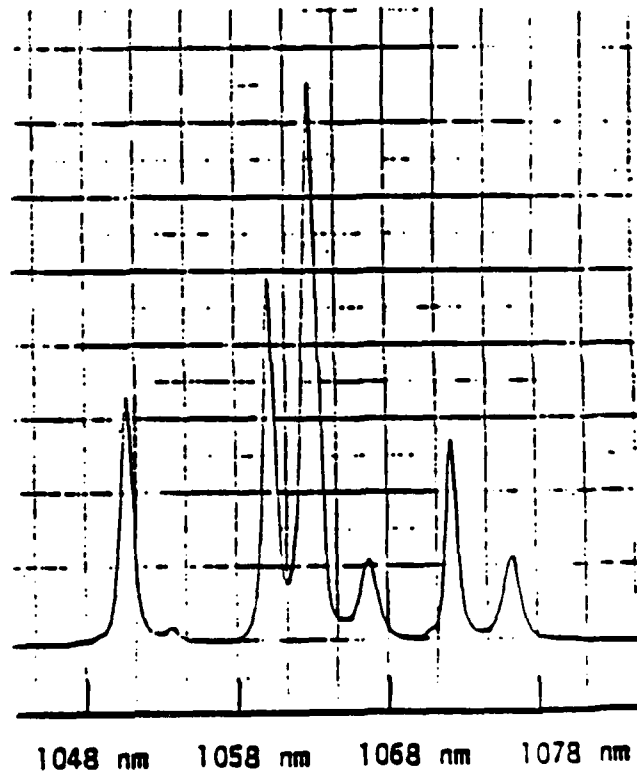
Figure 4.8--(a) Fluorescence Spectrum of Nd:YAG Fiber Pumped at 600 nm. (b) Detailed Spectrum around 900 nm. (c) Detailed Spectrum around 1060 nm.

efficiency $s_t = P_t/P_{abs}$ by $s_{1.06} = 0.592 s_t$.

3.2 Absorption

The same measurement arrangement described in Figure 4.4 was used to measure the absorption coefficient (α_a) of Nd:YAG fibers at the pump wavelength, except for the color filter which was replaced by an infrared filter to cut off the fluorescence emission. Even in small diameter fibers ($\simeq 35\,\mu$m) the residual pump power unabsorbed by the fiber at the peak absorption wavelength was found to vary linearly with the power incident on the fiber, i.e., neither saturation of the absorption line nor two photon absorption were present.

From the measured value of the crystal fiber transmission, after appropriate corrections for the lens transmission and Fresnel reflection at the fiber ends, we calculated a total attenuation factor of about 4.5 cm^{-1}. This factor is the sum of the fiber loss factor, which is usually less than 1 cm^{-1}, and considered to be negligible compared to the absorption coefficient α_a. Similar values were obtained with all the Nd:YAG samples used regardless of their diameter and origin. To evaluate the amount of pump power absorbed by the fiber we therefore took the absorption coefficient to be 4.5 cm^{-1}.

In some experiments the pump pulse duration was only T = 600 μsec. The fraction η of steady state population inversion achieved at the end of these pulses was then only

$$\eta = 1 - e^{-T/\tau_f} = 1 - e^{\frac{-600}{230}} \simeq 0.93 \tag{4.6}$$

The effective emitted fluorescence power was then taken to be P_t/η.

4. Test Fibers

A large number of Nd:YAG fibers were tested under this program, varying

in core size, diameter smoothness, and cladding situation. These included glass-clad and unclad fibers, ranging from 20 to 120 μm in diameter and from 4 to 8.3 mm in length. Glass-cladding processes for Nd:YAG fibers were developed under a contract with Litton Systems, Inc., and cladded fibers were made available for use in the laser studies of the present contract. For each fiber the fluorescence versus absorbed pump power curve was carefully measured and calibrated, and the slope efficiency of the device as a fluorescent source was recorded as a function of the fiber core dimension. A certain amount of spread was noted in the slope efficiency of fibers with similar core sizes, attributed to different levels of fiber propagation loss. In each class of fiber size we therefore selected the results obtained from the lowest loss fiber.

In the following we will discuss the fluorescence emission properties of five Nd:YAG single crystal fibers, and of a Nd:YAG crystal rod for comparison purposes. The crystal rod was a 3 mm diameter and 8.3 mm long bulk crystal, in which the interaction occurs between TEM modes. For convenience the test fibers were numbered 1 through 5, in decreasing fiber core diameter. Their physical characteristics are listed in Table 2, including diameter, length, approximate diameter variations and cladding material. Fiber No.1 is fiber No. 2-4 of Array No. 2, an array of Nd:YAG fibers prepared earlier in this contract for resonant laser studies. All eleven fibers of this array were tested, and No. 4 was found to yield the best emission characteristics of all, as expected since it also produced the lowest threshold resonant fiber laser of this array.

Fiber No. 2 is the lowest loss fiber of an array of 5 diameter controlled fibers prepared by J. Nightingale at Stanford University under other auspices. These fibers were sandwiched between two pieces of Nd:YAG, where they were held in individual slots. The fibers were not bonded in the slots, but held in place by pressure. Mechanical protection was provided by a thin layer of gold deposited on

Table 4.2

Summary of the Properties of All Five Samples

No.	$\phi(\mu m)$	L(mm)	Coating	$P_{abs}/P_{p,inc}$	$s_t(\%)$	$s_{1.06}(\%)$
	3000 (∞)	8.3	Air	0.82	0.91	0.54
1	120	7.5	Epoxy	0.82	0.95	0.56
2	48	6.0	Gold	0.79	0.51	0.30
3	45	5.3	Epoxy	0.76	1.00	0.59
4	41	4.0	Glass	0.71	3.3	1.95
5	20	~4	Glass	0.71	2.1	1.27

the slots, which coated the outside surface of the fibers.

Fiber No. 3 is Fiber No. Y-116 (see Table 4.2). Its end-faces were polished as described in Section II.B. Fibers No. 4 and 5 are glass-clad fibers clad by an extrusion method under the Litton program as described above. They have high index glass cladding ($n_2 = 1.772$), and have respective diameters of 41 and approximately 20 μm. They were also mounted in a glass capillary prior to polishing. Fiber No. 5 is the smallest diameter crystal fiber optically tested to date.

E. Experimental Results

1. Emission curves

The output characteristic curves of all 6 samples are shown in Figure 4.9. The first general observation that can be made is that regardless of the fiber diameter and pump power level, the fluorescence signal was found to grow almost linearly with pump power. Second, with the exception of Fibers No. 2 and 5, the slope efficiency of the fiber devices increases as the fiber radius is reduced (see Fig. 4.9). Third, in the best case (Fiber No. 4 of Table 4.2) the maximum output in the 1.064 μm line was in excess of 6 mW for an absorbed pump power of only 200 mW. The total fluorescence output in the 1.064 and 0.9 μm lines was approximately 10 mW.
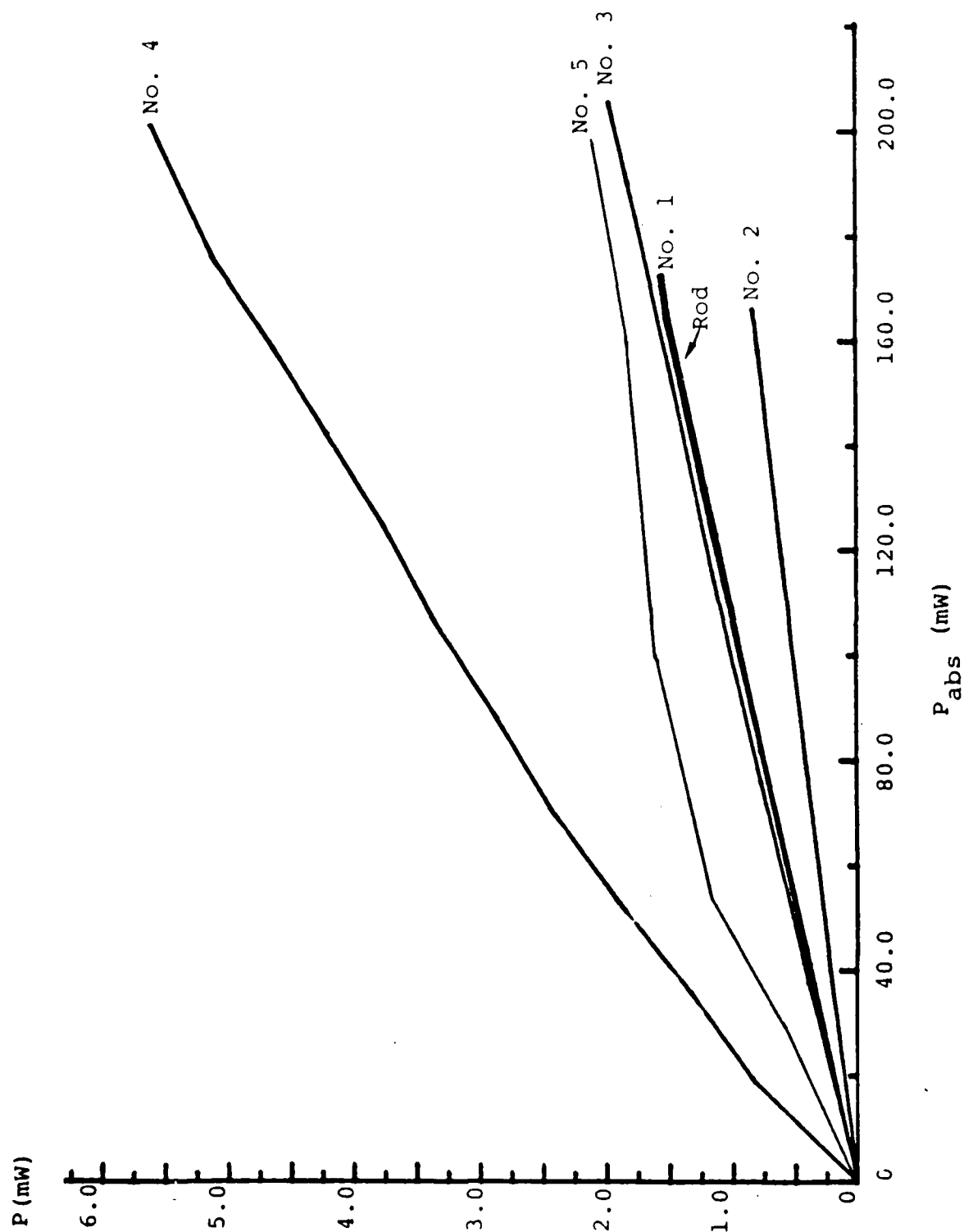
Figure 4.9--Total Fluorescence Output Powers versus Absorbed Pump Power for All Fiber Fibers Pumped near 600 nm.

These figures compare favorably with the sub-mW power levels currently available from commercial superluminescent laser diodes. However, the general behavior of the emission curves do suggest that the onset of superfluorescence was not reached in any of the tested fibers. To verify this point, we conducted two sets of independent measurements, described in the following sections.

2. Fluorescence Spectrum

The various fluorescence lines of Nd:YAG in the vicinity of 1.064 μm exhibit different stimulated emission cross sections and are therefore expected to experience different optical gains. As the pump power launched in a sample of Nd:YAG is increased this differential gain should result in a preferential growth of the highest fluorescence peaks of the material. In particular, the superfluorescent regime should be characterized by a definite increase of the dominant fluorescence line, and a drastic reduction in the relative height of the weaker fluorescence lines.

The fluorescence spectrum of a Nd:YAG bulk crystal was recorded in the 1.064 μm range, when the crystal was excited with a low level of pump power (about 10 mW incident on the crystal) at 514.5 nm. The spectrum was similar to the spectrum in Figure 4.8(c). In this low gain configuration, the intensity of the second highest peak, normalized to the intensity of the highest peak (see Figure 4.8(c)), respectively), is about 0.619. A similar intensity ratio was measured using Fiber No. 2 (also at low pump power). In both the rod and the fiber, this ratio was found to gradually decrease as the pump power was increased, as anticipated. In the rod the ratio was down to 0.559 (9.7 %) at an incident pump power of 2.0 watts (average intensity of about 80 kW/cm^2). In the fiber it was down to 0.571 (7.7 %) at 235 mW (about 30 kW/cm^2), which is consistent with the fact that the drop should scale like the pump intensity.

This evolution of the emission spectrum with excitation power, although

-- 188 --

significant, is certainly not as intense as what can be expected from a high gain medium. It tends to confirm our tentative conclusion that superfluorescence was not attained in our fibers in the conditions of our experiments.

3. Coupling to a Single Mode Fiber

The second set of measurements which was carried out to support this conclusion aimed at analyzing the mode content of the fluorescence emission. The Nd:YAG fibers having a large V number support a total number of guided modes N given by:

$$V = \frac{2\pi a}{\lambda}\sqrt{n_1^2 - n_2^2} \qquad (4.7)$$

$$N \simeq \frac{V^2}{2} \qquad (4.8)$$

where n_1 and n_2 are the refractive index of the core and cladding, respectively, a is the core radius, and λ is the signal wavelength. For the fiber under consideration (No. 4), $n_1 = 1.818$, $n_2 = 1.772$, and $a = 20.5\ \mu m$, so that $V = 50.3$ and the number of modes is $N \simeq 1000$. Of these N modes only the fundamental mode can be efficiently coupled into a single mode fiber. The fractional amount of fluorescence signal which can be coupled into a single mode fiber is therefore an indication of the relative amount of power carried by the fundamental mode in the signal. A large fractional power in the fundamental (i.e. highest gain) mode is expected at the onset of superfluorescence.

The experimental set up used to perform this measurement is shown in Figure 4.10. The output signal from the Nd:YAG fiber was first recollimated with a 10X objective, filtered to eliminate the residual unabsorbed pump power, and focussed into a short strand of single mode fiber with a second microscope objective. The silica fiber was single mode at 1.064 μm. The second objective was selected to
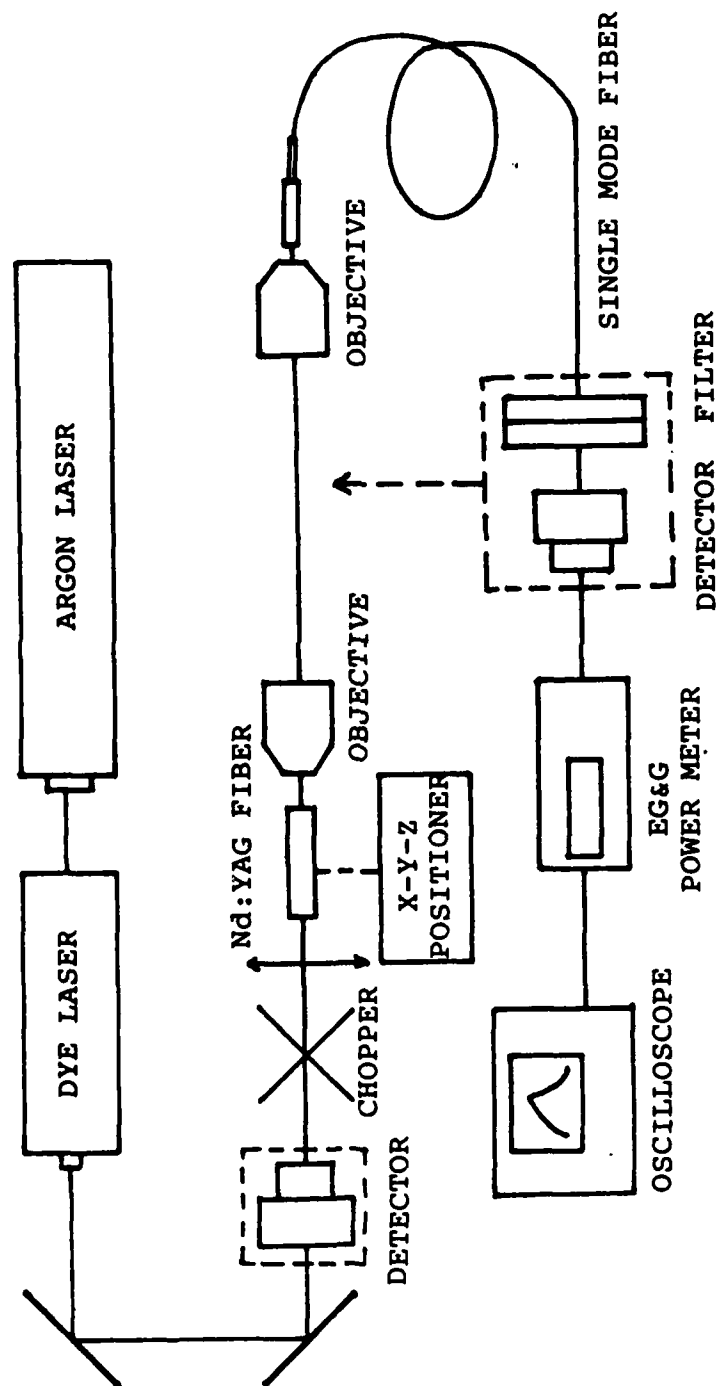
Figure 4.10—Schematic of Measurement Arrangement of LP_{01} Mode Output.

maximize the fiber throughput. We measured the ratio of the output power P_1 emerging from the second objective to the output P_2 from the fiber end. We found a ratio of P_2/P_1 of about 1/2000. Since it is reasonable to assume that the coupling efficiency of the fundamental mode into the fiber was less than unity, and generally on the order of 50 %, we can conclude that the fundamental mode made up about 2/2000, or 1/N, of the Nd:YAG fiber output. This ratio was found to be independent of the pump power launched into the crystal fiber. This test shows that (1) of the 5 mW of power generated by Fiber No. 4 at maximum excitation (see Figure 4.9), only 2-5 μW can be usefully coupled into a single mode fiber; and (2) no significant differential modal gain was present at an excitation intensity of about 10 kW/cm^2.

4. Discussion

4.1 Gain

As mentioned earlier, it was expected that the onset of superfluorescence, characterized by a nonlinear growth of the signal, would occur for a single pass gain on the order of 16 to 20 dB. The above results suggest that even in the smallest diameter fibers, and at the highest available pump powers, the gain was not sufficient to reach superfluorescence. It was expected that the single pass gain g in a Nd:YAG fiber could be:

$$g = \frac{\sigma \tau_f}{h\nu_p} \cdot \frac{P_{abs}}{A_p} F \qquad (4.9)$$

where $\sigma = 3.2 \times 10^{-19}$ cm^2 is the stimulated emission cross section, $\tau_f = 230\,\mu sec$ is the fluorescence lifetime of the upper laser state, $A = \pi a^2$ is the fiber core area, $h\nu_p = 2.15 \times 10^{-19} J$ is the pump photon energy (at $\lambda_p = 590$ nm), and F is a dimensionless overlap factor. When the fiber is pumped with the fundamental pump mode (LP$_{01}$), F is equal to 2.1 for the fundamental signal mode, and to a lower,

positive value for higher order signal modes. When the fiber is pumped uniformly, i.e. with a superposition of all the guided pump modes, F is equal to unity for all signal modes.

Using these numbers, it can be calculated that the single pass gain of the LP_{01} mode in Fiber No. 4 ($a = 20.5 \ \mu$m) is 0.24 dB/mW for the fundamental pump mode, and 0.11 dB/mW for a uniform pump distribution. At the maximum tested pump power of $P_{abs} = 200 \ mW$, the gain was therefore expected to be in the range of 23 to 48 dB, depending on the exact pump distribution in the fiber. The corresponding LP_{01} gain values for the other test fibers are summarized in Table 4.4.

It is clear from these gain estimations that for most fibers with diameters of 50 μm or smaller, superfluorescence should have been observed for absorbed pump powers of 200 mW. Yet the fact that the fluorescence spectrum of the emission did not change significantly with pump power level certainly indicates that the emission was not superradiant. It can therefore be inferred that the single pass gain was smaller than calculated. The model developed above assumes a perfect alignment between the pump and signal modes, which is a difficult condition to achieve in practice. A less than optimum fiber alignment, especially angularly with respect to the input pump beam, would result in a less than unity launching efficiency, the launching of higher order pump modes and a poorer signal-to-pump modal overlap. This argument is supported by numerous experimental observations of the strong dependence of the fluorescence output power on the angular alignment of the fiber. It was also observed in independent measurements that the gain in Nd:YAG fibers may be somewhat smaller than predicted for an LP_{01} pump mode, so that it is believed that the F factor may be closer to unity than to 2.1.

Another possibility is that the theoretical gain required to reach superfluorescence may be larger than 16-20 dB. The model used to derive this figure made a number of assumptions, including that of a single fluorescence line. In practice this situation

is not true for Nd:YAG, which exhibits several groups of fluorescence lines emanating from the same electronic state. This may well induce competition between the emission lines and somewhat increase the gain requirement. This effect has not been quantified under this study.

4.2 Fiber Loss

It is useful to evaluate the theoretical fluorescence output of a Nd:YAG fiber in the linear regime, i.e., below the superfluorescence threshold. If the Nd:YAG fibers were operated in this regime, one would expect, for a lossless fiber, a slope efficiency

$$s_t = P_t/P_{abs} = \frac{h\nu_s}{h\nu_p} \times \frac{\Omega^+}{4\pi} \qquad (4.10)$$

where $\Omega^+ = 2\pi[1 - cos(sin^{-1}(NA))]$ is the fiber solid angle in the forward direction, related to the fiber numerical aperture N.A. For Fiber No. 4, N.A. $\simeq (1.820^2 - 1.771^2)^{1/2} \simeq 0.42, \Omega^+ \simeq 0.58$, and s_t should be on the order of 2.8%. This value agrees well with the measured value of 3.3 % (see Table 4.2). It supports our belief that Fiber No. 5, and all fibers tested, were operated in the linear regime.

The primary motivation behind recording the absolute fluorescent level from a variety of fibers was to gain an understanding of the influence of the gain and loss on the superfluorescence emission. However, it appears that a direct quantitative comparison of the behavior of the fibers (and rod) is difficult for a number of reasons. First, the relative amount of fluorescence signal recaptured by the rod outer surface and subsequently recollimated and detected, is difficult to evaluate; in a fiber this problem does not arise due to the small transverse size of the fiber. Second, the fiber loss depends on the fiber diameter variations and cladding material, and therefore varies in an unknown fashion from fiber to fiber. Finally, the fiber loss is highly mode dependent, higher order modes experiencing much higher propagation losses than low order modes. The situation is therefore such that (1) comparison to

our theroretical model is difficult, and (2) direct comparison of the quantitative fluorescence power emission of fibers and rods is irrelevant.

However, a number of interesting qualitative conclusions can be drawn concerning each fiber, discussed below.

(1) The largest fluorescence signals were observed in Fiber No. 4. Measurements of propagation loss for this fiber under a contract with Litton Systems, Inc. indicated a very low loss coefficient for the fundamental mode (about 0.1 dB/cm at 1.06 μm), 3 to 10 times smaller than in unclad fibers of similar diameter. It also exhibited the highest measured ratio of gain (per unit pump power) to loss of any fiber laser of comparable or larger diameter. The fact that the highest gain to loss ratio fiber also yields the highest fluorescence signal is in agreement with both intuitive thinking and the predictions of our theoretical model.

(2) Fiber No. 3, with a similar diameter but epoxy as a cladding material yielded a smaller slope efficiency than Fiber No. 4, by a factor of 3-4. This difference can clearly not be attributed to the small difference in fiber diameters, but rather to the 3-10 fold loss reduction brought about in Fiber No. 4 by its index-matched cladding. These values were observed for several epoxy and glass clad fibers of similar diameter. This result would tend to indicate that the cladding reduces the loss of not only the LP_{01} mode, as inferred from oscillator measurements, but also of most higher order modes.

(3) Fiber No. 3 is partially clad with gold as a result of the polishing process it underwent (see Section II-C). It exhibited the lowest slope efficiency of all tested devices. This poor performance is believed to be caused by high propagation losses induced by the presence of a metallic cladding. Possibly higher than normal losses for the LP_{01} mode of this fiber were independently suggested by resonant oscillator tests (done under other auspices). As higher order modes would suffer even higher losses than the fundamental mode, the hypothesis of a significant propagation loss

induced by a metallic coating is a satisfactory explanation of our observations.

(4) The smallest diameter fiber tested (Fiber No. 5) was initially expected to exhibit the highest slope efficiency. However, its optical transmission, measured in the visible range away from an electronic absorption of Nd^{3+}, was much lower than that of any reasonably good crystal fiber, suggesting a loss coefficient on the order of $\alpha_l = 3.5$ cm^{-1} (for a multimode transmission). As a result, the relative absorbed pump power P_{inc}/P_{abs}, computed in Table 4.2 assuming a low loss fiber, needs to be corrected for this fiber by the factor

$$\gamma = \frac{\alpha_a}{\alpha_a + \alpha_\ell} \times \frac{1 - e^{-(\alpha_a + \alpha_e)\ell}}{1 - e^{-\alpha_a \ell}} \tag{4.11}$$

With $l = 4$ mm and $\alpha_a = 4.5$ cm^{-1}, $\gamma = 0.56$. The multimode fluorescence signal propagating in this fiber can also be expected to suffer similar losses. Therefore the slope efficiency of this device would have been at least $1/\gamma$, i.e. about twice as large as what was observed, had the fiber loss been more reasonable.

Inspection of this fiber prior to the cladding process revealed sizeable diameter variations, on the order of 25 % peak to peak, as well as a slow tapering of the diameter between 10-15 and 20-25 μm over a centimeter length. To simplify the already complex process involved in the generation of such small fibers, no attempt was made to actively control the fiber diameter during growth. The poor diameter stability of the fiber explains the high loss and strong mode scattering observed in this fiber, and its relatively low performance.

Figure 4.9 also shows that the slope of Fiber No. 5 is much less linear than that of the other samples. As the pump power was increased the fluorescence growth was found to roll off sharply. Two mechanisms have been suggested for this effect. First, nonlinear absorption in Nd:YAG, with the concommitant emission of a fluorescence signal in the blue part of the spectrum; this mechanism requires high pump power intensities, which would explain that it is observed only in the smallest diameter

fiber, and to a lesser extend in Fiber No. 4. Second, variation of the pump input coupling efficiency as the pump power is increased, due to the power dependent mode size of the pump laser beam; only Fiber No. 5 was small enough to be strongly susceptible to this dependence. This phenomenon was ..ot investigated any further because of the high loss of this fiber, but is kept in mind as a potential future point of interest.

F. Conclusions

The above analysis of fluorescence emission in Nd:YAG fibers leads to several interesting conclusions. Although we failed to observe the output characteristics anticipated from theoretical considerations for a superfluorescent device, we did observe a high multimoded output signal from 20-50 μm core diameter fibers. Conversion slope efficiencies in excess of 1% (in the forward direction) were also routinely recorded in several samples, corresponding to a net improvement by a factor of 3-4 over unguided bulk devices. In this respect alone the advantage of a fiber configuration was definitely established. This study also included fluorescence emission testing of 20 μm core, glass-clad Nd:YAG fibers. To the best of our knowledge these are the smallest single crystal fibers for which such emission data have been obtained.

Fluorescence spectrum analysis indicated the presence of a small degree of superfluorescence at the highest pump intensities tested, yet not nearly as much as what was expected from theoretical predictions. This point was confirmed by other experimental observations, in particular a poor mode discrimination, leading to a low coupling efficiency of the emitted signal to a single mode fiber. It is believed that the actual optical gain in the fibers may have been somewhat smaller than calculated, and/or that the gain threshold for superfluorescence predicted by the theory is underestimated. It was suggested that the multiplicity of fluorescence lines

in Nd:YAG, which was not included in our model, may be responsible for the latter.

A positive aspect of this investigation is that it emphasized the importance of loss reduction in single crystal fiber devices. The highest conversion efficiencies were observed in the lowest loss fibers, and the lowest conversion efficiencies in the highest loss fibers. With regard to this loss issue it was made clear that the presence of an index-matched cladding greatly reduced the fiber loss not only for the lowest order mode, as was shown in other studies, but probably also for higher order modes. This conclusion is important as it points out future directions in the development of superfluorescent fiber lasers.

At the end of this study, it became apparent that the search for superfluorescence in active fibers needs to address the possibility of utilizing even smaller diameter fibers than we did. The development of single mode waveguides is clearly the most logical next step in this area, again with an emphasis on small propagation losses. In the single crystal fiber area, this goal may not be achieved in the near future with Nd:YAG, although some loss reduction can definitely be expected for the 20 μm fibers ($V \simeq 24$) developed for this work. Nd-doped MgO:LiNbO$_3$ fibers, studied elsewhere in this report as resonant oscillators, may offer a more direct solution, as diffusion cladding methods available for this material are expected to provide near single mode waveguides in the near future. Despite the unknown represented by their residual susceptibility to photorefractive damage, we believe that they currently represent the most promising material in a fiber form to be evaluated as superfluorescent sources. Finally, further theoretical studies of superfluorescence in multiple line materials, although not crucial, may provide a better description of the behavior of these fibers.

V. OPTICAL ISOLATOR AND ISOLATED SOURCE USING YIG

A. Introduction

It is a well known fact that laser characteristics can be adversely affected by light reflected back into the laser cavity. Narrow linewidth and high-stability lasers are particularly sensitive to retro-reflections. The surfaces producing the retro-reflections create, in essence, an external cavity which competes with the laser cavity, degrading the laser linewidth, frequency stability, and amplitude stability. In particular, the desirable characteristics of the fiber lasers developed under this contract could be adversely affected by optical feedback.

One way of avoiding the optical feedback problem is through the use of an optical isolator. An optical isolator is a device which allows optical energy to pass in one direction with little attenuation, and blocks optical energy traveling in the opposite direction with large attenuation.

A miniature optical isolator which is compact, rugged, and adjustment free has been developed under this contract which is suitable for use with fiber lasers. The non-reciprocal operation of the isolator is obtained by exploiting the Faraday effect. Polarized light travelling in one direction is rotated with the opposite handedness as light traveling in the opposing direction. If the amount of Faraday rotation is 45 degrees, then light traveling between two polarizers set at 45 degrees with respect to one another will be passed when traveling in one direction, and blocked when traveling in the other direction.

B. Miniature Optical Isolator

1. Description

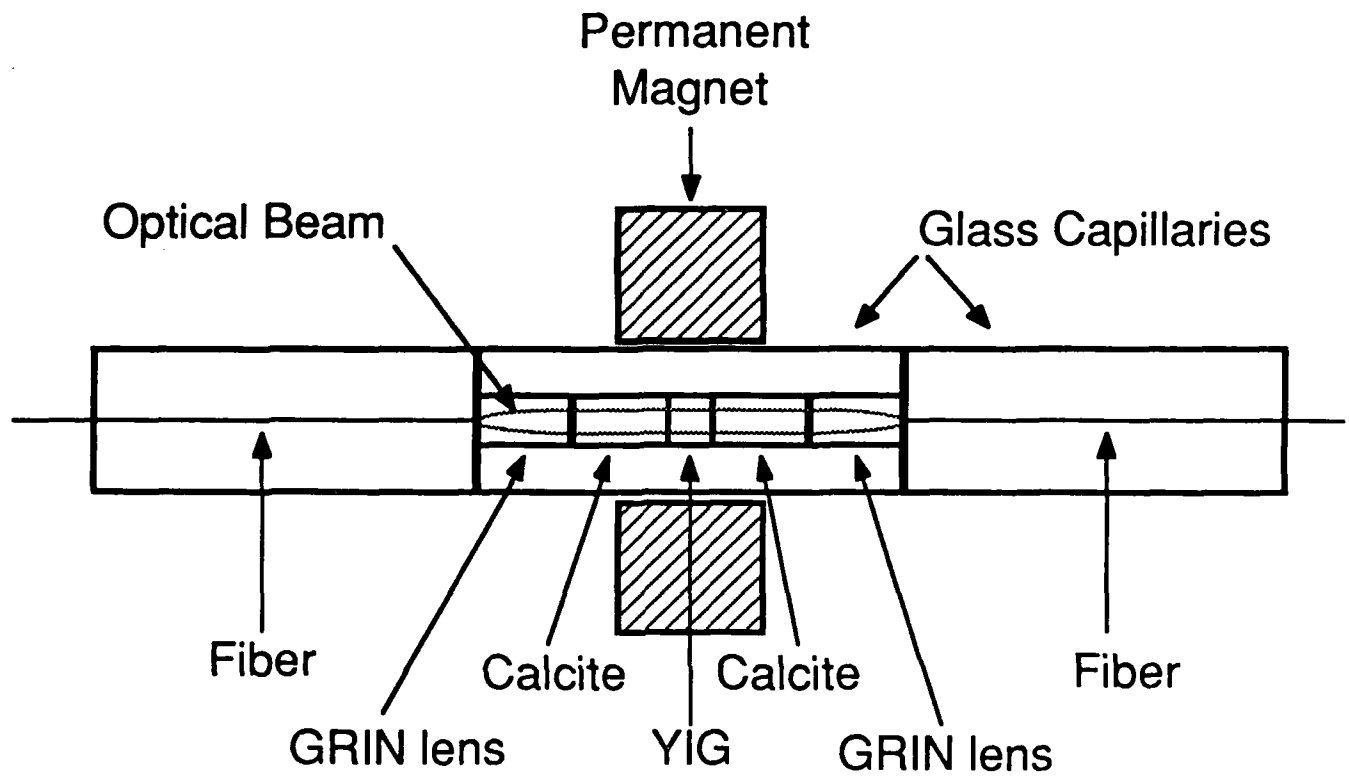The miniature optical fiber isolator is shown in Figure 5.1. In the center of

Figure 5.1--Miniature Optical Isolator.

the device is a section of YIG cylinder in bulk form. On either side of the YIG are calcite crystals, and outside of the calcite crystals are GRIN lenses which collimate the optical energy from one optical fiber and into the other optical fiber, on opposite sides of the device.

2. Principle of Operation

The operation of the device is as follows. The output of a fiber laser is coupled into a single-mode optical fiber. This fiber leads to the miniature isolator. Let this fiber be the input fiber. The gradient index lens collimates the light emanating from the fiber into an expanded parallel beam . The collimated beam passes through the calcite crystal. The calcite crystal is oriented such that the plane of polarization of the ordinary ray is in the vertical direction. The ordinary and extraordinary beams are separated spatially after traversing a finite length of the calcite crystal, due to Poynting vector walk-off of the extraordinary beam, i.e. double refraction. The separated beams then pass through a length of YIG crystal which is resident in a saturating axial magnetic field. The length of YIG is such that a 45 degree rotation in the plane of polarization is produced. The spatially separated and polarization rotated beams then pass through a second length of calcite crystal, where the ordinary beam remains undeflected and the extraordinary beam propagates at a slightly different angle with respect to the ordinary ray again due to Poynting vector walk-off, as in the first length of calcite crystal. The following GRIN lens focuses the separated beams into two separated spots. The output fiber is positioned to accept the ordinary beam and not the extraordinary beam, acting as a spatial filter Thus, input light vertically polarized and traveling in the forward direction will pass through the device with little attenuation.

Light traveling in the reverse direction is not transmitted as described above. When light enters the output fiber of the isolator, the first calcite crystal separates

the beam into ordinary a d extraordinary beams. The extraordinary beam is slightly deflected, as in the input case, and is later rejected due to the spatially filtering action of the fiber on the other side of the device. The ordinary ray now needs to be considered. This ray traverses the YIG crystal and receives a 45 degree rotation in its plane of polarization. This rotation does not bring the plane back to the vertical direction however, but due to the non-reciprocal nature of the Faraday effect, the plane of polarization rotates into the horizontal plane. This direction of polarization now appears to the second calcite crystal as an extraordinary beam, and is deflected from the path of an ordinary beam. The fiber at the far end of the isolator rejects this beam, as it has been displaced from the fiber core position after travelling the length of the calcite crystal. Thus both returning beams are rejected by the isolator by the non-reciprocal polarization rotation, double refraction, and spatial filtering on the return path.

C. Isolation of a Fiber Laser

1. Evaluation of Laser Stabilization

A Nd:YAG fiber laser, developed previously under this program, was tested in conjunction with the miniature optical isolator. The goal was to measure the improvement in amplitude stability of an isolated fiber laser over a non-isolated fiber laser.

2. Controlled Feedback

Several methods of introducing feedback into the fiber laser were considered, not a trivial task to perform in a simple, controllable, and easily analyzable fashion. Reflective splices or mirrors at the end of a fiber would certainly provide feedback to the laser, but it would be difficult to measure and control the amount of feedback being generated. It was desired to be able to introduce or remove the feedback

signal without otherwise disturbing the optical circuit, so that any degradation or improvement in laser performance with and without the optical isolator could be directly attributed to the action of the isolator. Also, the testing method chosen should have the characteristic of allowing the discrimination of feedback induced laser noise from laser noise originating from other sources.

The feedback to the fiber laser was provided by a Sagnac loop. A Sagnac loop, or interferometer, consists of a single fiber directional coupler which has the two output fibers connected together through a fiber delay line loop, as shown in Figure 5.2. Light entering the coupler is split into two parts, each part traveling around the Sagnac loop in opposite directions. The two optical signals enter the same directional coupler, this time in the reverse direction, are recombined, and travel back towards the source. The amount of feedback can be easily controlled by adjusting the coupling coefficient of the directional coupler, or by adjusting the coupling between the optical isolator and the input fiber to the Sagnac loop.

Also included in the Sagnac loop was a phase modulator. The purpose of the phase modulator was to provide phase modulation sidebands. The two counter-propagating optical signals are both phase modulated by the phase modulator. After passing through the directional coupler, the recombination of the two phase modulated optical carriers results in constructive and destructive interference. This interference occurs at the same frequencies as the phase modulation sidebands. In this way, the phase modulation sidebands are converted to amplitude modulation sidebands by the Sagnac interferometer. Thus, the amplitude modulated optical carrier fed back into the laser allows the easy identification of laser noise induced by feedback from the Sagnac loop. The controlled optical feedback simulates a real optical system, which often unavoidably returns laser power back to the laser.
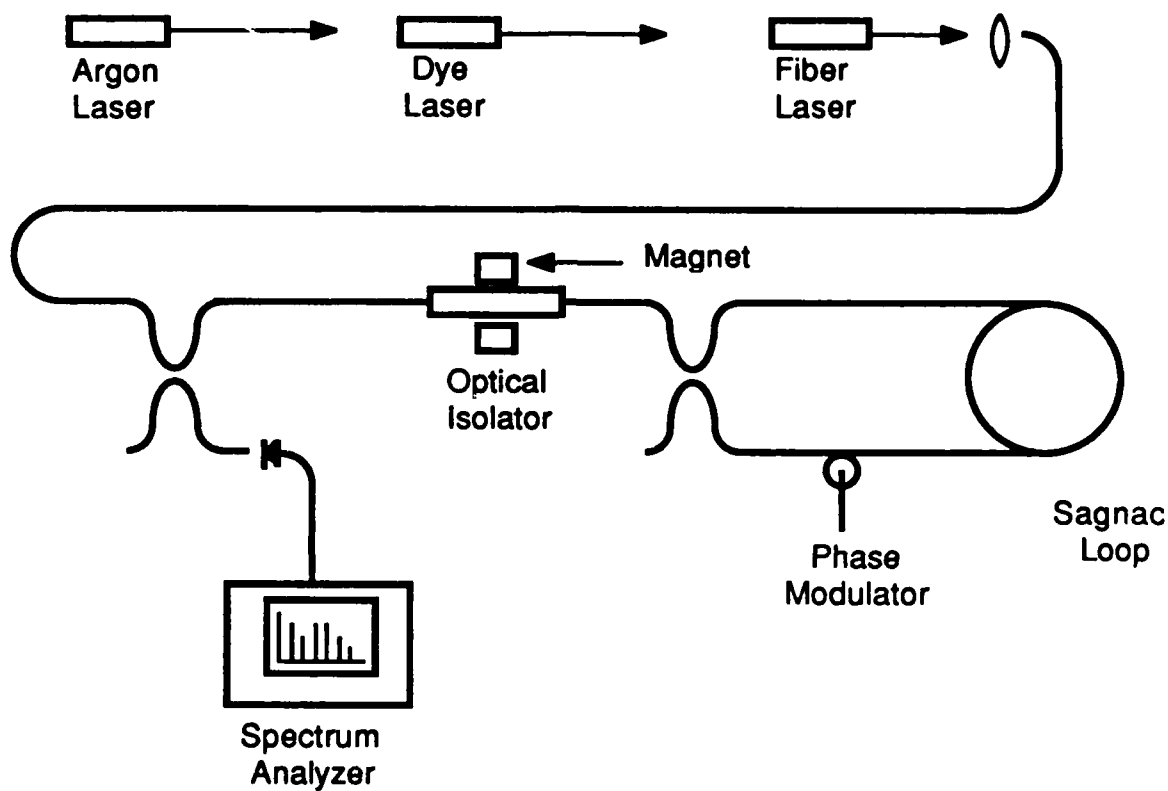
Figure 5.2--Experimental Set-up used to Determine the
Improvement in the Noise Characteristics
of the Nd:YAG Crystal Fiber Laser when
Operated with the Prototype Optical Isolator.

3. Controlled Feedback Experiment

The experimental set-up used to test the isolated fiber laser is also shown in Figure 5.2. The principle of operation of the test was to provide modulated feedback into the fiber laser, and to look for disturbance in the fiber laser output related to the modulated feedback. The modulation of the feedback allowed the discrimination between the effects of feedback and other possible sources of noise.

Three tests were performed. The first test was to measure the output characteristics of the fiber laser without any feedback. The second test was to measure the output characteristics of the fiber laser in the presence of optical feedback. The third test was to evaluate the degree of isolation provided by the functioning optical isolator in the fiber circuit following the fiber laser.

An argon laser emitting approximately 2 watts at 514 nm in the green was used to pump a dye laser emitting approximately 200 mW at 590 nm in the yellow, which was then used to pump a Nd:YAG fiber laser developed earlier under this program. The fiber laser emitted 1.3 μm light at approximately 2.5 mW. Approximately 50% of the output from the Nd:YAG fiber laser was coupled into a 1.3 μm single-mode telecommunication fiber. This fiber passed through a directional coupler where some of the light was tapped off for laser noise monitoring purposes. The other output of the first fiber coupler was used to controllably reflect light back to the fiber laser.

The feedback to the fiber laser was provided by a Sagnac loop, consisting of a second fiber coupler and approximately 550 meters of 1.3 μm single-mode fiber. The Sagnac loop contained a PZT phase modulator. The phase modulator was driven at approximately 450 kHz and with a large enough amplitude to generate many sidebands. The drive level was set to maximize the 8th, 9th, and 10th harmonics, where a good signal-to-noise ratio could be obtained.

The optical isolator was situated between the laser and the Sagnac loop. The

fiber-to-fiber insertion loss of the optical isolator in this experiment was measured to be approximately 1.7 dB. Two air gaps existed in the tested implementation of the optical isolator. Approximately .8 dB of the insertion loss could be due to the .2 dB Fresnel reflection at each air-glass interface. In the desired implementation of the optical isolator without air gaps, the insertion loss should be less than 1 dB.

4. Experimental Results

The spectral characteristics of the fiber laser under the condition of no optical feedback were measured by physically decoupling the Sagnac loop from the optical isolator. Displayed in Figure 5.3 is output of the fiber laser detected with a PIN photodiode under the condition of no feedback, as viewed on a spectrum analyzer. The increasing amount of noise around D.C. is due largely to the argon laser. However, at frequencies greater than 3 MHz, the noise level of the laser has dropped to near that of the electronic noise floor of the spectrum analyzer. This is the region of the laser output spectrum which was used for the laser noise measurements. Again, this is the output of the fiber laser without any feedback from the Sagnac loop, which was physically disconnected at the time.

The second test was performed with the fiber circuit as shown in Figure 5.2, including all the elements of the optical isolator except for the removal of the permanent magnet around the optical isolator. The removal of the permanent magnet deactivated the optical isolator, allowing light to be transmitted equally in both directions. The reason for leaving the deactivated optical isolator in the optical circuit was to avoid the effects of inserting or removing optical elements of the isolator from the fiber circuit. This was important in terms of avoiding introducing unnecessary insertion loss, which would provide some isolation of the fiber laser on its own, and could be erroneously attributed to action of the optical isolator. With all the elements of the optical circuit shown in Figure 5.2 in place,
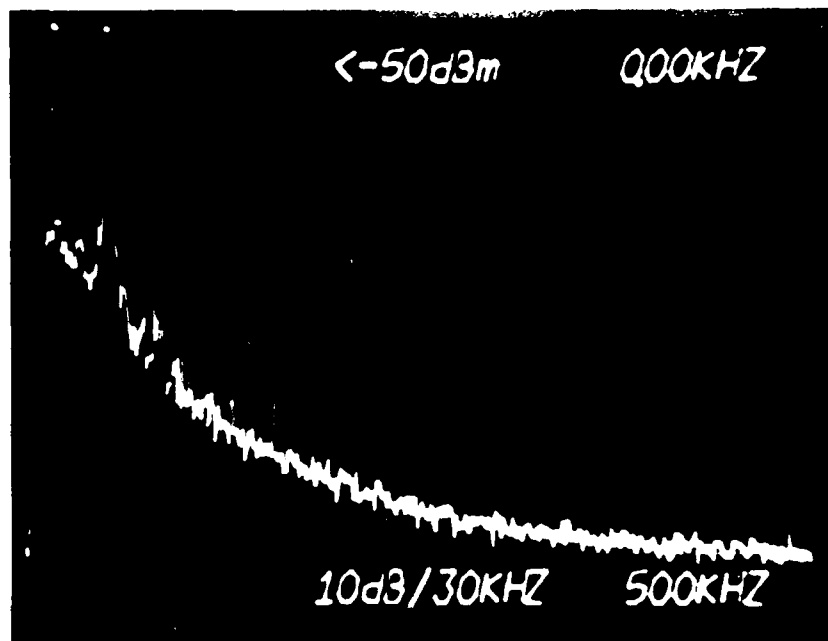
Figure 5.3--Output of the Nd:YAG Fiber Laser without
Feedback. The Large Amount of Noise at
Low Frequencies is from the Argon and Dye
Lasers preceding the Fiber Laser.

except for the magnet, the effect of the optical feedback from the phase modulated Sagnac loop into the fiber laser was then measured at the output of the first coupler and displayed on the spectrum analyzer. In Figure 5.4(a), the output spectrum of the fiber laser is displayed after the Sagnac loop was connected to the output of the isolator components, minus the permanent magnet. The Sagnac loop provided a large amount of optical feedback to the isolator and the laser, as the lack of the permanent magnet prevented the proper operation of the optical isolator. The degradation in the fiber laser output is clearly visible as large intensity fluctuations at the same locations as the phase modulated side bands generated in the Sagnac loop.

The third test was performed with the permanent magnet placed over the optical isolator components, resulting in a functional optical isolator. The output of the isolated fiber laser was measured at the output of the first coupler. The reduction in laser noise sidebands related to the modulation frequency of the phase modulator in the Sagnac loop was identified, and attributed to the action of the miniature optical isolator. With the addition of the permanent magnet around the optical isolator components, a dramatic reduction in noise sidebands in the fiber isolator output can be noted. This is displayed in Figure 5.4(b). The reduction in the noise sidebands can be seen to be approximately 40 dB in this experiment.

Improved accuracy in the adjustment of the calcite crystals can be expected to further increase the rejection ratio of the isolator.

5. Conclusion

We have designed, fabricated, and tested a miniature optical isolator which provided a feedback suppression ratio of 40 dB and an insertion loss of 1.7 dB when tested with a fiber laser developed previously under this program. The miniature optical isolator is a polarizing optical isolator, which is desirable for fiber lasers. In
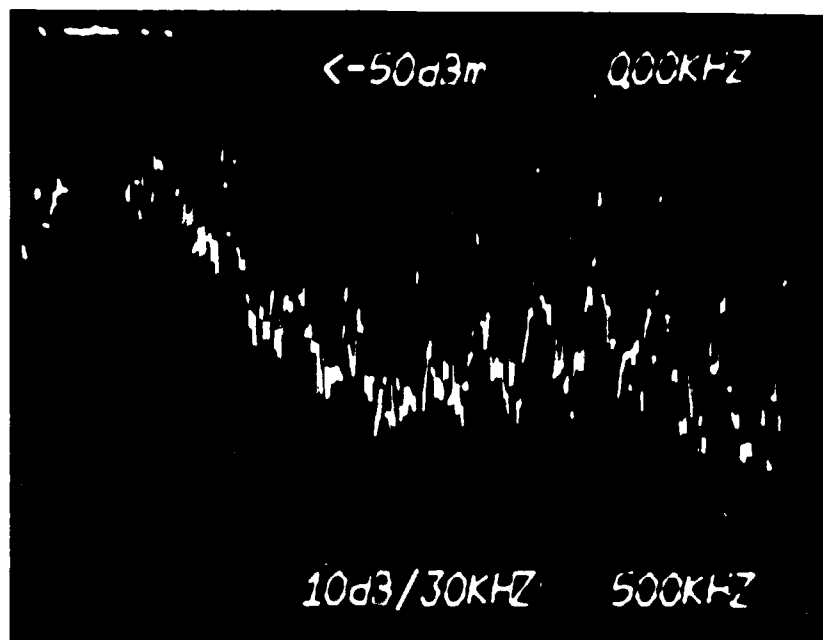
Figure 5.4(a)--Output of the Nd:YAG Fiber Laser with Feedback
from a Sagnac Loop Containing a Phase Modulator
Operating at .45 MHz. The Phase Modulator is
Being Driven Hard, Maximizing the 8th, 9th, and
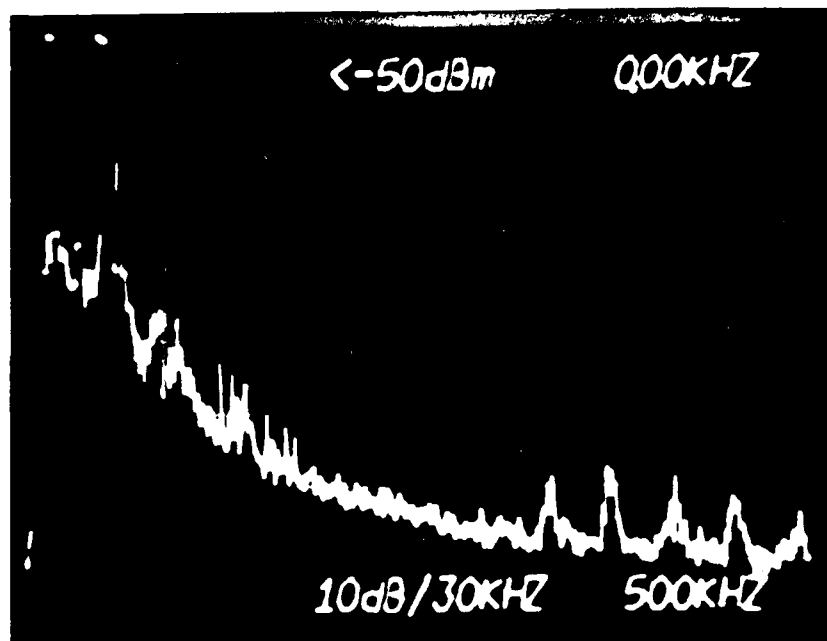10th Sidebands. Optical Isolator Deactivated.

Figure 5.4(b)--Output of the Nd:YAG Fiber Laser with Feedback,
and the Prototype Optical Isolator Activated.
Note the 40 dB Reduction in the Noise Sidebands
of the Fiber Laser, even with Non-optimal Adjust-
ment of the Optical Isolator.

addition, the potential applications of the isolator extend to many other types of

fiber systems.

END

Feb.

1988

DTIC